194(3), 2023

COMBUSTION ENGINES

Ergonomics and automation

Compliance: the regulations 2017/1151, EN 42341:2014, US EPA 40CFR 1065, 40CFR part 50

- Automation of measureme
- On-line measurement o
- Air buoyancy correctio
- Dynamic analysis of the quality of weighing
- Environmental conditions module

Automotive laboratories

RADWAG Wagi Elektroniczne
26-600 Radom, ul. Toruńska 5
tel. 48 386 60 00, e-mail: radom@radwag.pl

radwag.com

Due to the dynamic development of machine and vehicle powertrains, the "Combustion Engines" scientific journal, while retaining its historical title, currently publishes works related not only to internal combustion engines, but also other powertrains, including hybrid drives, electric drives and fuel cells.

PTNSS Supporting Members
Członkowie wspierający PTNSS

BOSMAL Automotive Research and Development Institute Ltd
Instytut Badań i Rozwoju Motoryzacji BOSMAL Sp. z o.o

Motor Transport Institute
Instytut Transportu Samochodowego

Institute of Aviation
Sieć Badawcza Łukasiewicz – Instytut Lotnictwa

Automotive Industry Institute
Sieć Badawcza Łukasiewicz – Przemysłowy Instytut Motoryzacji

Sieć Badawcza Łukasiewicz – Poznański Instytut Technologiczny

AVL List GmbH

Solaris Bus & Coach S.A.

Air Force Institute of Technology
Instytut Techniczny Wojsk Lotniczych

Military Institute of Armoured & Automotive Technology
Wojskowy Instytut Techniki Pancernej i Samochodowej

Toyota Motor Poland Ltd. Sp. z o.o.

RADWAG Balances and Scales
RADWAG Wagi Elektroniczne

MS Mechatronic Solutions Group

FOGO Sp. z o.o.

COMBUSTION ENGINES
A Scientific Magazine

2023, 194(3)

Year LXII

PL ISSN 2300-9896
PL eISSN 2658-1442

Publisher:
Polish Scientific Society of Combustion Engines
60-965 Poznan, pl. M. Skłodowskiej-Curie 5, Poland
tel.: +48 61 6475966, fax: +48 61 6652204
E-mail: sekretariat@ptnss.pl
WebSite: http://www.ptnss.pl
Papers available on-line: http://combustion-engines.eu

Contents

Publisher:
Polish Scientific Society of Combustion Engines
60-965 Poznan, pl. M. Sklodowskiej-Curie 5, Poland
tel.: +48 61 6475966, fax: +48 61 6652204
E-mail: sekretariat@ptnss.pl
WebSite: http://www.ptnss.pl

Subscriptions
Send subscription requests to the Publisher's address.
Cost of a single issue PLN 65.

Preparation for print
ARS NOVA Publishing House
60-782 Poznan, ul. Grunwaldzka 17/10A

Circulation: 60 copies

Printing and binding

Zakład Poligraficzny Moś i Łuczak, sp. j.,
Poznań, ul. Piwna 1

The journal is under the patronage of the Transport Committee of the Polish Academy of Sciences

The journal is registered and listed in the Polish and international database

Papers published in the
Combustion Engines
quarterly receive 100 points as stated by the Notification of the Minister of Education and Science dated 17 July 2023.

Declaration of the original version
The original version of the Combustion Engines journal is the printed version.

Cover
I – MAN D2862 Hydrogen Dual Fuel Engine *(www.man.eu)*;
background *(sunset, sun, glare, stones, sea, clouds – www.peakpx.com)*
IV – Graforce and Kawasaki Gas Turbine Europe GmbH
(www.businesswire.com/)

Article citation info:
Glogowski M, Wozniak M, Szydlowski T, Siczek K, Study on selected parameters of engine with the active combustion chamber. Combustion Engines. 2023;194(3):3-12. https://doi.org/10.19206/CE-165830

Michal GLOGOWSKI
Marek WOZNIAK
Tomasz SZYDLOWSKI
Krzysztof SICZEK

Combustion Engines
Polish Scientific Society of Combustion Engines

Study on selected parameters of engine with the active combustion chamber

ARTICLE INFO

Received: 15 March 2023
Revised: 27 April 2023
Accepted: 30 April 2023
Available online: 17 May 2023

The present study was focused on the combustion engine with a variable compression ratio (VCR), namely the four-stroke air-cooled engine with the active combustion chamber (ACC). An indicated pressure, torque, power, and specific fuel consumption of that engine were investigated experimentally as a goal of the present study. Experiments were conducted using two versions of an engine. Two parameters particularly influencing the ACC engine performance including the maximum compression ratio CR_{max} and the indicator γ_{fm} determining the correct operation of the ACC system, were described. It was found that the ACC engine allowed avoiding detonation combustion without changing the amount and composition of the combustible mixture, and even without delaying the ignition advance angle. In addition, the possible range of control of the combustion process allowed the ACC engine to operate with different types of hydrocarbon fuels, for example, in the form of petrol with various alcohol admixtures. The very intense flow of the combustible mixture inside the cylinder of the ACC engine allowed describing the combustion in the ACC engine with zero-dimensional mathematical models with the dual Vibe function providing the proper characterization of the heat release process. The use of very high maximum compression ratios allows the ACC engine to operate to a certain extent as a Homogeneous Charge Compression Ignition (HCCI) engine with high lambda coefficients.

Key words: *combustion engine, active combustion chamber, variable compression ratio*

1. Introduction

Each internal combustion engine has its characteristic design parameter called the geometric compression ratio which is the ratio of the maximum volume of the combustion chamber at the bottom dead center (BDC) piston position and the minimum volume of the combustion chamber at the top dead center (TDC) piston position. In conventional engines such design parameter is constant, which is not optimal from the point of view of the heat release in the combustion process and emissions, especially under altering conditions of load and speed during city driving [26]. The most common combustion parameters responsible for the loss of efficiency in an SI engine are knock, load fluctuations, misfiring, cycle by cycle fluctuations, etc. [48].

The improvement of the ecological and energetic performances of the modern piston engines is possible using, among other tools, variable compression ratio playing as one of the engine operation regulators [51]. Variable compression ratio (VCR) is more often applied in compressed ignition (CI) engines [15, 18, 27, 30, 36, 37], to name a few, and less in spark ignition (SI) engines supplied with various fuels, to which group belonged the engine investigated in the presented study.

In most known configurations of VCR engines, inter alia presented further in the article, the CR is changed in a predetermined way by additional elements, often based on an existing algorithm, and therefore with some delay in response to the measured value of pressure in the combustion chamber. To the authors' knowledge, the engine with active combustion chamber (ACC) analyzed in the present study is the first solution in which a variable compression ratio is implemented in the conditions of a vibrating system consisting of an auxiliary piston and a spring cooperating with it. This enables a much faster adaptation of the combustion chamber volume to the current value of the pressure inside it.

The study was aimed to determine an indicated pressure, torque, power, and fuel consumption of such an engine.

2. Present state of the development of VCR and ACC engines

2.1. The research on VCR engines

There are some studies on various VCR systems utilized in various engines.

López et al. [29] reported that the use of two-stage VCR systems allowed the extraction of high thermal efficiency with high CR at lower loads and extended knock-free high load operation with low CR. However, slow CR transitions led to fuel consumption penalties, pointing to the need for optimizing the control strategies of the VCR system. After such an optimization fuel consumption was reduced up to 4% compared to the fixed CR.

Wittek et al. [54] applied a two-stage VCR system to a mass production engine. They reported that switching to low CR took last less than 1 s. The fuel consumption can be lowered at part load in a wide area of the map. The investigated VCR engine exhibited a slightly higher friction than the base engine.

Using a series of eight-cylinder engines supplied with gasoline, Caris and Nelson [13] investigated the effect of CR on volumetric efficiency, mean effective pressure and indicated thermal efficiency. The best performance of the engine was obtained at an intermediate CR.

Ferrey et al. [17] noticed that coupling the VCR engine with the variable valve actuation (VVA) technologies was beneficial for the combustion process therein. There exists thermodynamic benefit from the enhancement of the geometric CR (CR > 18:1) in combination with VVA compared to VVT strategies, thanks to the use of Atkinson/Miller cycles. For the high compression ratio combustion

chamber geometries used with early or late intake valve closing strategies, an indicated efficiency enhanced up to 12 or 13% between compression ratio 10:1 and 18–20:1 at low loads (BMEP < 8 bar).

Nuthan et al. [38] conducted studies in wide open throttle condition (WOT) for speed range from 1200 rpm to 1800 rpm on a single-cylinder four-stroke VCR SI engine supplied with an equal-volume blend of methanol/gasoline fuel. The 14° BTDC ignition timing was maintained for all three different CRs (8, 9 and 10). Enhancing the latter from CR8 to CR10 for the methanol/gasoline blend increased combustion efficiency by enhancing the peak pressure and net heat release value by 27.5% and 30%, respectively at a speed of 1600 rpm. They reported that at CR10 at all engine speeds there was a 25% increase in BTE, and BSFC reduction by 19%, lowering CO and HC emissions by 30–40%. The NO_x emission enhanced with the increase of CR.

Qasemian et al. [40] studied effects of varied CR of biofueled SI engines on their thermal balance and waste heat recovery potential. They found that the heat loss to brake power ratio (Q_{ht}/W_b) was enhanced with the increase in the compression ratio. In addition, an enhancement of the compression ratio lowered the exhaust power to heat loss ratio (Q_{ex}/Q_{ht}) for all studied fuels. There existed a direct relationship between the ethanol in fuel content and Q_{ex}/Q_{ht} ratio. As the percentage of ethanol in fuel enhanced, the Q_{ex}/Q_{ht} ratio rose. Thus, the more the ethanol in the fuel and the less the compression ratio, the more the potential for the waste heat recovery of the IC engine.

Abdel and Osman [1] investigated the influence of the variable CR on the engine performance with various ethanol-gasoline fuel blends. They found that, for each fuel blend, there is an optimum CR giving the maximum indicated power.

Ozcan and Yamin [39] elaborated a computer simulation model of a variable-stroke-length LPG (liquefied petroleum gas) supplied, single-cylinder, four-stroke, SI engine. Numerical analysis was carried out at various engine speeds and corresponding power and torque.

Yuh and Tohru [58] studied the effect of higher CRs in two-stroke engines. They found a decrease in fuel consumption for each unit rise in CR in the range of 6.6–13.6. The maximum CR was limited due to knock and enhanced in thermal load.

Some researchers were also focused on emission analysis for a VCR engine [3, 24].

Studies on two-stroke and four-stroke engines showed the increased performance of the engine with VCR [2, 21].

The gain in efficiency beyond a certain CR can be strongly limited due to other influencing factors such as heat loss and friction [45].

There exists the upper limit of CR for the combination of fuel and SI engine beyond which there is fall in efficiency [49].

Roy et al. [46] noticed that compression ratio strongly affected the performance of an SI engine at different load conditions. Therefore, the VCR engine can be an effective solution to the problems encountered while operating an engine at varying load conditions. VCR engines allow more flexibility to the user, improvement in brake power, brake thermal efficiency, and torque while weakening emissions and specific fuel consumption.

Bas et al. [6] studied brake power and brake-specific fuel consumption of a variable compression ratio spark-ignited engine equipped with different spark plugs (conventional, iridium and platinum). They investigated the effects of hydrogen enrichment and VCR on engine operation at various speeds. They obtained higher performance values with iridium and platinum spark plugs compared with the conventional spark plug at all hydrogen fractions, engine speeds and compression ratios. The platinum spark plug enhanced the engine performance more than the iridium one.

Hammermueller et al. [23] found that especially for turbocharged SI engines, the variable geometrical compression ratio is beneficial in terms of part load efficiency and maximum power output. Using a conrod-based two-stage VCR system with an eccentric piston pin bearing, they analyzed the influencing parameters resulting from the fired engine operation, such as dynamic pressure stimulation in the crankshaft oil supply or the acceleration of the internal oil columns. The tests were conducted on a three-cylinder full engine in the entire engine map, for the speed range up to 6500 rpm, loads up to BMEP equal to 21 bar both in high and low compression ratio. They found, that only so called "hydraulic pretension" of the support chamber provided stiff force transmission in the low compression ratio stage.

Basu et al. [7] studied the performance of a VCR S.I. four-stroke engine with electrical loading and air cooling supplied with the blends of butanol and ethanol with proportions 10, 20, 30 and 40% in petrol. The brake thermal efficiency and brake specific fuel consumption (BSFC) were compared for the above-mentioned blends for different compression ratios and loads. They found that the brake thermal efficiency enhanced and the BSFC weakened with an increase of blend amount in petrol and no knocking occurred during the engine operation. The engine ran smoothly up to 40% blends in each case. The maximum efficiency was obtained for a 40% blend.

Using the homogeneous charge compression ignition engine supplied with gasoline fuel, Babagiray et al. [5] studied the effect of compression ratio, engine speed inlet air temperature, lambda value, and research octane number value on indicated mean effective pressure, indicated thermal efficiency, maximum pressure rise rate, specific fuel consumption, cyclic differences, and emissions including unburned hydrocarbons, carbon monoxide, and nitrogen oxide. The engine operation condition characterized by the compression ratio of 12, intake air temperature of 333 K, lambda value of 1.8, engine speed of 935 rpm, and RON40 was found as the optimal one for the HCCI engine. At this point, 5.08 of indicated mean effective pressure, 35% of indicated thermal efficiency, 243.28 g/kWh of specific fuel consumption, 4.43 bar/CA of maximum pressure rise rate, and 3% of COV_{imep} occurred. The optimum values of engine emissions were of 355.586 ppm for UHC, of 3% for CO, and very small value ppm for NO_x, respectively.

Depending on the performance necessity of a vehicle its VCR engine operates at compression ratios being varied via changing the combustion chamber volume. It is thermody-

namically beneficial, as the engine map shows [52]. At low power levels, such an engine operates at a higher CR to capture low fuel consumption while at high power levels the engine operates at low CR to limit knocking. The optimum CR is affected by inlet air temperature, engine coolant temperature, exhaust gas temperature, engine knock, fuel type, the octane rating of fuel, and other parameters. Also, the operating temperature is maintained at optimum allowing obtaining high combustion efficiency.

Rakopoulos et al. [41] elaborated a comprehensive, quasi-dimensional, two-zone combustion model allowing the prediction of the combustion characteristics, performance, nitric oxide (NO), and carbon monoxide (CO) emissions of high-speed spark-ignition engine. The model is validated on an experimental, Ricardo E6, mono-cylinder, high-speed SI engine operational over a wide range of compression ratios and (fuel-air) equivalence ratios (EQR). The engine was supplied with gasoline and operated under various CR and EQR values at WOT position.

2.2. The VCR strategy realization

The VCR strategy can be realized through [47, 56]:

- articulated monohead (Saab)
- piston of variable deck height (Daimler-Benz)
- eccentrics on crankshaft bearings (FEV)
- multilink rod-crank mechanisms (Nissan)
- secondary moving piston or valve in cylinder head (Ford)
- gear-based crank mechanisms (MCE-5)
- precisely shifted cylinder block with cylinder head assembly (Self-Developed Design).

Some realizations of VCR strategy include moveable cylinder block [14, 55], use of eccentric bearings for crankshaft and connecting rod and use of adjustable lever rod between crankshaft and connecting rod [8, 11, 22, 25, 33-35, 42, 43, 45, 50].

Roy et al. [46] elaborated the VCR engine with a cylinder head which was equipped with an actuator-driven movable ram for varying the clearance volume, and thus the compression ratio.

Wos et al. [56] elaborated and test engine with variable combustion chambers volume realized by the shifting of the cylinder block with head assembly perpendicularly to the crankshaft axis, causing the variation of the engine CR from 19 to 9.

López et al. [29] elaborated a two-stage VCR system applied to a downsized SI engine. The VCR mechanism comprised an eccentric element in the small end of the connecting rod, rotated to enhance/lower the effective connecting rod length, achieving the CRs of 12.11:1 and 9.56:1.

Wittek et al. [54] developed a VCR system comprising a connecting rod with eccentrically piston pin suspension and hydraulic moment support. Stiffness of support mechanism was affected by engine speed and load. System was robust against variations of pressure, temperature, and aeration in the oil feed stream. Dissipation effects occurring in hydraulic support pistons were negligible.

Brevick [10] developed a "Pressure Reactive Piston (PRP)" technology with modification of the piston geometry. The mechanism had a secondary piston in the secondary cylinder, which reciprocated inside the combustion chamber. The spark plug was installed in the secondary piston, which lowered the space requirement for exclusive mounting of the secondary piston.

Lin and Yang [28] proposed a dual shaft control variable compression ratio (DSC-VCR) engine based on a gear-driven eccentric sleeve. This DSC-VCR allowed for double larger gears to share the load, and for the engine operation with a larger eccentric size and a narrower adjustment range than for the other similar mechanisms. This mechanism allowed the engine operation with a larger overexpansion ratio (OER, the ratio of expansion stroke and compression stroke) under all conditions to increase engine efficiency.

The VCR engine comprising two control shafts rotating 180 degrees in the same direction to adjust the CR ratio was described in [32]. Timing gears were utilized for the rotation of the control shafts with two sets of journals. The first set of journals was concentric with the timing gears and mounted in conventional bushings in the crankcase. The second set of journals was eccentrically located on the control shaft. The eccentricity provided a change of cylinder head height relative to the crankshaft. The eccentric journals were mounted in eccentric bushings. The eccentric bushings were mounted in the cylinder jug.

The interesting realization of VCR in SI engine was achieved using the concept of the active combustion chamber (ACC) [20], presented in the next subchapter.

2.3. The ACC engine

The ACC engine is an engine in which it is possible to change not only the compression ratio, but also the method / degree of expansion, which in a way influenced the introduction of the name of the engine as a unit with an active combustion chamber. It is the inherent ability of the ACC engine to change the expansion ratio, which is practically not used in the currently used engines. The favorable course of the combustion process, and indirectly of charge exchange, characterized, inter alia, by the absence of detonation combustion, obtained by controlling the compression ratio, is mainly visible at very high maximum compression ratios above 20:1 [20, 21]. However, the existing limitations as to the possibility of increasing the overall efficiency of the combustion process in the implementation of the VCR strategy prompted the authors to consider the use of the additional degree of freedom to control the combustion process and charge exchange, which is provided by the variable expansion ratio to increase the said efficiency.

Figure 1 shows schematically the principle of operation of variable expansion in the ACC engine.

The diagram in Fig. 1 shows the essence of the ACC engine operation using the four mutual positions of the crank-piston system and the movable piston in the ACC system. The first item is when ignition occurs. The second is TDC, the characteristic position of the crank-piston system with a slight displacement of the additional piston from the ACC system. The third position is the maximum displacement of the auxiliary piston from the ACC system and a slight displacement of the crank/piston system. The last fourth is the completion of essential ACC operation (reaching the first minimum) of the engine cycle.

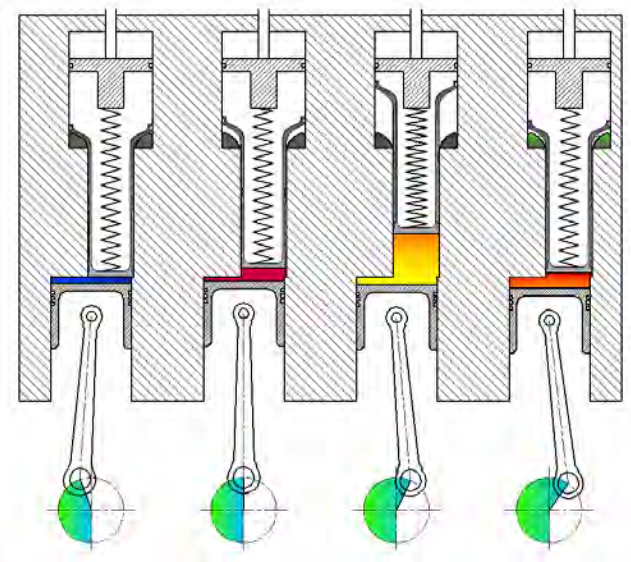

Fig. 1. The principle of variable expansion in the ACC engine

Figure 2 showed changes in the compression ratio in an engine with the ACC system within a fragment of one working cycle. The changes in the compression ratio were presented against the compression ratio values of the old and new SI engines, and the selected compression ratio values determined by the control system, achievable in an engine with a VCR system. The width of the blue lines corresponds to the observed fluctuations in the CR value.

In the exemplary ACC engine, the compression ratio, which the ACC automatically varied from a maximum of 17.5:1 to 16.7:1 over the compression stroke, changed by only 0.8 per cycle without causing detonation in the ACC engine cylinder. In the expansion stroke of the engine, the changed CR value, due to the ACC system operation, even reached the value of 13.2:1.

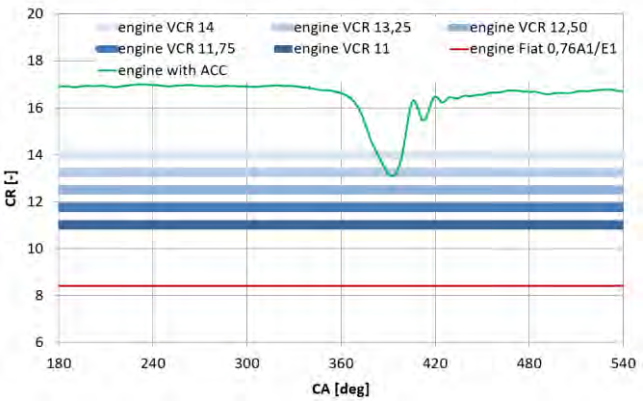

Fig. 2. CR changes in an engine with ACC within a portion of a single working cycle against the background of constant CR values in old and new SI engines and fixed CR values actuated by the control system in an engine with a VCR system

It can be seen from Fig. 2 that the concept of compression ratio regarding the ACC engine is strict, therefore the concept of the maximum compression ratio CR_{max} has been introduced. The maximum compression ratio is the compression ratio the ACC engine being achieved with the lowest position of the auxiliary piston in the ACC system (Fig. 1), expressed by equation (1):

$$CR_{max} = \frac{V_s + V_{C_{min}} + V_{ACC_{min}}}{V_{C_{min}} + V_{ACC_{min}}} \quad (1)$$

where: V_s – displacement volume, V_{Cmin} – the smallest possible volume of the combustion chamber, V_{ACCmin} – volume of the combustion chamber at blocking pressure.

During the bench tests, to obtain the lowest position of the additional piston in the ACC system, the blocking pressure p1 (i.e. the pressure at which the ACC system did not operate) was used, the value of which was experimentally determined to be equal to 14 bar, but it is not a constant value, but rather a design value. Referring to Fig. 1, the maximum compression ratio is to be understood as the compression ratio corresponding to the relative position of the auxiliary piston in the position in Fig. 1a and the position of the main piston in the position of Fig. 1b. To maintain the safe operation of the ACC engine, the movement of the additional piston was limited by the elastic support. As a result, further increasing the blocking pressure would cause a further, but only up to hundredths of a millimeter, asymptotic movement of the auxiliary piston towards the main piston, resulting in only a negligible increase in the maximum compression ratio. Therefore, the use of the wording VCR used in the understanding of the previous designs of engines with a VCR system in relation to the ACC engine must be considered inadequate. The displacement of the additional piston in the ACC system during the compression stroke is not constant not only under the conditions of a fixed working cycle, but even within a segment of such a cycle characterized by slight changes in pressure in the cylinder, because it has an oscillating nature with an amplitude that automatically adapts to the current pressure conditions in the chamber combustion.

3. The indicator determining the correct operation of the ACC engine

For the ACC engine, one indicator was distinguished, which was called the main design parameter of the ACC system, denoted by the symbol γ_{fm}. When introducing the indicator γ_{fm} to the analysis, which is responsible for the dynamic properties of the ACC system, it was assumed that it should not be associated with the pressure unit.

The indicator γ_{fm} was defined by the ratio of the additional area in the combustion chamber expressed in cm^2 to the mass expressed in kilograms of the complete additional piston, i.e., also considering the masses of sealing rings and O-rings connected to it. The indicator γ_{fm} was described by equation (2).

$$\gamma_{fm} = \frac{\pi d_1^2}{4m} \sim 0.7854 \frac{d_1^2}{m} \quad (2)$$

where: γ_{fm} – the indicator determining the correct operation of the ACC engine [cm^2/kg], d_1 – diameter of the additional piston in the combustion chamber [cm], m – mass of the additional piston [kg].

The diameter d_1 was shown in Fig. 3, while the other diameter d_2 also shown therein was selected in such a way as

to obtain the highest possible value of the indicator γ_{fm} while ensuring good pneumatic support properties.

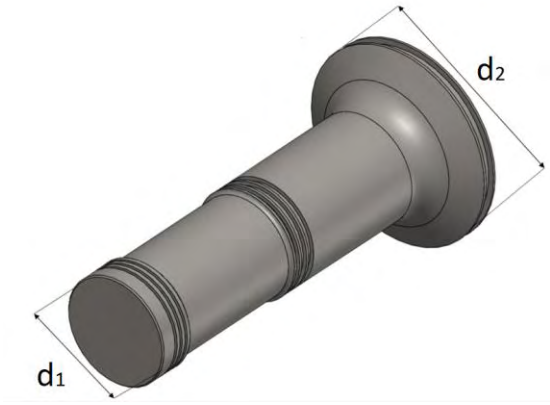

Fig. 3. Additional piston ACC system with its characteristic diameters d_1 and d_2

It should be added, it is desirable that its value does not deviate from the number one hundred taken as the reference value, since then the values of the phase shift after TDC corresponding to obtaining the maximum displacement of the ACC system piston with respect to the main piston were close to the minimum. During the iterative numerical and experimental design of an additional ACC system with an additional piston made of aluminium alloys, a favourable value of the indicator γ_{fm} was obtained, equal to 88 cm^2/kg. In the case of using magnesium alloys for this purpose, the value of 100 cm^2/kg was successfully exceeded even without obtaining the optimal strength properties of the piston [16].

During several years of experimental research, it was also noticed that for the proper engine functioning, the value of the indicator γ_{fm} should not be less than 75 cm^2/kg. Otherwise, the reaction of the system will be so delayed that the losses may outweigh the benefits, or, in the extreme case, the engine cycle will be distorted (broken), which has been observed many times during the tests.

This note does not apply to slow speed engines, i.e., not exceeding 1200 rpm, where lower values may apply due to the available cycle times, especially in large cylinders above 1000 cm^3. In such cylinders, the concept of multiplying the ACC system could also be possible or the use of more favourable proportions in the system itself, due to the amount of free space available in the cylinder head to be used. However, this requires further research.

At the initial stage of the research, in one of the tested ACC engines, solutions were applied in which the value of the indicator γ_{fm} was less than 70 cm^2/kg, or even less than 66 cm^2/kg, but the effects were completely destructive additionally combined with uncontrolled detonations before and after the TDC point. At the current stage of construction development, the indicator threshold γ_{fm} = 88 cm^2/kg has been exceeded, thus the first positive results, for a CR_{max} value above 19:1, were obtained.

The graph in Fig. 4 shows the values of the previously and currently used values of the indicator γ_{fm} and the range of their effective use is marked with a black dashed line. It should be emphasized that the black dashed line is an imaginary line, especially in the horizontal course of the value, which is primarily the result of the research observation, while its curvilinear part is a parabola reflecting uniformly accelerated motion with the assumed initial speed of an additional piston in the ACC system, calculated in a simplified mathematical model [16].

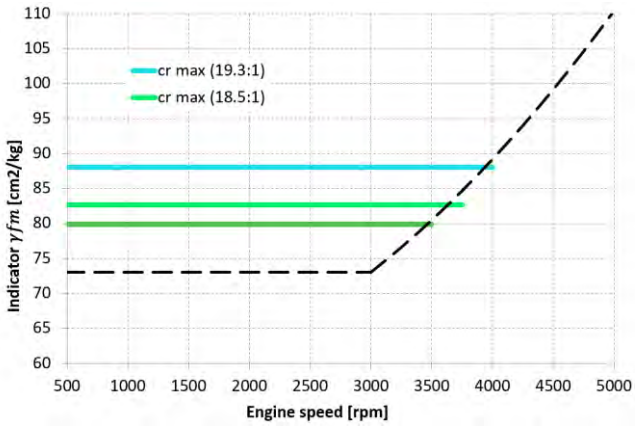

Fig. 4. The effect of the indicator γ_{fm} on the achieved maximum ACC engine speed

It can be seen from Fig. 4 that the increase in value corresponds to an increase in maximum engine speed ACC, but for that increased CR_{max} values can also be obtained. Unfortunately, the value of the main design parameter should not be associated directly with CR_{max} value, because there is always such a value of CR_{max} beyond which the phenomenon of detonation combustion occurs, caused by exceeding the auto-ignition temperature during compression. The reaction time of the additional piston can be too long to prevent such combustion even for the indicator γ_{fm} values above 100 cm^2/kg.

4. Materials and methods

The experimental tests were carried out on test stands (engine dynamometers) in which two different types of brakes were used, loading the tested ACC engines. The first was a water brake that enabled smooth load regulation and the use of wide range of loads and rotational speeds of the tested engine. This type of brake was used to measure an original air-cooled Fiat 126p twin cylinder SI engine (652 cc, 18 kW/4500 rpm, 42 Nm/3200 rpm) with a modified cylinder head incorporating an ACC system allowing a CR_{max} = 17.5:1. The second brake, on the other hand, was in the form of a generator (power generator) with known characteristics, connected with resistors of specific resistance and a voltmeter, enabling the load power to be determined. Another brake was used to load the air-cooled CI engine driving the original generator set PROTON OASIS-3. This air-cooled single-cylinder direct injection (DI) diesel engine (463 cc, 6.2 kW/6.8 kW at 3000 rpm) was modified to be SI one by introducing a cylinder head with the ACC system enabling the achievement of CR_{max} = 18.5:1 and CR_{max} = 19.3:1 in a stepwise manner. The use of the existing generator set to load the tested engine caused a certain inconvenience, consisting in the fact that its operating range (rotational speed) was electronically limited from the bottom, which meant that the engine could only be loaded in the speed range from 1750 rpm to 3750 rpm and only in this

range it was possible to test ACC engines on the stand. On both stands power, torque, and fuel consumption of the investigated combustion engines were determined. For the case of Fiat 126p engine it was also measured indicated pressure and temperature of exhaust gases.

The simulation tests of the ACC engine operation were performed with the use of proprietary software implemented in the C++ environment. Detailed simulation model was described in [16]. The mathematical model was based on the standard physical zero-dimensional [4, 19, 24] engine description with an additional mechanical oscillator [12, 31, 59]. The simulation model comprised over 200 parameters to reflect engine geometry variables, physical gas constants and their mixtures occurring in the ACC engine. The description of the model presented in this article was limited to the field of Vibe's [19] function application, modified by Bonatesta et al. [9]. The modified Vibe's function for the ACC motor correctly defines the generated heat for up to 80% of the engine load [16].

5. Results and discussion

5.1. Rated parameters and engine exhaust gas temperature

The values of specific fuel consumption (efficiency) achieved during the tests for several selected engine speeds and the rated load are shown in Fig. 5. The results are selected from more favourable measurements and approximated to the assumed engine speeds. The line width was associated with an error of measurement of ±4%. Single points where exceptionally good values of specific fuel consumption were obtained were omitted due to the impossibility of repeating the parameters of the mixture composition due to the carburettor supply system.

The specific fuel consumption values are shown in three colors in Fig. 5. Dark green color indicates the results achieved in the air-cooled four-stroke ACC engine with the maximum compression ratio CR_{max} = 17.5:1 and the largest range of engine speeds from 750 to 3750 rpm. In the case of this graph, it is worth noting the minimum speed of the ACC engine.

The light green color was used for the engine with the maximum compression ratio CR_{max} = 18.5:1, while the blue color was for the engine with CR_{max} = 19.3:1, i.e., with the highest compression ratio used during the tests. Such a high value of the compression ratio was achieved by rebuilding the diesel engine from a power generator with a CR = 20.5:1. As mentioned earlier, the rotational speed was limited by the electronic system cooperating with the generator (power generator) to a value of 3650 rpm. Therefore, during the tests, the speed value of 3500 rpm was adopted as a safe value. Using the base 1.5L four cylinder DVVT engine supplied with gasoline and the same engine with dual shaft control variable compression ratio (DSC-VCR) Lin et al. [28] conducted comparative studies for the 3 cases: the maximum torque case with 1750 rpm (case 1), the maximum power case with 5500 rpm (case 2), and the high efficiency case with 2300 rpm and a 75% load (case 3). For the consecutive case numbers, the BSFC was equal to 260, 330 and 220 Nm, respectively. The DSC-VCR decreased BSFC by about 6.19%, 8.07%, and 8.67% in comparison to the base engine for each case. Under case 1 the BSFC was close or lower compared to the cases of ACC engines analyzed in the present study.

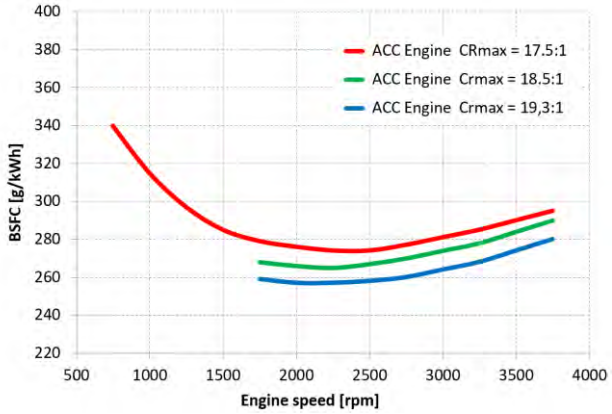

Fig. 5. The specific fuel consumption (BSFC) as a function of rotational speed for three CR_{max} values in the ACC engine

Another parameter which is important from the point of view of the ACC engine as a power generating device is its power to displacement ratio (power related to one liter of cubic capacity), as shown in Fig. 6. Obtained values of such a ratio did not exceeded value of 25 kW/L. In this case, the ACC engine in the previous two-valve versions without the variable valve timing system and turbo boost should be compared with naturally aspirated engines up to approximately 3750 rpm. When this value is exceeded, the torque starts to drop significantly, making the engine less efficient due to the falling in cylinder filling.

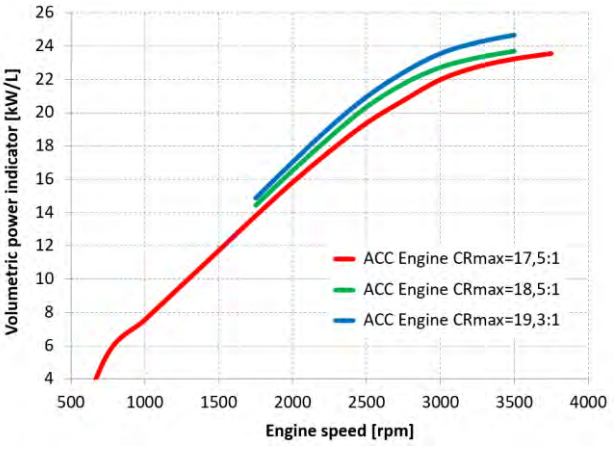

Fig. 6. Power for the maximum torque of the ACC engine with a displacement of one liter obtained for three CR_{max} values

For better illustration of the ACC engine ratings, Fig. 7 showed the full loaded engine torque to displacement ratio (engine torque related to one liter of displacement) in function of engine speed. Obtained values of such ratio did not exceeded value of 82 Nm/L.

For the comparison during mentioned studies using base 1.5 L four-cylinder DVVT engine supplied with gasoline and the same engine with dual shaft control variable compression ratio (DSC-VCR) [28] the engine torque was equal to 210, 190 and 155 Nm, for the case 1, case 2, and case 3,

respectively. These values related to the consecutive values of the loaded engine torque to displacement ratio including 140, 126 and 103 Nm/L, respectively. For the case 1 such values were 1.4-1.9-fold higher compared to the cases of ACC engines analyzed in the present study. The DSC-VCR increased the torque by about 6.57%, 4.81%, and 6.19% in comparison to the base engine for each case.

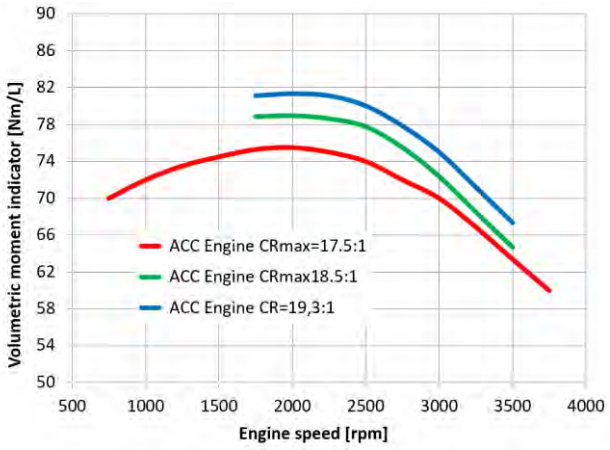

Fig. 7. Full load torque for the ACC engine with a displacement of one liter obtained at different maximum compression ratios

Another parameter for assessing the operating ACC engine was the exhaust gas temperature measured close to the exhaust valve, i.e., at a distance not exceeding 100 mm from the valve surface in the cylinder, shown in Fig. 8. It was noticed that the maximum exhaust temperature measured at this point did not exceed 530°C at full engine load, while the temperature measured in the base engines was greater than 150°C to 350°C at the same load and rotational speed. For the comparison during studies on the movable cylinder block VCR and multi-fuel 660 cc engine with a maximum power of 3.7 kW supplied with gasoline, the exhaust gas temperature values vary in range 720–820°C for the CR = 7:1, in range 700–800°C for the CR = 8.5:1, and in range 660–770°C for the CR = 10:1, respectively. The highest values of the exhaust gas temperature were observed for the lowest brake power values for all CR values studied [44].

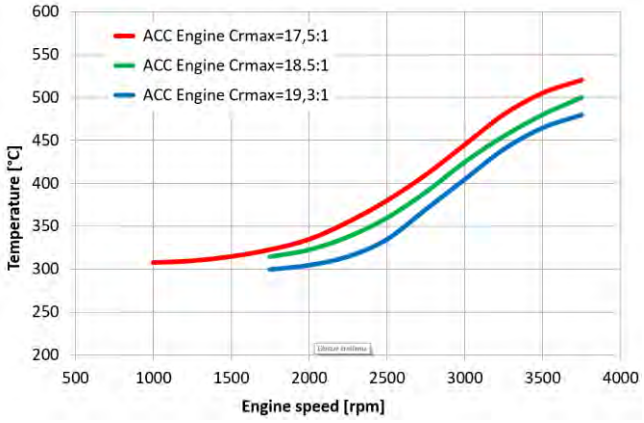

Fig. 8. Exhaust gas temperature measured in the ACC engine as a function of engine speed for maximum engine torque and various compression ratios

5.2. Indicator charts

The selected four indicator plots shown in Fig. 9 to Fig. 12 include the results of research work on the ACC engine with CR_{max} = 17.5:1. The choice was made due to two parameters: the load of at least 80% and the rotational speed, because the mutual relation of these parameters has a decisive influence on the course of the pressure indicated in the engine cylinder.

The diagram in Fig. 9 is an example of the indicator pressure course with the greatest influence of the ACC system, which is mainly due to the low engine speed and good dynamic properties of the ACC system, because the value of the indicator γ_{fm} used in the measurements was of about 80 cm^2/kg. The indicated pressure course was characterized by flattening responsible for energy recuperation by the ACC system.

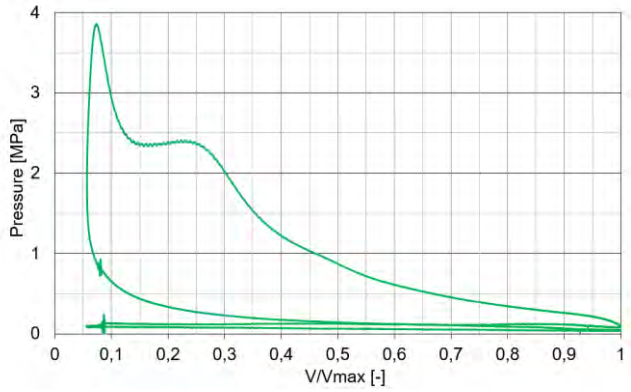

Fig. 9. Indicated pressure in the ACC engine under CR_{max} = 17.5: 1 at engine speed of 1000 rpm

This flattening gradually faded away as the speed increased, as shown in the subsequent graphs of Fig. 10 and Fig. 11. For an engine speed above 4000 rpm, the recuperation effect disappeared due to the decreasing displacement of the additional piston in the ACC system and increasing delays in its return.

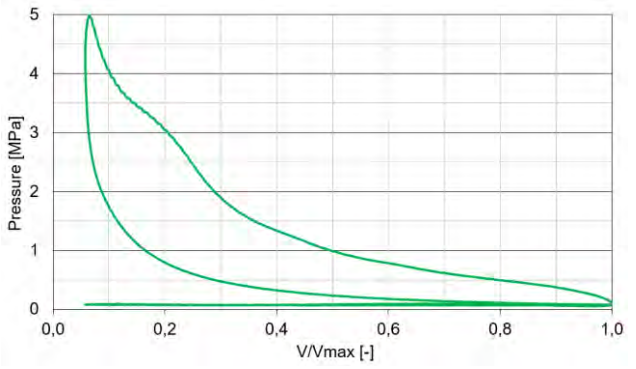

Fig. 10. Indicated pressure in the ACC engine under CR_{max} = 17.5: 1 at engine speed of 1900 rpm

In Figure 11, the influence of the ACC system at a speed of 3750 rpm became barely visible. This rotational speed can be considered a limiting one, because after exceeding it, only the registered movement of the additional piston indicated that the ACC system was active.

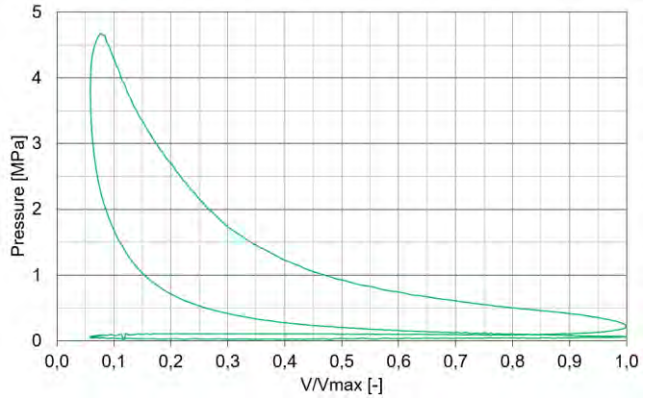

Fig. 11. Indicated pressure in the ACC engine under CR_{max} = 17.5: 1 at engine speed of 3750 rpm

Figure 12 shows the influence of the ACC system on the smooth running of the engine – pressure amplitude. It shows the indicated pressure graph (green) and the corresponding phase shift of the additional piston (APPS) in the ACC system in relation to the engine piston (deep pink). The diagrams clearly correlate with each other: the higher amplitude of the indicated pressure always corresponds to the higher amplitude of the lift of the additional piston in the ACC system. Of course, the degree of self-regulation carried out in a single cycle by the ACC system depends primarily on several parameters, which include: the main design parameter, engine speed, and pressures p_1 acting on area $(\pi d_1^2)/4$ of the upper surface of additional piston and p_2 acting on area $(\pi d_1^2 - d_2^2)/4$ of its bottom surface being outside the area affected by gas pressure in the engine cylinder [16].

The ACC system, operating in accordance with the diagram in Fig. 1, increases the volume of the combustion chamber mainly on the expansion stroke. The magnitude of this change depends on the pressure amplitude in the cylinder. Thus, higher pressure is accompanied by a greater change in volume caused by the ACC system, and the final consequence is a reduction in the very amplitude of the pressure in the cylinder during the combustion process. At this point it should be noted that this specific amplitude equalization is an essential feature of the ACC engine and takes place whenever there is a reaction of the ACC system. The best results are achieved at low engine speeds and in such conditions the differences for the same dose of the air-fuel mixture are reduced to 1%.

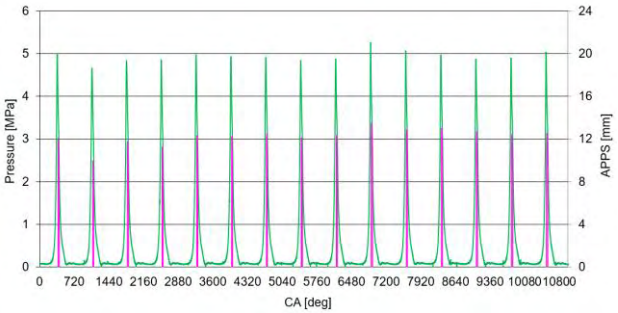

Fig. 12. Influence of the ACC system on the uniformity of indicated pressure amplitudes

6. Summary

The ACC engine allows avoiding detonation combustion without changing the amount and composition of the combustible mixture, and even without delaying the ignition advance angle. It allowed also to obtain lower fuel consumption and temperature of exhaust gas compared to the case of the combustion engines with fixed CR values. With enhancement of CR values for ACC engine it was observed a decrease of specific fuel consumption and temperature, end increase of volumetric torque and volumetric power indicators in whole range studied of engine speeds. In addition, the possible range of control of the combustion process allowed the ACC engine to operate with different types of hydrocarbon fuels, for example, in the form of petrol with various alcohol admixtures, as described in [53, 57]. The very intense flow of the combustible mixture inside the cylinder of the ACC engine allowed describing the combustion in the ACC engine with zero-dimensional mathematical models with the dual Vibe function providing the proper characterization of the heat release process [20]. The use of very high maximum compression ratios allows the ACC engine to operate to a certain extent as an HCCI engine with high lambda coefficients.

Nomenclature

ACC	active combustion chamber
BDC	bottom dead center
CI	compression ignition
CR	compression ratio
HCCI	homogeneous charge compression ignition
APPS	additional piston phase shift
SI	spark igniton
TDC	top dead center
VCR	variable compression ratio
VVA	variable valve actuation
VVT	variable valve timing

Bibliography

[1] Abdel-Rahman AA, Osman MM. Experimental investigation of varying the compression ratio of SI engine under different ethanol–gasoline fuel blends. Int J Energy Res. 1997;21(1): 31-40. https://doi.org/10.1002/(SICI)1099-114X(199701)21:1%3C31::AID-ER235%3E3.0.CO;2-5

[2] Aina T, Folayan CO, Pam GY. Influence of compression ratio on the performance characteristics of SI engine. Adv Appl Sci Res. 2012;3(4):1915-1922.

[3] Al-Baghdadi S, Maher AR. Effect of compression ratio, equivalence ratio and engine speed on the performance and emission characteristics of SI engine using hydrogen as a fuel. Renew Energy. 2004;29(15):2245-2260. https://doi.org/10.1016/j.renene.2004.04.002

[4] Aldikas AC. Heat transfer characteristics of a spark-ignition engine. J Heat Transfer. 1980;102(2):189-193. https://doi.org/10.1115/1.3244258
[5] Babagiray M, Kocakulak T, Ardebili SMS, Calam A, Solmaz H. Optimization of operating conditions in a homogeneous charge compression ignition engine with variable compression ratio. Int J Environ Sci Te. 2022;9:1-22. https://doi.org/10.1007/s13762-022-04499-9
[6] Bas O, Akar MA, Seri H, Özcanli M. Performance of an SI engine with different spark plugs, VCR and H2 addition. Sigma J Eng Nat Sci. 2020;38(4):1951-1961. https://sigma.yildiz.edu.tr/article/149
[7] Basu D, Phulli S, Kotebavi V. Performance analysis of a VCR SI engine using petrol alcohol blends. 2014 Power and Energy Systems: Towards Sustainable Energy. 2014:1-5. https://doi.org/10.1109/PESTSE.2014.6805264
[8] Beroff J. Internal combustion engine with variable capacity and compression ratio. European Patent EP20010400802. 2005.
[9] Bonatesta F, Waters B, Shayler PJ. Burn angles and form factors for wiebe function fits to mass fraction burned curves of a spark ignition engine with variable valve timing. Int J Engine Res. 2010;11(2):177-186. https://doi.org/10.1243/14680874JER05009
[10] Brevick J. Design and development of a pressure reactive piston (PRP) to achieve variable compression ratio. Department of Energy Contract FC02-99EE50576, Final Technical Report 2000:44-49.
[11] Brevick JE. Variable compression ratio piston. US Patent 5755192A. 1998.
[12] Brzeski P, Pavlovskaia E, Kapitaniak T, Perlikowski P. The application of inerter in turned mass absorber. Int J Nonlinear Mech. 2015;70:20-29. https://doi.org/10.1016/j.ijnonlinmec.2014.10.013
[13] Caris DF, Nelson EE. A new look at high compression engines. SAE Technical Paper 590015. 1959. https://doi.org/10.4271/590015
[14] Clarke JR, Tabaczynsky RJ. Internal combustion engine with adjustable compression ratio and knock control. US Patent 6135086A. 2000.
[15] Dasore A, Rajak U, Panchal M, Reddy VN, Verma TN, Chaurasiya PK. Prediction of overall characteristics of a dual fuel CI engine working on low-density ethanol and diesel blends at varying compression ratios. Arab J Sci Eng. 2022; 2:1-8. https://doi.org/10.1007/s13369-022-06625-8
[16] Dabrowski A, Glogowski M, Kubiak P. Improving the efficiency of four-stroke engine with use of the pneumatic energy accumulator-simulations and examination. Int J Automot Techn. 2016;17:581-590. https://doi.org/10.1007/s12239-016-0058-1
[17] Ferrey P, Miehe Y, Constensou C, Collee V. Potential of a variable compression ratio gasoline SI Engine with very high expansion ratio and variable valve actuation. SAE Int J Engines. 2014;7(1):468-487. https://doi.org/10.4271/2014-01-1201
[18] Ganji PR, Vysyaraju RKR, Surapaneni SR, Kumar BK. Enhancement of combustion characteristics of VCR diesel engine by optimizing engine parameters. SN Appl Sci. 2021;3(8). https://doi.org/10.1007/s42452-021-04739-6
[19] Ghojel JI. Review of the development and applications of the Wiebe function: A tribute to the contribution of Ivan Wiebe to engine research. Int J Engine Res. 2010;11(4):297-312. http://dx.doi.org/10.1243/14680874JER06510
[20] Glogowski M, Kubiak P, Šarić Ž, Barta D. New theoretical cycle for active combustion chamber engine. The Archives of Automotive Engineering. 2019;83(1):23-42. https://doi.org/10.14669/AM.VOL83.ART2
[21] Glogowski M, Kubiak P, Szufa S, Piersa P, Krukowski M. The use of the Fourier series to analyze the shaping of thermodynamic processes in heat engines. Energies. 2021; 14(8):2316. https://doi.org/10.3390/en14082316
[22] Gooijer LHD. A reciprocating piston mechanism. European Patent EP2620614 A1. 2013.
[23] Hammermueller B, Orlowsky K, Hanciogullari D, Pischinger S. Experimental analysis of the system behavior of a two-stage variable compression ratio (VCR) system in fired SI-engine operation. Int J Engine Res. 2022;23(10):1619-1633. https://doi.org/10.1177/14680874211032382
[24] Heywood JB. Internal combustion engine fundamentals, 2nd ed. New York: McGraw-Hill; 2018.
[25] Hiyoshi R, Aoyama S, Takemura S, Ushijima K, Sugiyama T. A study of a multiple-link variable compression ratio system for improving engine performance. SAE Technical Paper 2006-01-0616. 2006. https://doi.org/10.4271/2006-01-0616
[26] Joshi MP. Variable compression ratio (VCR) engine – a review of future power plant for automobile. Int J Mech Eng Res Develop. 2012;2(1):9-16.
[27] Kumar C, Rana KB, Tripathi B. Effect of diesel-methanol-nitromethane blends combustion on VCR stationary CI engine performance and exhaust emissions. Envir Sci Pollut R. 2019; 26(7):6517-6531. https://doi.org/10.1007/s11356-018-04058-1
[28] Lin J, Yang S. A predictive study of a new VCR engine with high expansion ratio and high-efficiency potential under heavy load conditions. Energies. 2020;13:1655. https://doi.org/10.3390/en13071655
[29] López JJ, García A, Monsalve-Serrano J, Cogo V, Wittek K. Potential of a two-stage variable compression ratio downsized spark ignition engine for passenger cars under different driving conditions. Energ Convers Manage. 2020;203:112251. https://doi.org/10.1016/j.enconman.2019.112251
[30] Manimaran R, Mohanraj T, Venkatesan M. ANN modeling for forecasting of VCR engine performance and emission parameters fueled with green diesel extracted from waste biomass resources. Envir Sci Pollut R. 2022;29(34):51183-51210. https://doi.org/10.1007/s11356-022-19500-8
[32] Meirovitch L. Fundamentals of Vibrations; McGraw-Hill. New York, USA, 2001.
[33] Mendler C. High-efficiency VCR engine with variable valve actuation and new super-charging technology. Final Report of the NETL Contract Number DE-EE0005981. 2018. https://doi.org/10.2172/1545742
[34] Meyer M, Frank VDS. Internal combustion reciprocating piston engine. European Patent EP1811151 A2. 2007.
[35] Moteki K, Aoyama S, Ushijima K. A study of a variable compression ratio system with a multi-link mechanism. SAE Technical Paper 2003-01-0921. 2003. https://doi.org/10.4271/2003-01-0921
[36] Moteki K, Fujimoto H, Aoyama S. Variable compression ratio mechanism of reciprocating internal combustion engine. US Patent 6505582 B2 2003.
[37] Murugapoopathi S, Ramachandran T, Rajaganapathy C. Theoretical performance on energy and exergy analysis of methyl esters of rubber seed oil fueled on supercharged VCR engine. Environ Dev Sustain. 2022;8:1-20. https://doi.org/10.1007/s10668-022-02642-7
[38] Nayyar A, Sharma D, Soni S, Mathur A. Experimental investigation of performance and emissions of a VCR diesel engine fueled with n-butanol diesel blends under varying engine parameters. Environ Dev Sustain. 2017;24(25):20315-20329. https://doi.org/10.1007/s11356-017-9599-8
[39] Nuthan PBS, Pandey JK, Kumar GN. Impact of changing compression ratio on engine characteristics of an SI engine

fueled with equivolume blend of methanol and gasoline. Energy. 2020;191:116605. https://doi.org/10.1016/j.energy.2019.116605
[40] Ozcan V, Yamin JAA. Performance and emission characteristics of LPG powered four stroke SI engine under variable stroke length and compression ratio. Energ Convers Manage. 2008;49:1193-1201. https://doi.org/10.1016/j.enconman.2007.09.004
[41] Qasemian A, Haghparast SJ, Azarikhah P, Babaie M. Effects of compression ratio of bio-fueled SI Engines on the thermal balance and waste heat recovery potential. Sustainability. 2021;13(11):5921. https://doi.org/10.3390/su13115921
[42] Rakopoulos DC, Rakopoulos CD, Giakoumis EG, Kosmadakis GM. Numerical and experimental study by quasi-dimensional modeling of combustion and emissions in variable compression ratio high-speed spark-ignition engine. J Energ Eng. 2021;147(5):1-22. https://doi.org/10.1061/(ASCE)EY.1943-7897.0000780
[43] Rapan G, Rapan I. Variable compression ratio engine. Romanian Patent RO115662B. 2000.
[44] Riley MB. Internal Combustion Engine with Variable Combustion Chambers and Increased Expansion Cycle, US Patent 5341771 A. 1994.
[45] Rinu T, Sreesankaran M, Jeevan J, Dileep MP, Manjunath P. Experimental evaluation of the effect of compression ratio on performance and emission of SI engine fueled with gasoline and n-butanol blend at different loads. Perspectives in Science. 2016;8:743-746. https://doi.org/10.1016/j.pisc.2016.06.076
[46] Roberts M. Benefits and challenges of variable compression ratio (VCR). SAE Technical Paper 2003-01-0398. 2003. https://doi.org/10.4271/2003-01-0398
[47] Roy A, Mishra C, Jain S, Solanki, N. A new design to achieve variable compression ratio in a spark ignition engine. Innovative Design, Analysis and Development Practices in Aerospace and Automotive Engineering (I-DAD 2018) 2018;2: 388-396. https://doi.org/10.1007/978-981-13-2718-6_37
[48] Shaik A, Moorthi NSV, Rudramoorthy R. Variable compression ratio engine: a future power plant for automobiles – an overview. P I Mech Eng D-J Aut. 2007;221(D9):1159-1168. https://doi.org/10.1243/09544070JAUTO573
[49] Shetty S, Jose A, Shrinivasa RBR. Comparison of performance and combustion analysis of a VCR SI engine using audio transducers. Mater Today-Proc. 2021;46(7):2798-2806. https://doi.org/10.1016/j.matpr.2021.02.603
[50] Rao SG, Paul PJ, Mukunda HS. Biomass derived producer gas as a reciprocating engine fuel – an experimental analysis. Biomass Bioenerg. 2001;21:52-72. https://doi.org/10.1016/S0961-9534(01)00014-9
[51] Takahashi N, Aoyama S, Moteki K, Hiyoshi R. A study concerning the noise and vibration characteristics of an engine with multiple-link variable compression ratio mechanism. SAE Technical Paper 2005-01-1134. 2005. https://doi.org/10.4271/2005-01-1134
[52] Takalkar M, Khan I. Study of variable compression ratio engine (VCR) and different innovations to achieve VCR. International Journal for Research in Applied Science and Engineering Technology. 2017;5(11):1473-1478. https://doi.org/10.22214/ijraset.2017.11213
[53] Tomar SK, Mishra R, Bisht S, Kumar S, Saxena G. Design of variable length connecting rod for VCR engine. International Journal of Engineering Research and Applications (IJERA) 2014, Special Issue: International Conference on Emerging Trends in Mechanical and Electrical Engineering (ICETMEE) 13th-14th March 2014, 280-285.
[54] Topgül T, Yücesu H, Çinar C, Koca A. The effects of ethanol-unleaded gasoline blends and ignition timing on engine performance and exhaust emissions. Renew Energ. 2006; 31(15):2534-2542. https://doi.org/10.1016/j.renene.2006.01.004
[55] Wittek K, Geiger F, Andert J, Martins M, Cogo V, Lanzanova T. Experimental investigation of a variable compression ratio system applied to a gasoline passenger car engine. Energ Convers Manage. 2019;183:753-763. https://doi.org/10.1016/j.enconman.2019.01.037
[56] Wong VW, Stewart M, Lundholm G, Hoglund A. Increased power density via variable compression/displacement and turbocharging using the al-var-cycle engine. SAE Technical Paper 1998-981027. 1998. https://doi.org/10.4271/981027
[57] Wos P, Kuszewski, H, Ustrzycki A. Exhaust emission features of variable compression ratio (VCR) diesel engine. Journal of KONES Powertrain and Transport. 2010;17(3):3-6.
[58] Yücesu SH, Topgül T, Çinar C, Okur, M. Effect of ethanol–gasoline blends on engine performance and exhaust emissions in different compression ratios. Appl Therm Eng. 2006;26(17-18):2272-2278. https://doi.org/10.1016/j.applthermaleng.2006.03.006
[59] Yuh M, Tohru G. The effect of higher compression ratio in two-stroke engines. Yamaha Motor Co Ltd. SAE 2008-931512:355-362.
[60] Zhan YL, Wan BY, Wang XZ, Hu YH. A simulation model for the main engine of the modern container ship. Machine Learning and Cybernetics. Proc. IEEE 2004 Int. Conf. 2004; 5:2996-3002. https://doi.org/10.1109/ICMLC.2004.1378546

Michal Glogowski, DEng. – Faculty of Process and Environmental Engineering, Lodz University of Technology, Poland.
e-mail: *michal.glogowskip.lodz.pl*

Wozniak Marek, DEng. – Department of Vehicles and Fundamentals of Machine Design, Lodz University of Technology, Poland.
e-mail: *marek.wozniak.1@p.lodz.pl*

Siczek Krzysztof, DSc. DEng. – Department of Vehicles and Fundamentals of Machine Design, Lodz University of Technology, Poland.
e-mail: *ks670907@p.lodz.pl*

Tomasz Szydlowski, DEng. – Department of Vehicles and Fundamentals of Machine Design, Lodz University of Technology, Poland.
e-mail: *tomasz.szydlowski@p.lodz.pl*

Article citation info:
Szymański GM, Cywka B, Mokrzan D, Prokopowicz W. Estimation of fuel consumption in a jet engine based on vibration signal parameters. Combustion Engines. 2023;194(3):13-20. https://doi.org/10.19206/CE-166278

Grzegorz Marek SZYMAŃSKI
Bartłomiej CYWKA
Daniel MOKRZAN
Wojciech PROKOPOWICZ

Combustion Engines
Polish Scientific Society of Combustion Engines

Estimation of fuel consumption in a jet engine based on vibration signal parameters

ARTICLE INFO

Received: 15 March 2023
Revised: 17 April 2023
Accepted: 17 May 2023
Available online: 1 June 2023

This paper proposes the use of vibroacoustic signal parameters to estimate the fuel consumption of a miniature GTM-400 engine. The method for testing engine vibrations is presented, followed by an analysis of the results obtained. Two vibration point measures were selected to build a fuel consumption model. The models obtained were verified, after which those that best describe the real fuel consumption of the engine were selected. The paper proves that the vibration signal, in addition to its applications in jet engine diagnostics, can be used to determine engine performance, which can contribute to reducing the complexity of construction and increasing the economics of engine operation.

Keywords: *vibroacoustics, jet engine, fuel consumption, estimation, statistical analysis*

1. Introduction

Today, one of the requirements of machines is to achieve the highest possible levels of efficiency. For machines with rotating components, this problem is often optimised by increasing their rotational speed [22]. Due to the impossibility of perfectly balanced rotors, some energy is converted into oscillations [1, 14, 19]. Unwanted oscillations can cause damage or failure, so it is important to monitor them properly at all times. The analysis of vibration measurements of equipment, characterised not only by the high precision in determining the damaged components and the type of damage [7, 26, 31], but also by the possibility of continuously monitoring their condition [21]. In addition, the analysis of the vibroacoustic signal can be used to determine the operating parameters of the machinery. In the papers [4, 24, 32] the authors proposed using the time-frequency representation of the vibration signal to determine the instantaneous shaft speed of the wind turbine gearbox and the internal combustion engine. The authors of the study presented in [13] showed that the use of a vibroacoustic signal and wavelet transformation can be used to identify the composition of the fuel used to power the engine. However, in this article, the authors have proposed the use of vibration signal parameters to estimate the fuel consumption of a GTM-400 miniature turbine jet engine.

Currently, many methods have been developed to measure the mass flow rate of fluids. Referring to the work [28] flow meters can be divided into four groups, depending on the parameter directly measured by them, i.e.: velocity, volume, mass, indirect parameters (e.g. differential pressure).

Most for the methods of measuring fluid output affect the pressure drop of the flowing fluid [11]. In addition, each of these methods requires the installation of dedicated sensor in a strictly defined location on the equipment, which increases the complexity of the design, production costs, and machine operation [5, 18]. The method proposed in this paper allows the use of a vibroacoustic signal, nowadays increasingly used for diagnostic purposes [3], to estimate the mass intensity of the fuel that feeds a turbine engine. The advantages of using this method to determine fuel flow rate are the high accuracy of the estimation, the lack of interference with the fluid flow, and the increased economy of the design.

2. Vibration test methods for aircraft engines

Nowadays for most aircraft engines in service by condition, it is essential to collect data on the vibration of its components [10, 20]. In paper [29], the author proposed a classification of vibration transducers according to the measured parameter (displacement, velocity, acceleration), the need for power supply (active and passive transducers), the relative or absolute measurement of vibrations and the contact or lack thereof with the object under test. Each transducer has its limitations, related to its operating principle. Turbine engines, due to their high rotor speeds, are characterised by high-frequency vibrations, and therefore the most accurate measurements of their vibrations are obtained using accelerometers. The most commonly used acceleration sensor is a piezoelectric crystal. These sensors produce an electrical signal in response to dynamic loads; however, due to the high impedance of the system, piezoelectric sensors require converters to transform the signal into one suitable for the rest of the system [1, 2].

With device-mounted vibration transducers, the strongest signal and one with the least interference can be obtained at or as close to the rotating component as possible. For design reasons, this is often not feasible. The solution that gives the best results, as presented in the [19, 30] works, is to test vibrations in the motor bodies, in the immediate vicinity of the bearings.

All machine-mounted transducers have their own mass; for vibration measurements of lightweight structures, the mass of the sensors can affect the results obtained. Some machines, due to their design, do not allow the use of vibration transducers mounted on their structure. In these cases, the use of noncontact vibration sensors is justified. Most noncontact vibration sensors operate on the principle of emitting and receiving laser light reflected from the structure [33].

The use of a vibroacoustic signal in the machine diagnosis process enables the detection of malfunctions before they lead to damage and allows the indication of faulty components. This reduces operating costs by reducing the frequency of servicing, replacement of individual engine units, and faster removal of malfunctions. In addition, continuous inspection of the aircraft structure results in increased flight safety and, through more efficient use of engine components, reduces the negative impact on the environment [6, 16].

3. Research methodology

The subject of the study was a GTM-400 miniature turbine jet engine with a thrust of 400 N, built on a test stand. The engine has a single-rotor design. There is a single 14-blade radial compressor stage on the shaft and a single-stage 23-blade axial turbine. The engine has an annular combustion chamber with backflow and an uncontrollable convergent nozzle. The rotor is supported by two ball bearings. An electric starting system, fuel pump, engine control module, and battery are built into the engine. The maximum engine speed is 80,000 rpm. The following sensors were placed on the test stand: temperature and pressure of the working medium, engine thrust and mass intensities of fuel and air. The engine diagram is shown in Fig. 1.

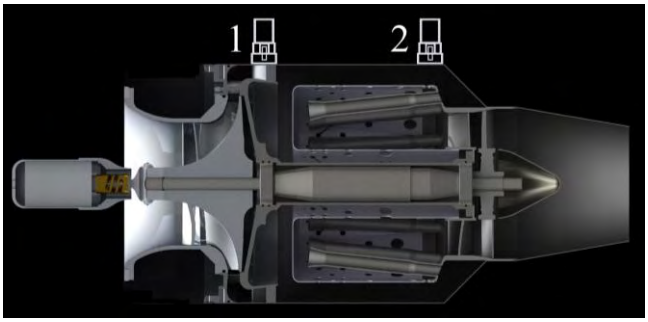

Fig. 1. Diagram of the GTM-400 motor with schematic representation of the accelerators 1, 2

To test the vibration parameters of the motor, three 'TYPE 4391' piezo transducers from Brüel & Kjær were attached to the body and test stand. CCLD transducers 'TYPE 2647' also from Brüel & Kjær were used for impedance matching of the sensors. Picture of the engine with the transducers attached to it is shown in Fig. 2.

The use of uniaxial transducers was necessary due to the high temperatures reached by the surfaces to which the sensors were attached [25]. Accelerometers were screwed onto pads previously glued to the test object. Cyanoacrylate adhesive was used. The method used to attach the transducers allows for correct measurements to be obtained and does not require interference with the engine structure. The disadvantages of the method used include the need for a prior preparation of the surface to be bonded and temperature limitations related to the properties of the glue [27]. Transducers process the vibration signal in the axis perpendicular to test stand. Transducer 1 was mounted in the fan bearing plane. In order to measure vibrations in the same axis as transducer 1, transducer 2 was not mounted in the plane of the turbine bearing, but as close as possible to the turbine. Transducer 1 is significantly larger than the other because the adapter that was previously mounted to it has been left on. The adapter does not affect the operation of the transducer, it was not removed for service reasons – to avoid wear on the accelerometer threads. The test bench shown in Fig. 2 is not a proposal for a fully developed system and is only used to investigate the possibility of using vibroacoustic parameters to estimate fuel consumption.

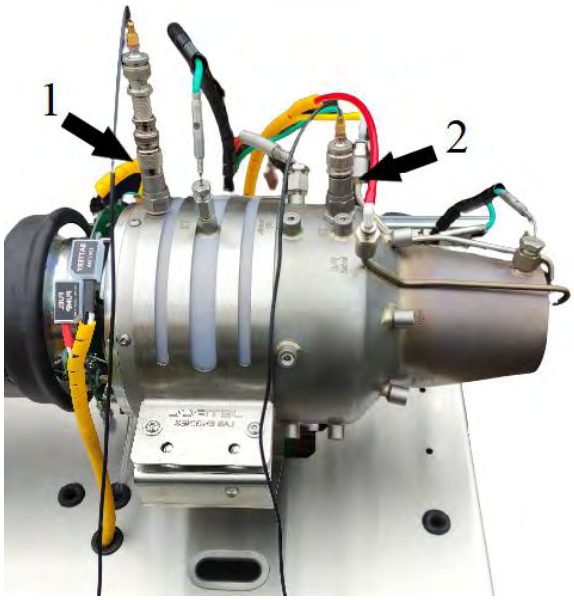

Fig. 2. Location of accelerometers on the test bench

4. Analysis of research results

4.1. Results of fuel consumption measurements

Research into the estimation of the fuel consumption of a jet engine required measuring the amount of fuel delivered to the combustion chamber. The engine control system was used to measure this amount. Measurements were made at a sampling rate of 10 Hz and performed for seven operating settings of the engine. The results in Table 1 are the averages of 100 measurements.

Table 1. Results of jet engine fuel consumption measurements

Setup of engine power	Fuel consumption [ml/min]	Deviation of fuel consumption [ml/min]
1	240.26	3.48
2	378.08	3.29
3	469.87	5.75
4	587.86	6.12
5	769.99	5.31
6	1043.17	5.20
7	1135.20	10.12

4.2. Analysis of vibration measurement results

One method of describing vibration signals in the amplitude domain is the use of point measures [9, 12, 19]. They allow the vibration signal to be characterised by a single number. Thanks to this description of the vibration parameters, it is easy to determine changes in the vibroacoustic signal resulting from changes in the state of the object. Point measures used in vibroacoustic diagnostics can be

divided according to the work [8] into dimensions and dimensionless. The dimensional point measures most commonly used for analysis include [9, 17]:

– effective amplitude:

$$s_{RMS} = \sqrt{\frac{1}{N}\sum_{i=1}^{N}(s_i)^2} \tag{1}$$

where: s_i is instantaneous signal value, N is number of signal samples analysed.

Takes greater account of large values of instantaneous amplitude, is sensitive to the occurrence of high amplitudes and is the most commonly used point measure due to its proportionality to process power. In view of the previous points, and the fact that high power processes occur at the test points, for the purposes of this study, RMS describes the processes taking place better than average amplitude,

– peak amplitude:

$$s_{PEAK} = \max|(s_i)| \tag{2}$$

is used to evaluate impulse processes, e.g. clearance, impact, etc.

Dimensionless discriminants are quotients of the corresponding dimensional score measures, they include, but are not limited to, the following:

– crest factor:

$$CF = \frac{s_{PEAK}}{s_{RMS}} \tag{3}$$

– kurtosis:

$$\beta = \frac{\frac{1}{N}\sum_{i=1}^{N}(s_i)^4}{\left[\frac{1}{N}\sum_{i=1}^{N}(s_i)^2\right]^2} \tag{4}$$

Figure 3 shows the time course of the vibration acceleration signals recorded during the jet engine tests.

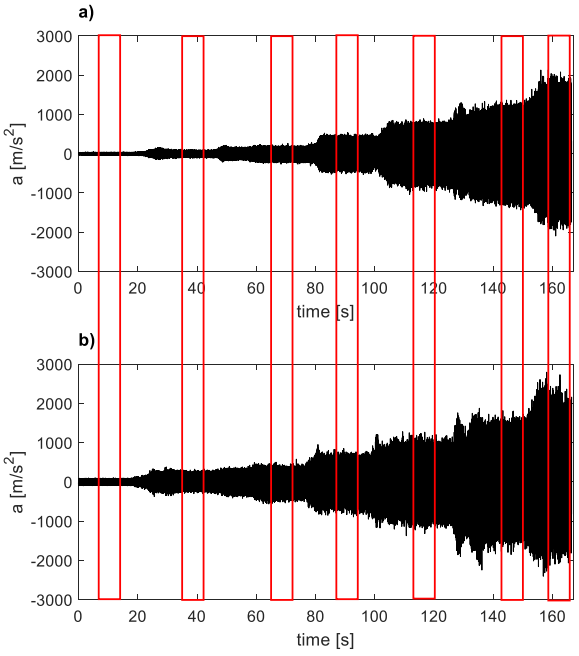

Fig. 3. Time history of vibration signals: a) recorded on the fan bearing axis, b) recorded on the turbine bearing axis

The red rectangles indicate the time windows in which the signal was analysed for different motor operating settings. The results of the point measure calculations for the vibration accelerations recorded in the fan bearing axis are shown in Table 2.

Table 2. Measurement results of vibration acceleration parameters recorded in the fan bearing axis

Setup of engine power	Crest Factor [–]	Kurtosis [–]	a_{PEAK} [m/s]^2	a_{RMS} [m/s]^2
1	5.48	3.09	54.33	9.92
2	4.98	2.96	114.04	25.39
3	4.43	2.84	264.05	60.09
4	2.99	1.93	538.30	179.80
5	3.85	2.44	892.45	269.36
6	3.10	2.05	1365.59	462.34
7	2.46	1.72	2082.55	851.68

Figure 4 shows the variation of the vibration acceleration parameters (recorded on the fan bearing axis) as a function of the engine fuel consumption at different operating points.

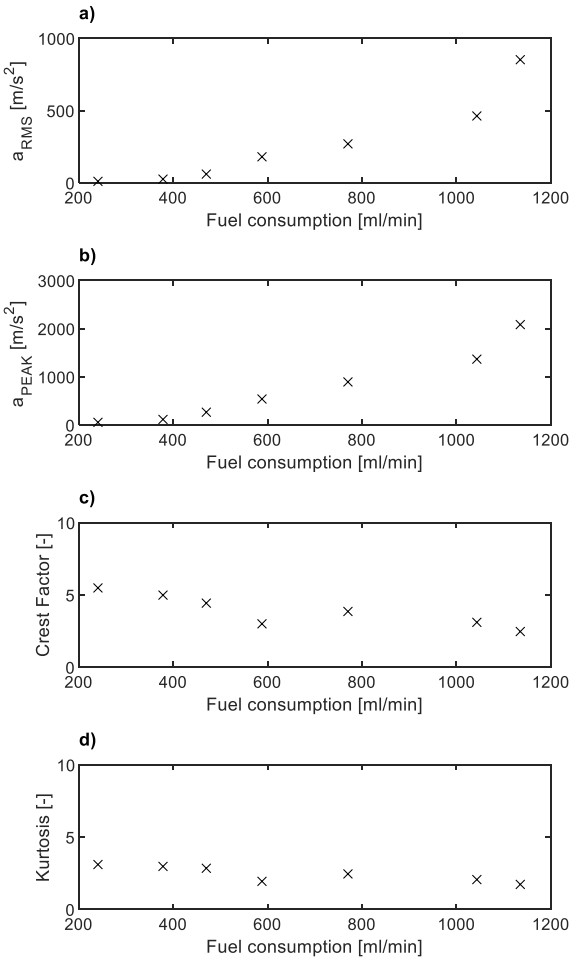

Fig. 4. Dependence of point measures of vibration signals a) RMS, b) PEAK, c) Crest Factor, d) Kurtosis, recorded in the fan bearing axis on fuel consumption

The results of the point measure calculations for the vibration accelerations recorded on the turbine bearing axis are shown in Table 3.

Table 3. Results of measurements of vibration acceleration parameters recorded on the turbine bearing axis

Setup of engine power	Crest Factor [–]	Kurtosis [–]	a_{PEAK} $[m/s]^2$	a_{RMS} $[m/s]^2$
1	5.62	3.31	139.58	24.89
2	4.47	2.87	333.85	74.71
3	4.73	2.94	579.82	122.53
4	4.66	2.88	852.26	203.27
5	4.38	2.68	1280.56	312.64
6	4.07	2.71	1816.91	454.68
7	4.42	2.93	2730.94	617.68

Changes in vibration acceleration parameters (recorded on the turbine bearing axis) in relation to the fuel consumption of the engine at different operating points are shown in Fig. 5.

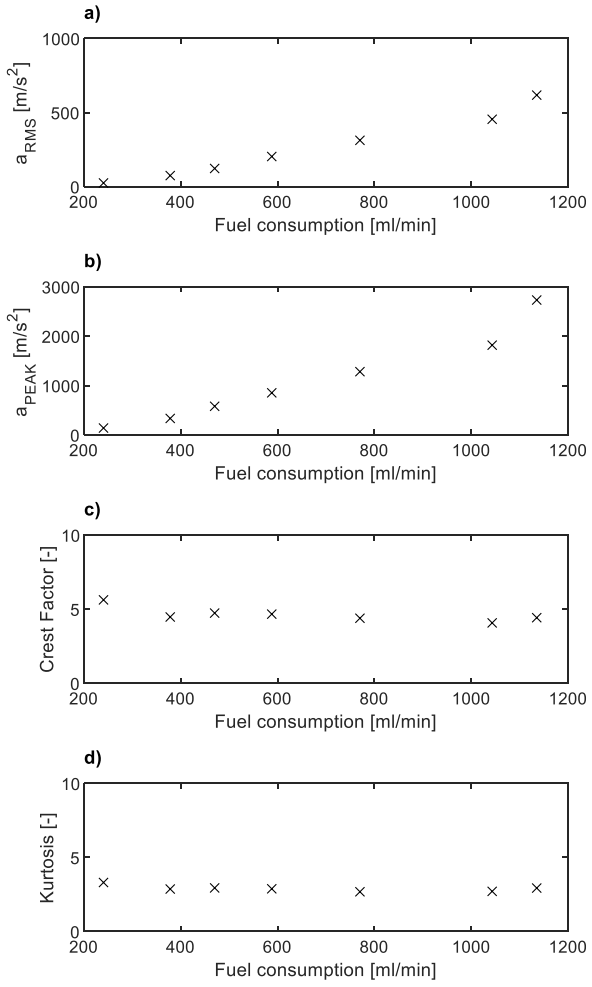

Fig. 5. Dependence of point measures of vibration signals a) RMS, b) PEAK, c) Crest Factor, d) Kurtosis, recorded at the turbine bearing axis on fuel consumption

Based on an analysis of Fig. 4 and 5, it was concluded that, for further research, a_{RMS} and $_{aPEAK}$ measures will be used, as the values of the kurtosis and crest factor do not meet the conditions of the explanatory variable in the modelling process (unambiguity and sufficient width of the field of change relative to the explanatory variable).

4.3. Fuel consumption modelling

One method to find the relationship between dependent and independent variables is to develop a model using statistical analysis tools. Least squares regression analysis is most commonly used to develop models, which in the general case can be written with the equation [23]:

$$\mathbf{Y} = \mathbf{X} \cdot \beta + \varepsilon \tag{5}$$

where: $\mathbf{Y}$ – vector of explanatory variable, β – vector of model coefficients, $\mathbf{X}$ – matrix of the explanatory variables, ε is the i-th noise term, that is, random error.

The study proposed five models described by equations (6–10). The models were named as follows: power1 – equation (6), power2 – equation (7), polly1 – equation (8), polly2 – equation (9), exp1 – equation (10).

$$FC^{power1}(a) = \beta_1 \cdot a^{\beta_2} \tag{6}$$

$$FC^{power2}(a) = \beta_1 \cdot a^{\beta_2} + \beta_3 \tag{7}$$

$$FC^{poly1}(a) = \beta_1 \cdot a + \beta_2 \tag{8}$$

$$FC^{poly2}(a) = \beta_1 \cdot a^2 + \beta_2 \cdot a + \beta_3 \tag{9}$$

$$FC^{exp}(a) = \beta_1 \cdot \exp(\beta_2 \cdot a) \tag{10}$$

where: FC is fuel consumption, a is parameter of vibration acceleration, β_i are model coefficient.

The results of modelling using the RMS value of vibration accelerations recorded at the fan bearing axis are shown in Fig. 6, while a graphical interpretation of the modelling results, in which the explanatory variable was the peak value of vibration accelerations, is shown in Fig. 7.

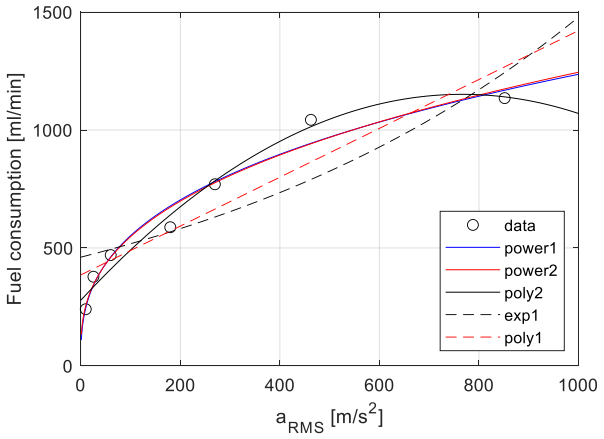

Fig. 6. Relationship between the fuel consumption of the tested jet engine and the RMS value of the vibration acceleration recorded on the fan bearing axis

Figure 8 shows the results of the modelling using an explanatory variable in the form of the RMS value of the vibration accelerations recorded on the turbine bearing axis, and Fig. 9 shows a graphical interpretation of the modelling results using the peak value of the vibration accelerations.

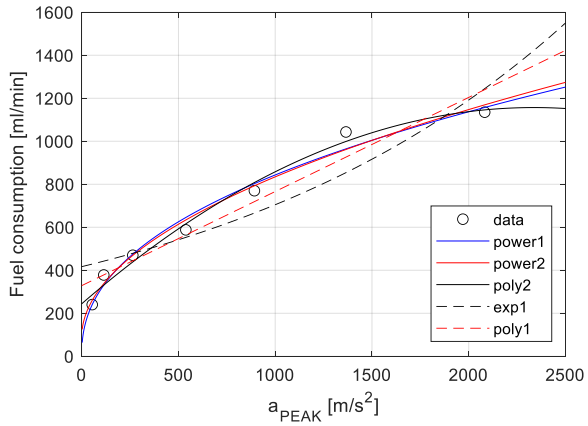

Fig. 7. Relationship between the fuel consumption of the tested jet engine and the maximum value of vibration accelerations recorded on the fan bearing axis

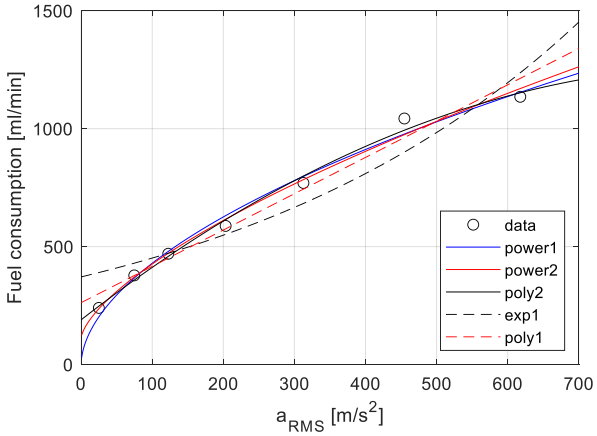

Fig. 8. Relationship between the fuel consumption of the tested jet engine and the RMS value of the vibration acceleration recorded on the turbine bearing axis

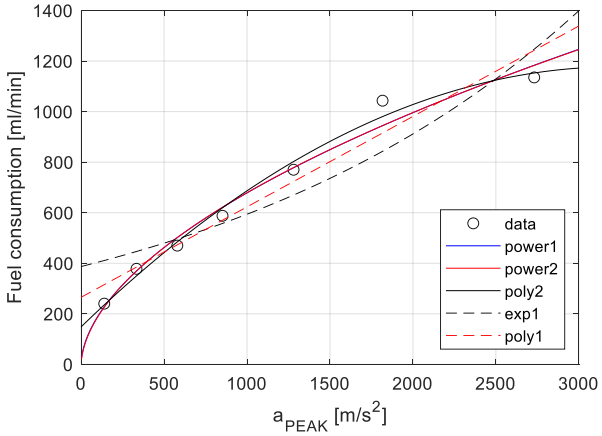

Fig. 9. Relationship between the fuel consumption of the tested jet engine and the maximum value of vibration accelerations recorded on the turbine bearing axis

Based on the analysis of Fig. 6–9, it was found that the model described by the exponential function (10), cannot be used to model the fuel consumption of a jet engine from vibration signals, as its course is divergent from the trend of the analysed data. Therefore, the model verification process was limited to the power and polynomial functions described by equations (6–9).

4.4. Verification of the models

Regression models determined by the least squares method should be statistically verified. The verification of the determined models was caried out by determining a series of statistics. First, the degree of fit of the model to the real data was determined. For this purpose, the coefficient of determination R^2 was determined, which indicates how much of the variability in the explained variable was explained by the model. As part of the model verification, statistical tests were performed to verify the significance of the regression model coefficients using Snedecor's F distribution. On the other hand, the Student's t distribution was used to test hypotheses to determine the significance of individual regression coefficients [15]. During the regression model verification process, a significance level of 0.05 was assumed. It was determined that a regression model would be positively verified if: the coefficient of determination is greater than or equal to 0.80, the model coefficients are statistically significant (F-value and pValue < 0.05).

Tables 4 and 5 show the results of the verification of the model in which the explanatory variable was the RMS value of the vibration accelerations recorded on the bearing axis of the fan.

Table 4. Results of verification of power models based on the RMS value of vibration accelerations recorded on the fan bearing axis

Estimated coefficients	$a_{RMS-FUN}$			
	power1		power2	
	R^2 = 0.97		R^2 = 0.97	
	F= 2.28e–06		F = 0.0009	
	Estimate	pValue	Estimate	pValue
β_1	110.1	0.0042	88.6	0.44
β_2	0.35	0.00014	0.38	0.066
β_3	–	–	44.3	0.85

Table 5. Results of verification of polynomial models based on the RMS value of vibration accelerations recorded in the fan bearing axis

Estimated coefficients	$a_{RMS-FUN}$			
	poly1		poly2	
	R^2 = 0.87		R^2 = 0.98	
	F = 0.002		F = 0.0003	
	Estimate	pValue	Estimate	pValue
β_1	1.04	0.002	–0.0014	0.0087
β_2	385.7	0.0024	2.28	0.001
β_3	–	–	278.4	0.0016

Based on the analysis of the results in Tables 4 and 5 and Fig. 6, it was concluded that the power2 model should be discarded because its coefficients are not statistically significant and the poly2 model because there is a local extreme in the model, which results in the model not meeting the unambiguity condition.

Tables 6 and 7 show the results of the model verification based on the maximum value of the vibration accelerations recorded on the axis of the fan bearing.

Analysis of the results in Tables 5 and 6 and Fig. 7 made it possible to conclude that the power2 and polly2

models could not be used for modelling for the same reasons as for models based on the RMS value of vibration accelerations.

Table 6. Results of the verification of power models based on the maximum value of vibration accelerations recorded on the fan bearing axis

Estimated coefficients	$a_{PEAK-FUN}$			
	power1		power2	
	$R^2 = 0.98$		$R^2 = 0.98$	
	F = 7.64e–07		F = 0.00033	
	Estimate	pValue	Estimate	pValue
β_1	42.9	0.0081	22.65	0.46
β_2	0.43	5.09e–05	0.51	0.026
β_3	–	–	88.9	0.57

Table 7. Polynomial model verification results based on the maximum value of vibration accelerations recorded on the axis of the fan bearing

Estimated coefficients	$a_{PEAK-FUN}$			
	poly1		poly2	
	$R^2 = 0.94$		$R^2 = 0.99$	
	F = 0.00031		F = 0.00019	
	Estimate	pValue	Estimate	pValue
β_1	0.43	0.0003	–0.00016	0.022
β_2	328.5	0.0013	7.92	0.0013
β_3	–	–	6.76	0.0024

Tables 8 and 9 show the results of the verification of the models based on the peak value of the vibration accelerations recorded on the turbine bearing axis.

Table 8. Results of verification of power models based on the RMS value of vibration accelerations recorded on the turbine bearing axis

Estimated coefficients	$a_{RMS-TURBINE}$			
	power1		power2	
	$R^2 = 0.99$		$R^2 = 0.99$	
	F = 2.88e–07		F = 0.0001	
	Estimate	pValue	Estimate	pValue
β_1	35.3	0.0048	14.5	0.32
β_2	0.54	2.03e–05	0.66	0.0063
β_3	–	–	112.5	0.28

Table 9. Results of verification of polynomial models based on the RMS value of vibration accelerations recorded at the turbine bearing axis

Estimated coefficients	$a_{RMS-TURBINE}$			
	poly1		poly2	
	$R^2 = 0.97$		$R^2 = 0.99$	
	F = 3.61e–05		F = 5.21e–05	
	Estimate	pValue	Estimate	pValue
β_1	1.54	3.61e-05	–0.0012	0.053
β_2	262.5	0.0008	2.35	0.0008
β_3	–	–	189.8	0.0037

Based on the analysis of the results in Tables 8 and 9, it was concluded that the power2 and poly2 models should be discarded as their coefficients are not statistically significant.

Tables 10 and 11 show the results of the model verification based on the maximum value of the vibration accelerations recorded on the turbine bearing axis.

Table 10. Results of the verification of power models based on the maximum value of vibration accelerations recorded at the turbine bearing axis

Estimated coefficients	$a_{PEAK-TURBINE}$			
	power1		power2	
	$R^2 = 0.98$		$R^2 = 0.98$	
	F = 9.36e–07		F = 0.000451	
	Estimate	pValue	Estimate	pValue
β_1	14.8	0.027	15.62	0.55
β_2	0.55	5.61e–05	0.54	0.037
β_3	–	–	–7.26	0.97

Table 11. Polynomial model verification results based on the maximum value of vibration accelerations recorded on the turbine bearing axis

Estimated coefficients	$a_{PEAK-TURBINE}$			
	poly1		poly2	
	$R^2 = 0.95$		$R^2 = 0.98$	
	F = 0.0002		F = 0.00011	
	Estimate	pValue	Estimate	pValue
β_1	0.36	0.0002	–9.85e–05	0.056
β_2	265.5	0.0039	0.63	0.0009
β_3	–	–	148.3	0.0201

The analysis of the results in Tables 10 and 11 allowed us to conclude that the power2 and polly2 models could not be used for modelling, as their coefficients are not statistically significant.

On the basis of the verification carried out, the following models were found to meet the criteria for the signals recorded on the fan bearing axis:

$$FC^{power1}_{a_{RMS-FUN}}(a) = 110.1\, a^{0.35}_{RMS-FUN} \quad (11)$$

$$FC^{polly1}_{a_{RMS-FUN}}(a) = 1.04\, a_{RMS-FUN} + 385.7 \quad (12)$$

$$FC^{power1}_{a_{PEAK-FUN}}(a) = 42.9\, a^{0.43}_{PEAK-FUN} \quad (13)$$

$$FC^{polly1}_{a_{PEAK-FUN}}(a) = 0.43\, a_{PEAK-FUN} + 328.5 \quad (14)$$

However, for signals recorded on the turbine bearing axis, the models described by the equations can be used:

$$FC^{power1}_{a_{RMS-TURBINE}}(a) = 35.3\, a^{0.54}_{RMS-TURBINE} \quad (15)$$

$$FC^{polly1}_{a_{RMS-TURBINE}}(a) = 1.54\, a_{RMS\,-\,TURBINE} + 262.5 \quad (16)$$

$$FC^{power1}_{a_{PEAK-TURBINE}}(a) = 14.8\, a^{0.55}_{PEAK-TURBINE} \quad (17)$$

$$FC^{polly1}_{a_{PEAK-TURBINE}}(a) = 0.36 \cdot a_{PEAK-TURBINE} + 265.5 \quad (18)$$

Based on an analysis of the fit of the models to the input data based on R^2, it was concluded that for the vibration acceleration parameters recorded in the fan bearing axis, the

model described by Eq. (13) is the best used and for the data recorded in the turbine bearing axis by relation (15).

5. Conclusions

This paper presents a method to measure the vibrations of the GTM-400 miniature turbine engine and proposes models of its fuel consumption using point measurements of the vibroacoustic signal. A verification of the proposed models was carried out, and it was determined which models describe fuel consumption the most accurately. Based on the research carried out, it can be shown that:

- vibroacoustic signal parameters can be used to analyse many aspects of machine operation,
- measures of effective and peak amplitude allow the fuel consumption model of the GTM-400 engine to be created,
- kurtosis and crest factor do not fulfil the conditions of an explanatory variable in the modelling of the fuel consumption of the engine under investigation,
- the use of an exponential function does not allow a correct fuel consumption model to be proposed,
- the proposed fuel consumption models provide a high level of representation of real-world fuel consumption, as confirmed by their verification,
- the proposed estimation method allows fuel consumption to be determined without interfering with the design of the engine systems,
- future research should verify the models for different external conditions through in-flight engine tests.

Acknowledgements

The presented results have been cofinanced from the subsidies appropriated by the Ministry of Science and Higher Education – 0416/SBAD/0004.

Nomenclature

s_i	instantaneous signal value	RMS	Root Mean Square value of signal
N	number of signal samples analysed	PEAK	peak value of signal
FC	fuel consumption		

Bibliography

[1] Adams M. Rotating machinery vibration: from analysis to troubleshooting. 2nd edition, CRC Press, Taylor & Francis Group 2009.

[2] Alili B, Hafaifa A, Iratni A. Faults detection based on fuzzy concepts for vibrations monitoring in gas turbine. Diagnostyka. 2020;21(4):67-77. https://doi.org/10.29354/diag/129581

[3] Alotaibi M, Honarvar Shakibaei Asli B, Khan M. Non-invasive inspections: a review on methods and tools. Sensors. 2021;21:8474. https://doi.org/10.3390/s21248474

[4] Avramchuk VS, Kazmin VP. Estimation of combustion engine rotation speed based on vibration signal analysis. KEM. 2016;685:436-440. https://doi.org/10.4028/www.scientific.net/kem.685.436

[5] Baker R. Flow Measurement Handbook. Industrial designs, operating principles, performance, and applications. 2nd Edition, Cambridge University Press 2016.

[6] Balicki W. The needs and methods of diagnostics of aeronautical turbine engines. Proceedings of the Institute of Aviation. No. 199. Scientific publications of the Institute of Aeronautics 2009.

[7] Boguś P, Cieszyński M, Merkisz J. Multiresolution analysis of vibration signals acquired from locomotive Diesel engine for classification of engine states basing on signal statistical parameters. Combustion Engines. 2017;168(1):68-72. https://doi.org/10.19206/CE2017-111

[8] Bouaouiche K, Menasria Y, Khalifa D. Detection of defects in a bearing by analysis of vibration signals, Diagnostyka. 2023;24(2):1-7. https://doi.org/10.29354/diag/162230

[9] Cempel C, Haddad SD. Vibroacoustic Condition Monitoring, Ellis Horwood, New York 1991 (translate from polish) Bookmark.

[10] Chachurski R, Balicki W, Głowacki P. Aircraft power units. Part 3: Diagnostics. Military Academy of Technology 2016.

[11] Crabtree M. The Concise Industrial Flow Measurement Handbook. A definitive practical guide. CRC Press, Taylor & Francis Group 2020.

[12] Czechyra B, Szymański GM, Tomaszewski F. Assessment of cam valves clearance in internal combustion engine based on parameters of vibration – methodological assumption. Combustion Engines. 2004;118(1):51-59. https://doi.org/10.19206/CE-117424

[13] Fabiś P, Flekiewicz B, Flekiewicz M. On board recognition of different fuels in SI engines with the use of dimensional and non-dimensional vibration signal parameters. Combustion Engines. 2009;136(1):69-75. https://doi.org/10.19206/CE-117222

[14] Fabry S, Ceskovic M. Aircraft gas turbine engine vibration diagnostic. Czech Technical University in Prague. Magazine of Aviation Development. 2017;5(4):24-28.

[15] Grajek L, Kałuszka M. Statistical conclusion – models and methods. Scientific-Technical Publishing House, Warsaw 2000.

[16] Gubran AA, Sinha JK. Shaft instantaneous angular speed for blade vibration in rotating machine. Mech Syst Signal Pr. 2014;44(1-2):47-59. https://doi.org/10.1016/j.ymssp.2013.02.005

[17] Jałowiecki A, Fidali M, Krol A. Investigation of rolling bearing lubrication condition. Diagnostyka. 2021;22(4):51-58. https://doi.org/10.29354/diag/144123

[18] LaNasa P, Loy Upp E. Fluid flow measurement, a practical guide to accurate flow measurement. 3rd edition. Butterworth-Heinmann 2014.

[19] Łączkowski R. Vibroacoustics of machinery and equipment. Wydawnictwa Naukowo-Techniczne, Warsaw 1983.

[20] Marsili R, Tomassini R, Rossi G. A calibration technique for non contact measurement systems of jet engine blades vibration during operation. 2017 IEEE International Workshop on Metrology for AeroSpace (MetroAeroSpace). Padua, Italy 2017;489-495. https://doi.org/10.1109/MetroAeroSpace.2017.7999624

[21] Merkisz J, Waligórski M. Recognition of combustion process irregularities in small volume displacement diesel engines with the use of non-dimensional characteristics of the

vibration signal. Combustion Engines. 2017;169(2):18-23. https://doi.org/10.19206/CE-2017-204
[22] Muszynska A. Vibrational diagnostics of rotating machinery malfunctions. International Journal of Rotating Machinery. 1995;1(3-4):237-266. https://doi.org/10.1155/S1023621X95000108
[23] Ogundare J. Understanding least Squares estimation and geomatics data analysis. Wiley 2019.
[24] Peeters C, Leclerc Q, Antoni J, Guillaume P, Helsen J. Vibration-based angular speed estimation for multi-stage wind turbine gearboxes. IOP Conf. Series: Journal of Physics: 2017;842:012053. https://doi.org/10.1088/1742-6596/842/1/012053
[25] Piezoelectric charge accelerometer types 4391 and 4391-V. 2022. https://www.bksv.com/-/media/literature/Product-Data/bp2039.ashx
[26] Randall R. Vibration-Based Condition Monitoring: Industrial, Aerospace and Automotive Applications. Wiley 2011.
[27] Serridge M, Licht TR. Piezoelectric accelerometers and vibration preamplifiers. Brüel & Kjær 1987.
[28] Spitzer D. Industrial flow measurement. 3rd ed. The Instrumentation, Systems, and Automation Society 2005.
[29] Sujatha C. Vibration, Acoustics and Strain Measurement, Theory and Experiments. Springer 2023. https://doi.org/10.1007/978-3-031-03968-3
[30] Szymański GM, Misztal W. Analysis of measurement points sensitivity of vibration signals on the stand of jet engine. Combustion Engines. 2017;171(4):279-282. https://doi.org/10.19206/CE-2017-448
[31] Szymański GM, Tomaszewski F. Diagnostic aspects of natural frequencies of selected elements of internal combustion engines. Logistics 2010.
[32] Zimroz R, Urbanek J, Barszcz T, Bartelmus W, Millioz F et al. Measurement of instantaneous shaft speed by advanced vibration signal processing – application to wind turbine gearbox. Metrology and Measurement Systems. 2011;4:701-712. https://hal.science/hal-00661222
[33] Sujatha C. Vibration and Acoustics: Measurement and Signal Analysis. 1st ed. New York, McGraw-Hill Education 2010.

Prof. Grzegorz M. Szymański, DSc., DEng. – Institute of Transport, Poznan University of Technology, Poland.
e-mail: *grzegorz.m.szymanski@put.poznan.pl*

Bartłomiej Cywka, Lt, MEng. – 31st Tactical Air Base, Poznan-Krzesiny, Poland.
e-mail: *bartlomiej.cywka@gmail.com*

Daniel Mokrzan, MEng. – Institute of Transport, Poznan University of Technology, Poland.
e-mail: *daniel.mokrzan@put.poznan.pl*

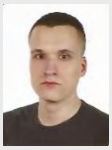

Wojciech Prokopowicz, Col. DEng. – Inspectorate of Armed Forces Support, Bydgoszcz, Poland.
e-mail: *wojciech.prokopowicz@put.poznan.pl*

Article citation info:
Pielecha I, Szwajca F, Stępień Z. Potential of ethanol and butanol in reducing deposits of SIDI engine injectors. Combustion Engines. 2023;194(3):21-31. https://doi.org/10.19206/CE-167898

Ireneusz PIELECHA
Filip SZWAJCA
Zbigniew STĘPIEŃ

Combustion Engines
Polish Scientific Society of Combustion Engines

Potential of ethanol and butanol in reducing deposits of SIDI engine injectors

ARTICLE INFO

Received: 25 April 2023
Revised: 29 May 2023
Accepted: 9 June 2023
Available online: 14 June 2023

The operation of conventional (hydrocarbon) fuels causes certain effects in the internal combustion engine. Despite the satisfactory efficiency of internal combustion engines, their fuel systems, particularly the injectors, are subject to constant fouling. The article analyzes the possibility of reducing the deposit of high-pressure gasoline injectors using the alcohol addition of ethanol and butanol. The study was conducted under the engine and non-engine conditions. Fuel injection timing was analyzed when fueling with different mixtures, and non-engine analyses were conducted to determine changes affecting the injectors. The results indicate the possibility of reducing injector hole coking using ethanol and butanol as a 20% additive to the base fuel.

Key words: *spark ignition engine, direct fuel injection, fuel injector deposits, ethanol, butanol*

1. Introduction

The global policy for reducing pollutants from the road transport sector currently concerns regulated harmful components of exhaust gases such as NO_x, CO, CO oxide, HC unburned hydrocarbons, particulate matter PM, and CO_2 carbon dioxide emissions as a component of GHG (greenhouse gases).

On April 17, 2019, Regulation (EU) No. 2019/631 of the European Parliament and of the Council defining CO_2 emission standards for new passenger cars and for new light commercial vehicles repealing Regulations (EC) No. 443/2009 and (EU) No. 510/2011 [16] was introduced. On 8 June 2022, the European Parliament adopted a Regulation of the European Parliament and of the Council (EU) that amends Regulation (EU) No 2019/631 concerning more stringent CO2 emission standards for new passenger cars and light commercial vehicles, aligning with the EU's ambitious climate targets. The European Parliament advocated for a 20% reduction in average CO2 emissions by 2025, a 55% reduction by 2030, and a 100% reduction by 2035, compared to the levels recorded in 2021.

Alcohols are interesting alternative to commercially utilized fuels, independently or blended with gasoline or diesel. Incorporating alcohol fuels can be a viable solution towards reducing the emission of harmful exhaust constituents, including greenhouse gases, into the atmosphere. However, to make the most of this solution, a comprehensive understanding of alcohol fuel properties and their compatibility with modern engine designs is crucial. Among the alcohols, ethanol and butanol are considered the most promising bio-components for existing conventional fuels. Since 2009, the European RED (Renewable Energy Directive) and FQD (Fuel Quality Directive) have acknowledged the potential of ethanol by permitting a maximum content of 10% (V/V) in motor gasoline while also encouraging the development of Flex Fuel Vehicles (FFVs) capable of running on fuel containing up to 85% (V/V) ethanol.

In 2011, a consortium consisting of the European Commission's Joint Research Centre, the European Council for Automotive R&D (EUCAR) and CONCAWE presented possible future scenarios for meeting the requirements of the Renewable Energy Directives and Fuel Quality Directive, among which some assumed the introduction of fuels with higher ethanol content such as E20 [4]. In June 2013, CEN/TC19/WG38 published a report (CEN/TR 16514) on "E10+" fuels, particularly concerning E20/25. These are fuels for SI engines containing between 20% (V/V) and 25% (V/V) ethanol in their composition. As a result, the European Commission proposed conducting further studies on the feasibility of introducing E20/E25 fuels to the market, considering that previous studies have already shown their great potential for reducing emissions of GHG and other harmful components emitted by internal combustion engines into the atmosphere. Furthermore, augmenting the ethanol content in the fuel would yield several favorable outcomes, such as reducing vapor pressure and elevating the octane number of the fuel. As part of a new agreement between the European Commission and CEN, the Commission agreed to fund a project on expanded research on E20/E25 fuels, together with ePURE (European Renewable Ethanol). This research aimed to understand better and comprehensively assess the environmental impact of E20/25 fuel, improve the energy efficiency of engines, and identify obstacles that need to be overcome before this type of fuel can be marketed [16]. On 11 December 2018, the European Parliament and the Council issued Directive 2018/2001, commonly called the RED II Directive or the Biofuels Directive. This directive outlines various measures aimed at supporting the utilization of energy derived from renewable sources and supporting the advancement of renewable energy sources as a whole. The directive sets renewable energy consumption targets for 2021-2030 and strongly promotes biofuel production from waste. The RED II Directive recasts and repeals previous legislation (Directive 2009/28/EC, Directive (EU) 2015/1513 and Council Directive 2013/18/EU) establishing a mutual system for all European Union countries to promote energy from renewable sources in various sectors of the economy. This means increasing the share of renewable

energy in the energy mix by 2030 in sectors such as electricity, heating and cooling, and transport [5].

To date, much research has been carried out on blends of conventional fuels with various alcohols for evaluating the performance of internal combustion engines. Nevertheless, there has been a notable lack of recognition and comprehensive explanation regarding the impact of certain properties of the tested alcohols on engine performance and operational characteristics. The progression of the mixture formation process holds significant importance in a DISI (Direct Injection Spark Ignition) engine, considering that the fuel is injected directly into the engine cylinder. Direct fuel injection generally allows for better mixture formation than indirect injection engines. The significance of the fuel injection process in a DISI-type engine arises from several factors, including the higher fuel injection pressure, precise control over injection pressure variations, and the timing and quantity of fuel delivery [3, 23]. The formation of the fuel-air mixture is contingent upon various aspects, such as the internal structure of the liquid stream, the atomization process, and fuel evaporation characteristics [21–23]. Notably, the internal structure of the jet stream during injection plays a pivotal role as it directly influences the jet atomization process and vaporization properties [13, 14, 21]. Generating any deviation or disturbance in the optimized atomized fuel spray pattern, such as: changing the jet angle, disturbing the assumed atomization symmetry of the spray pattern, increasing the penetration, or increasing the average diameter of atomized fuel droplets, has a deteriorating effect on engine emissions and performance [20, 23]. The formation process of the combustible mixture in the engine cylinders is prone to interference, influenced by several critical factors. Among these factors, the key determinants include the special quality and timing of fuel atomization, the velocity and penetration depth of atomized fuel droplets, the effective control of mixture movement (swirl), the interaction between atomized fuel droplets and the chamber walls/piston bottom, the inherent physical and chemical properties of the fuel, as well as the prevailing temperature and pressure conditions within the chamber. Disruptions to the fuel atomization process can lead to undesirable outcomes, including an augmented accumulation of fuel on the walls of the combustion chamber, prolonged fuel evaporation time caused by larger droplet sizes, and unregulated evaporation of fuel absorbed by deposits formed on the injector tips. Igniting a poorly mixed and improperly composed mixture can result in untimely, uncontrolled ignition timing and combustion failure during the exhaust stroke. Consequently, this gives rise to elevated emissions of harmful exhaust constituents, accompanied by heightened fuel consumption, diminished engine performance, erratic operation, and challenges initiating the engine [3]. Even a small amount of deposits formed in the channels and around the outlet ports of the fuel injectors of DISI engines uncontrollably changes both quantitatively and qualitatively the injection process by limiting the magnitude of the fuel outflow rate from the injector [14, 25], distorting the spray pattern of the jets [14], deteriorating the quality of the spray [25], and adversely interacting the fuel jets with the turbulence of the air supplied to the combustion chambers [3, 23]. In the latest designs of reciprocating internal combustion engines, including the DISI type, preventing the formation of injector deposits has a decisive impact on the engine's maintenance of the manufacturer's declared performance characteristics as well as performance and emissions. Therefore, an issue of particular interest is the propensity of various fuels to form injector deposits in DISI engines and their effect on the emission of standardized and non-standardized exhaust components into the atmosphere. Deposits forming in the injector outlet channels affect the flow rate, jet penetration depth and spray cone angle and the start and end of injection. They can change the injectors' spray characteristics, which, in turn, can affect the engine cylinder's charge formation and combustion processes [3, 11, 21–23, 26]. External coke deposits around the injector outlet ports are mainly formed from burnt fuel and, to a lesser extent, from lubricating engine oil. They cause distortions in the spray pattern of the fuel, flushing the combustion chamber walls and piston crown with fuel and consequently increasing fuel consumption and emissions (especially HC and PM) [3, 22, 23]. Internal injector deposits are formed exclusively from fuel. They diminish the fuel injection flow rate into the combustion chambers by restricting the cross-sectional area of the injector openings. This has the effect of increasing the average droplet diameter of the atomized fuel, the quantitative ratio of fuel-air mixing (air excess ratio "λ") and increasing the fuel evaporation time [3, 22, 23]. As a result, this leads to decreased engine efficiency and performance and increased fuel consumption.

Including alcohol, such as ethanol, in the fuel has a favorable impact on maintaining clean injectors. Unlike gasoline, alcohol is a single-component fuel without double bonds, granting it greater thermal stability. Ethanol, for instance, comprises merely two carbon atoms and, notably, one oxygen atom, resulting in an oxygen content of 35%. Consequently, the combustion of ethanol yields minimal amounts of soot. While the mechanisms behind soot formation and injector deposits differ in DISI engines, primarily due to the substantially higher temperature required for soot formation compared to deposit formation, it can be anticipated that the presence of ethanol in the fuel would lead to significantly reduced injector deposits compared to gasoline. In addition, ethanol has a lower heat of phase transition, resulting in a lower injector nozzle temperature than when the engine is fueled with gasoline [24]. Apart from the numerous benefits of ethanol in mitigating deposit formation on DISI engine injectors, it does have one drawback: its lower boiling point in comparison to gasoline. Consequently, including ethanol in gasoline blends leads to a reduced T90 temperature compared to pure gasoline, potentially fostering the formation of injector deposits. However, numerous studies have demonstrated the advantages of ethanol or gasoline-ethanol blends regarding their diminished propensity for injector deposit formation [1, 6, 7, 10, 18].

The motivation for the project presented in the article was to study the effect of the admixture of alcohol (ethanol or butanol) to gasoline on the formation of deposits of DISI engine fuel injectors. Quantitative and qualitative changes

in the injected fuel dose were used as criteria for evaluating deposit formation. The novelty of the work lies in combining the study of changes in the size of the injection time of a single dose of fuel, due to the formation of injector deposits, carried out using a standardised, pan-European engine test methodology, with the evaluation of changes in fuel atomization quality based on the study of the macroscopic atomization indices of a fuel jet in a constant-volume chamber using laser illumination.

2. Ethanol and butanol as fuel additives

When evaluating the selection of alcohol-gasoline blends as a fuel for spark-ignition internal combustion engines, various crucial fuel properties must be taken into account, considering the engine's requirements. While the energy content per unit mass, indicated by the calorific value, is vital in assessing the fuel's overall energy characteristics, the calorific value relative to the fuel's volume plays a significant role in determining fuel injection timing and, consequently, the formation of a high-quality fuel-air mixture over time, potentially influencing engine performance. This aspect holds particular significance in the fuel injection system used in modern engines, namely direct fuel injection. In this system, the precise amount of fuel required for optimal engine operation is delivered to the combustion chambers by adjusting the injection duration, which is contingent upon the engine's operating conditions [26].

Ethanol and butanol are the most promising alcohol-based biocomponents for current conventional fuels. These alcohols possess advantageous functional, operational, and environmentally friendly properties, enabling a reduction in the reliance on hydrocarbon fuels for powering engines [15]. Thus far, ethanol has garnered more extensive usage, blended in varying ratios with gasoline and widely adopted as fuel for spark-ignition engines in numerous countries. This is likely attributed to the abundance of research focused on ethanol, both in terms of understanding its properties and practical application, facilitating its earlier and broader implementation as a fuel either in its pure form or as an additive. The comparatively lower production cost of ethanol than butanol is also a significant factor. However, given the manifold advantages of butanol over ethanol and its properties, which closely resemble those of gasoline, it is believed to possess greater potential for future green fuel applications.

Table 1 contains a comparative analysis of selected properties of gasoline, n-butanol and ethanol.

Both butanol and ethanol have a higher density than gasoline. Butanol, on the other hand, has a higher density than ethanol, so its maximum allowable proportion in blends with gasoline is less than that of ethanol, given the requirements in EN 228 for gasoline (blend) density. As the content of n-butanol and ethanol in a mixture with gasoline increases, the heating value of the mixture decreases in an approximately linear fashion. However, due to the higher calorific value of n-butanol relative to ethanol on both a unit weight and volume basis, the calorific value of a mixture containing n-butanol decreases less as the n-butanol content increases compared to a corresponding increase in ethanol. Therefore, gasoline blends containing a certain amount of n-butanol will lower engine fuel consumption compared to gasoline blends with the same ethanol content [2, 8, 9].

Table 1. Physical and chemical properties of gasoline, n-butanol and ethanol

Properties	gasoline	n-butanol	ethanol
Chemical formula	Complex mixture of compounds	C_4H_9OH	C_2H_5O
LOB [–]	95	94–96	110
Density [kg/m^3]	753	810	790
Mass calorific value [MJ/kg]	42.9	33.3	26.8
Volumetric calorific value [MJ/dm^3]	32.3	27.0	21.2
Latent heat of vaporization [kJ/kg]	380–500	716	904
Mass participation „C” [%]	86	65	52
Mass participation „H” [%]	14	13.5	13
Mass participation „O” [%]	0	21.5	35
Viscosity [mPa·s]	0.4–0.8	2.57	1.08
Boiling point [°C]	199	118	78
Excess air ratio [–]	14.7	11.2	9.0

An increase in ethanol content in the gasoline mixture will result in a rise in octane number. This is highly advantageous due to the possibility of using such fuel in engines with a higher compression ratio and, therefore, higher efficiency. This offers the possibility of avoiding using octane-raising additives in such fuels. Unlike ethanol, n-butanol has an octane number close to gasoline, and therefore increasing its share in the mixture with gasoline will not change the octane number. Thus, considering this utility parameter, butanol is more easily convertible with gasoline than ethanol.

When used as a fuel in blends with gasoline for spark-ignition (SI) engines, butanol offers several advantages over ethanol. Notably, butanol exhibits lower hygroscopicity, superior miscibility with gasoline, and a higher heating value, resulting in lower fuel consumption compared to blends containing ethanol. Furthermore, when blended with gasoline, butanol has a lower blending vapor pressure than ethanol, facilitating compliance with the requirements of EN 228. However, it is important to acknowledge certain drawbacks of butanol compared to ethanol when blended with gasoline. These include a lower octane number, reduced heat of vaporization, and higher density and viscosity, which may contribute to an increased tendency to form harmful deposits in the fuel injection system, as well as in engine components such as valves, intake ports, and combustion chambers. In summary, when utilized in gasoline-alcohol fuel blends for SI engines, butanol exhibits greater potential in terms of performance characteristics compared to ethanol.

The various thermophysical properties of alcohols can cause significant differences in both their atomization and spray structure and evaporation characteristics [17].

The application of alcohol as a fuel admixture is very important because it provides several benefits, such as reducing greenhouse gas emissions, reducing emissions of toxic exhaust components, increasing energy safety, and improving many fuel performance properties, including knock combustion resistance [19]. Knock combustion is a major barrier to achieving higher thermal efficiency in

reciprocating internal combustion engines [12, 17, 19]. The fuel atomization process heavily influences the performance of a spark-ignition (SI) engine, particularly a direct-injection engine fueled by a gasoline-alcohol blend. Consequently, numerous researchers are devoting their efforts to conducting further studies and enhancing this process, specifically mitigating the adverse effects of injector deposits [12].

3. Methodology

3.1. Methodology of engine testing

The rapid development and widespread use of gasoline direct injection (GDI) systems have made it necessary to develop test methodologies and evaluate the tendency of gasoline of different compositions to form destructive fuel injector deposits. Initially, the available, European-wide test methodologies developed by the CEC (Coordinating European Council for the Development of Performance Tests for Transportation Fuels, Lubricants and Other Fluids) only included evaluations of deposits formed on various engine components, but only with indirect injection. Therefore, the automotive industry demanded the development of a generally applicable, recognized test procedure to evaluate and distinguish between fuels that meet and do not meet the requirements of engine and fuel injection system manufacturers for keeping the fuel injection system clean during engine operation. In 2016, the CEC formed a new TDG-F-113 DISI Working Group and began developing a test procedure to meet the above expectations. Finally, in December 2017, a procedure was published that received the CEC designation F-113-KC and the name: VW EA111 DISI Injector Deposit Test. The widely known and used VW EA111 BLG type engine (Table 2) was used as the test tool.

Table 2. Technical specifications of the VW EA111 BLG engine used for testing

Type	–	4-cyl., in-line (wall-guided mixture formation system)
Displacement	cm^3	1390
Cylinder bore.	mm	76.5
Piston stroke	mm	75.6
No. of valve/cyl.	–	4
Compression ratio	–	10:1
Max power	kW	125 kW at 6000 rpm
Max torque	Nm	220 Nm at 1750–4500 rpm
Aftertreatment systems	–	Tree-way catalysts, closed feedback loop
Emission norm	–	EU4

The engine under consideration is a direct-injection configuration incorporating a combined boost system that combines mechanical supercharging and turbocharging, following the "downsizing" approach. The fuel injection system employed in this engine is of the wall-guided type, and it utilizes electromagnetically controlled injectors featuring six injection holes. The procedure allows conducting fuel evaluation, including DCA (Deposit Control Additive), according to two tests, i.e.:

- CEC F-113-KC "Keep-Clean" Test Procedure: This is a 48 h test during which the engine is operated under constant speed (2000 rpm) and constant load (56 Nm) conditions. It allows evaluation of the base or refined fuel in terms of its ability to keep the injectors clean.
- CEC F-113-CU "Clean-Up" Test Procedure: Includes a 48 h part of the "Dirty-Up" test performed according to the "Keep-Clean" test and a 24 h part of the "Clean-Up" test in which the engine operates under the same conditions as in the "Dirty-Up" or "Keep-Clean" test. The test allows evaluating the cleaning properties of the fuel used in the "Clean-Up" part of the test.

The evaluation criterion for assessing the propensity of the fuel to generate injector deposits during the test is the variation in the width of the electrical pulse governing the fuel injection duration. As the deposits gradually accumulate both externally and internally within the injector, this duration progressively lengthens. Figure 1 illustrates a visual representation of the fuel injector, highlighting the presence of external deposits near the fuel outlet apertures.

Fig. 1. View of the fuel injector and external deposits in the area of the fuel outlet holes – VW EA111 BLG test engine

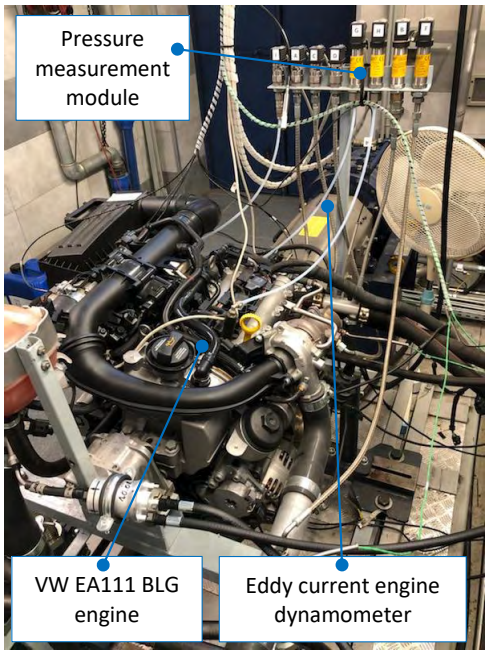

Fig. 2. Engine test stand (INIG-PIB)

Figure 2 shows a general view of the test bench for testing according to test procedure CEC F-113, on which tests were carried out at INiG-PIB. The project's tests were conducted per the CEC F-113-KC procedure (VW EA111 BLG) – 2022 edition.

3.2. Methodology of model testing

The static tests were conducted using a constant volume chamber (2.2 dm^3) into which fuel was injected at 10 MPa from a high-pressure injector without air back pressure

(Fig. 3). During the analyzes in the constant volume chamber, the same injector was used on which the engine tests were carried out. The same base fuel was used in the tests. The atomized fuel jet was evaluated using two systems: a) a camera together with a halogen light source – for the evaluation of spray geometric indexes; b) a camera and laser illumination system for the evaluation of the cross-section of the injected fuel jet. Laser illumination was generated using NG:YAG 532 mm pulsed laser light. The circular laser beam was converted into a so-called "light knife" in the collimator.

Fig. 4. View of the control panel for the operation of a test stand equipped with an isochoric chamber

The injection time was 0.5 ms, and the signal was generated from a Sequencer device (Fig. 4). Recording of images at 10 kHz was performed using an HSS 5 LaVision camera (with a resolution of 512 × 512 pixels). A Nikkon AF Nikkor 24-85 mm 1:2.8-4 D lens was used. Image analysis was carried out using DaVis 10 software.

3.3. Method of processing optical test results

Analysis of the images was conducted for:

- fuel spray, analyzing the range, area and cone angle of the jet (Fig. 5a); this research was based on measuring the side spray of fuel with halogen lighting;
- cross-sectional area of the fuel jet with detailed analysis of each jet cross-sectional area (Fig. 5b).

4. Fuels used in the study

The project's engine tests used three motor gasolines varying in composition including:

- CEC RF-12-09 batch 11 – base (reference fuel)
- CEC RF-12-09 batch 11 + 20% (V/V) ethanol
- CEC RF-12-09 batch 11 + 20% (V/V) butanol

The choice of reference gasoline was based on its popularity for research applications and availability across Europe. RF-12-09 batch 11 gasoline is a fuel with a high tendency to form deposits on intake valves used to calibrate Mercedes M102E and Mercedes M111 research engines.

The restriction of the alcohol admixture to 20% (V/V) was due to the engine manufacturer's requirements for the maximum allowable alcohol content in petrol. The physicochemical properties of the fuel samples prepared for testing are shown in Table 3.

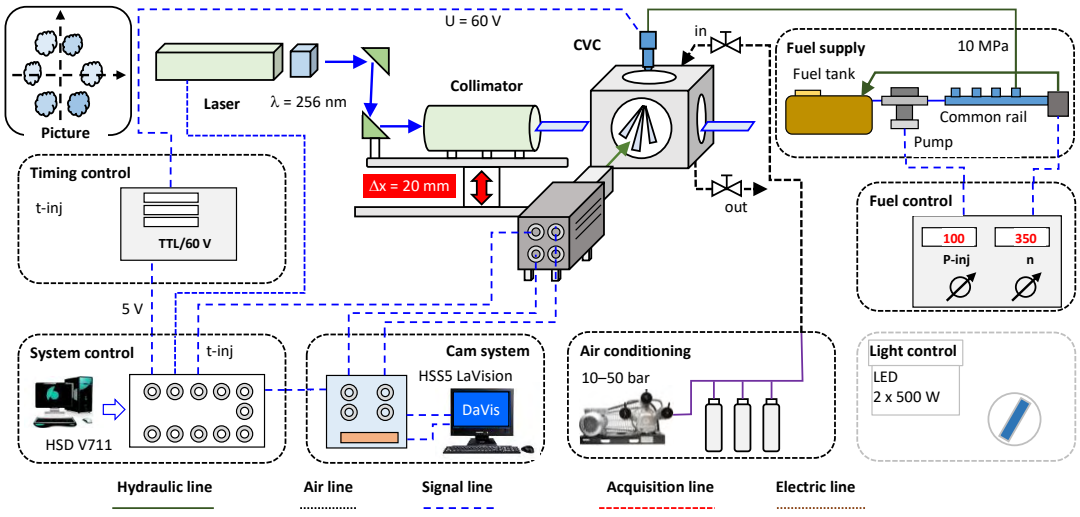

Fig. 3. Schematic of fuel atomization tests using laser illumination – cross-section of all fuel jets

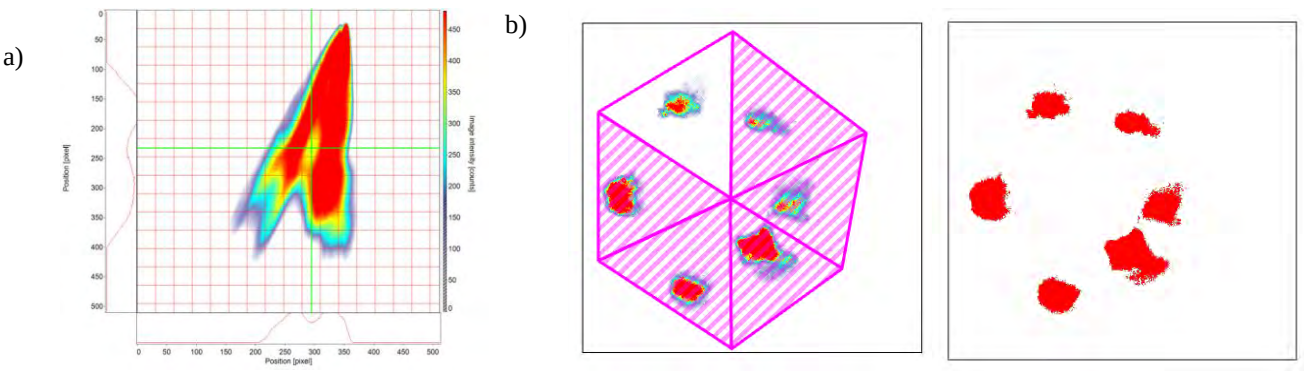

Fig. 5. Davis 7 software panel for analysis of individual areas of fuel injection: a) macroscopic analysis; b) stream cross-section analysis

5. Results discussion

5.1. Analysis of engine tests

Figure 6 shows a comparison of the changes in fuel injection times obtained during tests conducted according to the CEC F-113-KC procedure for the three fuels tested. The first test (base fuel) evaluated the ability of the raw fuel without alcohol admixture to keep the injectors clean.

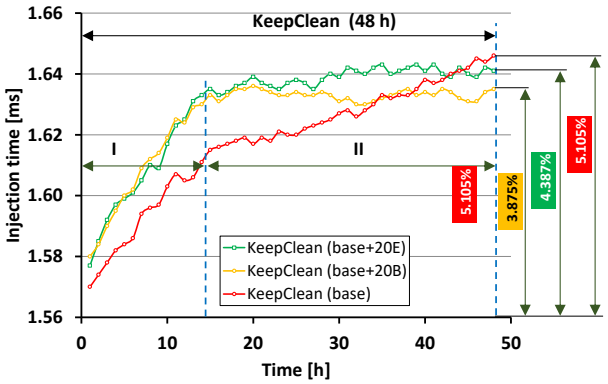

Fig. 6. Results comparison of the fuel's ability without and with alcohol admixture to maintain the cleanliness of DISI engine injectors according to the CEC F-113-KC procedure

Test two (base fuel + 20E) evaluated the same raw fuel admixed with 20% (V/V) ethanol according to the same procedure, and test three (base fuel + 20B) evaluated fuel admixed with 20% (V/V) butanol. The test result is the averaged difference in the electrical pulse width controlling the fuel injectors' opening time in a single fuel injection, measured before and after the test.

Due to the highly fluctuating and rapidly changing nature of the measured pulse, characterized by both high frequency and significant amplitude variations over time, determining the total pulse width or injection time solely by comparing its magnitudes at the beginning and end of the test could result in substantial errors. To mitigate this, a methodology based on a trend function is employed, as it provides more reliable and representative values compared to those based solely on the endpoints of the measurement. By utilizing this approach, average calculations of the electrical pulse widths controlling the injection time are obtained at the start and conclusion of the test. The test result is determined by calculating the difference between the average widths of the electrical pulse controlling the time of a single fuel injection at the beginning and end of the test. This difference is expressed as a percentage [%], indicating the increase in width. A larger difference indicates a greater tendency of the fuel to form injector deposits.

It is important to consider that the characteristics of each engine design, the combustion process strategy, injector design, and operating conditions significantly influence the development and severity of injector deposition phenomena. Therefore, the final evaluation of a fuel is based on the progression of deposit formation and the size of injector deposits observed over a specific period. Thus far, evaluations of fuels using the procedure above have been conducted in various European laboratories affiliated with the CEC (Coordinating European Council), specifically

Table 3. Physical and chemical properties of gasoline samples prepared for engine testing

Parameter	Unit	RF-12-09 batch 11	RF-12-09 batch 11 + 20% (V/V) ethanol	RF-12-09 batch 11 + 20% (V/V) butanol	Test method
		1	2	3	
Density at temperature 15°C	kg/m^3	734.4	747.2	753,9	PN-EN ISO 12185
Research octane number (LOB)	-	96.3	98.3	98,8	PN-EN ISO 5164
Motor octane number (LOM)	-	87.1	87.7	88,7	PN-EN ISO 5163
Sulfur content	mg/kg	5.0	3.7	3,5	PN-EN ISO 20846
Induction period	minutes	> 360	> 360	> 360	PN-EN ISO 7536
Resin content present	mg/100ml	0.5	1.0	2,5	PN-EN ISO 6246
Hydrocarbon content of type:					PN-EN 15553
– olefin	% (V/V)	5.5	< 4.0	< 4.0	
– aromatic	% (V/V)	27.8	21.5	23.1	
Benzene content	% (V/V)	0.36	0.3	0.3	PN-EN 238:2000 +A1
Oxygen content	% (m/m)	< 0.1	7.53	4.94	PN-EN 1601
The content of oxygen-containing organic compounds:					
– methanol	% (V/V)	< 0.80	< 0.17	< 0.17	PN-EN 1601
– ethanol	% (V/V)	< 0.80	20.4	< 0.17	
n-butanol	% (V/V)	< 0.80	< 0.17	20.2	
– isopropyl alcohol	% (V/V)	< 0.80	< 0.17	< 0.17	
– tert-butyl alcohol	% (V/V)	< 0.80	< 0.17	< 0.17	
– isobutyl alcohol	% (V/V)	< 0.80	< 0.17	< 0.17	
– other oxygen-containing organic compounds	% (V/V)	< 0.80	< 0.17	< 0.17	
Fractional composition:					PN-EN ISO 3405
– IBP	°C	32.9	36.7	36.7	
– end of distillation temperature	°C	196.9	196.5	198.0	
– distills	% (V/V)	97.9	98.2	98.5	
– residue	% (V/V)	1.1	1.0	1.0	
– losses	% (V/V)	1.4	0.8	0.5	
– evaporation temp. 10%, T10	°C	52.4	52.8	61.7	
– evaporation temp. 50%, T50	°C	106.8	72.7	102.6	
– evaporation temp. 90%, T90	°C	173.2	152.3	153.4	

through the efforts of the CEC TDG F-113 Working Group. These evaluations have allowed for determining result repeatability using statistical analysis based on the Student's t-distribution.

It has been determined that a minimum absolute difference of 1.8% in the magnitude of the electrical pulse width is required to distinguish between the two results with a 90% confidence interval. Comparing the results of the CEC F-113-KC tests for the three tested fuels (as shown in Figure 3), the average increase in calculated injection time for the reference fuel was 5.105%, for the reference fuel with 20% (V/V) ethanol admixture was 4.387%, and for the reference fuel with 20% (V/V) butanol admixture was 3.875%. Previous research has identified several key properties of unrefined fuel that significantly affect the formation of injector deposits, including T90 temperature, fuel sulfur, olefin and aromatics content, as well as vapour pressure, density, IBP, and octane number [22, 23]. However, all the tested fuels were based on the same reference fuel (RF-12-09 batch 11), resulting in small differences in their physicochemical properties, primarily attributed to adding ethanol or butanol. Additionally, the final result is influenced by the complex interaction of various fuel properties, which can have intricate and difficult-to-determine effects on deposit formation. Analyzing the final results obtained for the three fuels, it can be observed that, from a perspective of repeatability, these results should be considered comparable and statistically evaluated. Notably, the pattern of deposit formation during the 48-hour test period is of interest. In the case of the reference fuel, a nearly linear increase in deposits formed throughout the test can be observed (as shown in Figure 3).

Consequently, after a 15-hour test run, the calculated increase in injection time of a single fuel dose is 2.936% (Area I). Subsequently, between 15 hours and 48 hours, the increase in injection time of a single fuel dose changes from 2.936% to 5.105% (Area II). The situation differs for the reference fuel with a 20% (V/V) ethanol admixture, where the increase in injection time of a single fuel dose follows a logarithmic trend. After approximately 15 hours of the test run, a clear deviation in the trend of deposit formation can be observed at an increase in injection time of a single fuel dose of 3.942% (Area I). Then, between 15 and 48 hours of the test, the increase in injection time of a single fuel dose changes from 3.942% to 4.387% (Area II). A similar trend is observed for the reference fuel with a 20% (V/V) butanol admixture, where a distinct break in sediment formation occurs at an increase in injection time of a single fuel dose of 3.748% after about 15 hours (Area I). Subsequently, between 15 and 48 hours of the test, the increase in injection time of a single fuel dose changes from 3.748% to 3.875% (Area II). Hence, in the case of fuels blended with alcohol, the formation of deposits stabilizes after approximately 15 hours of testing. The differences in the trend and rate of injector deposit formation for different fuels can be attributed to the intensity of deposit precursor formation processes, the strength of adhesion to the surface, and the simultaneous self-cleaning processes of injectors [22, 23]. After the formation and stabilization of deposit precursors on the injector surface, their growth and removal processes determine the subsequent course of deposit formation. A linear pattern occurs when deposit formation and removal processes occur concurrently, with a constant predominance of fouling. Thus, it can be hypothesized that fuels containing alcohol (in the case of the tests described here, ethanol or butanol) have a lower tendency to foul the fuel injectors. This is because, due to the linear increase in fuel injection time caused by non-alcohol-containing fuels, the level of injector fouling created will exceed that of alcohol-containing fuels due to their stabilization after a certain period.

5.2. Analysis of optical tests

An optical analysis of the fuel spray is shown in Fig. 7. As can be seen from the images, there is some variation in the geometry of the recorded areas. Very similar extents of the jet can be seen. The variation relates to changes in the fuel concentration in the jet, as the degree of exposure of the images is slightly different. Analysis of the ethanol base fuel spray indicates a higher fuel concentration in the jet's core than in the other spray cases.

A detailed macroscopic analysis is shown in Fig. 8. Very similar values of the spray area can be seen, which is differentiated only in the range t = 750–1000 us to the beginning of fuel outflow (Fig. 8a). Identical values of penetration indicate (Fig. 8b) that it is necessary to analyze further quantities, which will adequately enable the evaluation of changes in the fuel spray, using different additives to the base fuel. For this reason, the jet cone angle was determined (Fig. 8c), which already indicates clear differences in fuel atomization. For the base fuel, this angle obtains almost constant values (about 40 deg). With butanol addition, this angle is greater: at the beginning of the atomization, about 50 deg and then decreases to about 40 deg. The atomization of the fuel from the injector running on fuel with ethanol addition shows a higher value of this angle from 55 deg at the beginning of atomization to about 43 deg after about 1 ms.

The results of the tests using laser illumination are shown in Fig. 9. Image analyses were performed in multiple cross-sections (from about 5 to 25 mm) from the maximum penetration. The spray areas shown indicate differences in the spray created by the three differently contaminated injectors. The use of the base fuel indicates a reduction in the cross-sectional area of the orifices, resulting in limited areas of some outflow orifices. The ethanol additive reduces fuel outflow to the least extent, as indicated by the large cross-sectional areas of the plumes. The use of butanol as an additive reduces the cross-sectional flow areas somewhat, but the reduction is not as significant as when only the base fuel is used.

A detailed assessment of the number of pixels in each isolated injected fuel jet is shown in Fig. 10. The data included are for the cross sections shown in Fig. 9. These analyses confirm that ethanol as an additive obtains the largest spray area. However, these changes are not very large. It should be noted that optical tests were conducted on the same base fuel, and the changes obtained are due to measurements of the injector, which was fed with different fuels.

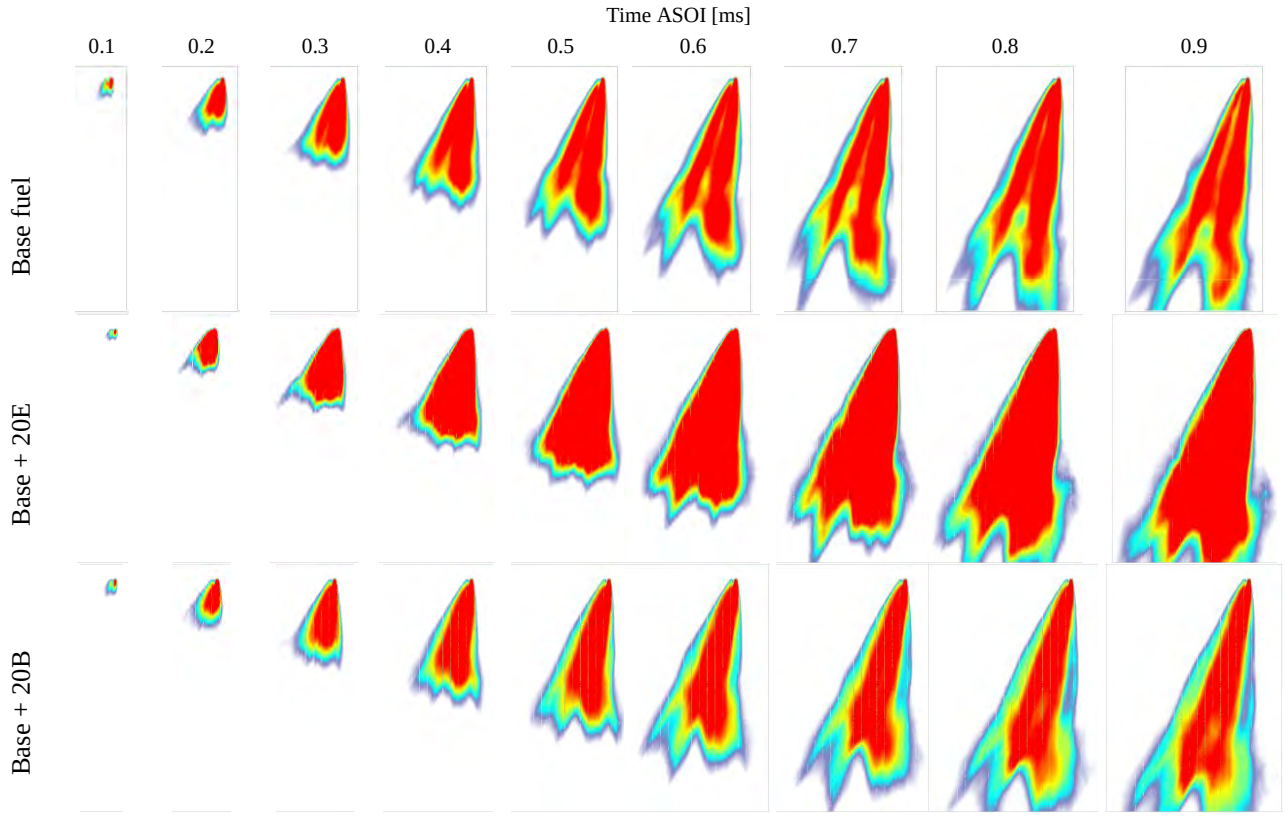

Fig. 7. Sequence of fuel spray images from the tested injectors

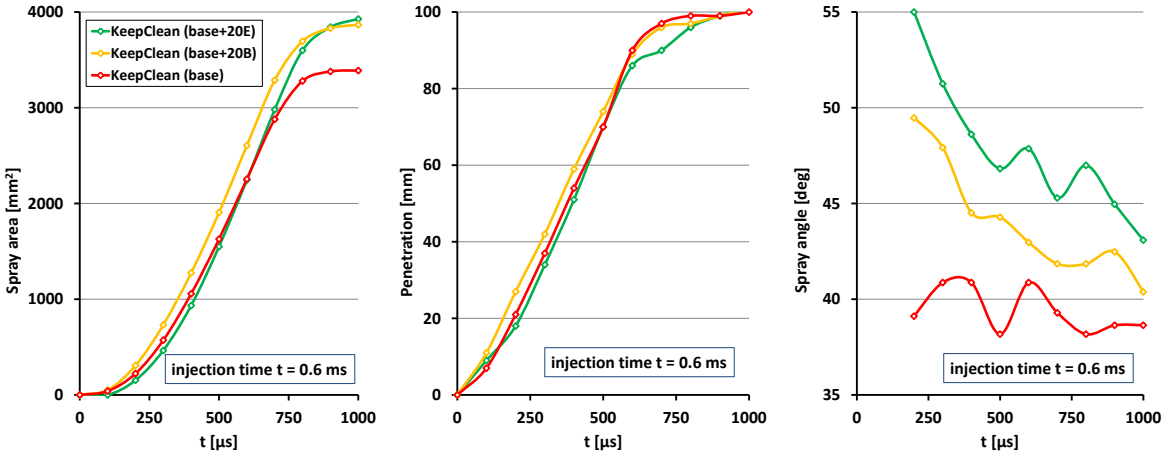

Fig. 8. Macroscopic indicators of fuel sprays

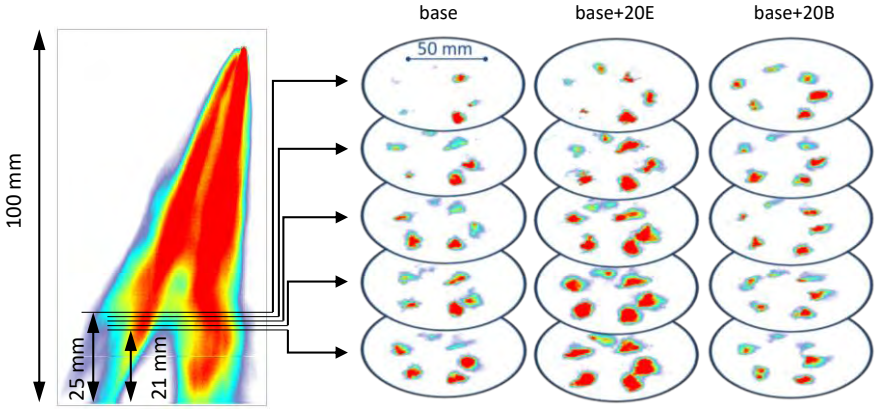

Fig. 9. Representation of the stream cross-section location with results (the results refer to successive tests of fuel atomization; t_{inj} = 0.6 ms; t = 1 ms)

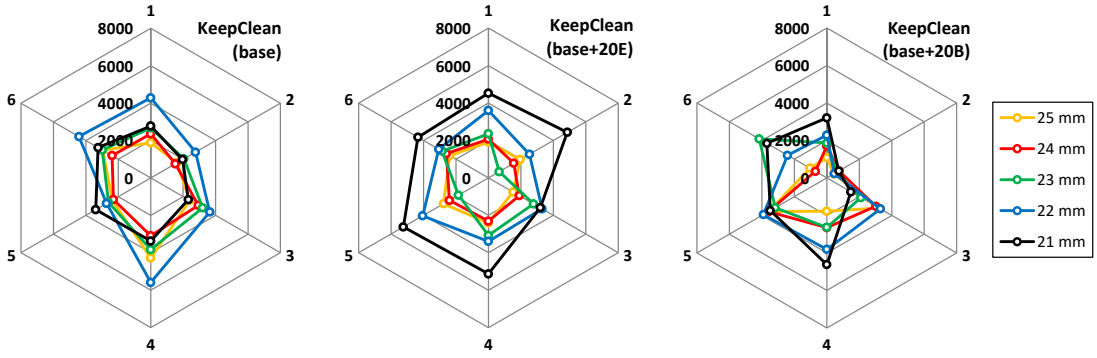

Fig. 10. Areas of the fuel stream from Fig. 9, including the isolation of each fuel stream

Figure 11 shows the total pixels from the fields of all injector orifices in a given unit of time to the beginning of fuel atomization. Instantaneous injection area values are included in Fig. 11a, while Fig. 11b shows trend lines for the three summed injection areas. The analysis results presented here show that the flow diameters of the injectors increase when base fuel additives are used. The use of fuel additives significantly increases the fuel flow area. The increase in area is more than 20% compared to the base fuel.

a)

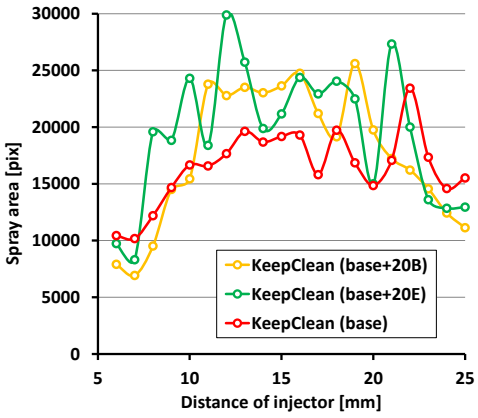

b)

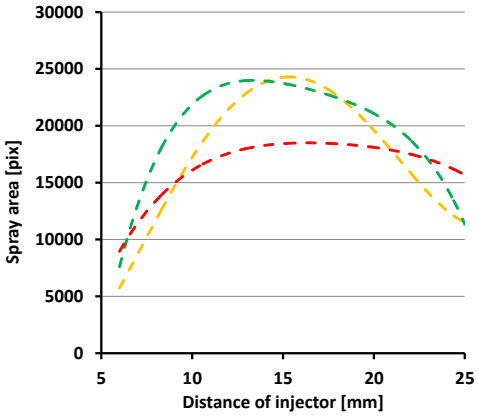

Fig. 11. Total area value of fuel jets over the full range of analysis (a) and averaged area values determined by a polynomial (n = 4) trend line

In addition, an analysis of the structure of the outflow holes was performed using a microscope. One of the elements of such tests was the determination of the different diameters of the actual bore of the working injector (Fig. 12). The results indicate that the pinhole is partially coked, as its diameters are different. The differences obtained are up to 30%.

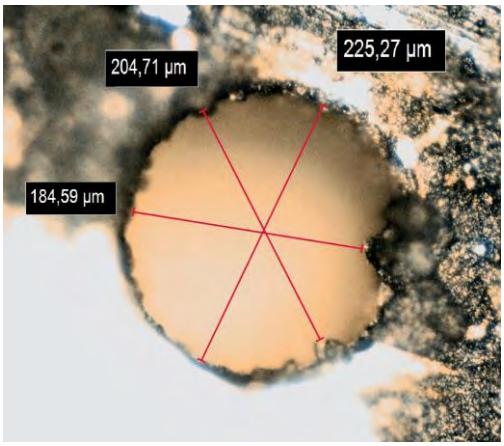

Fig. 12. Example values defining injector hole diameter

In the next stage of the work, an optical analysis of all the holes of the working injector was carried out (Fig. 13). These studies indicate varying deposition of the holes. The analyzed images do not clearly indicate large changes in injector orifice contamination. Thus, a full contamination analysis requires both engine and bench tests with their support by optical data.

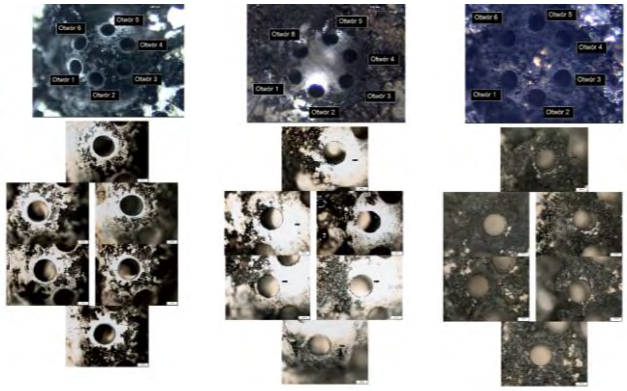

KeepClean (base) | KeepClean (base + 20B) | KeepClean (base + 20E)

Fig. 13. Images of the injector tip and holes after testing

6. Conclusion

The experimental work evaluated the effect of adding alcohols (ethanol, butanol) to the fuel on forming deposits in the injector holes. A direct injection system with multi-hole injectors was analyzed. A comprehensive evaluation was made by combining tests on a multi-cylinder engine, optical tests using laser illumination and magnification photography.

By analyzing the change in fuel injection time during a 48-hour test on an engine dynamometer, it was proven:

1. The addition of 20% V/V alcohol increases the injection time relative to the reference fuel RF-12-09 batch 11.
2. After 15 hours of the test, the relative increase in injection time was 2.936%, 3.942% and 3.748% respectively for the use of reference fuel, ethanol admixture and butanol admixture.
3. After 48 hours of testing, the relative increase in injection time was 5.105%, 4.387% and 3.875% for the use of reference fuel, ethanol admixture and butanol admixture, respectively.
4. In the case of fuel containing an admixture of alcohol, there is a balancing of the processes of formation and removal of deposits after only a few hours of testing.
5. Alcohol-containing fuels have a lower tendency to contaminate fuel injectors.

Based on optical studies of the development of the fuel jet from the injectors used during the engine tests, it was noted:

1. As a result of recording the jet outflow parallel to the axis, a change in the jet shape was noticed without an increase in jet penetration.
2. The use of an alcohol admixture in the fuel after 48 hours of injector operation results in an increase in the spray area and cone angle (parallel view) relative to the use of the reference fuel.
3. The type of alcohol used has no significant effect on the resulting surface area of the sprayed fuel (parallel view; perpendicular view).
4. The largest cross-sectional area of the jet occurs at a distance of about 15 mm from the tip of the injector.

Photographing the injector holes with 1,000 times magnification allowed to:

1. Determine the location of deposit accumulation depending on the fuel used.
2. Indication of the base + 20E mixture as the one where the highest amount of deposits occurs on the outer part of the atomizer. The smallest deposit on the outer part was obtained using base + 20B.

Acknowledgements

This article was prepared according to the statutory work entitled: “Improvement and stabilization of pro-ecological performance of an internal combustion engine by admixture of alcohol to gasoline"; order number: 0043/TE/22 (TE-4101-31/22) INiG-PIB under the order of the Ministry of Science and Higher Education and research work 0451/ SBAD/0337 (Poznan University of Technology).

Nomenclature

20B	the addition of 20% V/V butanol
20E	the addition of 20% V/V ethanol
ASOI	after start of injection
CEC	Coordinating European Council
CNG	compressed natural gas
DCA	deposit control additive
DISI	direct injection spark ignition
ePURE	European Renewable Ethanol
EUCAR	European Commission's Joint Research Centre, the European Council for Automotive R&D
FFVs	flex fuel vehicles
FQD	fuel quality directive
GDI	gasoline direct injection
GHG	greenhouse gases
ISC-FCM	in-service conformity – fuel consumption monitoring
LPG	liquefied petroleum gas
RED	Renewable Energy Directive
λ	air excess ratio

Bibliography

[1] Ashida T, Takei Y, Hosi H. Effects of fuel properties on SIDI fuel injector deposit. SAE Technical Paper 2001-01-3694, 2001. https://doi.org/10.4271/2001-01-3694

[2] Castagliola MM, De Simio L, Iannaccone S, Prati MV. Combustion efficiency and engine-out emissions of a SI engine fueled with alcohol/gasoline blends. Appl Energy. 2013;111:1162-1171. https://doi.org/10.1016/j.apenergy.2012.09.042

[3] Czerwinski J, Comte P, Stepien Z, Oleksiak S. Effects of ethanol blend fuels E10 and E85 on the non-legislated emissions of a flex fuel passenger car. SAE Technical Paper 2016-01-0977, 2016. https:/doi.org/10.4271/2016-01-0977

[4] Directive 2003/30/EC of the European Parliament and of the Council of 8 May 2003 on the promotion and the use of biofuels or other renewable fuels for transport. https://eur-lex.europa.eu/legal-content/EN/ALL/?uri=CELEX:32003L0030

[5] Directive (EU) 2018/2001 of the European Parliament and of the Council of 11 December 2018 on the promotion of the use of energy from renewable sources. https://eur-lex.europa.eu/legal-content/EN/TXT/?uri=CELEX:32018L2001

[6] DuMont RJ, Cunningham LJ, Oliver MK, Studzinski MK, Galante-Fox JM. Controlling induction system deposits in flexible fuel vehicles operating on E85. 2007. SAE Technical Paper 2007-01-4071, 2007. https://doi.org/10.4271/2007-01-4071

[7] DuMont RJ, Evans JA, Feist DP, Studzinski WM, Cushing TJ. Test and control of fuel injector deposits in direct injected spark ignition vehicles. SAE Technical Paper 2009-01-2641, 2009. https://doi.org/10.4271/2009-01-2641

[8] Fourier E, Simon G, Seers P. Evaluation of low concentrations of ethanol, buthanol BE, and ABE with gasoline direct-injection, spark-ignition engine. Fuel. 2016;181:396-407. https://doi.org/10.1016/j.fuel.2016.04.135

[9] Galloni E, Fontana G, Staccone S, Scala F. Performance analyses of a spark-ignition engine firing with gasoline-butanol blends at partial load operation. Energy Convers Manag. 2016;110:319-326. https://doi.org/10.1016/j.enconman.2015.12.038
[10] Hergueta C, Bogarra M, Tsolakis A, Essa K, Herreros JM. Butanol-gasoline blend and exhaust gas recirculation, impact on GDI engine emissions. Fuel. 2017;208:662-672. https://doi.org/10.1016/j.fuel.2017.07.022
[11] Joedicke A, Krueger-Venus J, Bohr P, Cracknell R, Doyle D. Understanding the effect of DISI injector deposits on vehicle performance. SAE Technical Paper 2012-01-0391, 2012. https://doi.org/10.4271/2012-01-0391
[12] Kale R, Banerjee R. Optical investigation of flash boiling and its effect on in-cylinder combustion for butanol isomers and iso-octane. Int J Engine Res. 2021;22(5):1565-1578. https://doi.org/10.1177/1468087420917241
[13] Lee S, Oh Y, Park S. Characterization of the spray atomization process of a multi-hole gasoline direct injector based on measurements using a phase Doppler particle analyser. Proc Inst Mech Eng Part D J Automob Eng. 2013;227(7):951-965. https://doi.org/10.1177/0954407013483244
[14] Mitroglou N, Nouri JM, Yan Y, Gavaises M, Arcoumanis C. Spray structure generated by multi-hole injectors for gasoline direct injection engines. SAE Technical Paper 2007-01-1417, 2007. https://doi.org/10.4271/2007-01-1417
[15] Moon S, Huang W, Li Z, Wang J. End-of-injection fuel dribble of multi-hole diesel injector: Comprehensive investigation of phenomenon and discussion on control strategy. Appl Energy. 2016;179:7-16. https://doi.org/10.1016/j.apenergy.2016.06.116
[16] Regulation (EU) 2019/631 of the European Parliament and of the Council of 17 April 2019 setting CO_2 emission performance standards for new passenger cars and for new light commercial vehicles, and repealing Regulations (EC) No 443/2009 and (EU) No 510/2011. https://eur-lex.europa.eu/legal-content/EN/TXT/?uri=CELEX:32019R0631
[17] Rubio-Gomez G, Corral-Gomez L, Rodriguez-Rosa D, Sanchez-Cruz FA, Martinez-Martinez S. A comparative study of the effect of compression ratio on the efficiency and flame development angle in a cooperative fuel research engine fueled with binary gasoline–alcohol blends. Int J Engine Res. 2021;22(2):569-580. https://doi.org/10.1177/1468087419859104
[18] Russell M, Cummings J, Cushing T, Studzinski W. Cellulosic ethanol fuel quality evaluation and its effects on PFI intake valve deposits and GDI fuel injector plugging performance. SAE Technical Paper 2013-01-0885, 2013. https://doi.org/10.4271/2013-01-0885
[19] Singh AP, Sharma N, Kumar V, Agarwal AK. Experimental investigations of mineral diesel/methanol fueled reactivity controlled compression ignition engine operated at variable engine loads and premixed ratios. Int J Engine Res. 2021; 22(7):2375-2389. https://doi.org/10.1177/1468087420923451
[20] Skogsberg M, Dahlander P, Lindgren R, Denbratt I. Effects of injector parameters on mixture formation for multi-hole nozzles in a spray-guided gasoline DI engine. SAE Technical Paper 2005-01-0097, 2005. https://doi.org/10.4271/2005-01-0097
[21] Song H, Xiao J, Chen Y, Huang Z. The effects of deposits on spra,y behaviors of a gasoline direct injector. Fuel. 2016;180: 506-513. https://doi.org/10.1016/j.fuel.2016.04.067
[22] Stępień Z. Utility-exploitation potential of butanol as an alternative fuel designed for car SI engines. Nafta-Gaz. 2020;2:126-135. http://doi.org/10.18668/NG.2020.02.07
[23] Stępień Z, Pielecha I, Cieślik W, Szwajca F. The impact of alcohol admixture with gasoline on carbon buildup and fuel injectors performance. Eksploat Niezawodn. 2022;24(2): 226-236. https://doi.org/10.17531/ein.2022.2.4
[24] Taniguchi S, Yoshida K, Tsukasaki Y. Feasibility study of ethanol applications to a direct injection gasoline engine. SAE Technical Paper 2007-01-2037, 2007. https://doi.org/10.4271/2007-01-2037
[25] Wang B, Badawy T, Jiang Y, Xu H, Ghafourian A, Hang X. Investigation of deposit effect on multi-hole injector spray characteristics and air/fuel mixing process. Fuel. 2017; 191:10-24. https://doi.org/10.1016/j.fuel.2016.11.055
[26] Xu H, Wang C, Ma X, Sarangi AK, Weall A, Krueger-Venus J. Fuel injector deposits in direct-injection spark-ignition engines. Prog Energy Combust Sci. 2015;50:63-80. https://doi.org/10.1016/j.pecs.2015.02.002

Prof. Ireneusz Pielecha, DSc., DEng. – Faculty of Civil and Transport Engineering, Poznan University of Technology, Poland.
e-mail: *ireneusz.pielecha@put.poznan.pl*

Filip Szwajca, MEng. – Faculty of Civil and Transport Engineering, Poznan University of Technology, Poland.
e-mail: *filip.szwajca@put.poznan.pl*

Prof. Zbigniew Stępień, DSc., DEng. – Performance Testing Department, Oil and Gas Institute – National Research Institute, Poland.
e-mail: *stepien@inig.pl*

Article citation info:
Nakashima K, Matsunaga K, Uchiyama Y, Yoshida M. Development of measurement apparatus of piston assembly friction in a small motorcycle engine. Combustion Engines. 2023;194(3):32-37. https://doi.org/10.19206/CE-168330

Kohei NAKASHIMA
Kota MATSUNAGA
Yosuke UCHIYAMA
Masao YOSHIDA

Combustion Engines
Polish Scientific Society of Combustion Engines

Development of measurement apparatus of piston assembly friction in a small motorcycle engine

ARTICLE INFO

Received: 14 May 2023
Revised: 14 June 2023
Accepted: 14 June 2023
Available online: 7 July 2023

This study developed a friction measurement apparatus with a floating cylinder liner in a small motorcycle engine. In this measurement apparatus, joint plates were installed in the grooves on the outer periphery of the floating liner, and then the plates, as well as load washers of piezo type, were mounted in the cylinder block at both the thrust and the anti-thrust sides. A stepped ring, protruding inward, was mounted on the top of the floating liner so that cylinder pressure acting on the stepped portion was balanced in the vertical direction. Thus, it was possible to measure the friction in the sliding directions of the piston. Using this apparatus, the effect of the engine operating period on friction was investigated in a piston micro-dimpled with a fine particle bombarding process. Results indicated that, at low engine speeds, friction decreased with the operating period, but at high engine speeds, friction decreased after 10 hours of operation, and then increased after 20 hours of operation.

Key words: *piston assembly friction, floating cylinder liner, piston, fine particle bombarding, micro dimple*

1. Introduction

Small motorcycle engines are required not only to have excellent acceleration performance but also to have excellent economic efficiency, i.e., less expensive engines with low fuel consumption rates. To improve fuel efficiency, it is effective to reduce engine friction, especially piston assembly friction (the friction between the piston, the piston rings, and the cylinder liner) [2, 8, 10, 12]. Two measurement methods have been mainly used to measure this piston assembly friction during engine operation. One is the floating liner method, in which load washers are fixed between the lower portions of the floating liner and the cylinder block on the thrust and the anti-thrust sides [1, 3, 4, 6, 9, 18, 20–22]. The other is the three-component force sensor method, in which three-component force sensors are fixed, either at 8 points between the outer periphery of the floating liner and the inner periphery of the block on the thrust side, or at 3 points each between the outer periphery of the floating liner and the inner periphery of the block, on both the thrust and the anti-thrust sides [5, 7, 11, 13, 19]. Both methods require a prototype floating liner, but the first floating liner method requires fewer sensors and fewer engine modifications than the three-component force sensor method. So there are more reports on friction measurements using the floating liner method. Our previous study developed a friction measurement apparatus with a floating liner for an eco-mileage vehicle engine, by using components of a small motorcycle engine as much as possible [14, 15]. In this measurement apparatus, joints plates were inserted in the grooves on the outer periphery of the floating liner, machined from the periphery of a commercially available air-cooled cylinder, and then load washers were mounted between the joint plates and the cylinder block, at both the thrust and the anti-thrust sides. To suppress lateral displacement due to piston thrust force, clamping bolts were also mounted to the cylinder block at four sides: thrust, anti-thrust, front, and rear. This enabled measuring the piston assembly friction when the intake and the exhaust valves were not activated, i.e., no cylinder pressure was applied. This current study significantly modified the structure of the upper part of the floating liner from our previous measurement apparatus, so that the force due to the pressure in the cylinder was not transmitted to the floating liner. Thus, it was possible to measure piston assembly friction even when the intake and the exhaust valves were activated, and cylinder pressure was applied. Into this new measurement apparatus, a micro-dimpled piston with a fine particle bombarding (FPB) process [15–17] was installed. Such micro-dimpled pistons enjoy reduced friction compared with untreated pistons [15–17] and reduced total engine friction with increasing engine operating period [16]. However, no report has measured piston assembly friction with a micro-dimpled piston for each cycle and examined the effect of the engine operating period on its friction. This study investigated in detail how piston assembly friction with a micro-dimpled piston changed with the engine operating period compared to before break-in.

2. Experimental apparatus and method

Figures 1 and 2 show the friction measurement apparatus with the floating liner. As in our previous study, this measurement apparatus employed a four-stroke, air-cooled, horizontal, single-cylinder, gasoline engine for a commercially available small motorcycle (bore × stroke = 39 mm × 41.4 mm) [14, 15]. The crankcase of this engine was cut, and a cover was attached to the cut of the crankcase. The engine was then rotated from horizontal to vertical. For the floating liner, the outer periphery of the air-cooled cylinder (an aluminum finned cylinder with a cast-iron liner) was turned, and the grooves for the joint plates were machined on its outer periphery at the thrust and the anti-thrust sides. In addition, the top of the liner was machined, and an aluminum alloy stepped ring was mounted on the top of the liner, protruding inward. Cylinder pressure acting on the

stepped portion was balanced in the vertical direction, so that the force due to the pressure in the cylinder was not transmitted to the floating liner. Joint plates were installed in the grooves on the outer periphery of the floating liner, and then piezo type load washers were mounted between the joint plates and the cylinder block, at both the thrust and the anti-thrust sides. Thus, only vertical force (piston assembly force) was applied to the joint plates, and from there to the load washers. An O-ring was installed between the stepped ring of the floating liner and the spacer immediately above it for gas sealing. The compression ratio became 7.3 after installing the stepped ring and the spacer. In addition, to suppress lateral displacement due to piston thrust force, circular thin-disk springs were attached to the upper and lower sides between the floating liner and the cylinder block. A strain-gage pressure transducer was also attached to the spark plug hole when measuring the cylinder pressure.

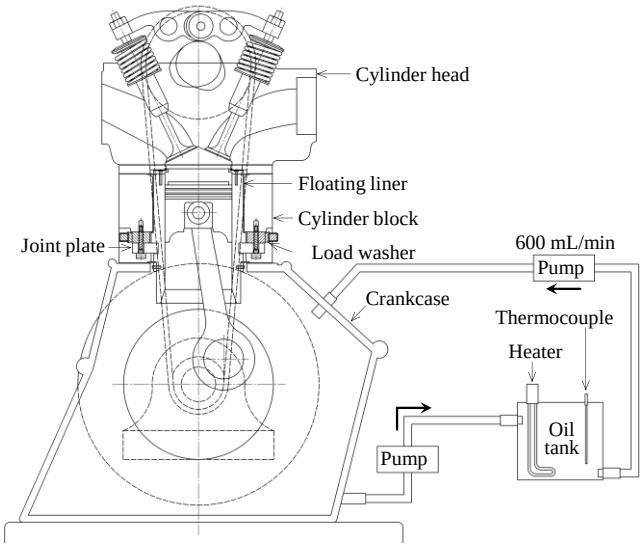

Fig. 1. Measurement apparatus of piston assembly friction

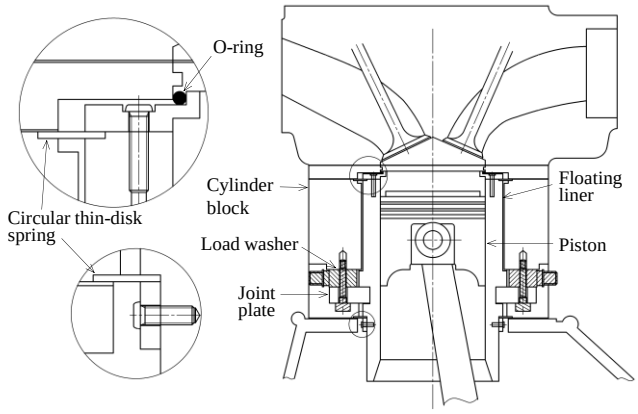

Fig. 2. Friction measurement system with floating liner

Bore surface temperature was adjusted with a temperature controller, by installing heaters in the cylinder block at the thrust, the anti-thrust, and the rear sides, and thermocouples at the front and the rear sides. The oil temperature was also adjusted with a temperature controller by installing a heater and a thermocouple in an oil tank outside the engine, as in our previous study [14, 15]. The lubricating oil, at fixed temperature, was pumped from the oil tank to a pipe on the upside of the crankcase, and then supplied from its pipe to the crankshaft at a flow rate of 600 mL/min, as shown in Fig. 1.

Figure 3 shows the micro-dimpled piston and its surface shape on the piston skirt. In this micro-dimpled piston, ceramic particles with a diameter of 45 μm were air-blasted onto a commercially available standard piston, which had a streaked sliding surface on the skirt, except for three grooves in the skirt. The top land of the piston was also machined away from contact with the stepped ring of the floating liner.

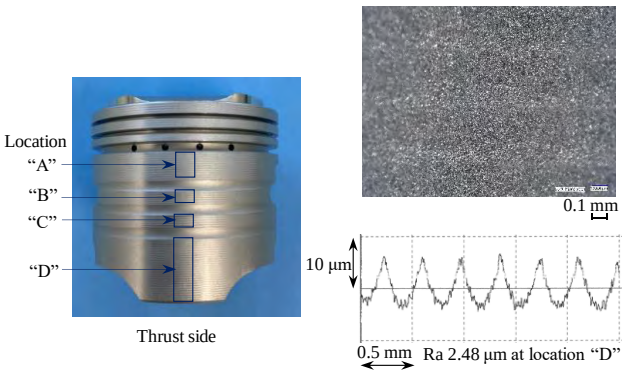

Fig. 3. Micro-dimpled piston and surface shape on the piston skirt

Table 1 shows the experimental rings, which are standard parts of a commercially available engine. These rings had been fully run in our previous study [15].

Table 1. Experimental piston rings

[mm]

Top ring	Second ring	Oil ring
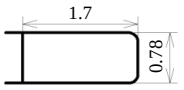	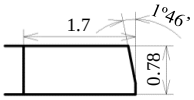	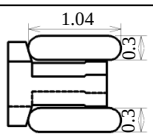
End clearance 0.08 mm Tension 3.2 N Chrome plating	End clearance 0.15 mm Tension 4.4 N Phosphate	End clearance 0.52 mm Tension 11.2 N Chrome plating

The floating liner had been fully operated in advance, with a standard untreated piston, and its roughness of the sliding surface on the liner bore was Rz_{JIS} 0.90~1.56 μm (Ra 0.12~0.19 μm).

The experimental lubricating oil was Honda genuine Ultra Green with a lower viscosity for low-fuel consumption engines. The kinematic viscosities of the lubricating oil measured with the Redwood viscometer were 30.3 mm^2/s at 40°C, 15.8 mm^2/s at 60°C, and 10.4 mm^2/s at 80°C.

The engine was operated by motoring, and the experiments were conducted according to the procedure shown in Fig. 4. That is, a new dimpled piston was installed in this measurement apparatus, and then without any break-in operation, the piston assembly friction was measured at engine speeds of 800 rpm, 1000 rpm, 1200 rpm, and 1400

rpm, at temperatures of 40°C, 60°C, and 80°C, respectively. Next, after running at 80°C and 1400 rpm for 10 hours, the friction was measured under these same conditions. Furthermore, after running at 80°C and 1400 rpm for another 10 hours (meaning after 20 hours in total at 80°C and 1400 rpm), friction was again measured under these same conditions.

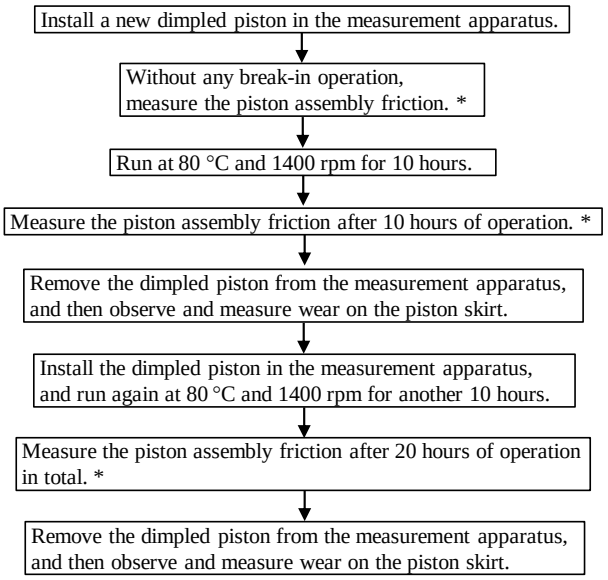

* Measurement conditions:
40 °C, and 800 rpm, 1000 rpm, 1200 rpm and 1400 rpm
60 °C, and 800 rpm, 1000 rpm, 1200 rpm and 1400 rpm
80 °C, and 800 rpm, 1000 rpm, 1200 rpm and 1400 rpm

Fig. 4. Experimental procedure

3. Results and discussion

Figures 5 and 6 show the effect of the engine operating period on piston assembly friction at 60°C, first at 1000 rpm and then at 1400 rpm, respectively. In Figs. 5 and 6, crank angles of –360º, 0º, and 360º represent engine top dead center (TDC); –180º and 180º bottom dead center (BDC). During the piston downward stroke (from –360º to –180º in the intake stroke, and from 0º to 180º in the expansion stroke), a downward force is applied to the liner, and during the piston upward stroke (from –180º to 0º in the compression stroke, and from 180º to 360º in the exhaust stroke), an upward force is applied to the liner. So these forces are indicated as negative force and positive force, respectively. In Fig. 5, at 60°C and 1000 rpm, as the engine operating period increased, friction decreased around TDC and BDC, as well as during the compression and the expansion strokes. In addition, the longer the operating period, the lower the friction reduction rate. In Fig. 6, at 60°C and 1400 rpm, friction after 10 hours of operation decreased around TDC and BDC and during the compression stroke, compared to before break-in operation (0 hours of operation). However, friction after 20 hours of operation was almost the same as that after 10 hours of operation, around TDC and BDC and during the compression and expansion strokes. During the intake and the exhaust strokes, except around TDC and BDC, friction after 20 hours of operation increased beyond that after 10 hours.

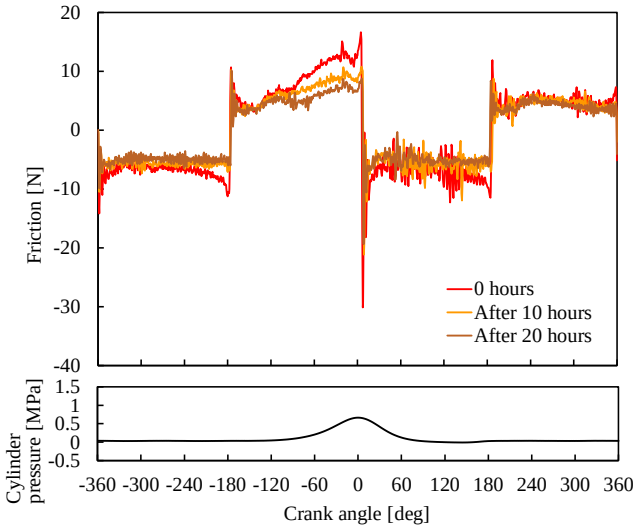

Fig. 5. Piston assembly friction at 60°C and 1000 rpm

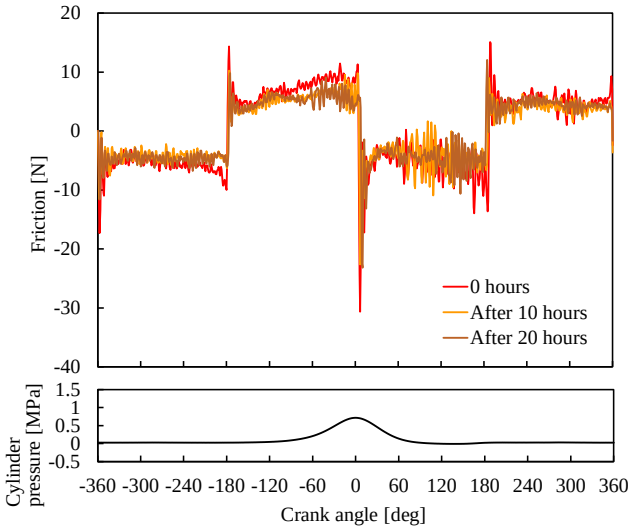

Fig. 6. Piston assembly friction at 60°C and 1400 rpm

Figures 7 to 9 show the effect of the engine operating period on the friction mean effective pressure (FMEP) at 40°C, 60°C, and 80°C, respectively. Here the FMEP was obtained by integrating the absolute value of friction at crank angles of –360° to 360° and dividing by the stroke volume. As the engine operating period increased, the FMEP decreased in each temperature, except at 1200 rpm and 1400 rpm after 20 hours of operation. At 1200 rpm and 1400 rpm, the FMEP after 20 hours of operation was higher than that after 10 hours of operation. When the engine speed increased, the FMEP decreased, both before break-in operation (0 hours of operation) and after 10 hours of operation. After 20 hours of operation, at 40°C and 60°C, the FMEP decreased as the engine speed increased from 800 rpm to 1200 rpm, and at 80°C, the FMEP decreased as the engine speed increased from 800 rpm to 1000 rpm. But at 40°C at more than 1200 rpm, the FMEP hardly changed, and at 60°C at more than 1200 rpm, and at 80°C at more than 1000 rpm, the FMEP increased.

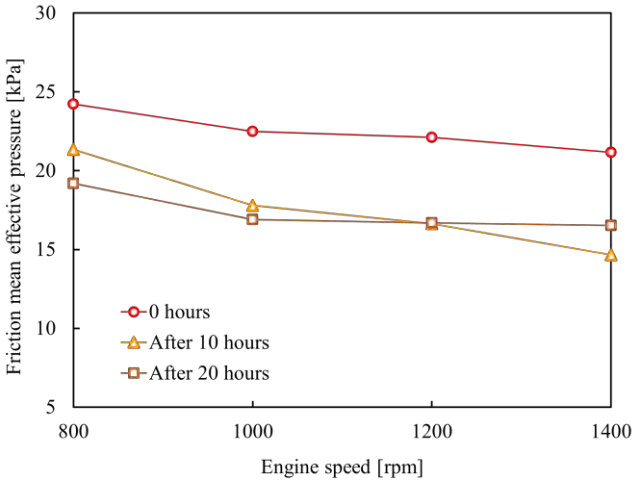

Fig. 7. Friction mean effective pressure at 40°C

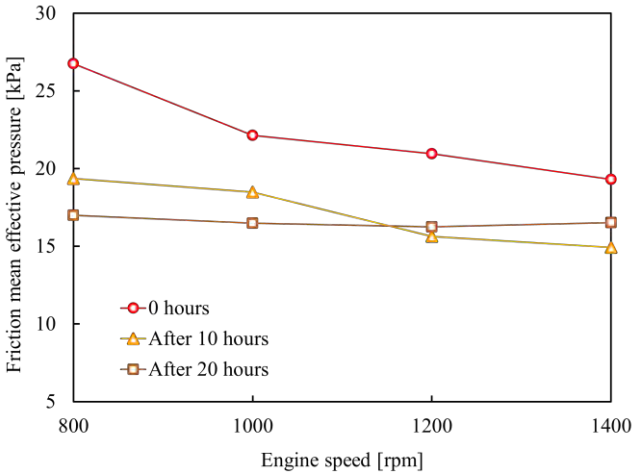

Fig. 8. Friction mean effective pressure at 60°C

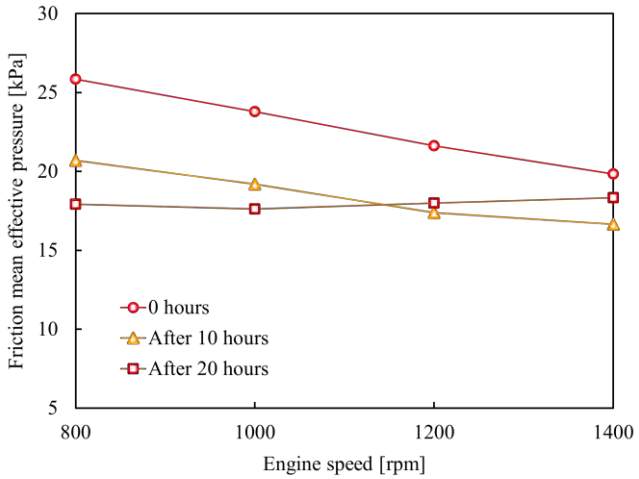

Fig. 9. Friction mean effective pressure at 80°C

When the sliding surface of the piston was observed after 10 hours and after 20 hours of operations, the wear of streaks was visually confirmed in locations "C" and "D" of the skirt. Therefore, the amount of wear on streaks in skirt "C," "D1" (upper part of "D") and "D2" (lower part of "D") was measured by using a surface roughness measuring instrument. Figure 10 shows the maximum amount of wear on streaks in skirt "C," "D1" and "D2" after 10 hours and after 20 hours. In Fig. 10, the maximum amount of wear after 10 hours was 1.5~3.0 μm on the thrust side, and 1.0~3.0 μm on the anti-thrust side. The maximum wear after 20 hours increased by 0.5~1.0 μm compared to that after 10 hours, but the amount of wear per hour tended to decrease.

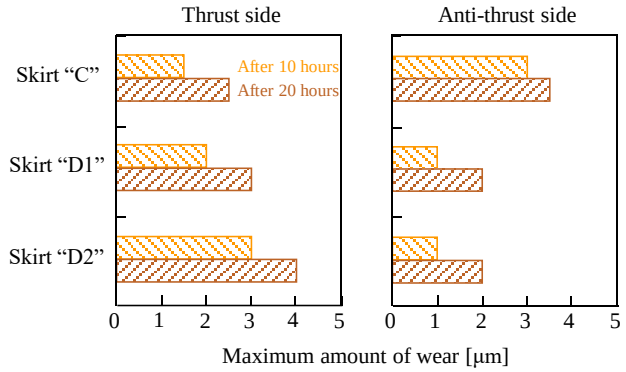

Fig. 10. Maximum amount of wear on streaks in lower skirt of piston after 10 hours and after 20 hours

Figure 11 shows the observation results of the worn part of skirt "C" after 10 hours and after 20 hours. In Fig. 11, the wear on both the thrust and the anti-thrust sides tended to be wider after 20 hours than after 10 hours, but after both 10 hours and 20 hours, micro-dimples remained even on the worn surfaces of the streak, and no significant difference was observed on them.

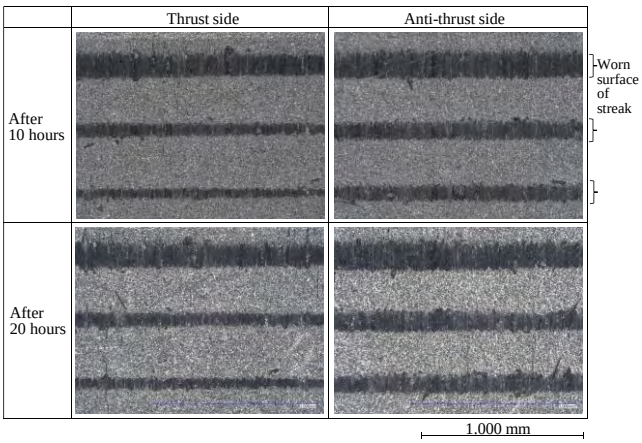

Fig. 11. Observation results of worn part at piston skirt "C" after 10 hours and after 20 hours

It seemed that, at 800 rpm and 1000 rpm, the longer the engine operating period, the greater the wear of the sliding surface, decreasing pressure (the normal load per area) on the sliding surface, and the less dominant the severe mixed lubrication, reducing the FMEP. In this measurement apparatus, the lubricating oil was supplied to the crankshaft, and was then splashed onto the cylinder by the rotation of the crankshaft. Therefore, as the engine speed increased, the amount of oil supplied to the piston per unit time increased. It was thought that, with increased engine speed, the

amount of oil supplied to the piston increased, and then friction around TDC of compression stroke (around 0º) decreased, reducing the FMEP except after 20 hours of operation. It also seemed that, after 20 hours of operation, because the wear on the streak of skirt had increased, forming a suitable sliding surface, hydrodynamic lubrication became dominant at 1200 rpm and 1400 rpm, and then friction increased during the intake and the exhaust strokes (where the piston thrust force weakened), except around TDC and BDC, increasing the FMEP.

4. Conclusions

Using a small motorcycle engine, a friction measurement apparatus with a floating liner was constructed, so that the force due to the cylinder pressure was not transmitted to the floating liner. Utilizing this measurement apparatus, the influence of engine operating period on friction with a micro-dimpled piston was examined. Results indicated that, at engine speeds of 800 rpm and 1000 rpm, friction decreased with the engine operating period. At more than 1000 rpm, friction decreased after 10 hours of operation, but then friction increased after 20 hours (to a level greater than after 10 hours). In addition, both before break-in operation (0 hours of operation) and after 10 hours, friction decreased with increasing engine speed. However, after 20 hours, friction increased when engine speed exceeded 1200 rpm at 60°C, and 1000 rpm at 80°C.

Acknowledgements

We would like to thank undergraduate students Mr. Kenta Aoki, and Mr. Yuki Okada, of Meijo University at that time, for fruitful cooperation during this experimental work. We would also like to thank Fujikihan Co., Ltd. for treating the piston surfaces with the FPB process, and Asano Machining Industry Co., Ltd. for helping to measure the piston surface with a roughness measuring instrument, and to observe the piston surface with a microscope.

Nomenclature

BDC	bottom dead center
FMEP	friction mean effective pressure
FPB	fine particle bombarding
Ra	calculated average roughness
Rz_{JIS}	10-point average roughness
TDC	top dead center

Bibliography

[1] Furuhama S., Takiguchi M. Measurement of piston frictional force in actual operating diesel engine. SAE Technical Paper 790855. 1979. https://doi.org/10.4271/790855

[2] Hoshi M. Reducing friction losses in automobile engines. Tribol Int. 1984;17(4):185-189. https://doi.org/10.1016/0301-679X(84)90017-3

[3] Iijima N, Aoki S, Imamura J, Takiguchi M. An experimental study on effect of lower tension piston rings on piston friction and lubricating oil consumption. Transactions of the Society of Automotive Engineers of Japan. 2009;40(6): 1477-1482. https://doi.org/10.11351/jsaeronbun.40.1477 (in Japanese).

[4] Ito A, Yamasaka K, Okamoto D, Morimoto T. A comparison for measurement devices for piston friction force by means of floating liner method. Transactions of the Society of Automotive Engineers of Japan. 2017;48(3):635-640. https://doi.org/10.11351/jsaeronbun.48.635 (in Japanese).

[5] Itoh Y, Konomi T, Iwashita Y. Analysis of piston friction on firing conditions by 3-component force sensor method. Transactions of the Society of Automotive Engineers of Japan. 1988;37:163-169 (in Japanese).

[6] Kanai S, Taresawa C, Fujiwara N. Friction reduction technology of the piston for gasoline engine. Transactions of the Society of Automotive Engineers of Japan. 2013;44(2):381-386. https://doi.org/10.11351/jsaeronbun.44.381 (in Japanese).

[7] Konomi T, Nohira H, Murakami M, Sanda S. Effects of piston skirt profile on friction loss and oil film behaviour. Proceedings of IMechE C465/011/93. 1993:147-154.

[8] Kovach J, Tsakiris E, Wong L. Engine friction reduction for improved fuel economy. SAE Technical Paper 820085. 1982. https://doi.org/10.4271/820085

[9] Madden D, Kim K, Takiguchi M. Part 1: Piston friction and noise study of three different piston architectures for an automotive gasoline engine. SAE Technical Paper 2006-01-0427. 2006. https://doi.org/10.4271/2006-01-0427

[10] Matsumoto K. Friction reduction in an internal combustion engine. Journal of the Japan Society of Mechanical Engineers. 1976;79(694):870-876. https://doi.org/10.1299/jsmemag.79.694_870 (in Japanese).

[11] Murakami M, Konomi T, Nohira H, Maeda Y, Nakada M. Analysis of piston frictional force under engine firing condition – effects of surface characteristics of piston skirt on friction. Transactions of the Society of Automotive Engineers of Japan. 1991;22(4):70-73 (in Japanese).

[12] Nakada M. Trends in engine technology and tribology. Tribol Int. 1994:27(1):3-8. https://doi.org/10.1016/0301-679X(94)90056-6

[13] Nakanishi K, Okada Y, Sera K, Minami K, Kadota I. Teardown analysis for piston assembly friction with optimization controls. Honda R&D Technical Review. 2010;22(1): 154-159.

[14] Nakashima K, Uchiyama Y. Experimental development of apparatus to measure piston assembly friction in an eco-mileage vehicle engine. Combustion Engines. 2019;177(2): 55-59. https://doi.org/10.19206/CE-2019-210

[15] Nakashima K, Uchiyama Y. Influence of piston surface treatment on piston assembly friction in an eco-mileage vehicle engine. Combustion Engines. 2022;188(1):18-23. https://doi.org/10.19206/CE-142552

[16] Ogihara H, Kido T, Yamada H, Murata M, Kobayashi S. Technology for reducing engine rubbing resistance by means of surface improvement. Honda R&D Technical Review. 2000;12(2):93-98.

[17] Ogihara H. Research into surface improvement for low friction pistons. SAE Transactions Journal of Engines. 2005, 114(3), 1182-1190. https://doi.org/10.4271/2005-01-1647

[18] Okamoto M, Iwashita T. Piston rings for automotive engine. Engine Technology. 2002;4(3):98-103 (in Japanese).

[19] Tabata H, Kaneko N, Mihara Y. Improvement in accuracy of piston frictional force measurement using floating liner engine. Tribology Online. 2017;12(3):141-146. https://doi.org/10.2474/trol.12.141

[20] Takiguchi M, Takimoto T, Asakawa E, Nakayama K, Someya T. A study of friction force reduction on piston skirt (Effect of width, roughness and resin coating). Transactions of the Japan Society of Mechanical Engineers B. 1997; 63(611):2587-2592. https://doi.org/10.1299/kikaib.63.611_2587 (in Japanese).

[21] Wakuri Y, Soejima M, Kitahara T, Nunotani M, Kabe Y. Characteristics of piston ring friction: Influences of lubricating oil properties. JSME International Journal Ser. C. 1995; 38(3):593-600. https://doi.org/10.1299/jsmec1993.38.593

[22] Yoshida H, Kusama K, Sagawa J. Effects of surface treatments on piston ring friction force and wear. SAE Technical Paper 900589. 1990. https://doi.org/10.4271/900589

Prof. Kohei Nakashima, DEng. – Faculty of Vehicle and Mechanical Engineering, Meijo University, Japan.
e-mail: *nakasima@meijo-u.ac.jp*

Yosuke Uchiyama, MEng. – Faculty of Vehicle and Mechanical Engineering, Meijo University, Japan.
e-mail: *193431002@ccalumni.meijo-u.ac.jp*

Kota Matsunaga, BEng. – Faculty of Vehicle and Mechanical Engineering, Meijo University, Japan.
e-mail: *190446070@ccalumni.meijo-u.ac.jp*

Prof. Masao Yoshida, DEng. – Automotive Junior College, Aichi University of Technology, Japan.
e-mail: *yoshida@aut.ac.jp*

Article citation info:
Szumska EM, Jurecki R. Technological developments in vehicles with electric drive. Combustion Engines. 2023;194(3):38-47. https://doi.org/10.19206/CE-168219

Emilia M. SZUMSKA
Rafał JURECKI

Combustion Engines
Polish Scientific Society of Combustion Engines

Technological developments in vehicles with electric drive

ARTICLE INFO

Received: 16 May 2023
Revised: 11 June 2023
Accepted: 12 June 2023
Available online: 15 June 2023

The fleet of electric vehicles is systematically growing. Many passenger car manufacturers are already reporting that after 2030, vehicles equipped with electric propulsion will account for half of the models produced. Vehicles equipped with an electric drive include: battery-powered electric vehicles, hybrid electric vehicles and fuel cell electric vehicles. Over the years, these vehicles have undergone constant change. The aim of this paper was to review trends in the development of pure electric vehicles and plug-in hybrid vehicles.

Key words: *electric drive; electric vehicle; plug-in hybrid vehicle, hybrid electric vehicle*

1. Introduction

The electric powered vehicles are gaining an increasing share of the passenger vehicle market. There are three types of electric vehicles: battery electric vehicles (EV), hybrid electric vehicles (HEV), and vehicles equipped with fuel cells electric vehicles (FCEV). Despite the many challenges facing electric drive technology, there is a great reason to be optimistic about its future. New technologies in the field of electric vehicle drive systems have great potential to stimulate the development of intelligent and sustainable transport [56, 59]. Despite the many challenges facing electric drive technology, there are good reasons to be optimistic about its future [12, 32, 44].

The automotive industry is currently facing a profound transformation toward electric mobility. Diverse electric vehicle models in different price ranges available from automakers are resulting in a noticeable increase in EV sales. In Europe, sales of electric passenger vehicles in 2021 increased by over 65% compared to 2020. In 2021, electric vehicles accounted for 17% of all passenger cars sold in Europe [28]. In the first half of 2022, electric passenger vehicles reached an 11.1% share of European's overall automotive market [26].

Car manufacturers put close attention to the customers' likings. Based on the observation of the increase in interest in electric cars and the increase in sales of electric models, car manufacturers are form their offer. Carmakers aiming to gain a greater share of the electric vehicle market offer a wide range of models with electric drives to appeal to a growing group of consumers. The offer of each passenger car manufacturer includes models with hybrid or electric drives. These trends are observed both in the sector of small and city passenger cars, as well as sports cars and SUVs. According to the report [62], over the last 2 years, all car manufacturers have increased sales of electric vehicles. The development of electric drive technology is also taking place in light commercial vehicles. Electric and hybrid heavy-duty vehicles have already been developed. They are currently the subject of extensive testing and research [37]. Research shows that consumers who are interested in buying an electric vehicle pay attention primarily to its range, charging time, and purchase price [15, 40, 65]. The continuous development of battery technology already allows you to cover an increasingly longer distance on a single charge [60]. In addition, with the use of fast chargers, battery charging times have also been significantly reduced [54, 61, 64]. However, the high cost of purchasing an electric vehicle is a barrier for many potential buyers. In many countries, subsidies and financial incentives are available for EV buyers to attract potential customers. In addition, many cities offer facilities for electric car owners in the form of parking fee exemption, toll road exemption, and bus lane use [14, 34, 38].

Among the charging technologies for electric vehicles, wireless charging methods can be distinguished. It can be a flexible and promising alternative to standard plug-in battery chargers [7, 45]. Wireless charging is easier to use as it does not require a cable to be connected to the vehicle. This is a technology still in development. However, thanks to properly placed charging infrastructure, it will be possible to recharge the battery (e.g. in parking lots or while waiting at red lights), which will further extend the range [24, 33, 68].

Many automobile concerns have set themselves ambitious plans to increase the share of vehicle models with electric drives in the entire assortment of vehicles produced. The Volkswagen Group assumes that in 2030 every second vehicle produced will be equipped with an electric drive. It should also be emphasized that in 2021 Volkswagen was the second largest car manufacturer in the world [35, 48], and the share of battery electric vehicles in its total sales volume was 5.1%. The Stellantis Group, which brings together the following brands: Citroen, DS Automobiles, Jeep, Fiat, Opel, and Peugeot, announced a new strategy in March 2022, which assumes the sale of 5 million purely electric vehicles by 2030 [20, 57].

Asian automobile companies also have extensive vehicle electrification plans. Toyota is a pioneer in the production of hybrid vehicles. The Prius, unveiled in 1997, was the first widely available and mass-produced hybrid vehicle, which continues to be very popular. Toyota has not put a purely electric model into production until 2021. With its

recently announced strategy, Toyota aims to introduce 30 new EV models by 2030 [3, 19]. Nissan plans to introduce 23 new electric models, including 15 new electric models by 2030. The company aims to achieve more than 50% share of electric vehicles in total global vehicle sales for the Nissan and Infiniti brands by 2030 [47]. Honda plans to introduce 30 electric models to the global market by 2030, with a production volume of more than 2 million vehicles per year. The company has announced that by 2040 it will completely phase out the production of gasoline-powered cars. In addition, Honda intends to engage in research and development of new battery technologies [58].

Ford Group has ambitious plans to develop electric vehicle technology. The corporation intends to introduce three new electric passenger vehicles and four new electric commercial vehicles in Europe by 2024. Planned sales are more than 600,000 electric vehicles by 2026 in the European market only. In addition, Ford plans to open one of Europe's largest commercial vehicle battery plants in Turkey [25].

Plans to increase the share of electric cars are observed in the luxury and sports car sectors. For example, Mercedes-Benz assumes that in 2025, 50% of the planned revenues will come from the sale of EV and plug-in hybrid vehicles. In 2021, Mercedes-Benz sold 2.4 million vehicles, of which 4% were EV vehicles [42, 43]. The BMW Group predicts that at least half of the vehicles sold in 2030 will be BEV models [9]. In 2021, the share of electric vehicles in the total number of vehicles sold was 4% [21, 42]. The Volvo Group assumes that by 2025, electric cars will account for half of the models produced, and after 2030, all models produced will be equipped with electric drives [67]. In 2021, about 4% of vehicles sold by the concern were models equipped with an electric drive [65, 66]. In its strategy, Audi concern assumes that by 2025 its offer will include more than 20 fully electric models. The concern clearly focuses on electromobility and plans to invest around EUR 18 billion in electrification and hybridization in the years 2022-2026. From 2026, two fully electric models will be available. A key element of Audi's electrification strategy is a new factory in China, where a state-of-the-art production facility for all-electric Audi models will be built by the end of 2024 [5].

Electrification of means of road transport is an opportunity to reduce CO_2 emissions. The Green Deal for Europe (GDE) presented by the European Commission in 2019 assumes the achievement of zero net greenhouse gas emissions by 2050. The intermediate goal of the GDE is to reduce net greenhouse gas emissions by at least 55% by 2030 compared to 1990. The document also contains legal regulations responding to the challenges in the transport sector related to reducing energy consumption and increasing the use of the so-called clean energy, more efficient use of modern infrastructure, and reduced environmental impact [16]. In "Fit for 55" announced on 14 July 2021 the European Commission announced a package of legislative postulates. One of the calls is the introduction of CO_2 emission limits for passenger vehicles and light-duty vehicles. Starting in 2030, new vehicles are assumed to emit less CO_2 (compared to 2021) by an average of: 37.5% – for passenger cars and 31% – for light-duty vehicles. CO_2 emission limits have also been set for trucks and other heavy-duty vehicles. The new regulations oblige manufacturers to reduce their CO_2 emissions (compared to 2019) by an average of 15% by 2025, and then by 30% by 2030 [22]. The "Fit for 55" project assumes that from 2035 all new passenger vehicles and light-duty vehicles will be completely emission-free. Member States will be obliged to develop infrastructure for electric vehicle charging and increase the number of hydrogen refueling stations.

Technologies used in EVs can increase the flexibility of their use, which can be important in energy management optimization systems. The possibility of using electric vehicles in systems supplying energy to the electric network of the Vehicle-to-Grid (V2G) and Vehicle-to-Home (V2H) type means that electric vehicles can change their role from a means of transport into an energy storage system. V2G systems can reduce the pressure on the grid during peak EV charging and connect the vehicle to the grid to use electricity more rationally [4, 51, 70]. V2H and V2G systems mainly consist of battery management software, equipment supporting two-way transmission of electricity, and communication modules between the vehicle and the power grid. A properly designed V2G and V2H systems are aimed at optimizing charging costs for owners of electric vehicles while providing auxiliary services to the grid [4, 10].

Electric vehicle drives are undergoing continuous development. New technologies related to energy storage, charging methods, or energy transfer allow electric vehicles to become more accessible to average consumers. The aim of this paper is to present trends in the development of electric-powered vehicles. The paper provides a review of electric drive vehicles and the development of electric drive technology in vehicles over the years.

2. Electric-drive vehicles

Classification of electric vehicle propulsion systems can be done by electrification level. The main parameter for this classification is considered to be the amount of electricity that drives the vehicle. This is determined by the energy capacity of the battery, which determines the amount of energy expended and recuperated [69]. Vehicles equipped with electric drive include:

- battery electric vehicle (EV) – a vehicle with an electrochemical battery as the energy source and an electric motor as the drive unit
- hybrid electric vehicle (HEV) – a vehicle that combines an internal combustion engine and an electric motor – the internal combustion engine is the main energy source
- plug-in hybrid vehicle (PHEV) – a vehicle in which electric and combustion drives work together, but the electric drive is the main drive
- fuel cell electric vehicle (FCEV) – a vehicle in which a fuel cell and an electro-chemical battery cooperate, and the drive unit is an electric motor.

The specifications of vehicles with electric drive systems are summarized in Table 1.

Table 1. Technical features of vehicles with an electric drive train

Type of vehicle	Drive system	Power unit	Energy sources
BEV – Battery Electric Vehicle	Electric motor drives	Electric machine	Battery charged from the electrical grid
HEV – Hybrid Electric Vehicle	Internal combustion engine	HEV – Hybrid Electric Vehicle	Internal combustion engine
PHEV – Plug-in Hybrid Electric Vehicle	Electric motor drives	PHEV – Plug-in Hybrid Electric Vehicle	Electric motor drives
FCEV – Fuel Cell Electric Vehicle	Electric motor drives	Electric machine	Fuel cells

3. Development of electric drive technology in passenger vehicles

In order to determine the development trends in the field of electric drives used in vehicles, the parameters of selected drive components were analyzed. On the basis of the report [52], models of electric and plug-in hybrid passenger cars of various segments were selected. A few of the longest-running models on the market were chosen. In the case of electric vehicles (EV), the following technical parameters were analyzed: total power, top speed, battery nominal capacity, range, and curb weight. For plug-in hybrid vehicle analyses, the parameters selected were: internal combustion total power, electric machine total power, battery nominal capacity, electric range, and fuel consumption.

3.1. Technological developments in electric vehicle propulsion

Electric passenger vehicles from the four categories highlighted in the European Commission's Regulation [30] were investigated:

– B-segment small cars: Peugeot iOn, Renault ZOE
– C-segment medium cars: Nissan Leaf, Volkswagen e-Golf
– D-segment large cars: Tesla Model 3
– E-segment executive cars: Tesla Model S.

According to reports [1, 59, 71] the models under discussion are the longest-produced electric vehicles on the market and are still very popular with customers.

The first parameter under consideration is total power (Fig. 1). The drive unit in electric vehicles is exclusively an electric motor. Its task is to convert the electrical energy from the battery into mechanical energy used to drive the wheels of the vehicle. Total vehicle power is not constant and may depend on many factors such as ambient temperature, battery temperature and state of charge, battery type, battery state of age and battery age.

As can be observed on Fig. 1, the total power of electric vehicles has been increasing over the years. In the B-segment of small passenger cars, the available total power of the Peugeot iOn was increased by only 4% over the production period (2009-2022), while that of the Renault ZOE (over a much shorter period: 2012-2022) was increased by as much as 286%. For electric vehicles in the C-segment of medium-sized passenger cars, the available total power has also increased over the years. In the Nissan Leaf, the available total power has been increased by 158% compared to the first version of this model in 2010. The VW e-Golf in the years 2014-2022 recorded a slight increase in engine power of 18%. Tesla models from the D-large car segment and the E-executive car segment recorded a significant increase in total power, with 96% and 186% respectively.

Fig. 1. The total power output of the selected electric vehicle models from the start of their production until 2022

Due to the increase in total power in the electric car models analyzed, there was also an increase in top speed (Fig. 2). However, while the increase in top speed in vehicle segments B and C was small (up to around 8%), increases of 20% and 61% were noted in vehicle segments D and E.

Fig. 2. The top speed of the selected electric vehicle models analyzed from the start of their production until 2022

An important parameter affecting the functionality of an electric vehicle is the battery nominal capacity. Figure 3 shows the battery nominal capacity over the years of production of electric models.

Fig. 3. The battery nominal capacity of the selected electric vehicle models from the start of their production until 2022

The amount of energy stored depends on the energy capacity of the battery. Energy storage technology is still undergoing significant advances, such as in the area of materials used in cathodes and anodes. Current studies are aimed at obtaining the highest possible energy density and high energy density at the same time, while reducing the size and weight of the battery. As shown in Fig. 3, the nominal battery capacity increased in the analyzed models of electric vehicles. The nominal battery capacity has slightly increased in the Peugeot iOn, by 10%. Over the years of production, the nominal battery capacity of the Nissan Leaf (by 158%) and Renault ZOE (by 111%) has been significantly increased. For Tesla vehicles, the nominal battery capacity has been increased by 61% on the Model 3 and 18% on the Model S, respectively.

The popularity of electric vehicles is largely determined by their functional features. One of the important parameters taken into account by future users is the range. The range can be defined as the distance that an electric vehicle can travel from fully charging the battery to its discharge to the limit level. From the point of view of especially new EV users, range is a key issue in the operation of this type of vehicle. The concern about the limited range of electric vehicles causes a phenomenon called "range anxiety" [13, 49, 50]. A properly placed charging network can reduce range anxiety. The problem with EV use is the long battery charging time, which, depending on the battery capacity and charging method, can take up to several hours. Figure 4 shows the range of the analyzed EV models during their production period.

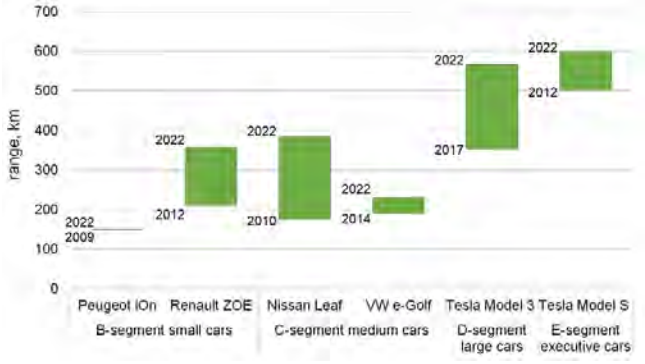

Fig. 4. The battery nominal capacity of the selected electric vehicle models from the start of their production until 2022

As shown in Fig. 4, the range of most of the analyzed vehicles has increased. This is mainly due to the development of energy storage technology. In the initial period of production, the analyzed vehicle models from the B and C segments showed a similar range. Compared to that period, the largest increase in range was recorded for Nissan Leaf (by 120%) and Renault ZOE (by 80%). It is worth mentioning that these vehicles saw the largest increase in nominal battery capacity during their production period. The range of the VW e-Golf has been extended by 20%. Based on the information provided by the manufacturers of the analyzed models from 2022, the range varied. Electric vehicles in the B segment had a range from 150 to about 400 km. In the case of C-segment electric vehicles, the range arrays from 230 km to approximately 400 km. In the case of Tesla's Model 3, the range has been extended by 60% compared to the first generation of this vehicle. In the Tesla Model S over the years of production (2012-2022), the range increased by 20%. In 2022, the range of Tesla vehicles from segments D and E was even 600 km.

The increase in battery capacity not only extends the range but also results in an increment in EV weight. The increase in battery capacity not only extends the range but also results in an increase in the curb weight of electric vehicles. In the analyzed models of vehicles from segments B and C, the increase in curb weight was small, up to 10% over the years of production. The relatively highest increase in curb weight was recorded for the Tesla Model 3 (20%). Figure 5 presents the curb weight of the analyzed vehicle models over the years of production.

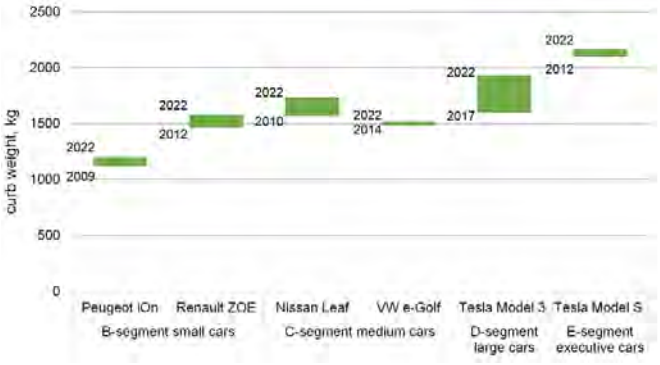

Fig. 5. Curb weight of the selected electric vehicle models from the start of their production until 2022

3.2. Technological developments in plug-in hybrid vehicles

In recent years, plug-in hybrid vehicle technology has undergone significant development. For this reason, selected models of passenger cars with the plug-in hybrid drive from the following segments were analyzed:

– B-segment small cars: Chevrolet Volt, Ford Fusion Energi
– D-segment large cars: Volvo V60 Plug-in Hybrid
– J- sport utility cars: Mitsubishi Outlander PHEV, Audi Q7 e-tron
– S- sport coupés: Porsche Panamera S E-Hybrid, BMW i8.

Selected hybrid vehicles are vehicles relatively the longest available on the market according to reports [2, 18, 63]. The chosen models represent different segments, so they have different parameters of the drive system components.

In plug-in hybrid vehicles, the combustion engine is intended to support the electric drive. Fig. 6 shows a comparison of the power of internal combustion engines in the analyzed PHEVs. As can be seen, the power of the internal combustion engine in-creased in each of the analyzed PHEV models during their production period. On most selected models, ICE power has been increased slightly. The largest increase in ICE power was recorded in J-segment vehicles (Audi Q7 e-tron) and S-segment vehicles (Porsche Panamera S E-Hybrid), by 32%.

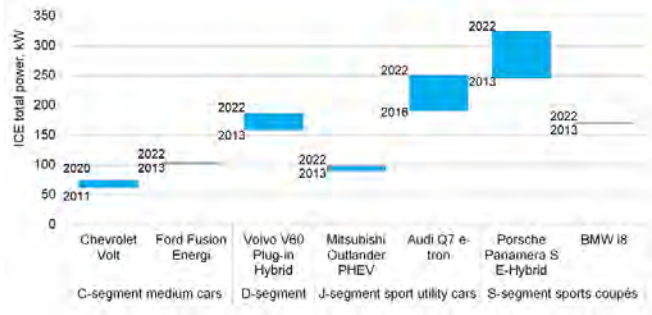

Fig. 6. Internal combustion engine power of the selected PHEV models from the start of their production until 2022

The basic propulsion system of plug-in hybrid vehicles is the electric drive. The electric drive system carries out the movement of the vehicle while the internal combustion engine is turned off. Figure 7 shows the power of the electric motor in PHEV models during their production period.

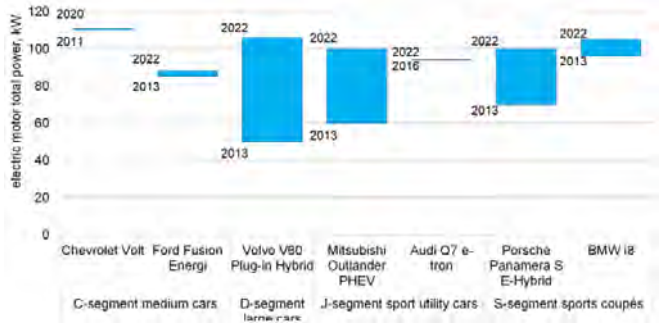

Fig. 7. Electric motor total power of the selected PHEV models from the start of their production until 2022

Over the years of production, the total power of the electric motor has increased in most of the analyzed PHEV models. Among the selected vehicles, the largest in-crease in electric motor power was shown by the S-segment model, the Volvo V60 (up 112%). The total power of the electric motor in the Mitsubishi Outlander and Porsche Panamera S E-Hybrid has also been significantly increased, by 67% and 43% respectively.

Studying the growth of available power from both combustion and electric drives, it can be seen that the total power increased and ranged between 185 and 424 kW. However, the percentage increase in power was not identical for all models. From an almost imperceptible increase in total power for the Ford Fusion to more than 40% for the Volvo v60 and Mitsubishi Outlander.

Figure 8 presents the nominal capacity of the batteries used in selected PHEV models over the years of production. In the two analyzed vehicles, the battery capacity remained unchanged. In other vehicles, the nominal capacity of the batteries was increased.

The nominal battery capacity of the Chevrolet Volt has been slightly increased by 15%. Over the years of production, the battery capacity of the Porsche Panamera S E-Hybrid has significantly increased by 90%. For the Volvo V60, Mitsubishi Outlander and BMW i8, the nominal battery capacity has increased by nearly 70%. The nominal battery capacity of the hybrid drive system determines the electric range. Figure 9 presents the electric range of the analyzed models of plug-in hybrid vehicles over the years of production.

Fig. 8. Battery nominal capacity of the selected PHEV models from the start of their production until 2022

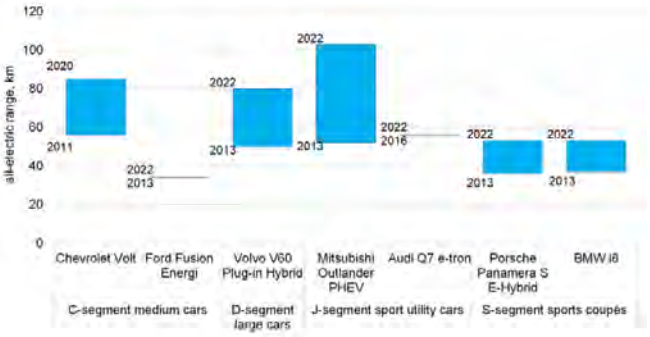

Fig. 9. The electric range of the selected PHEV models from the start of their production until 2022

In the first versions of the analyzed PHEV models, the electric range includes 34 km to 56 km. Extending the range resulted in a growth in the energy capacity of the battery. According to the manufacturers, in the 2022 PHEV versions, the electric range was from 35 km to 104 km. Over the years of production, the electric range of the Mitsubishi Outlander has approximately doubled. The electric range was significantly extended for the Volvo V60 (60%), the Chevrolet Volt (52%), the Porsche Panamera S E-Hybrid (47%), and the BMW i8 (43%).

One of the factors determining the popularity of hybrid vehicles is the possibility of using two power sources. It is possible to recover energy during braking, as well as driving only with an electric motor over relatively short distances, especially at low speeds, e.g. in traffic jams. An important argument for using this type of vehicle is lower fuel consumption compared to the classic internal combustion drive. In PHEV vehicles, after the battery is discharged to the limit point, the vehicle uses the internal combustion engine. In each of the considered PHEV models, fuel consumption has been reduced over the years of production (Fig. 10).

In the initial production period, fuel consumption for C-segment vehicles given by manufacturers was about 6.3 dm^3/100 km. In the 2022 versions of PHEV models, the reported average fuel consumption was about 13% lower. In the analyzed models from the D and J segments, over the years of production, the fuel consumption indicated in

terms of fuel consumption ranges from 1.1 dm^3/100 km to 2.0 dm^3/100 km. Over the years of production of PHEV models in the S-segment, average consumption ranged from 2.0 dm^3/100 km to 2.1 dm^3/100km. Among the analyzed PHEV models, the largest reduction in fuel consumption over the years of production was recorded by the Volvo V60 (around 40% less). It is worth mentioning that among the selected PHEV models, it was the Volvo V60 that increased the battery capacity and electric motor power the most, resulting in a longer range in electric mode.

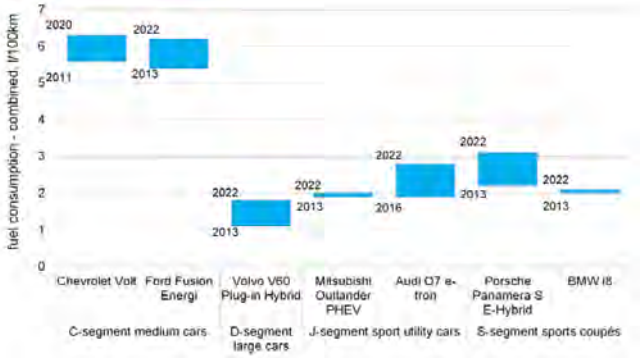

Fig. 10. Fuel consumption of the selected PHEV models from the start of their production until 2022

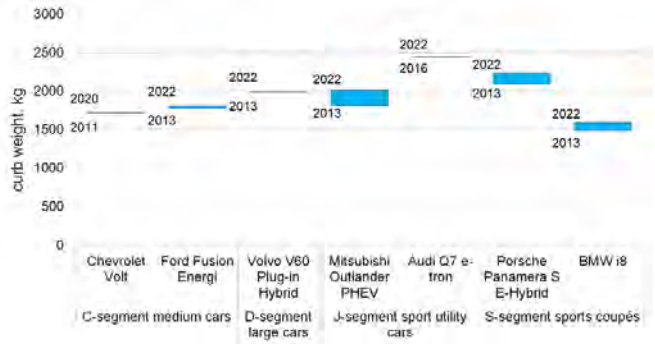

Fig. 11. Curb weight of the selected PHEV models from the start of their production until 2022

Plug-in hybrids are characterized by a much higher weight compared to conventional vehicles, as they are equipped with both a classic internal combustion engine and an electric drive. In addition, the large weight of the vehicle is affected by the weight of the battery. In PHEV, the battery has a much higher energy capacity than in other types of the hybrid drive. Figure 11 shows the curb weight of selected PHEV models over the years of production.

Of the vehicles analyzed, curb weight was slightly reduced in the Chevrolet Volt and Audi Q7 e-tron. For the other models, curb weight has slightly increased over the years of production. The Mitsubishi Outlander curb weight increased the most, by 11%.

4. Discussion

With the continued development of energy storage technology, the rapid expansion of the charging infrastructure, and the growing ecological awareness of society, vehicles equipped with electric drives (EV and PHEV) are expanding their market share [6, 11]. The energy capacity of the battery largely determines the range of an electric vehicle. Taking into account the values of the nominal energy capacity of the battery and the range provided by the manufacturers of the electric vehicle models analyzed earlier, the relationship between these parameters can be determined.

As the energy capacity of the battery increases, the range becomes longer (Fig. 12). Analyzing the parameters, based on the R^2 determination index, it can be seen that there is a correlation between these factors, especially for EVs it is very strong. A similar relationship occurs for plug-in hybrid vehicles.

Analyzing selected electric vehicle models, it can be observed that as the energy capacity of the battery increases, total power also becomes higher (Fig. 13). This was needed to ensure adequate range. In electric vehicles, the electrochemical battery is the source of energy. The battery capacity has a direct impact on EV operation. The currently used lithium-ion batteries provide a range of up to several hundred kilometers on a single charge with a relatively moderate lifespan [27, 39, 72]. The energy capacity decreases over time [17, 23, 29]. The high costs associated with the production of lithium-ion batteries contribute to the increase in vehicle prices, thus becoming a financial barrier for many potential buyers [36, 41, 53]. It is necessary to develop new technologies that enable the storage of large amounts of energy with the lowest possible weight.

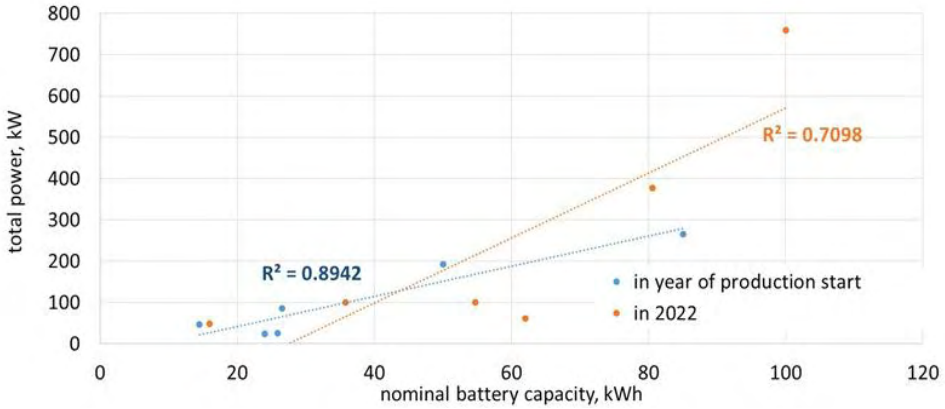

Fig. 12. Distribution of nominal battery capacity and range of EVs and PHEVs

Unfortunately, the increase in the electric capacity of the battery results in an in-crease in the weight of the vehicle (Fig. 14). There is a high correlation between these parameters. The coefficient of determination R^2 ranges from 0.85 to 0.97. Work is still being carried out to increase the battery capacity (energy density) without the need to enlarge them [8, 31, 46]. Research work on new battery technology could reverse this trend.

Taking into account the care for the natural environment, plug-in hybrid vehicles are an important alternative to electric vehicles. Compared to an electric vehicle, a PHEV has a combustion engine that is used when the battery is discharged. Plug-in hybrids provide a relatively long-range (electric and combustion). This means that the user does not have to worry about the range and plan routes taking into ac-count the available charging infrastructure. Driving in pure electric mode and regenerating energy during braking contributes to lower fuel consumption and emissions. In a plug-in hybrid, the electric drive is the main electric drive. The size of the battery should be selected so as to be able to provide the longest possible range in electric mode. Over the years, plug-in hybrid technology has undergone continuous development.

Taking into account the care for the natural environment, plug-in hybrid vehicles are an important alternative to electric vehicles. Compared to an electric vehicle, a PHEV has a combustion engine that is used when the battery is discharged. Plug-in hybrids provide a relatively long-range (electric and combustion). This means that the user does not have to worry about the range and plan routes taking into account the available charging infrastructure. Driving in pure electric mode and regenerating energy during braking contributes to lower fuel consumption and emissions. In a plug-in hybrid, the electric drive is the main electric drive. The size of the battery should be selected so as to be able to provide the longest possible range in electric mode. Over the years, plug-in hybrid technology has undergone continuous development.

As in the case of electric vehicles, PHEVs are significantly affected by the development of energy storage technology. Taking into account the parameters of the drive components provided by the manufacturers of the analyzed PHEV models, it can be seen that the increase in battery capacity translates into a longer electric range, which in turn reduces fuel consumption. The authors of the paper [55] studied the electric range value of a PHEV vehicle during regular driving on routes of various lengths. The results of the study showed that a route of about 20 km is covered between 15–35% in electric mode, a route measuring 40 km is carried out about 50% exclusively in electric mode, and a route of about 60 km is traveled about 75% using the electric drive. In most of the tested PHEV models, over the years of production, the electric range was extended, while fuel consumption was reduced. The increase in the energy capacity of the battery also contributes to the reduction of fuel consumption. In most of the tested PHEV models, the battery capacity has increased over the years of production, resulting in lower fuel consumption.

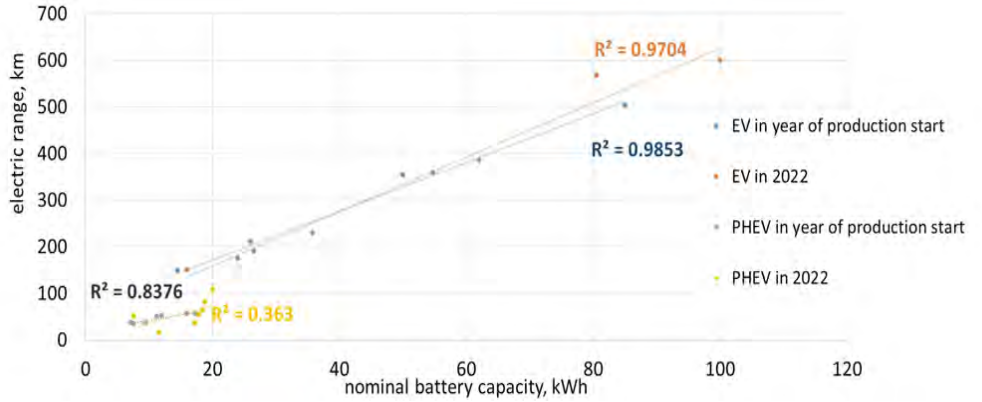

Fig. 13. Distribution of nominal battery capacity and total power of EVs

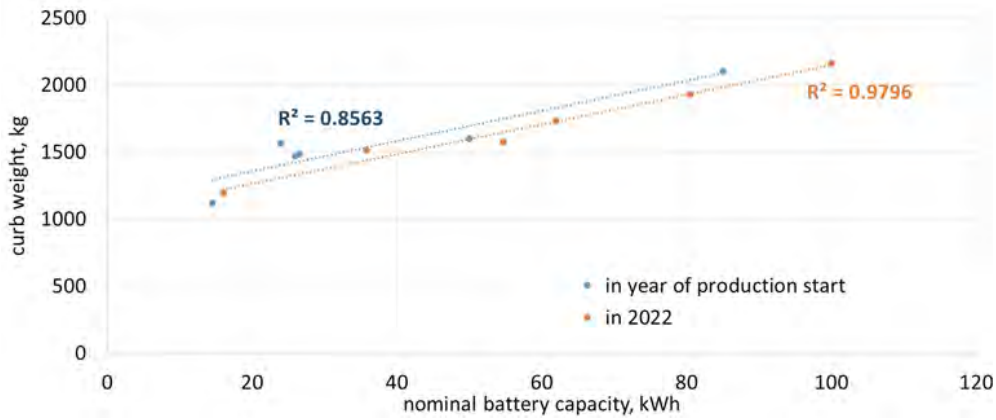

Fig. 14. Distribution of nominal battery capacity and curb weight of EVs

5. Conclusions

EU policy is aimed at reducing vehicles powered by internal combustion engines. Great emphasis is placed on the electrification of transport and the reduction of greenhouse gas emissions. Incentives and subsidies for the purchase of electric cars and the development of charging infrastructure may contribute to increasing the share of EVs in the automotive market.

Over the years, electric vehicles have undergone constant changes. The purpose of this work was to present trends in the development of electric vehicles. Based on the results of the analyses, it can be observed that over the years the energy capacity of the battery has increased with a slight increase in the weight of the vehicle. Thanks to the development of energy storage technology, a longer electric range could be achieved. An alternative to electric vehicles are plug-in hybrid vehicles. Compared to traditional hybrid electric vehicles, PHEVs are equipped with batteries with a higher energy capacity that can be charged from the power grid. In plug-in hybrid vehicles, the internal combustion engine is designed to support the electric drive after the battery is discharged. Over the past years, the energy capacity of the battery in plug-in hybrid vehicles has been increased, with a slight increase in the vehicle's curb weight. There was also an increase in the total power of the electric motor. This results in a longer electric range and lower fuel consumption.

Electric vehicles are currently one of the solutions to reduce greenhouse gas emissions in transport. During operation, EVs do not emit harmful substances into the air, unlike conventional combustion vehicles. There is still scope to further reducing greenhouse gas emissions over the entire life cycle of a vehicle, both in the operational phase by expanding the renewable energy infrastructure and in the production phase. Sustainability should not be limited to the use of hybrid or electric vehicles. It should take into account the modification of their construction by using new, more environmentally friendly, or recycled materials.

Nomenclature

EV	battery electric vehicles
FCEL	fuel cell vehicles
HEV	hybrid electric vehicles
ICE	internal combustion engine
ICEV	conventional vehicle
PHEV	plug-in hybrid electric vehicle
V2G	Vehicle-to-Grid
V2H	Vehicle-to-Home

Bibliography

[1] 100 best selling BEVs in 10 European countries. https://cleantechnica.com/2023/01/08/100-best-selling-bevs-in-10-european-countries/ (accessed on 18 January 2023).

[2] 2021 (Full Year) Europe: new car sales and market analysis. https://www.best-selling-cars.com/europe/2021-full-year-europe-new-car-sales-and-market-analysis/ (accessed on 20 January 2023).

[3] Akio Toyoda shares Toyota's strategy for achieving carbon neutrality through battery electric vehicles. https://pressroom.toyota.com/akio-toyoda-shares-toyotas-strategy-for-achieving-carbon-neutrality-through-battery-electric-vehicles/ (accessed on 12 January 2023).

[4] Amamra SA, Marco J. Vehicle-to-grid aggregator to support power grid and reduce electric vehicle charging cost. IEEE Access. 2019;7:178528-178538. https://doi.org/10.1109/ACCESS.2019.2958664

[5] Audi continues clear course towards e-mobility. https://www.audi.com/en/innovation/e-mobility/clear-course-towards-e-mobility.html (accessed on 12 January 2023).

[6] Austmann LM, Vigne SA. Does environmental awareness fuel the electric vehicle market? A Twitter keyword analysis. Energy Economics. 2021;101:105337. https://doi.org/10.1016/j.eneco.2021.105337

[7] Aydin E, Aydemir MT, Aksoz A, El Baghdadi M, Hegazy O. Inductive power transfer for electric vehicle charging applications: a comprehensive review. Energies. 2022;15:4962. https://doi.org/10.3390/en15144962

[8] Bastida-Molina P, Hurtado-Pérez E, Pérez-Navarro Á, Alfonso-Solar D. Light electric vehicle charging strategy for low impact on the grid. Environ Sci Pollut R. 2021;28:18790-18806. https://doi.org/10.1007/s11356-020-08901-2

[9] BMW Group report 2021. https://www.bmwgroup.com/en/report/2021/downloads/index.html?pdf-viewer=report (accessed on 12 January 2023).

[10] Borge-Diez D, Icaza D, Acikkapl E, Amaris H. Combined vehicle to building (V2B) and vehicle to home (V2H) strategy to increase electric vehicle market share. Energy. 2021;237: 121608. https://doi.org/10.1016/j.energy.2021.121608

[11] Canals Casals L, Etxandi-Santolaya M, Bibiloni-Mulet PA, Corchero C, Trilla L. Electric vehicle battery health expected at end of life in the upcoming years based on UK data. Batteries. 2022;8z:164. https://doi.org/10.3390/batteries8100164

[12] Casella V, Fernandez Valderrama D, Ferro G, Minciardi R, Paolucci M, Parodi L et al. Towards the integration of sustainable transportation and smart grids: a review on electric vehicles' management. Energies. 2022;15:4020. https://doi.org/10.3390/en15114020

[13] Chakraborty P, Parker R, Hoque T, Cruz J, Du L, Wang S et al. Addressing the range anxiety of battery electric vehicles with charging en route. Scientific Reports. 2022;12:5588. https://doi.org/10.1038/s41598-022-08942-2

[14] Chinoracky R, Stalmasekova N, Corejova T. Trends in the field of electromobility – from the perspective of market characteristics and value-added services: literature review. Energies. 2022;15:6144. https://doi.org/10.3390/en15176144

[15] Coffman M, Bernstein P, Wee S. Electric vehicles revisited: a review of factors that affect adoption. Transport Rev. 2017;37:79-93. 10.1080/01441647.2016.1217282

[16] Communication from the Commission to the European Parliament, the European Council, the Council, the European Economic And Social Committee and the Committee of the Regions the European Green Deal. https://eur-lex.europa.eu/legal-content/EN/TXT/?uri=CELEX%3A52019DC0640 (accessed on 12 January 2023).

[17] Costa N, Sanchez L, Ansean D, Dubarry M. Li-ion battery degradation modes diagnosis via Convolutional Neural Networks. J Energ Storage. 2022;55C:105558. https://doi.org/10.1016/j.est.2022.105558

[18] Dutta B, Hwang H-G. Consumers purchase intentions of green electric vehicles: the influence of consumers technological and environmental considerations. Sustainability. 2021;13:12025. https://doi.org/10.3390/su132112025
[19] Electric Vehicle market update. Manufacturer commitments & public policy initiatives supporting electric mobility in the U.S. & worldwide. https://blogs.edf.org/climate411/files/2022/04/electric_vehicle_market_report_v6_april2022.pdf (accessed on 12 January 2023).
[20] Electrification. Accelerating the drive to electrification. https://www.stellantis.com/en/technology/electrification?adobe_mc_ref= (accessed on 12 January 2023).
[21] Electromobility. https://www.bmwgroup.com/en/sustainability/our-focus/electromobility.html (accessed on 12 January 2023).
[22] European Parliament and Council of the European Union. Regulation (EC) No. 443/2009 of the European Parliament and of the Council of 23 April 2009 Setting Emission Performance Standards for New Passenger Cars As Part of the Community's Integrated Approach to Reduce CO_2 Emissions from Light-Duty Vehicles. 2009. https://eur-lex.europa.eu/legal-content/EN/TXT/PDF/?uri=CELEX:32009R0443&from=EN (accessed on 12 January 2023).
[23] Fanoro M, Božanić M, Sinha S. A review of the impact of battery degradation on energy management systems with a special emphasis on electric vehicles. Energies. 2022;15:5889. https://doi.org/10.3390/en15165889
[24] Feng H, Tavakoli R, Onar OC, Pantic Z. Advances in high-power wireless charging systems: overview and design considerations. IEEE Transactions on Transportation Electrification. 2020;6(3):886-919. https://doi.org/10.1109/TTE.2020.3012543
[25] Ford takes bold steps toward all-electric future in Europe; 7 new connected EVs support plans to sell 600K+ EVs annually by 2026. https://media.ford.com/content/fordmedia/fna/us/en/news/2022/03/14/Ford-Takes-Bold-Steps-Toward-All-Electric-Future-in-Europe.html (accessed on 12 January 2023).
[26] From boom to brake: is the e-mobility transition stalling?. Transport & Environment, 2022. https://www.transportenvironment.org/wp-content/uploads/2022/10/2022-10_Car-CO2-report-2022-recommandations-corrected.pdf (accessed on 12 January 2023).
[27] Gandoman FH, El-Shahat A, Alaas ZM, Ali ZM, Berecibar M et al. Understanding voltage behavior of lithium-ion batteries in electric vehicles applications. Batteries. 2022;8:130. https://doi.org/10.3390/batteries8100130
[28] Global EV Outlook 2022 securing supplies for an electric future. International Energy Agency, 2022. https://iea.blob.core.windows.net/assets/e0d2081d-487d-4818-8c59-69b638969f9e/GlobalElectricVehicleOutlook2022.pdf (accessed on 12 January 2023).
[29] Gómez Vilchez JJ, Smyth A, Kelleher L, Lu H, Rohr C, Harrison G et al. Electric car purchase price as a factor determining consumers' choice and their views on incentives in Europe. Sustainability. 2019;11:6357. https://doi.org/10.3390/su11226357
[30] Hall D, Wappelhorst S, Mock P, Lutsey N. European electric vehicle factbook 2019/2020. International Council on Clean Transportation (ICCT). https://theicct.org/sites/default/files/publications/EV-EU-Factbook-2020.pdf (accessed on 18 January 2023).
[31] Handbook on Battery Energy Storage System. Asian Development Bank. https://www.adb.org/publications/battery-energy-storage-system-handbook (accessed on 20 January 2023).
[32] Iqubal M, Sathiyan P, Stonier AA, Peter G, Shunmugham Vanaja D et al. An extensive critique on electric vehicle components and charging systems. Electric Vehicle Charging Technologies and Infrastructure. 2022;2022:3612032. https://doi.org/10.1155/2022/3612032
[33] Jang YJ, Jeong S, Lee MS. Initial energy logistics cost analysis for stationary, quasi-dynamic, and dynamic wireless charging public transportation systems. Energies. 2016;9:483. https://doi.org/10.3390/en9070483
[34] Jreige M, Abou-Zeid M, Kaysi I. Consumer preferences for hybrid and electric vehicles and deployment of the charging infrastructure: a case study of Lebanon. Case Studies on Transport Policy. 2021;9(2):466-476. https://doi.org/10.1016/j.cstp.2021.02.002
[35] Kaynar E, Rijk G. Quick charging the share prices. Faster EV adaptation can generate EUR 806 billion more equity value. Profundo, Amsterdam, Netherlands, 2022.
[36] Krishnan VV, Koszhy BI. Evaluating the factors influencing purchase intention of electric vehicles in households owning conventional vehicles. Case Studies on Transport Policy. 2021;9(3):1122-1129. https://doi.org/10.1016/j.cstp.2021.05.013
[37] Liimatainen H, van Vliet O, Aplyn D. The potential of electric trucks – An international commodity-level analysis. Appl Energ. 2019;236:804-814. https://doi.org/10.1016/j.apenergy.2018.12.017
[38] Macioszek E. The role of incentive programs in promoting the purchase of electric cars – review of good practices and promoting methods from the world. Lecture Notes in Networks and Systems. 2021;207:41-58. https://doi.org/10.1007/978-3-030-71708-7_4
[39] Małek A, Taccani R. Long-term test of an electric vehicle charged from a photovoltaic carport. The Archives of Automotive Engineering – Archiwum Motoryzacji. 2019;86(4):55-63. https://doi.org/10.14669/AM.VOL86.ART4
[40] Manutworakit P, Choocharukul K. Factors influencing battery electric vehicle adoption in Thailand – expanding the unified theory of acceptance and use of technology's variables. Sustainability. 2022;14:8482. https://doi.org/10.3390/su14148482
[41] Mau P, Eyzaguirre J, Jaccard M, Collins-Dodd C, Tiedemann K. The 'neighbor effect': simulating dynamics in consumer preferences for new vehicle technologies. Ecol Econ. 2008;68(1-2):504-516. https://doi.org/10.1016/j.ecolecon.2008.05.007
[42] Mercedes-Benz strategy update 2020. https://group.mercedes-benz.com/investors/events/capital-market-days/2020-mercedes-benz-strategy-update.html (accessed on 12 January 2023).
[43] Mercedes-Benz strategy update: electric drive. https://group.mercedes-benz.com/company/strategy/mercedes-benz-strategy-update-electric-drive.html (accessed on 12 January 2023).
[44] Mo T, Li Y, Lau K-T, Poon CK, Wu Y, Luo Y. Trends and emerging technologies for the development of electric vehicles. Energies. 2022;15:6271. https://doi.org/10.3390/en15176271
[45] Mohamed N, Aymen F, Alqarni M, Turky RA, Alamri B, Ali ZM et al. A new wireless charging system for electric vehicles using two receiver coils. Ain Shams Eng J. 2022;13:101569. https://doi.org/10.1016/j.asej.2021.08.012
[46] National Blueprint for lithium batteries. Federal Consortium for Advanced Batteries. https://www.energy.gov/sites/default/files/2021-06/FCAB%20National%20Blueprint%20Lithium%20Batteries%200621_0.pdf (accessed on 20 January 2023)

[47] Nissan unveils ambition 2030 vision to empower mobility and beyond. https://global.nissannews.com/en/releases/nissan-ambition-2030-vision-to-empower-mobility-beyond (accessed on 12 January 2023).
[48] On the Way to ZERO – The General Strategy. https://www.volkswagen-newsroom.com/en/on-the-way-to-zero-the-general-strategy-7226 (accessed on 12 January 2023).
[49] Pevec D, Babic J, Carvalho A, Ghiassi-Farrokhfal Y, Ketter W, Podobnik V. A survey-based assessment of how existing and potential electric vehicle owners perceive range anxiety. J Clean Prod. 2020;276:122779. https://doi.org/10.1016/j.jclepro.2020.122779
[50] Plug-In hybrids pull up Europe's plug-in market – October EV sales report. https://cleantechnica.com/2019/11/29/plug-in-hybrids-pull-up-europes-plug-in-market-october-ev-sales-report/ (accessed on 20 January 2023).
[51] Rahman MS, Hossain MJ, Lu J, Rafi FHM, Mishra S. A vehicle-to-microgrid framework with optimization-incorporated distributed EV coordination for a commercial neighborhood. IEEE Transactions on Industrial Informatics. 2020;16(3):1788-1798. https://doi.org/10.1109/TII.2019.2924707
[52] Regulation (EEC) No 4064/89 Merger Procedure. https://ec.europa.eu/competition/mergers/cases/decisions/m1406_en.pdf (accessed on 18 January 2023).
[53] Roadmap on advanced materials for batteries. European technology and innovation platform on batteries – Batteries Europe. https://energy.ec.europa.eu/system/files/2021-12/vol-3-008-2.pdf (accessed on 20 January 2023)
[54] Sadeghian O, Oshnoei A, Mohammadiivatloo B, Vahidinasab V, Anvari-Moghaddam A. A comprehensive review on electric vehicles smart charging: solutions, strategies, technologies, and challenges. Journal of Energy Storage. 2022;54:105241. https://doi.org/10.1016/j.est.2022.105241
[55] Šarkan B, Gnap J, Kiktová M. The importance of hybrid vehicles in urban traffic in terms of environmental impact. The Archives of Automotive Engineering – Archiwum Motoryzacji. 2019;85(3):115-122. https://doi.org/10.14669/AM.VOL85.ART8
[56] Skuza A, Jurecki R, Szumska E. Influence of traffic conditions on the energy consumption of an electric vehicle. Communications – Scientific Letters of the University of Zilina. 2023; 25(1):B22-B33. https://doi.org/10.26552/com.C.2023.004
[57] Stellantis long-term strategic plan. https://www.stellantis.com/content/dam/stellantis-corporate/investors/events/strategic-plan-2030/2022_03_01_Strategic_Plan.pdf (accessed on 12 January 2023).
[58] Summary of Honda briefing on automobile electrification business. https://hondanews.com/en-US/releases/summary-of-honda-briefing-on-automobile-electrification-business (accessed on 12 January 2023).
[59] Szumska E, Jurecki R, Pawełczyk M. Evaluation of the use of hybrid electric powertrain system in urban traffic conditions. Eksploat Niezawodn. 2020;22(1):154-160. https://doi.org/10.17531/ein.2020.1.18
[60] Szumska EM, Jurecki RS. Parameters influencing on electric vehicle range. Energies. 2021;14(16):4821. https://doi.org/10.3390/en14164821
[61] Szumska EM. Electric vehicle charging infrastructure along highways in the EU. Energies. 2023;16(2):895. https://doi.org/10.3390/en16020895
[62] The electric drive chargers forward. Annual Report. Implementing agreement for co-operation on hybrid and electric vehicle technologies and programmes (HEV TCP), 2022. https://ieahev.org/wp-content/uploads/2022/05/DIGITAL-HEVTCP_2022_Annual_Report_Final-with-Cover.pdf (accessed on 12 January 2023).
[63] Tsakalidis A, Thiel C. Electric vehicles in Europe from 2010 to 2017: is full-scale commercialisation beginning? An overview of the evolution of electric vehicles in Europe. EUR 29401 EN. Publications Office of the European Union, Luxembourg, Luxembourg, 2018; JRC112745. https://doi.org/10.2760/565748
[64] Ullah I, Liu K, Yamamoto T, Zahid M, Jamal A. Prediction of electric vehicle charging duration time using ensemble machine learning algorithm and Shapley additive explanations. International Energy Research. 2022;46:3. https://doi.org/10.1002/er.8219
[65] Verma M, Verma A, Khan M. Factors influencing the adoption of electric vehicles in Bengaluru. Transp Dev Econ. 2020;6:17. https://doi.org/10.1007/s40890-020-0100-x
[66] Volvo Car Group electrification strategy press conference. https://www.media.volvocars.com/global/en-gb/media/videos/210448/volvo-car-group-electrification-strategy-press-conference (accessed on 12 January 2023).
[67] Volvo Cars to be fully electric by 2030. https://www.media.volvocars.com/global/en-gb/media/pressreleases/277409/volvo-cars-to-be-fully-electric-by-2030 (accessed on 12 January 2023).
[68] Yang Y, El Baghdadi M, Lan Y, Benomar Y, Van Mierlo J, Hegazy O. Design methodology, modeling, and comparative study of wireless power transfer systems for electric vehicles. Energies. 2018;11:1716. https://doi.org/10.3390/en11071716
[69] Yong JY, Ramachandaramurthy VK, Tan KM, Mithulananthan N. A review on the state-of-the-art technologies of electric vehicle, its impacts and prospects. Renew Sustain Energy Rev. 2015;49:365-385. https://doi.org/10.1016/j.rser.2015.04.130
[70] Zagrajek K, Paska J, Sosnowski Ł, Gobosz K, Wróblewski K. Framework for the introduction of Vehicle-to-Grid Technology into the Polish electricity market. Energies. 2021;14:3673. https://doi.org/10.3390/en14123673
[71] Zhang Z, Tian R. Studying battery range and range anxiety for electric vehicles based on real travel demands. Proceedings of the Human Factors and Ergonomics Society Annual Meeting, Baltimore, MD, USA, 4-7 October 2021;65(1):332-336. https://doi.org/10.1177/1071181321651243
[72] Zhao G, Wang X, Negnevitsky M. Connecting battery technologies for electric vehicles from battery materials to management. iScience. 2021;25:103744. https://doi.org/10.1016/j.isci.2022.103744

Emilia M. Szumska, DSc., DEng. – Faculty of Mechatronics and Mechanical Engineering, Kielce University of Technology, Poland.
e-mail: *eszumska@tu.kielce.pl*

Prof. Rafał Jurecki, DSc., DEng. – Faculty of Mechatronics and Mechanical Engineering, Kielce University of Technology, Poland.
e-mail: *r.jurecki@tu.kielce.pl*

Article citation info:
Tomaszewski S, Grygier D, Dziubek M. Assessment of engine valve materials. Combustion Engines. 2023;194(3):48-51. https://doi.org/10.19206/CE-166569

Szymon TOMASZEWSKI
Dominika GRYGIER
Mateusz DZIUBEK

Combustion Engines
Polish Scientific Society of Combustion Engines

Assessment of engine valve materials

ARTICLE INFO

Received: 22 January 2023
Revised: 26 May 2023
Accepted: 28 May 2023
Available online: 27 June 2023

This paper presents an analysis of six sets of engine valves, each set consisting of one exhaust valve and one intake valve. Each pair of valves was used in an engine with different displacement and mileage. The valves were subjected to microscopic analysis, hardness measurement and chemical composition analysis using a glow discharge spectrometer and energy dispersive spectroscopy (EDS). The design and materials of the valves showed that both the intake and exhaust valves in their present form would be a strength of the engine.

Key words: *automotive, engine valves, valve steels*

1. Introduction

1.1. Types of engine valves

Intake and exhaust valves are very important engine components. The intake valve system allows clean air or the fuel-air mixture to enter the chamber and the exhaust valves force the exhaust gases out of the engine. Air enters the cylinder with the intake valves open. Combustion in the cylinder takes place when the intake valves are closed by means of a spring. Once combustion is complete, the camshaft opens the exhaust valves and the burnt gases flow out of the cylinder [2]. The spring keeps the valve connected to the camshaft as it moves. The valve system moves in the valve guide, which may be an integral part of the cylinder head or may be a separate unit pressed into the head [4].

The most commonly used type of valves are the globe valves shown in Fig. 1, they have the following variations [6, 10]:

1. Uniform valves, valves made entirely of a single grade of steel
2. Bimetallic valves, where the stem is made of a different grade of steel than the plug and the parts are friction-welded. Valves of this type are mainly intake valves
3. Hollow-tube valves, a type of valve made of a single grade of steel hollow in the middle and filled with nitrogen [11].

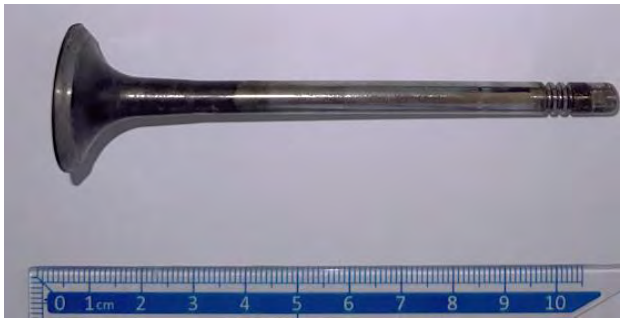

Fig. 1. Valve set No. 6

1.2. Steels for engine valves

Many factors can cause a valve to fail, such as thermal overload caused by operating temperatures of up to 775°C for exhaust valves and 450°C to 550°C [1, 8, 9] for intake valves, mechanical or longitudinal cyclic stresses, and exposure to chemically attacking metals [7, 8, 12], such as lead tetroxide, which can cause corrosion. Intake and exhaust valve materials differ due to the operating conditions under which they are subjected. Exhaust valves operate under much heavier conditions than inlet valves and are subjected to, among other things, high temperatures, complex chemical erosion of gasses and potential particles [5, 8]. In the production of uniform valves, the intake and exhaust valves are manufactured from different types of steel [8]. In the case of inlet valves, these are ferritic-martensitic steels, e.g. X45CrSi9-3 or X80CrNiSi20; in the case of outlet valves, austenitic steels, e.g. X53CrMnNiN21-9 or X50CrMnNiNbN21-9, are used. In the case of bimetal valves, the plug is made from X85CrMoV18-2 steel and the stem from a Cr-Si steel alloy such as X45CrSi9-3. In some situations, nickel alloys such as NiCr20TiAl designed for high-temperature service, thus providing high resistance to corrosion.

Table 1. Chemical composition of steel X45CrSi9-3

Object	Chemical composition [wt%]						
X45CrSi9-3	C	Mn	Si	P	S	Cr	Ni
	0.35–0.5	<0.7	2.0–3.0	<0.030	<0.030	8.0–10.0	<0.6

Table 2. Chemical composition of steel X53CrMnNiN21-9

Object	Chemical composition [wt%]						
X53CrMnNiN21-9	C	Mn	Si	P	S	Cr	Ni
	0.48–0.58	8–10	≤0.25	<0.045	<0.03	20–22	0.3–0.5

1.3. How engine valves are produced

The production of engine valves is a complex process starting with the selection of material, which is then cut to length in the form of steel rods supplied by the supplier and the ends are chamfered by grinding. The cut bars are then transferred to a hydraulic press, where they are

swelled and forged to form the valve disc [3]. In the case of bimetallic valves, the disc section is first joined to the stem section and then swelled and forged. The next step is to machine the valve face and disc according to the customer's order and, in addition, to machine the stem in order to achieve the right transition between disc and stem. Finally, the stem end is machined to produce the corresponding grooves, which are the connecting element between the valve and the rocker arm. Once the valves have been manufactured, they are tested to check for any defects using ultrasonic inspection and, finally, the valves are cleaned in an alkaline bath [6].

2. Research objective and method

2.1. Subject of the study

The subject of the tests conducted in this study was six sets of engine valves, each consisting of one intake valve and one intake valve, in order to evaluate engine valve materials. All that is known about each pair of valves is that they operated in an engine with a different displacement and drove a different mileage or, as in the case of pair number 3, experienced engine failure. Half of the valves worked in a diesel engine and the rest in a gasoline engine. The valves were labeled as follows:

Table 3. Overview of valve sets

Set 1	Petrol 2.0 mileage 200,000 km
Set 2	Diesel 1.9 TDI, mileage 250,000 km
Set 3	Diesel 1.9 broken timing belt
Set 4	Petrol 1.4, mileage 110,000 km
Set 5	Petrol 1.8 mileage 230,000 km
Set 6	Diesel 2.0 TDI mileage 200,000 km

2.2. Methodology of research

All tests were conducted on samples cut from valve cross sections. Microscopic examinations were performed using a Nikon Eclipse MA 200 metallographic microscope coupled to a Nikon CCD MA digital camera. The studies were carried out at magnifications ranging from 100× to 500× in the undigested state and after etching. The samples were etched electrolytically after which the images were taken again. Hardness measurements were made using the Vickers method with a Zwick Roell Z2.5 hardness tester under a load of 2 kgf (19.61 N) at 15 s. Four measurements plus a control measurement were made for each sample. The chemical composition was analyzed in two ways. One method was analysis with a LECO GDS-500 A fluorescence spectroscope using fluorescence excited optical emission spectroscopy. The second method used to study the chemical composition was energy dispersive spectroscopy (EDS) performed with a JEOL JSM-6610A scanning microscope.

3. Results

3.1. Microscopic results

On microscopic examination in the unpreserved state, oxide inclusions in the form of bands of fine spherical black particles and larger, irregularly shaped silicate inclusions, which are ellipses of various sizes, can be observed in the inlet valves (Fig. 2a). In the case of outlet valves, groups of oxide inclusions and bright, irregular inclusions of titanium nitride compounds are similarly observed (Fig. 2b).

Each tests show for the inlet valves a tempering troostite structure with carbide precipitations, indicating that the steel has gone through a high tempering process (Fig. 3b). In the case of the exhaust valves, an alloyed austenite structure with carbide precipitations can be observed (Fig. 3a). The etching tests showed different grain sizes for the bottom valves and varying amounts of carbides, which influenced the values of the hardness measurements.

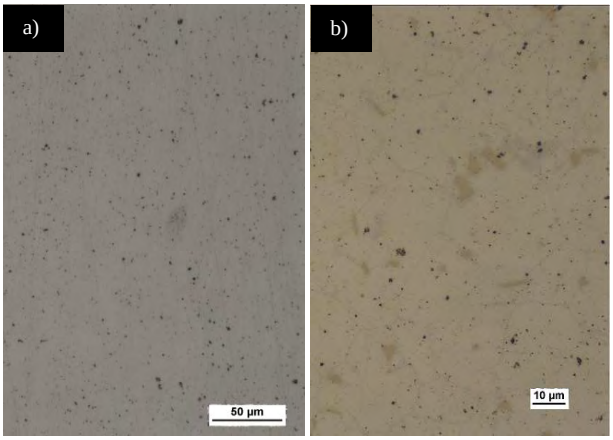

Fig. 2. (a) non-etched structure of the inlet valve from set 1 at (b) non-etched structure of the outlet valve from set 6

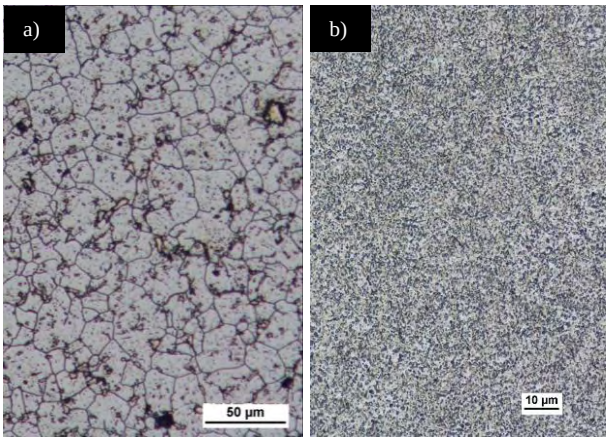

Fig. 3. a) alloyed austenite structure of the outlet valve from set 1 at b) troostite structure of the inlet valve from set 5

3.2. Chemical composition analysis

Investigations of the chemical composition with the fluorescence spectrometer were carried out in full for the sets 2,3,6; in addition, tests were made for the outlet valve of set 4 and for the inlet valve of set 5. The measurements showed that the outlet valves were made from a single steel grade, differing only minimally in the percent content of the elements. The steel from which the valves were made was 21-4NNbW, which is a medium-carbon heat-resistant alloy steel. In the case of the inlet valves, the valves were made from a single grade of steel, namely X45CrSi9-3, which is a medium-carbon heat-resistant chromium-silicon alloy steel and, as in the

Table 4. Chemical compositions of outlet valves

Object	Chemical composition [wt%]								
	C	Mn	Si	P	S	Cr	Ni	Nb	Ti
Set 2	0.535	9.33	0.264	0.007	0.003	21.29	3.62	1.82	0.028
Set 3	0.525	9.25	0.122	0.00	0.001	21.45	3.65	1.94	0.026
Set 4	0.572	9.12	0.332	0.01	0.005	21.21	3.66	1.77	0.03
Set 6	0.498	9.36	0.291	0.006	0.002	21.07	3.60	1.68	0.023

Table 5. Chemical compositions of inlet valves

Object	Chemical composition [wt%]								
	C	Mn	Si	P	S	Cr	Ni	Mo	Ti
Set 2	0.470	0.299	3.19	0.017	0.006	9.576	0.313	0.063	0.013
Set 3	0.455	0.268	3.34	0.009	0.006	9.754	0.172	0.033	0.012
Set 5	0.496	0.433	3.27	0.009	0.009	9.676	0.153	0.035	0.019
Set 6	0.471	0.314	3.53	0.005	0.008	8.955	0.087	0.032	0.026

case of the outlet valves, the same chemical composition contains the same elements with only minimal differences in elemental content. When tested by EDS, the valves tested were found to have similar significant element contents. In the case of the exhaust valves, the main elements with the highest content are Chromium at around 20%, Chromium at around 9% and Nickel at around 3%. As for the intake valves, similar values were found for the exhaust valves, with Chromium at around 9% and Silicon at around 3.5%. This allows us to conclude that the valves tested with EDS are made of the same steels as those tested with the glow spectrometer.

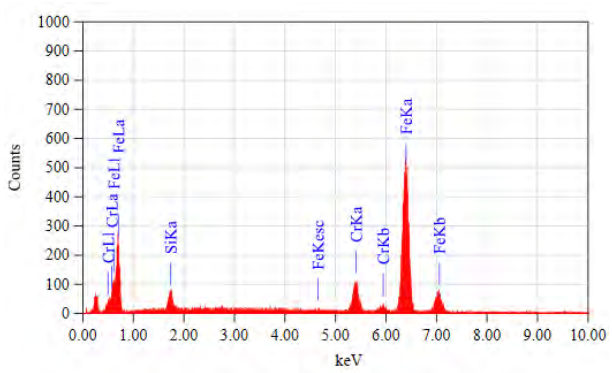

Fig. 4. EDS test spectrum for the inlet valve from kit no. 4

Table 6. Results of the chemical composition after EDS testing for the inlet valve from kit no. 4

Object	Chemical composition [wt%]		
Inlet valve no. 4	Fe	Cr	Si
	86.63	9.91	3.46

3.3. Results of hardness measurements

The results of the hardness measurements show a large discrepancy between the different valve samples, in the case of set No. 6 it can be seen that the inlet valve from this configuration obtained the highest average measurement result of 417.3 HV, while in the case of the outlet valves the second worst result was 321.6 HV and the best result was obtained by set No. 3, whose outlet valve obtained a value of 376.7 HV. The differences in hardness measurements are due to differences in microstructures and chemical compositions in the case of the inlet valve of set No. 6, it has the highest amount of silicon among the inlet valves, while the outlet valve of set No. 3 has the highest amount of chromium among the outlet valves.

Table 7. Averaged results of hardness measurements for sets 1-3

	Inlet valves	Outlet valves
Object	Average hardness [HV]	Average hardness [HV]
Set 1	353.2	323.3
Set 2	381.3	358.5
Set 3	394.0	376.7

Table 8. Averaged results of hardness measurements for sets 4-6

	Inlet valves	Outlet valves
Object	Average hardness [HV]	Average hardness [HV]
Set 4	378.9	303.4
Set 5	351.7	343.4
Set 6	417.3	321.6

4. Conclusions

On the basis of the tests carried out, it was found that in the case of the inlet valves, they were made from the X45CrSi9-3 steel grade, which is a medium-carbon alloy steel. These valves achieved quite varied hardness results, reaching higher hardness values compared to the valve steel in the exhaust valves. Testing in the undigested state showed the presence of oxides and silicates, which negatively affect the hardness and strength of the valves. In the pickled state, a tempering sorbite resulting from high tempering was identified. When analysing the chemical composition, we can note the presence of impurities in the form of sulphur and phosphorus, which negatively affect the hardness of the steel, but the high amount of chromium has a neutralising effect on the impurities. In addition, there are large amounts of silicon in the intake valve steels, plus the presence of elements such as titanium and manganese, which further affect the hardness and fineness of the steel. This allows us to conclude that the intake valve steel will perform well.

The steel grade of the exhaust valves is 21-4NNbW, which is a medium-carbon alloy steel. Similar to the inlet valves, the valves achieved quite different hardness measurements and these are due to the presence of an alloyed austenite structure. Tests in the undigested state showed a high presence of oxide inclusions and carbides affecting the hardness of the valves. In the case of the etched structure, the presence of a carbide structure in the alloy austenite matrix was identified. In the case of the chemical composition, we have the presence of impu-

rities in the form of sulphur and phosphorus, negatively affecting the hardness and strength of the steel. However, the presence of a large amount of chromium and manganese reduces the influence of the presence of impurities; in addition, the large presence of elements such as manganese, nickel and cobalt are strongly austenitic elements, which only confirms the presence of an alloy austenite structure. In addition, manganese, chromium and titanium increase the hardness of the steel. In summary, the steel from which the outlet valves are made will perform well.

The design and materials of the valves allow us to conclude that both intake and exhaust valves, in their current form, will be a strong part of the engine. On the other hand, the fact that different grades of steel are used for exhaust and intake valves is due to the difference in operating conditions.

Bibliography

[1] Adamaszek K, Suchecki A, Wisła M. Valve steel oxidation rate in the exhaust gases of diesel engines fueled with 5% biocomponent diesel oil. Combustion Engines. 2012; 149(2):22-29. https://doi.org/10.19206/CE-117037

[2] Feng Y, Tang H, Li C, Ma X. Failure analysis of internal combustion exhaust advances in engineering research. Proceedings of the 2015 International conference on Applied Science and Engineering Innovation 2015. https://doi.org/10.2991/asei-15.2015.47

[3] Hawryluk M, Krawczyk J, Zwierzchowski M, Janik M, Jaruzel J. Application of numerical modelling results to analyze and improve the industrial process of valve forging production. Obróbka Plastyczna Metali. 2019;30(4):291-306.

[4] Karamangil MI, Avci A, Bilal H. Investigation of the effect of different carbon film thickness on the exhaust valve. Heat Mass Transfer. 2007;44(5):587-598. https://doi.org/10.1007/s00231-007-0271-6

[5] Kumar GU, Mamilla VR. Failure analysis of internal combustion engine valves by using ANSYS. American International Journal of Research in Science, Technology, Engineering & Mathematics. 2014.

[6] Mallikarjuna V, Rajesh K, Basha SM. Process improvement in the manufacturing of engine valve. International Journal of Advanced Engineering Research and Science. 2016; 3(10):40-47. https://doi.org/10.22161/ijaers/3.10.9

[7] Pałuchowska M, Stępień Z. Evaluation of ethanol fuels in engine and field tests. Nafta-Gaz. 2017;73(2):97-104. https://doi.org/10.18668/ng.2017.02.04

[8] Pandey A, Mandloi RK. Effects of high temperature on the microstructure of automotive engine valves. Journal of Engineering Research and Applications. 2014;4(3):122-126. www.ijera.com/papers/Vol4_issue3/Version%201/X4301122126.pdf

[9] Pierce D, Haynes A, Hughes J, Graves R, Maziasz P, Muralidharan G, Shyam A et al. High temperature materials for heavy duty diesel engines: historical and future trends. Prog Mater Sci. 2019;103:109-179. https://doi.org/10.1016/j.pmatsci.2018.10.004

[10] Raghuwanshi N, Pandey A, Mandloi RK. Failure analysis of internal combustion engine valves: a review. International Journal of Innovative Research in Science, Engineering and Technology. 2012;1(2):173-181.

[11] Siczek K. The effect of the design and material parameters on the temperature gradient in lightweight valves in the valvetrains of combustion engines. Combustion Engines. 2013;153(2):94-100. https://doi.org/10.19206/ce-117006

[12] Suchecki A, Adamaszek K, Wisła M. Corrosion resistance of valve steel in diesel exhaust gas containing 5, 10 and 20% of FAME. Combustion Engines. 2013;152(1):51-55. https://doi.org/10.19206/ce-117012

Szymon Tomaszewski, BEng. – Faculty of Mechanical Engineering, Wroclaw University of Science and Technology, Poland.
e-mail: *246211@student.pwr.edu.pl*

Dominika Grygier, DSc., DEng. – Faculty of Mechanical Engineering, Wroclaw University of Science and Technology, Poland.
e-mail: *dominika.grygier@pwr.edu.pl*

Mateusz Dziubek, MEng. – Faculty of Mechanical Engineering, Wroclaw University of Science and Technology, Poland.
e-mail: *mateusz.dziubek@pwr.edu.pl*

Article citation info:
Andrych-Zalewska M. Investigation of processes in the WLTC test of a passenger car with a diesel engine. Combustion Engines. 2023; 194(3):52-62. https://doi.org/10.19206/CE-168328

Monika ANDRYCH-ZALEWSKA

Combustion Engines
Polish Scientific Society of Combustion Engines

Investigation of processes in the WLTC test of a passenger car with a diesel engine

ARTICLE INFO

Received: 5 June 2023
Revised: 14 June 2023
Accepted: 14 June 2023
Available online: 28 June 2023

The test results and their analysis was discussed in this article. The tests were carried out in accordance with the WLTP (Worldwide Light Duty Test Procedure), on a passenger car with a compression ignition engine. The analysis was conducted doe the following variables: vehicle speed, exhaust emission rate and fuel consumption volumetric rate. The subject of the research are exhaust emission components that are harmful to the health of living organisms: carbon monoxide, hydrocarbons and nitrogen oxides, as well as greenhouse gases. The research results have shown a very large range of values for carbon monoxide, organic compounds and nitrogen oxides emission rate characteristics. The average distance-specific emissions values of carbon monoxide, organic compounds and nitrogen oxides were very small and were in line with the Euro 6 requirements within a large margin. Correlation studies of the measured variables were conducted – between vehicle speed and exhaust emission rate as well as volumetric fuel consumption rates, and between exhaust emission rates and volumetric fuel consumption rates. The correlation studies have shown that the highest coefficient of determination in relation to vehicle speed was found for volumetric fuel consumption and carbon dioxide emission rate, and the weakest correlation for carbon monoxide emission rate and nitrogen oxides emission rate. The correlation between the rate of volumetric fuel consumption and carbon dioxide emission, as well as for hydrocarbon emission and methane emission rates, was found to be the strongest. The carbon monoxide emission rate was the least correlated with all the other measured variables. Dimensionless statistical characteristics of the measured variables were determined, such as: extreme values, range, mean value, median, standard deviation, kurtosis, skewness and coefficient of variation. For all of them, the mean value was much greater than the median, and the standard deviation was greater still, than both of those values. The numerical distributions for the values of exhaust emission rate and volumetric fuel consumption turned out to be leptokurtic and have right-sided asymmetry. The coefficient of variation analysis made it possible to assess that the most dynamic properties could be observed in organic compounds emission rate, followed by carbon monoxide and nitrogen oxides emission rates, and finally – the vehicle speed. Histograms of the examined processes were determined. The vehicle speed histogram was characterized by relative uniformity apart from the dominance of the idle speed. Histograms of exhaust emission rate variables were most frequently dominated by small values. The zero values occurred less frequently for the fuel consumption volumetric rate histogram. Based on the conducted research and the obtained data, a set of conclusions was drawn.

Key words: *diesel engine, exhaust emission, WLTC test*

1. Introduction

Type approval tests for LDV (Light Duty Vehicle) are carried out on a chassis dynamometers in the WLTC (Worldwide Light Duty Test Cycle) test in the European Union. This test is the replacement of the previous NEDC (New European Driving Cycle) test. This change took place along with the introduction of the Euro 6c standard – starting on September 1, 2017.

Results of the distance-specific emission obtained in the new test may be about (10–20)% greater than for the NEDC test. The entire WLTC test procedure is more dynamic, and the driving distance on which the measurements are recorded is almost twice as long. At the same time, the average speed in the new test is about 40% greater, and the share of complete stops has been halved.

Typically, emission and fuel consumption measurements obtained in driving tests mainly concern the averaged values of distance-specific exhaust emissions in tests or in individual phases. Exhaust emission rate data, expressed in relation to time, is less commonly included. These tests are made more difficult due to the fact that modern internal combustion engines tend to emit very low concentrations of exhaust components in many of their operating states, sometimes close to the lower boundary of measurement accuracy. Despite this, it is advisable to conduct research not only on the averaged values of exhaust emission characteristics, because the search for new possibilities of further reducing the exhaust emission limits from internal combustion engines always remains relevant.

2. Literature review and research goals

Paper [15] investigated typical dynamic vehicle traffic conditions in WLTC tests [6, 17] in order to simulate the PM emission from tribological elements in a car. Driving conditions have been found to have a major impact on particulate matter generation as a result of brake and tire wear processes. The testing approach proposed in the paper was to evaluate the impact of the share of acceleration and deceleration on particulate matter emissions.

Paper [1] analyzes the effectiveness of the FEV SimEx simulation software for simulating the operation of the drive system and the exhaust aftertreatment system in vehicles with compression ignition engines, in order to meet the requirements of the WLTP and RDE (Real Driving Emissions) procedures.

In [8], the engine operating states were analyzed in the rotational speed – torque coordinates in the operating conditions present in the WLTC test. The obtained results were used for a comparative assessment between various shares of LPG fuel in a dual-fuel diesel engine.

Paper [11] presents the results of the NEDC and WLTC tests of 14 passenger cars in order to analyze the carbon dioxide emissions. The tests were carried out in the years 2014–2016 at the request of the Dutch Ministry of Infrastructure and Environment and were aimed at examining the impact that the choice of test procedures had on exhaust emissions.

Another cited paper [16] used its research results to analyze the carbon dioxide emissions from the engines of a passenger car and a light truck in the WLTC test. Simulation tests were also carried out using CO_2MPAS (CO_2 Model for Passenger and Commercial Vehicle Simulation). Simulation tests of a turbocharged diesel engine in the WLTC test were analyzed in [5]. The results of the simulation tests were verified with the results obtained in empirical tests. The research results concerned energy and economic characteristics as well as exhaust emissions.

The authors of [14] undertook the task of evaluating the discrepancies in the results of exhaust emission and fuel consumption in type approval tests and other vehicle driving conditions. For this purpose, comparative tests were carried out in the WLTC test and in the CADC (Common Artemis Driving Cycle) test [17]. The paper presents the results of engine operating states expressed in the coordinates vehicle speed and acceleration.

The article [7] presents the method of verification of EURO III standard in real life conditions for special vehicles. The test object qualified as a special vehicle of N3G category was tested in road conditions along a defined route, and then the obtained measurement results were compared to the exhaust emission standard (EURO III) applicable for this vehicle in transient testing mode. A method of comparing the emission factors in road conditions with the indicators obtained on the engine dynamometer was proposed. An AVL mobile exhaust gas analyzers (PEMS) dedicated for the Real Driving Emissions (RDE) road tests were used in the research.

In paper [12] presents NO_x, CO, and solid particulate number PN emissions of 53 gasoline and diesel passenger cars type-approved in the EU after the entry into force of the WLTP and RDE (i.e., meeting the Euro 6d-TEMP and Euro 6d standards). Emissions data over WLTP and RDE tests on in-use vehicles was collected by the Joint Research Center (JRC) of the European Commission in the period 2018-2021. Emissions are characterized by powertrain, fuel type, and test procedure. All vehicles comply well with Euro 6 emission limits and no statistically significant differences are found in NO_x, CO, and PN emissions measured over the complete WLTP and RDE tests, both for gasoline and diesel vehicles.

Another paper [9] presents the test results of three cars equipped with spark-ignition engines with the same displacement. Both NEDC and WLTC tests were performed. The test results showed an ambiguous impact of the test type on fuel consumption. The average distance-specific exhaust emissions turned out to be higher in the WLTC test except for hydrocarbons, for which the results turned out inconclusive.

The goal of paper [3] was to analyze the correlation between carbon monoxide, hydrocarbons, nitrogen oxides and carbon dioxide emissions in different operating conditions of an internal combustion engine vehicle. The engine performance was tested on a chassis dynamometer in tests simulating real driving conditions for different vehicles, such as: traffic jams, non-congested urban traffic, extra-urban traffic and travel on highways and expressways. An analysis of the correlation dependence of the exhaust emission rate on the useful engine power and the correlation interdependence between the emission rate of individual exhaust components was carried out. Pearson's linear correlation, The Authors calculated and provided the Spearman's rank correlation, Kruskal's gamma correlation and Kendall's tau correlation coefficients. It was found that the exhaust emission rate in the test drive tests strongly depended on the dynamic states of engine operation.

Paper [4] presents the results of diesel particulate filters efficiency testing in order to reduce the number of emitted particles. The tests were carried out in real conditions, in an RDE test. using a passenger car. The results of this study confirmed the effectiveness of using particulate filters in accordance with the test procedure applicable in RDE tests. The results found in the literature concern in most cases only the dimensionless characteristics of the exhaust emission and fuel consumption variables, which are the functionals of these processes such as the average value. In the literature on the subject, basically no works could be found that would discuss the properties of the vehicle and engine operating states and the processes describing the exhaust emissions and fuel consumption, taking into account their dynamic properties.

Active grille shutter (AGS) design and implementation has been discussed in paper [2], a work that Tata Motors European Technical Centre (TMETC) has led for Tata Motors, and we have found that it improves the vehicle fuel economy in the real world. The program of work includes vehicle efficiency; fuel economy improvement, starting from optimizing current energy balance; vehicle level performance; investigation of parasitic losses; and introducing technologies, which can crawl back losses and increase the efficiency, thereby improving real-world fuel economy while reducing emissions.

Along with the stated research aim, with results as presented in this article, another aim was to learn about the properties of the vehicle speed characteristic, the exhaust emission rate, and the volumetric fuel consumption in the WLTC test. The main objectives of this research significantly exceed just determining the mean distance-specific exhaust emissions, that are commonly the main subjects of such studies in the literature, which characterize their originality.

The objectives of researching these variables were to relate to their statistical properties, correlations between variables, and their properties in the aspect of the obtained data.

3. Method

A passenger car with a four-cylinder diesel engine, a displacement of 1.5 dm^3 was the main test object used in this research. The vehicle's engine had a rated power of 96 kW and was eco-class for exhaust emissions meeting the norm Euro 6 AP. The car was equipped with a 6-gear manual gearbox. During the tests, fuel used in accordance with the applicable standards for diesel oil (PN-EN 590:2022-08).

The tests were carried out on a single roller chassis dynamometer. The emission tests concerned substances that were:

– harmful to the health of living organisms, such as: carbon monoxide, organic compounds and nitrogen oxides,
– promoting the formation of gasses driving the greenhouse effect, such as: carbon dioxide and methane.

The exhaust emission measurement system used: CFV-CVS exhaust gas sampling system, a set of analyzers equipped with dual-range analyzers, that enabled the measurement of concentrations of: carbon monoxide, hydrocarbons, non-methane hydrocarbons and methane, nitrogen oxides and carbon dioxide.

The measurements were made in a WLTC test. The following quantities were measured:

– vehicle speed – v,
– carbon monoxide exhaust emission rate – E_{CO},
– hydrocarbons exhaust emission rate – E_{HC},
– non-methane hydrocarbons exhaust emission rate E_{NMHC},
– methane exhaust emission rate – E_{CH4},
– nitrogen oxides exhaust emission rate – E_{NOx},
– carbon dioxide exhaust emission rate – E_{CO2},
– fuel consumption volumetric rate – q.

The analysis of the obtained data included:

– determining the average distance-specific exhaust emission – b and the average operational volumetric fuel consumption – Q,
– correlation studies between the exhaust emission rate and volumetric fuel consumption rate and the vehicle speed data,
– determining dimensionless statistical characteristics of the variables such as: vehicle speed, exhaust emission rate and volumetric fuel consumption rate,
– measuring the data values of: vehicle speed, exhaust emission rate and volumetric fuel consumption.

The total test exhaust emission – m is the integral of the emission rate of the substance measured in the time domain:

$$m = \int_0^T E(t)dt \tag{1}$$

where: T – test duration.

Volumetric fuel consumption in the test – V is:

$$V = \int_0^T q(t)dt \tag{2}$$

The road distance covered by the vehicle in the test was calculated using:

$$\mathbf{L = \int_0^T v(t)dt} \tag{3}$$

The average distance-specific exhaust emission in the test is the ratio of the exhaust emission to the distance traveled by the vehicle:

$$b = \frac{m}{L} \tag{4}$$

The average in-service volumetric fuel consumption in the test is the ratio of the volumetric fuel consumption and the distance traveled by the car:

$$Q = \frac{V}{L} \tag{5}$$

The determination coefficients between the exhaust emission rate and volumetric fuel consumption rate data, and the speed characteristic were obtained as a result of correlation studies between these variables.

The determined dimensionless characteristics of the measured parameters included: minimum value, maximum value, range, mean value, median, standard deviation, kurtosis, skewness and coefficient of variation.

Research on the measured variable values, such as: vehicle speed, exhaust emission rate and volumetric fuel consumption rate included determining the histograms of these variables.

4. Research results

The research results were obtained for: vehicle driving speed in the test, the exhaust emission rate and the volumetric fuel consumption rate. In order to reduce the share of high-frequency noise in the signals they were then subjected to a low-pass filtration with a fifth-order non-recursive filter [8]. Data analyzes were performed on already filtered signals.

Figure 1 shows the vehicle driving speed characteristic as measured in the test.

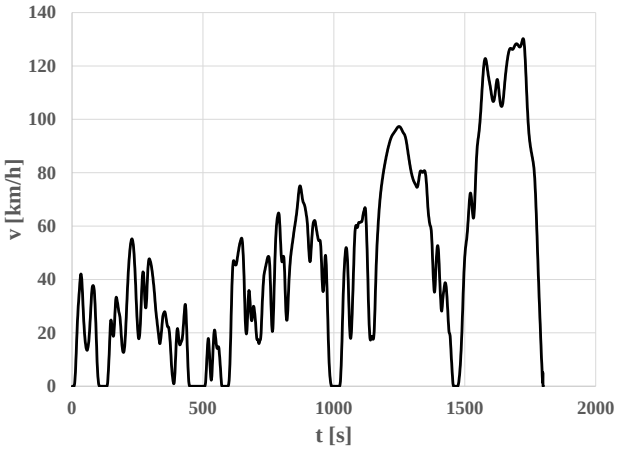

Fig. 1. Vehicle speed – v in the test

Figures 2–7 display the exhaust emission rates obtained in the test.

The very large range of values for carbon monoxide, organic compounds and nitrogen oxides emission rate was characteristic of this test.

Modern automotive diesel engines are characterized by very low distance-specific exhaust emission – to the point where sometimes the pollutants concentration in the exhaust gas diluted with air in the measuring system nears the concentration of pollutants in the air used for the dilution itself. Hence the emission rate of carbon monoxide, organic compounds and nitrogen oxides was close to zero in many parts of the test. This was not the case with carbon dioxide, the concentration of which was much greater than the concentration of other measured exhaust components.

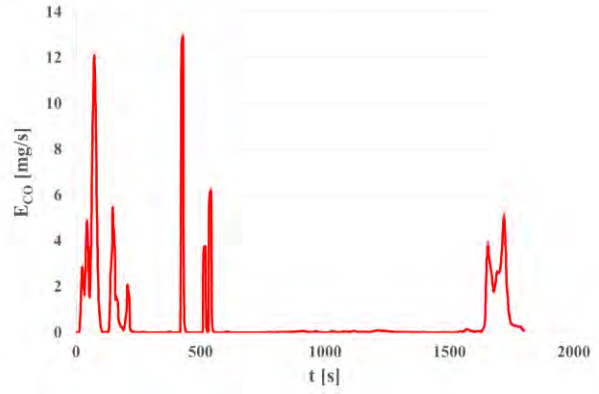

Fig. 2. Carbon monoxide exhaust emission intensity – E_{CO} in the test

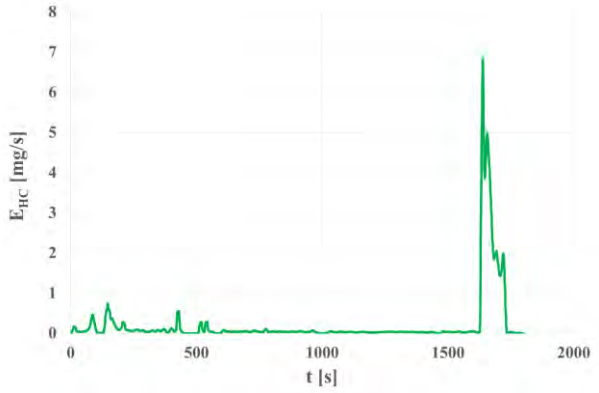

Fig. 3. Hydrocarbons exhaust emission intensity – E_{HC} in the test

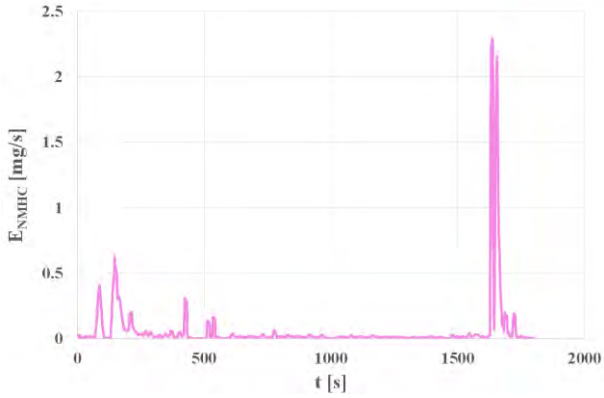

Fig. 4. Non-methane hydrocarbons exhaust emission intensity – E_{NMHC} in the test

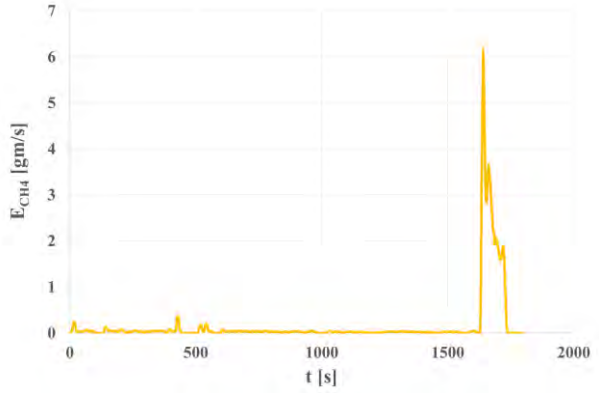

Fig. 5. Methane exhaust emission intensity – E_{CH4} in the test

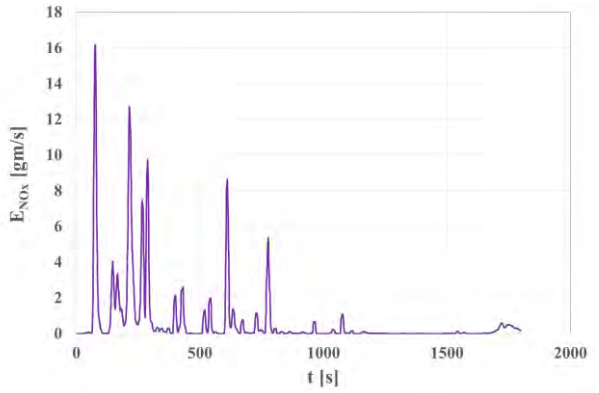

Fig. 6. Nitrogen oxides exhaust emission intensity – E_{NOx} in the test

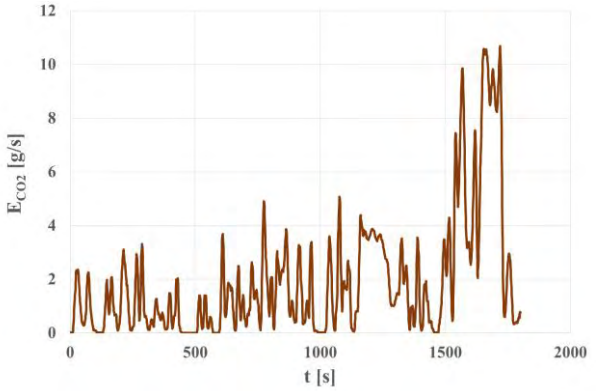

Fig. 7. Carbon dioxide exhaust emission intensity – E_{CO2} in the test

The volumetric fuel consumption by the car engine in the test was also measured (Fig. 8).

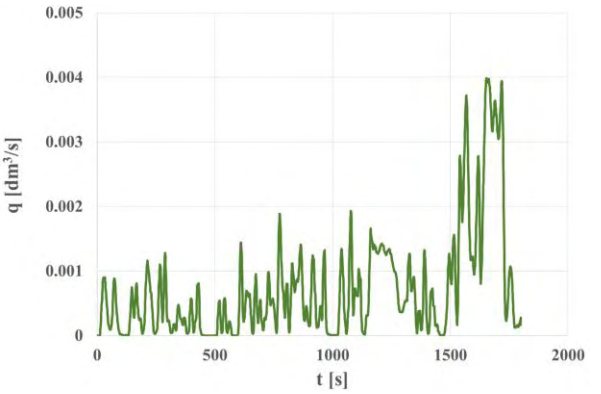

Fig. 8. Volumetric fuel consumption rate – q of the vehicle engine in the test

The volumetric fuel consumption rate was obviously strongly correlated with the fuel consumption rate.

5. Research analysis

Table 1 contains the mean distance-specific exhaust emission of the measured components as well as the average operating fuel consumption in the test.

The mean distance-specific emissions of carbon monoxide, organic compounds and nitrogen oxides measured had a very small value, which is characteristic trait of modern diesel engines. The same applies to operational fuel consumption.

Table 1. Mean distance-specific exhaust emissions and mean operational fuel consumption in the WLTC test

b_{CO}	mg/km	45.62
b_{HC}		17.13
b_{NMHC}		4.96
b_{CH4}		13.71
b_{NOx}		50.95
b_{CO2}	g/km	150.92
Q	dm^3/100 km	5.66

The distance-specific exhaust emission in the WLTC test allowed the vehicle to reach the Euro 6 norm limits with a large margin. The measured emissions could increase without exceeding the norm limits:

– for carbon monoxide emissions, the measured value would be permitted to increase by over 90%,
– for total hydrocarbons and nitrogen oxides, the measured value would be permitted to increase by 60%,
– for nitrogen oxides, the measured value would be permitted to increase by almost 40%.

Calculations were made to determine the correlation between the exhaust emission rate, the volumetric fuel consumption rate and the vehicle speed. Table 2 shows the coefficient of determination [5] between these variables.

The volumetric fuel consumption and carbon dioxide emission rate were most strongly correlated with the vehicle speed. While carbon monoxide and nitrogen oxide emission rates were the least correlated with vehicle speed. The correlation was stronger in the case of organic compounds – the coefficients of determination between vehicle speed and hydrocarbon emission rate, as well as between the vehicle speed and methane emission rate, were found to have a similar value.

Table 2. Coefficient of determination – R^2 between the exhaust emission rate, the volumetric fuel consumption rate and the vehicle speed

	R^2
E_{CO}	0.0028
E_{HC}	0.1708
E_{NMHC}	0.0499
E_{CH4}	0.1943
E_{NOx}	0.0077
E_{CO2}	0.5799
q	0.5834

Figures 9–12 include correlation diagrams between exhaust emission rates and volumetric fuel consumption rate and vehicle speed.

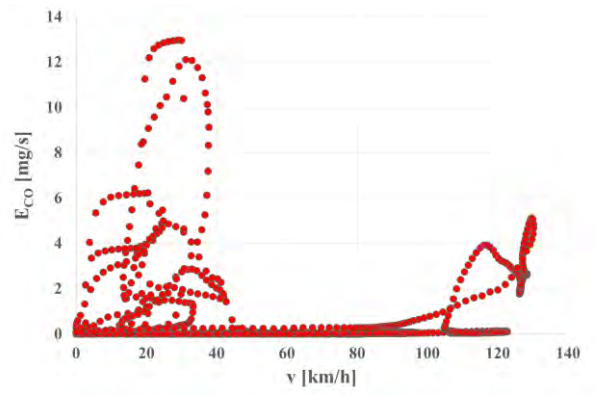

Fig. 9. Correlation between carbon monoxide emission rate – E_{CO} and vehicle speed – v

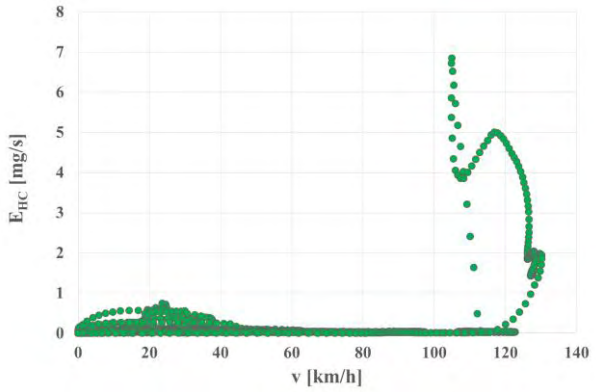

Fig. 10. Correlation between hydrocarbon emission rate – E_{HC} and vehicle speed – v

Correlation between the exhaust emission rates and the volumetric fuel consumption rate was also calculated. The coefficient of determination between these variables was calculated for each combination (Table 3).

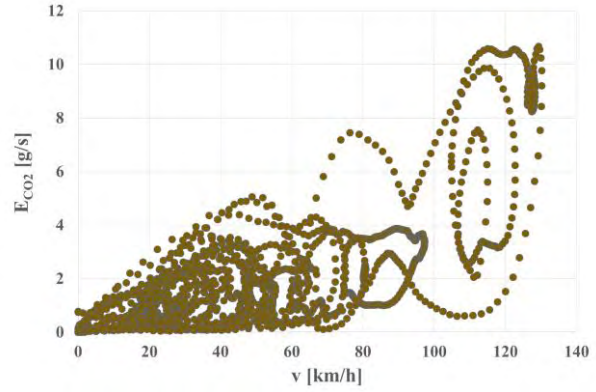

Fig. 11. Correlation between carbon dioxide emission rate – E_{CO2} and vehicle speed – v

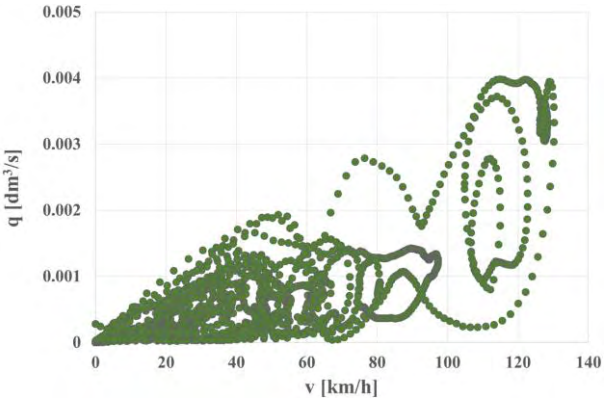

Fig. 12. Correlation between volumetric fuel consumption rate – q and vehicle speed – v

The volumetric fuel consumption and carbon dioxide emission rate were the most strongly correlated. There was obviously also a very strong correlation between the hydrocarbon emissions rate and the methane emissions rate. Strong correlation was also found between the emission rates of other measured hydrocarbon components. The correlation between the hydrocarbon emission rate, me-

thane emission rate, carbon dioxide emissions rate and the volumetric fuel consumption rate were all also relatively strong.

Table 3. Coefficients of determination – R^2 between the exhaust emission rates of all the measured exhaust components

	R^2						
	ECO	EHC	ENMHC	ECH_4	ENO_x	ECO_2	q
ECO							
EHC	0.0773						
ENMHC	0.0692	0.6621					
ECH_4	0.0626	0.9258	0.4012				
ENO_x	0.1590	0.0004	0.0054	0.0030			
ECO_2	0.0467	0.3638	0.1130	0.4040	0.0010		
q	0.0487	0.3691	0.1186	0.4082	0.0019	0.9966	

The lowest coefficient of determination was found for the correlation of carbon monoxide emission rate with all other variables except the nitrogen oxides emission rate. Also, the nitrogen oxides emission rate was very weakly correlated with other processes, apart from the emission rate of carbon monoxide.

Figures 13–17 are examples of correlation graphs between the exhaust emission rate and the volumetric fuel consumption rate.

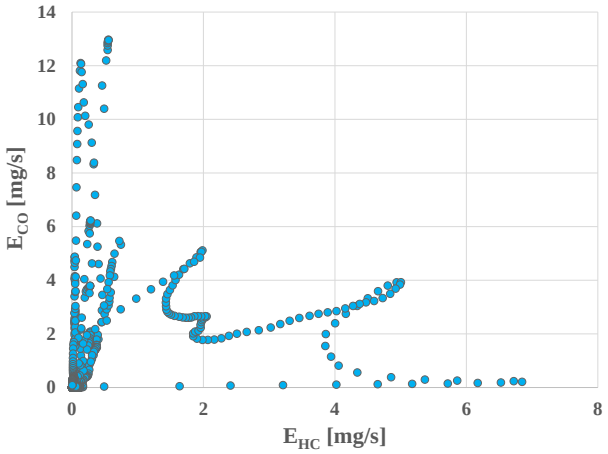

Fig. 13. Correlation between carbon monoxide exhaust emission rate – E_{CO} and hydrocarbon exhaust emission rate – E_{HC}

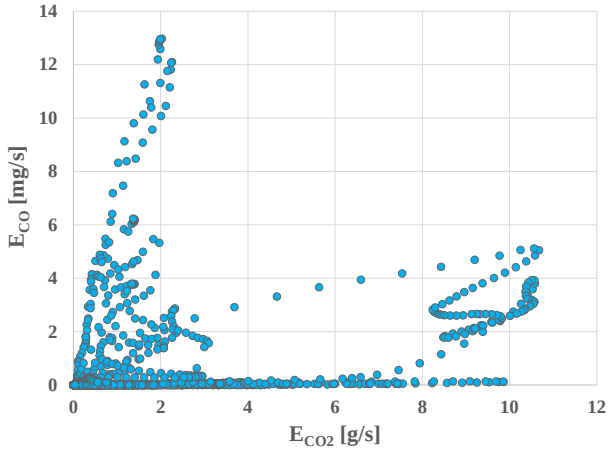

Fig. 14. Correlation between carbon monoxide exhaust emission rate – and carbon dioxide exhaust emission rate – E_{CO2}

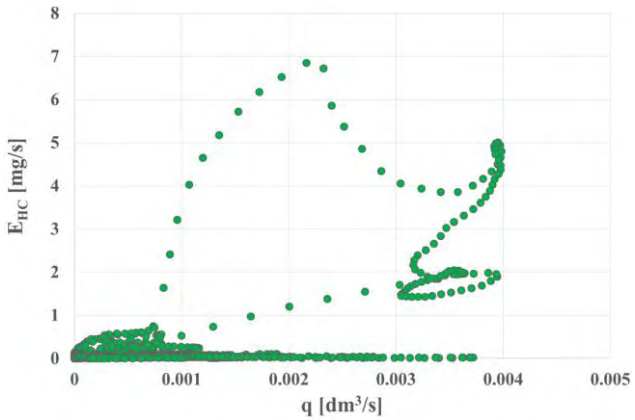

Fig. 15. Correlation between hydrocarbons exhaust emission rate – EHC and volumetric fuel consumption rate – q

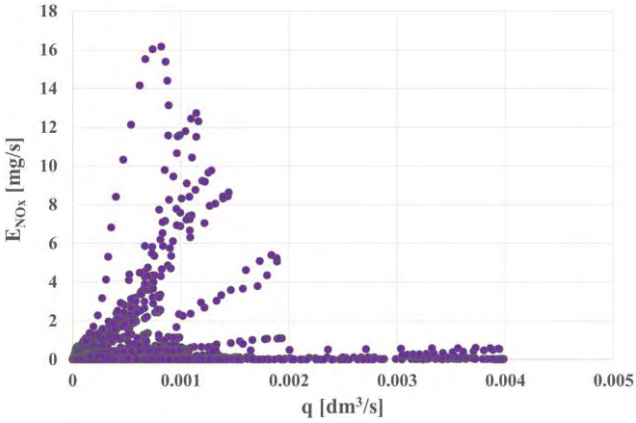

Fig. 16. Correlation between nitrogen oxides exhaust emission rate – ENO_x and volumetric fuel consumption rate – q

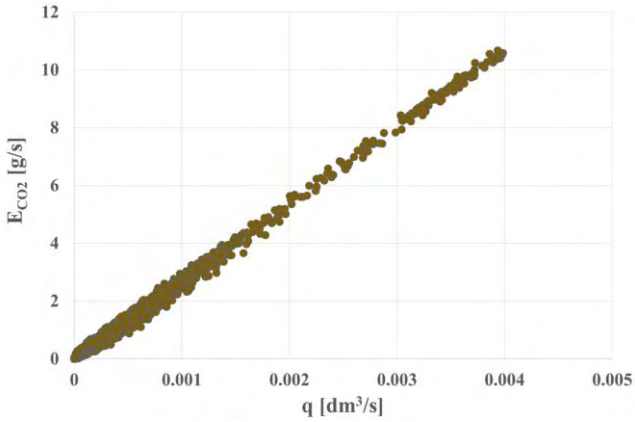

Fig. 17. Correlation between carbon dioxide exhaust emission rate – ECO2 and volumetric fuel consumption rate – q

Figure 18 shows the dimensionless statistical characteristics of the vehicle speed.

A characteristic of the vehicle speed data is that the median speed is close to the average speed in value.

Dimensionless characteristics of the statistical exhaust emission rates were also calculated (Fig. 19–24).

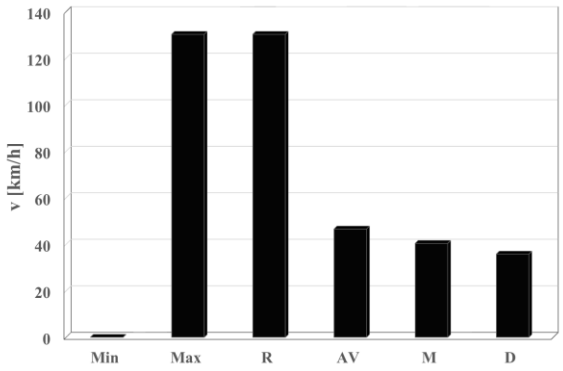

Fig. 18. Dimensionless statistical characteristics of the vehicle speed – v

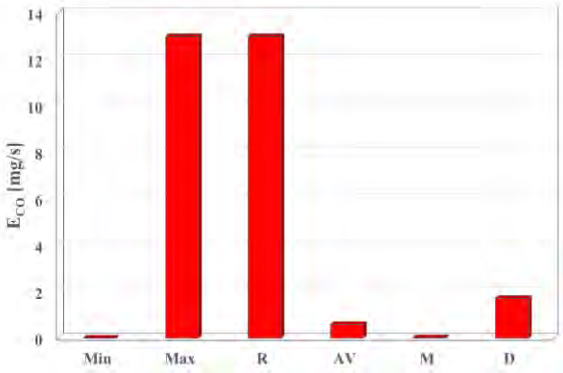

Fig. 19. Dimensionless statistical characteristics of carbon monoxide emission rate – E_{CO}

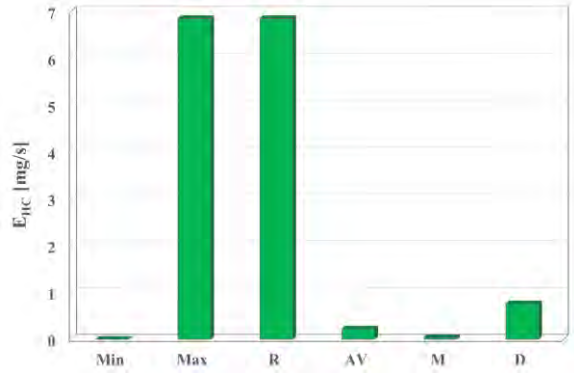

Fig. 20. Dimensionless statistical characteristics of hydrocarbons emission rate – E_{HC}

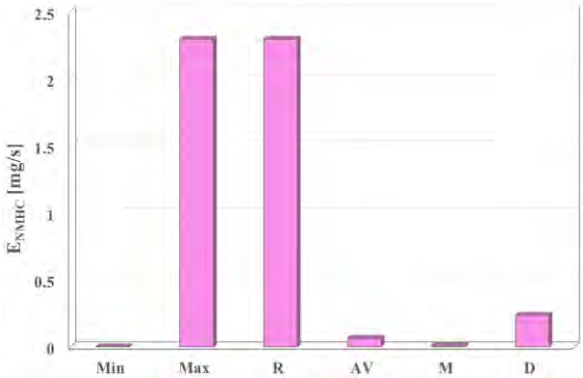

Fig. 21. Dimensionless statistical characteristics of non-methane hydrocarbons emission rate – E_{NMHC}

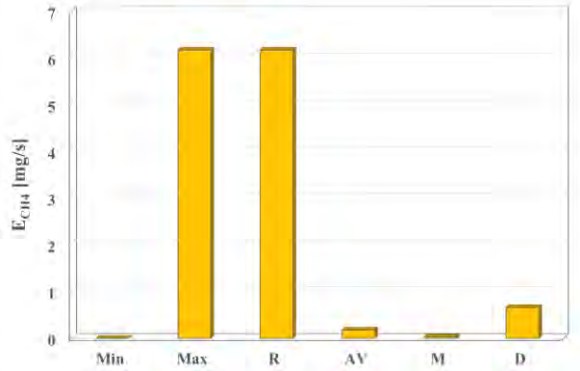

Fig. 22. Dimensionless statistical characteristics of methane emission rate – E_{CH4}

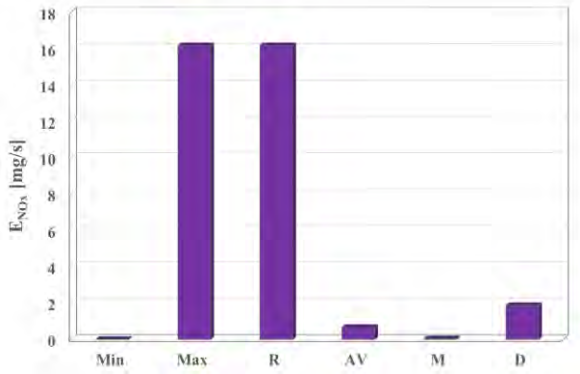

Fig. 23. Dimensionless statistical characteristics of nitrogen oxides emission rate – E_{NOx}

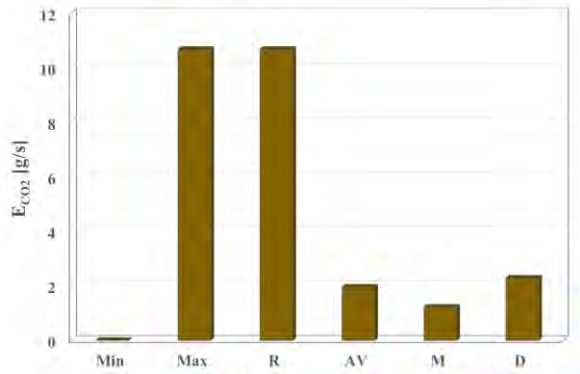

Fig. 24. Dimensionless statistical characteristics of carbon dioxide emission rate – E_{CO2}

For every substance's exhaust emission rate, the average value was much greater than the median, and the standard deviation of both of these values was much greater. The smallest differences occurred in the case of carbon dioxide emission rate.

Figure 25 presents dimensionless statistical characteristics of the volumetric fuel consumption rate.

The relationships between mean value, median and standard deviation for the volumetric fuel consumption rate were similar to those for the carbon dioxide emission rate.

Further on, kurtosis, skewness and coefficient of variation of the measured variables were determined (Fig. 26–28).

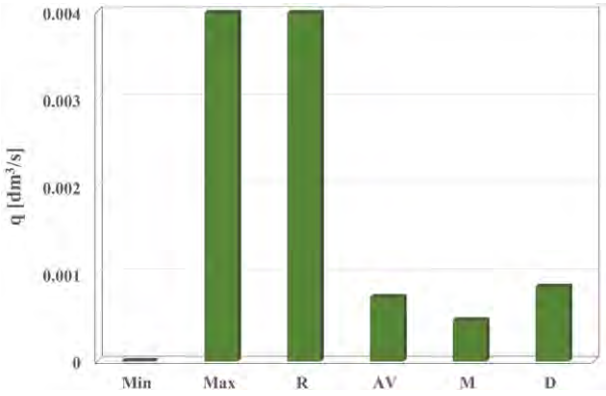

Fig. 25. Dimensionless statistical characteristics of the volumetric fuel consumption rate – q

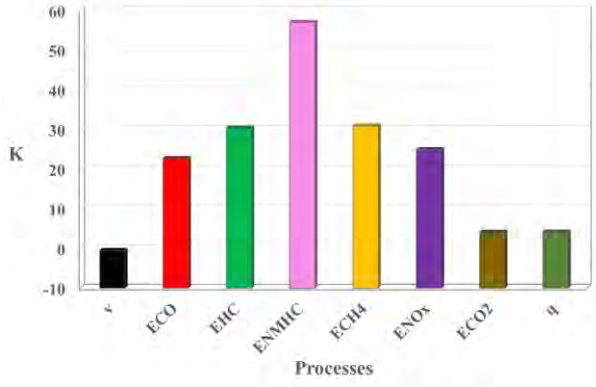

Fig. 26. Kurtosis – K of the measured variables

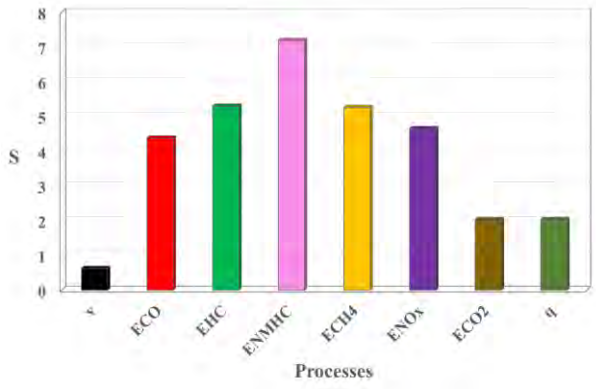

Fig. 27. Skewness – S of the measured variables

Kurtosis took on positive values for all the variables that have been measured in this research, except for the vehicle speed, so these are leptokurtic distributions. The kurtosis of the vehicle speed was slightly negative – it equalled –0.5, so the negative flattening of the distribution was not significant. Kurtosis of organic compounds emission rate was the highest in value, positive kurtosis of carbon dioxide emission rate and volumetric fuel consumption rate was the smallest.

The distribution skewness of all the variables presented was positive, so these distributions had a right-sided asymmetry. As in the case of kurtosis, the highest value of skewness was for the organic compounds emission rate, the smallest – for the vehicle driving speed, carbon dioxide emission rate and volumetric fuel consumption rate.

The coefficient of variation varies in their respective values significantly. The organic compounds emission rate had the strongest dynamic properties, followed by carbon monoxide and nitrogen oxides. The least dynamic properties were found for the vehicle speed, followed by the carbon dioxide emissions rate and the volumetric fuel consumption rate.

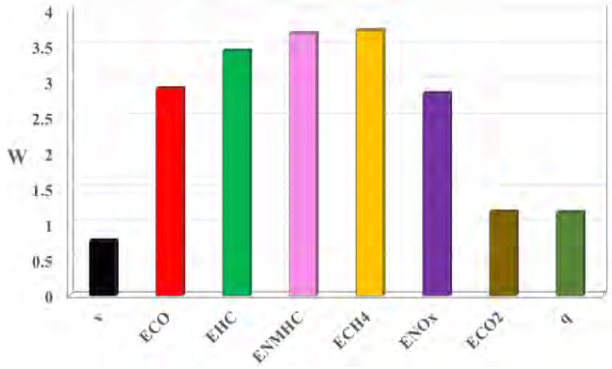

Fig. 28. Coefficients of variation – W of the measured variables

The results of the variables obtained in the study, in terms of their values, were made into histograms. This includes the histogram of the vehicle speed (Fig. 29).

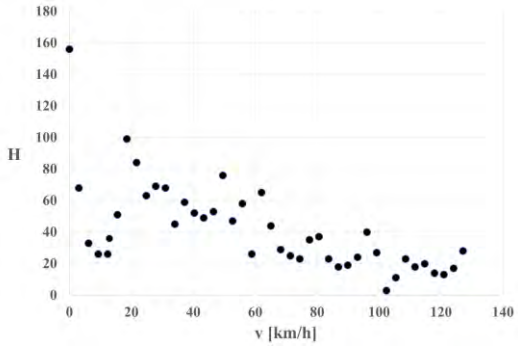

Fig. 29. Histogram – H of vehicle speed – v

The vehicle driving speed histogram was characterized by a relative uniformity, apart from the clear prominence of the zero speed point.

Figures 30–35 provide the remaining histograms of all the measured pollutants exhaust emission rates.

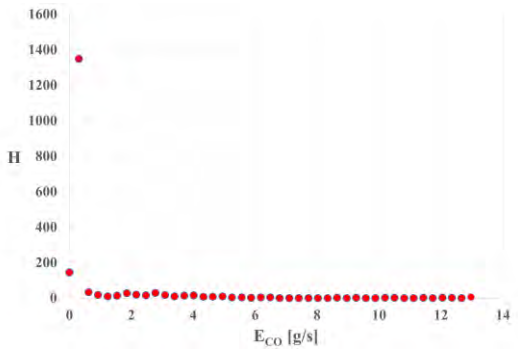

Fig. 30. Histogram – H of carbon monoxide exhaust emission rate – ECO

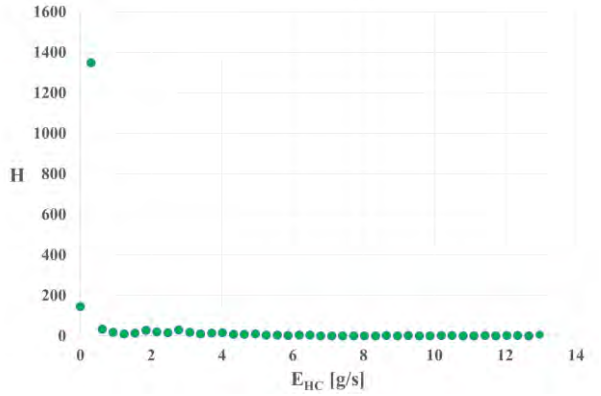

Fig. 31. Histogram – H of hydrocarbons exhaust emission rate – E_{HC}

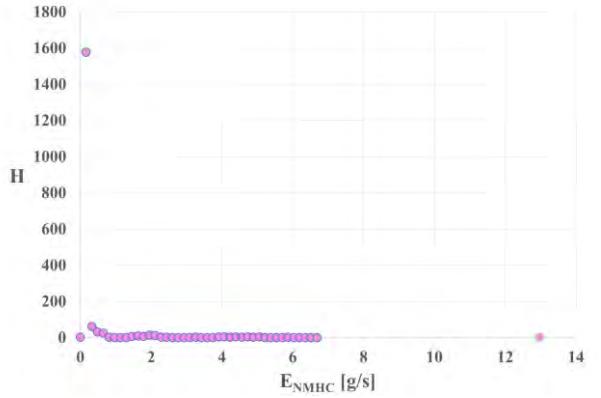

Fig. 32. Histogram – H of non-methane hydrocarbons exhaust emission rate – E_{NMHC}

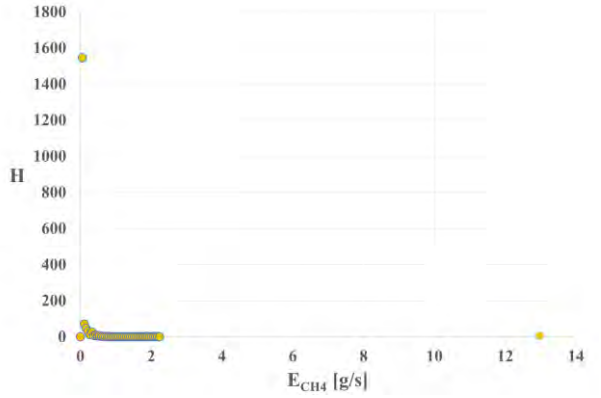

Fig. 33. Histogram – H of methane exhaust emission rate – E_{CH4}

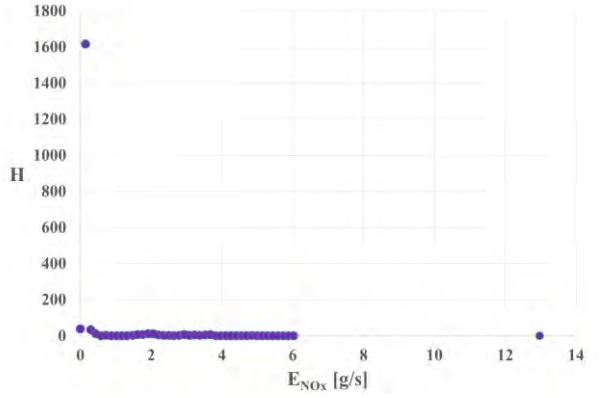

Fig. 34. Histogram – H of nitrogen oxides exhaust emission rate – E_{NOx}

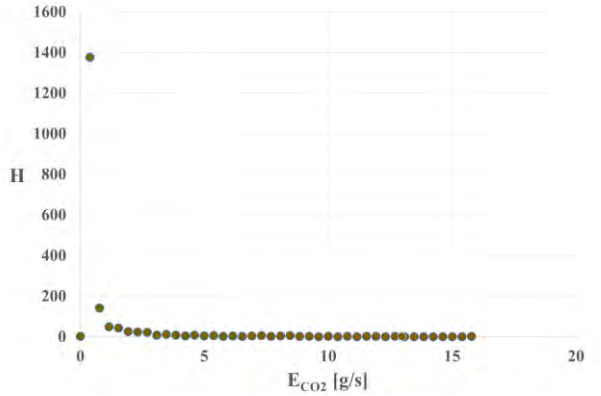

Fig. 35. Histogram – H of carbon dioxide exhaust emission rate – E_{CO2}

Histograms of exhaust emission rates were characterized by a clearly large share of points with small emission values. This was due to the very high values of the local maxima for these variables.

Figure 36 shows the histogram of the volumetric fuel consumption rate.

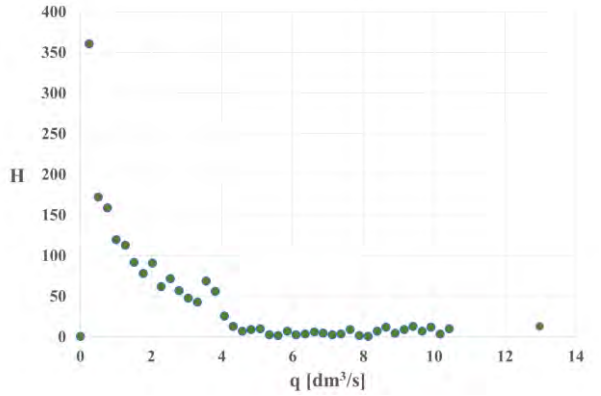

Fig. 36. Histogram – H of the volumetric fuel consumption rate – q

The volumetric fuel consumption rate histogram was notably different from the histograms of the exhaust emission rates, but a predominance in representation of low values could still be seen.

6. Conclusion

The recorded data of exhaust emission rates of measured substances, with the exception of carbon dioxide, were characterized by very low values, bordering on the measurement accuracy, for a significant share of the test duration. This should be expected in the case of modern diesel engines that meet the Euro 6 emission norm. The exhaust emissions were measured in the WLTC test, which led the authors to conclude the following:

1. The distance-specific emission of measured substances in the WLTC test was low enough to meet the Euro 6 requirements with a large safety margin: in the case of distance-specific emissions of carbon monoxide, that margin was over 90% of the limit value, even for distance-specific emissions of nitrogen oxides the margin was almost 40% of the limit.
2. The vehicle speed was weakly correlated with the carbon monoxide, nitrogen oxides and non-methane hydro-

carbons emission rates, while also being strongly correlated with the volumetric fuel consumption rate and the carbon dioxide emission rate.

3. The volumetric fuel consumption rate and carbon dioxide emission rate were found to be most strongly correlated. The correlation between the emission rates of organic compounds was also very strong. The carbon monoxide emission rate was the least correlated with all measured emission rates, except the emission rate of nitrogen oxides.
4. For all the obtained exhaust emission rates, the mean value was much greater than the median, while the standard deviation was much greater than both of those. The median value was close to the average value only in the case of the vehicle speed. For all the examined variables, except for the vehicle speed, kurtosis was positive. The kurtosis of the vehicle velocity was slightly negative, so the negative flattening of the distribution was not significant; the kurtosis value was observed for the organic compound emission rate, while the smallest positive kurtosis value could be seen for the carbon dioxide emission rate and the volumetric fuel consumption rate.
5. The skewness of all the measured variables distributions was positive. Hence these distributions had a right-sided asymmetry. As in the case of kurtosis, the highest value of skewness was found for the organic compounds emission rate, and the smallest – for the vehicle speed, carbon dioxide emission rate and volumetric fuel consumption rate.
6. Analysis of the coefficient of variation showed that the organic compounds exhaust emission rate had the most dynamic properties, followed by carbon monoxide and nitrogen oxides, and the vehicle speed was the least dynamic.
7. The vehicle speed histogram was characterized by a relative uniformity, apart from the very significant share of the point of zero speed. Histograms of exhaust emission rates were characterized by a clearly significant share of the small emission values; which was caused by the very large values of local maxima. The fuel consumption volumetric rate histogram was visibly different from the histograms of the exhaust emission rates, but the predominance of low process values was still observed.

Nomenclature

AV	average value
CH_4	methane
CO	carbon oxide
CO_2	carbon dioxide
D	standard deviation
E	pollutant emission rate
H	histogram frequency
HC	hydrocarbons
K	kurtosis
M	median
Max	maximum value
Min	minimum value
NMHC	non-methane hydrocarbons
NO_x	nitrogen oxides
q	volumetric fuel consumption rate
R	range
R^2	coefficient of determination
S	skewness
T	time
V	vehicle velocity
W	coefficient of variation
WLTC	Worldwide Harmonized Light Vehicles Test Cycle
WLTP	Worldwide Harmonized Light Vehicles Test Procedure

Bibliography

[1] Blanco-Rodriguez D, Vagnoni G, Holderbaum B. EU6 C-segment diesel vehicles, a challenging segment to meet RDE and WLTP requirements. IFAC-PapersOnLine. 2016; 49(11):649-656. https://doi.org/10.1016/j.ifacol.2016.08.094

[2] Chacko S, Alonso C, Solimene A, Simon J, Kallifronas DP. Fuel economy benefit of active grille shutters for real world, worldwide harmonized light vehicles test procedure, and real driving emission cycles. SAE Technical Paper 2022-01-5013. 2021. https://doi.org/10.4271/2022-01-5013

[3] Chłopek Z, Biedrzycki J, Lasocki J, Wójcik P. Emission intensity in various conditions of operation of the automotive internal combustion engine. Transport. 2019;34(4):490-498. https://doi.org/10.3846/transport.2019.11294

[4] Fuć P, Siedlecki M, Szymlet N, Sokolnicka B. Exhaust emissions from a Euro 6c compliant pc vehicle in real operating conditions. Journal of KONBiN. 2019;49(4):421-440. https://doi.org/10.2478/jok-2019-0094

[5] Giakoumis ES, Zachiotis AT. Investigation of a diesel-engined vehicle's performance and emissions during the WLTC driving cycle – comparison with the NEDC. Energies. 2017;10(2):240. https://doi.org/10.3390/en10020240

[6] ISO8178. Emission test cycles. https://dieselnet.com/standards/cycles/iso8178.php (accessed on 2022.10.02).

[7] Kaźmierczak A, Matla J. Method of verifying the emission level of the exhaust components of a special vehicle in relation to EURO III standard in road conditions. Combustion Engines. 2022;189(2):89-93. https://doi.org/10.19206/CE-143485

[8] Kneba Z, Stepanenko D, Rudnicki J. Numerical methodology for evaluation the combustion and emissions characteristics on WLTP in the light duty dual-fuel diesel vehicle. Combustion Engines. 2022;189(2):94-102. https://doi.org/10.19206/CE-143334

[9] Koszałka G, Szczotka A, Suchecki A. Comparison of fuel consumption and exhaust emissions in WLTP and NEDC procedures. Combustion Engines. 2019;179(4):186-191. https://doi.org/10.19206/CE-2019-431

[10] Lane DM, Scott D, Hebl M, Guerra R, Osherson D, Zimmer H. Introduction to statistics – open textbook library (umn.edu). 2023. https://onlinestatbook.com/Online_Statistics_Education.pdf

[11] Ligterink NE, van Mensch P, Cuelenaere RFA. NEDC – WLTP comparative testing. Report number: TNO 2016 R11285. October 2016. https://doi.org/10.13140/RG.2.2.19039.66723
[12] Morales V. Exhaust emissions of in-use Euro 6d-TEMP and Euro 6d vehicles in WLTP and RDE conditions, a comparison. SAE Technical Paper 2022-01-1023. 2023. https://doi.org/10.4271/2022-01-1023
[13] Otnes RK, Enochson L. Applied time series analysis: basic techniques. John Wiley & Sons, Inc. 1978.
[14] Sileghem L, Bosteels D, May J, Favre C, Verhelst S. Analysis of vehicle emission measurements on the new WLTC, the NEDC and the CADC. Transportat Res D-Tr E. 2014;32:70-85. https://doi.org/10.1016/j.trd.2014.07.008
[15] Theodoros G, Giorgio M., Heinz S. Analysis of WLTP typical driving conditions that affect non exhaust particle emissions. EUR 28273 EN. Luxembourg. Publications Office of the European Union 2016. JRC103870. https://publications.jrc.ec.europa.eu/repository/handle/JRC103870
[16] Tsiakmakis S, Fontaras G, Cubito C, Pavlovic J. Anagnostopoulos K, Ciuffo B. From NEDC to WLTP: effect on the type-approval CO_2 emissions of light-duty vehicles. EUR 28724 EN. Publications Office of the European Union, Luxembourg 2017, JRC107662. https://doi.org/10.2760/93419
[17] Worldwide emission standards. Passenger cars and light duty vehicles. Delphi. Innovation for the real world 2020/2021.

Monika Andrych-Zalewska, DEng. – Faculty of Mechanical Engineering, Wroclaw University of Science and Technology, Poland.
e-mail: *monika.andrych@pwr.edu.pl*

Article citation info:
Stoeck T. Repair methodology of a piezoelectric injector utilizing components obtained from selective decomposition. Combustion Engines. 2023;194(3):63-67. https://doi.org/10.19206/CE-167428

Tomasz STOECK

Combustion Engines
Polish Scientific Society of Combustion Engines

Repair methodology of a piezoelectric injector utilizing components obtained from selective decomposition

ARTICLE INFO

Received: 27 April 2023
Revised: 3 June 2023
Accepted: 5 June 2023
Available online: 1 July 2023

The paper presents an example of regeneration of a common rail piezoelectric fuel injector, which was carried out with using used parts. The most important stages of maintenance activities are listed, as well as the types of diagnostic tests performed on separate test benches. The obtained results indicate that this process can be effectively carried out with existing technological problems and lack of support from the manufacturer. At the same time, it was shown that, contrary to popular belief, cannibalisation does not have to be limited only to minor elements, but also to key components important from the point of view of the satisfactory technical condition and correct working of the fuel injector during further operation.

Key words: *common rail system, piezoelectric fuel injector, selective decomposition, regeneration process*

1. Introduction

Selective decomposition consists in obtaining spare parts from damaged products, as well as their control for reuse [26]. This process is one of the forms of recovery being used to maintain or restore the original technical condition in a relatively short time. For this reason, it is successfully used in the automotive services sector, where the efficient satisfaction of customer needs and requirements plays a significant role [3, 25, 27, 32]. In addition, it enables the repair of selected assemblies or subassemblies when new spare parts are not available on the market [16]. With regard to the fuel equipment of compression-ignition engines, this is related to the conscious policy of manufacturers who limit the regenerative capabilities of common rail fuel injectors. This mainly applies to solutions with a stack of piezoelectric crystals, for which replacement of the actuating and controlling components is not provided [13, 18]. As a result, their maintenance was reduced to cleaning, testing and possible replacement of a worn plunger and barrel assembly (needle with nozzle) for selected reference numbers. This is the opposite of systems with a classic electromagnetic coil, because over the years as many as three stages of repair have been implemented for them [10, 22]. Since they were introduced gradually, cannibalization was used for small parts that were not offered for sale. Examples include retaining pins, valve and needle springs, adjusting shims from specific selection groups, etc. [24].

Recently, the regeneration capabilities of piezoelectric fuel injectors have significantly improved. This is primarily due to the availability of specialized measuring equipment, which allows for full diagnostics [21]. In this regard, the key issue is the software with the manufacturer's data, because the knowledge of the limit ranges eliminates the need to look for alternative tests, e.g. drawing up reference characteristic curves to assess the method of fuel dosing [23]. In addition, modern testers offer comprehensive control of electrical components, and test benches are equipped with stack revitalisation functions, i.e. removing short circuits between crystals, as well as assigning new codes after repair [8, 12, 29]. Essentially, the only unresolved problem is the lack of original spare parts, which makes it difficult to restore the full efficiency of fuel injectors from selected manufacturers. Nevertheless, such actions are being taken, as shown in the discussed example.

2. Methods

2.1. Test object

The tests were carried out on a Denso G2P piezoelectric fuel injector, which was removed from the 2.2 D-CAT (Diesel Clean Advanced Technology) engine of a Toyota Corolla Verso passenger car with a mileage of 322,000 km.

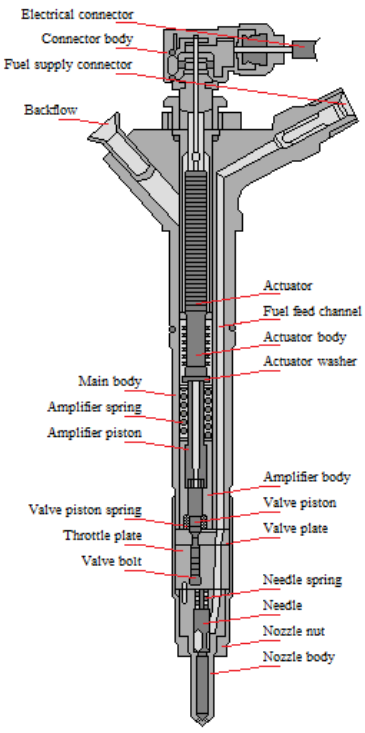

Fig. 1. Denso G2P fuel injector design: own study based on [7]

Fuel injectors of this type are the second generation of common rail systems (CRS), working at maximum operating pressures up to 180 MPa [5, 15]. Figure 1 shows the internal structure, detailing the elements of the hydraulic booster, control valve and nozzle. The listed components are analogous to the solutions from Bosch [1, 20]. A characteristic feature, however, is the movable part of the control valve, which in the form of an elongated plunger (screw) performs an additional sealing function. Unfortunately, laboratory and workshop practice shows that damage to its working surfaces is diagnosed relatively often, which results in an increased amount of fuel going to the fuel return overflow. In addition, the construction of the fuel injector practically did not take into account the adjusting shims, eliminating the possibility of additional correction of fuel dosing, which the manufacturer provided for solutions with an electromagnetically controlled valve [11, 14].

2.2. Test beds

The following equipment and instrumentation were used in the regeneration of the tested fuel injector:
– 12PSB test bench with a Stardex test kit,
– Mega Tester V3 piezoelectric actuator tester,
– Yizhan 13MP HDMI VGA microscope camera,
– Polsonic Sonic 9 ultrasonic cleaner,
– Facom E.316A200S electric torque wrench,
– vices, grips and workshop tools.

Fig. 2. 12PSB test bench with a Stardex test kit

The Stardex test kit included the Nova Ultima simulator, the Stream flow meter and the Prima cooling, filtering and damping module. The system was complemented by a PC computer with the Ubuntu Linux system, equipped with the necessary peripheral devices (Fig. 2). Its connection to the 12PSB test bench allowed for a comprehensive fuel injector check in automatic mode. Other control, repair and maintenance activities, including additional calculations, were carried out at separate laboratory stations.

2.3. Research plan

Figure 3 shows the test plan, the course of which is analogous to the standard procedures used in the maintenance of fuel injectors. Differences may result from the access to specific diagnostic equipment, as well as the type of irregularities found. For example, electrical tests are usually conducted on the main test bench [17]. However, their isolation makes it possible to detect damage to the crystal stack already at the initial stage, which makes further actions pointless. In the absence of a dedicated tester, a universal multimeter with a capacitance measurement function can be used [2, 4]. In turn, the suspicion of the presence of metal filings entering the fuel injector from a faulty pump will result in an earlier microscopic examination. In this way, they will not be removed during cleaning in an ultrasonic cleaner.

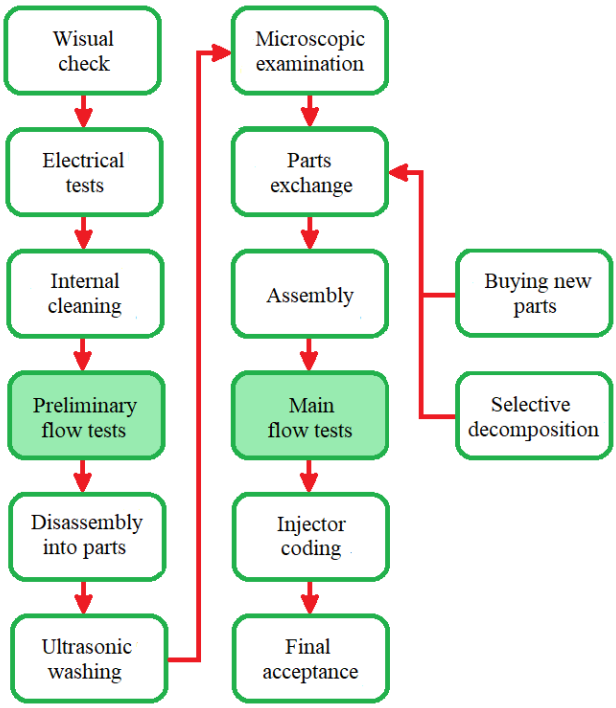

Fig. 3. The research plan for Denso fuel injector

3. Analysis results and discussion

3.1. Preliminary tests

During the external inspection, no external defects or missing components of the fuel injector were detected.

Fig. 4. Testing of the electrical parameters of the fuel injector

In the next step, electrical measurements were started, which were carried out using the Mega Tester V3 tester (Fig. 4). There was no breakdown of insulation between the actuator and the main body ($R_i = \infty$). In addition, almost exemplary results were obtained for the remaining parameters, as shown in Fig. 4. The capacitance of the crystal stack was C = 3.00 μF, and its resistance R = 1.01 MΩ, which is characteristic only for piezoelectric fuel injectors from this manufacturer. This value remained unchanged in the continuous R_C load test.

Then, flow tests were carried out on the 12PSB test bench with a Stardex test kit, the results of which are summarized in Table 1. It can be seen that the amount of fuel going to the overflow is definitely too high, which clearly indicates incorrect operation of the valve group [31]. In addition, incorrect values of the idling and pilot doses were obtained, taken in the range of the lowest operating pressures and activation times. The probable cause is the deterioration of the cooperation of the plunger and barrel assembly, i.e. grinding of the needle in the nozzle, and thus the failure very often encountered at high mileage [30].

Table 1. Results of the preliminary fuel injector flow test

Test number	Injection pressure p_{inj} [MPa]	Nozzle opening time t [μs]	Injection dosage d [ml/min]	
			Nominal range	Result
1	180	600	79.1±10.0	74.4
2	180	277	27.5±6.0	27.1
3	180	194	8.7±4.0	7.9
4	140	700	76.3±11.3	68.3
5	140	317	29.3±6.0	29.8
6	140	178	6.7±4.0	4.2
7	80	696	48.3±7.0	43.7
8	80	180	4.5±3.2	1.1
9	35	693	22.5±4.5	17.1
10	35	300	5.4±4.0	1.3
Test number	Injection pressure, p_{inj} [MPa]	Nozzle opening time t [μs]	Back flow r [ml/min]	
11	160	800	35.0±25.0	66.8

a)

b)

Fig. 5. Examples of assemblies after disassembly: a) hydraulic booster, valve, nozzle, b) piezoelectric actuator

Figure 5 shows the view of exemplary fuel injector components after disassembly. At this stage, it is possible to inspect the individual components in detail, as well as to carry out simple tests, e.g. checking the patency of the nozzle openings. The easiest way is to use the WD-40 multipurpose spray directly (Fig. 6). This test should be regarded as optional, usually performed when the nozzle tip is heavily coked or contaminated.

Fig. 6. Checking the patency of the nozzle openings

Fig. 7. Microscopic examination of the valve plunger

Before microscopic examination, all parts, except for the piezoelectric actuator, were subjected to baths in an ultrasonic cleaner and dried. The examination under high

magnification confirmed the previous assumptions. The edges of the valve plunger exhibited distinct signs of abrasive wear, similar to its working surfaces (Fig. 7). In turn, numerous longitudinal scratches were observed on the needle, which indicates the progressing process of its scuffing (Fig. 8). In addition, corrosion was found on some parts in contact with the fuel, such as the body of the hydraulic booster, throttle and valve plates. As a result, a decision was made to replace the actuating and controlling units, omitting the efficient piezoelectric actuator.

At present, the commercial offer includes only the nozzle group, produced, for example, by Warszawskie Zaklady Mechaniczne "PZL-WZM" [27]. The remaining components were obtained through selective decomposition of a low mileage injector, in which the non-replaceable stack of piezoelectric crystals suffered permanent damage.

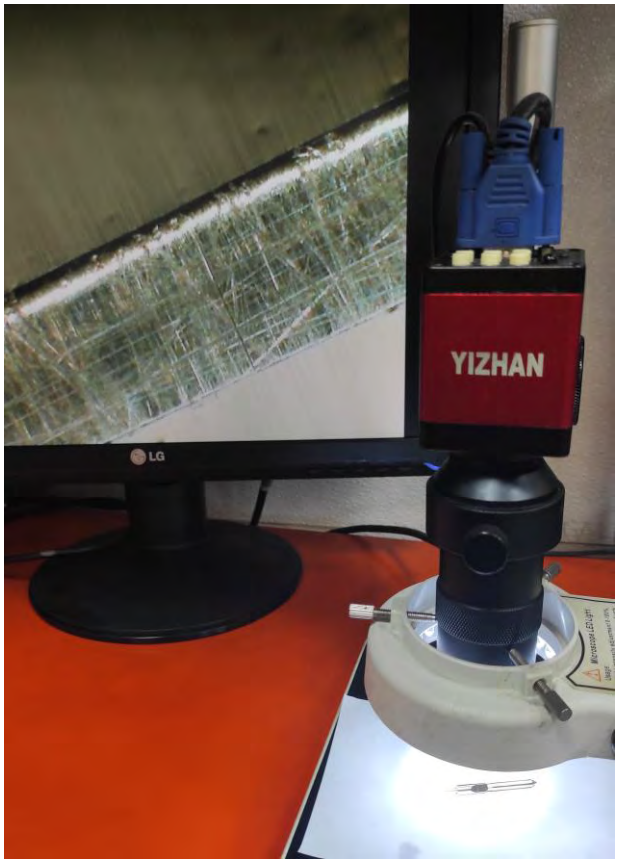

Fig. 8. Microscopic examination of the needle

Next, the assembly process was carried out. It should be noted that the assembly of the piezoelectric actuator must be carried out in the presence of diesel oil, as in the solutions of Bosch [9]. In this way, the possibility of falsifying test results in flow tests on the test bench is eliminated.

3.2. Main tests

Table 2 presents the results of flow tests of the fuel injector after regeneration. This process should be assessed positively, as the values of all doses were within the limit ranges specified by the manufacturer. In addition, a small amount of fuel going to the overflow indicates that the valve group and the hydraulic booster are working perfectly fine.

It is worth noting that during the repair the fuel injector receives new IMA (German: Injektor-Mengen-Abgleich) dosing correction codes. However, unlike solutions from other manufacturers, it is not enough to enter them into the engine control module (ECM), as the so-called zero dose calibration is also required. In this process, the system performs self-diagnosis, which consists in checking the method of fuel supply at various operating pressures and activation times. Essentially, only this stage ends the regeneration procedure, although it is not directly related to it.

Table 2. Results of the main fuel injector flow test

Test number	Injection pressure p_{inj} [MPa]	Nozzle opening time t [μs]	Injection dosage d [ml/min]	
			Nominal range	Result
1	180	600	79.1±10.0	77.1
2	180	277	27.5±6.0	31.3
3	180	194	8.7±4.0	10.4
4	140	700	76.3±11.3	73.2
5	140	317	29.3±6.0	33.6
6	140	178	6.7±4.0	6.5
7	80	696	48.3±7.0	53.1
8	80	180	4.5±3.2	3.3
9	35	693	22.5±4.5	25.0
10	35	300	5.4±4.0	4.4
Test number	Injection pressure p_{inj} [MPa]	Nozzle opening time t [μs]	Back flow r [ml/min]	
11	160	800	35.0±25.0	11.5

4. Conclusions

The presented example indicates that selective decomposition does not have to be limited solely to small components. This is because the complete main components, which are crucial for proper operation, have been replaced. At present, this is essentially the only way to regenerate Denso fuel injectors, assuming that the piezoelectric actuator has not been damaged. For the above reasons, service companies that repair fuel equipment do not sell used parts, nor do they return them to the manufacturer. The added value is participation in the chain of their acquisition and reuse, which is part of the term reverse logistics [6, 19].

Acquiring used parts can be done in various ways. Many of them come from injectors that have not been qualified for flow testing, for example due to incompleteness, lack of sealing, damage to the crystal stack, etc. They can be left by customers themselves, provided by friendly car workshops, or finally purchased on the secondary market. However, it should be emphasized that a necessary condition for their reuse is a good technical condition. This means that the main components of the executive and control assemblies must be completely free of corrosion and any mechanical damage (cracks, material defects, traces of rubbing, etc.) that could have a negative impact on the functionality of the injector. Therefore, before reuse, they should undergo procedures such as cleaning in ultrasonic cleaners, drying, and detailed microscopic inspections.

Acknowledgements

The tests were carried out at AUTO NEXT SERWIS automotive service company based in Szczecin, which provided the equipment and instrumentation necessary in the regeneration process of the tested fuel injector.

Bibliography

[1] Boecking F, Dohle U, Hammer J, Kampmann S. Passenger car common rail systems for future emissions standards. MTZ Worldwide 2005; 66: 14-16. https://doi.org/10.1007/BF03227771

[2] Clarke J. Testing piezoelectric injectors. Autobiz 2011;12:1-2.

[3] Fu F, Chen S, Sun L. Revenue and cannibalization: the effect of interchangeable design confronted remanufacturing processing. Processes 2021;497(9):1-25. https://doi.org/10.3390/pr9030497

[4] Günther H. Common Rail – Systeme in der Werkstattpraxis. Technik, Prüfung, Diagnose. Bad Wörihofen: Krafthand Verlag Walter Schultz GmbH, 2012.

[5] Hagen J, Herrmann OE, Weber J, Queck D. Better diesel combustion by further injector improvement. Auto Tech Review 2016;5(9):28-35. https://doi.org/10.1365/s40112-016-1198-4

[6] Janczewski J. Barriers to implementation processes of reverse logistics in the automotive services. The Academy of Humanities and Economics in Lodz Publishing House 2014;2(19):58-61.

[7] Jääskeläinen H, Ferrari A. Common rail fuel injection system components. DieselNet 2020;2.

[8] Kaczorowski M, Pilewski Z. The coding of IMA/ISA in piezoelectric injectors. Bosch Autospec 2017;66(4):7-9.

[9] Kaczorowski M, Pilewski Z. Piezoelectric injectors – pioneers of high pressures up to 2500 bar. Bosch Autospec 2017;65(3):7-10.

[10] Karpiuk W, Bor W, Smolec R. Possibilities of analysis of condition and repair of common-rail system injectors. Journal of KONES Powertrain and Transport 2018;23(4):209-216. https://doi.org/10.5604/12314005.1217208

[11] Konieczny Ł, Adamczyk B, Adamczyk G. Diagnostics and regeneration of common rail injectors. Scientific Journal of Silesian University of Technology. Series Transport 2015;86:65-73.

[12] Krivtsov SN, Krivtsowa TI. Variations in health of piezoelectric elements of the Common Rail electric hydraulic nozzles in the operating conditions. IOP Conference Series: Materials Science and Engineering 2021;1061:1-8. https://doi.org/10.1088/1757-899X/1061/1/012022

[13] Kruczyński SW, Mazuruk P, Chrupek B. The diagnosis and repair technology of injectors and high pressure pumps used in common rail systems. Proceedings of the Institute of Vehicles. 2014;100(4):133-134.

[14] Matsumoto S, Date K, Taguchi T, Herrmann OE. The new Denso common rail diesel solenoid injector. Auto Tech Review 2013;2:24-29. https://doi.org/10.1365/s40112-013-0459-8

[15] Oki M, Matsumoto S, Toyoshima Y, Ishisaka K, Tsuzuki N. 180 MPa piezo common rail system. SAE Technical Paper 2006-01-0274. 2006. https://doi.org/10.4271/2006-01-0274

[16] Ormon SW, Cassady CR. Cannibalization policies for a set of parallel machines. Annual Symposium Reliability and Maintainability (RAMS). Los Angeles 2004;540-545. https://doi.org/10.1109/RAMS.2004.1285503

[17] Osipowicz T. Research and analysis technical parameters not repair Diesel injectors. Buses – Technology, Operation, Transport Systems. 2015;6:172-175.

[18] Osipowicz T. Reduction of the common rail fuel injectors repair costs. Econtechmod. An International Quarterly Journal on Economics of Technology and Modelling Processes 2017;6(1):63-70.

[19] Premkumar R, Veera PKS, Babudass MN. Future directions of reverse logistics in gaining competitive advantages: a review of literature. International Journal of Supply Chain Management (IJSCM) 2015;4(1):39-48.

[20] Salvador FJ, Plazas AH, Gimeno J, Carreres M. Complete modelling of a piezo actuator last generation injector for diesel injection systems. Int J Engine Res. 2012;15(1):3-19. https://doi.org/10.1177/1468087412455373

[21] Stoeck T. Problems of regeneration of modern piezoelectric fuel injectors. Combustion Engines. 2022;191(4):3-8. https://doi.org/10.19206/CE-146700

[22] Stoeck T. Simplification of the procedure for testing common rail fuel injectors. Combustion Engines. 2020;180(1): 52-56. https://doi.org/10.19206/CE-2020-109

[23] Stoeck T, Abramek KF, Osipowicz T. Simplified methodology for testing common rail piezoelectric injectors taking into account reference characteristics. Engineering Review. 2021;41(2):54-61. https://doi.org/10.30765/er.1475

[24] Stoeck T, Abramek KF. Selected issues of reverse logistics in the servicing of common rail system injectors. Selected topics in applied logistics. AGH University Press. 2016;3: 410-418.

[25] Szczerba B, Białecka B. Analysis of reverse logistics of complaint products in an automotive company. Systems Supporting Production Engineering. 2017;6(7):243-254.

[26] Thierry M, Salomon M, Van Nunen J, Van Wassenhove L. Strategic issues in product recovery management. Calif Manage Rev. 1995; 37(2): 114-136. https://doi.org/10.2307/41165792

[27] Włodarczyk M, Janczewski J. Reverse logistics management in automotive services. Entrepreneurship – Education. 2013;9:185-203. https://doi.org/10.24917/20833296.9.12

[28] WUZETEM. Manufacturer of nozzle. Product range. PZL-WZM 2018:1-104.

[29] Yakimov IV, Bondarenko EV, Krivtsov SN, Krivtsova TI. Leak detection method for electrohydraulic injectors of diesel engines in operation. Proceedings of the International Conference Aviamechanical engineering and transport AVENT. 2018;158:448-452. https://doi.org/10.2991/avent-18.2018.86

[30] Yong Z, Bo Q, Daqing G, Guoyou M. Optimization of injector nozzle in high pressure common rail injection system. Journal of Mechanical Engineering Research and Developments. 2018;41(1):27-37. https://doi.org/10.7508/jmerd.2018.01.004

[31] Yordanov N, Hadjiev K, Stankov E. Experimental simulation of common rail electromagnetic injectors wearing. International Scientific Journal. 2018;12(4):208-211.

[32] Żurawski P. Optimization of the combustion chamber strength of aluminum pistons in diesel engines using the DuralBowl technology. Combustion Engines. 2023;192(1):91-96. https://doi.org/10.19206/CE-153000

Tomasz Stoeck, DEng. – Faculty of Mechanical Engineering and Mechatronics, West Pomeranian University of Technology in Szczecin, Poland.
e-mail: *tstoeck@wp.pl*

Article citation info:
Czerwiński J, Mayer A, Mayer J, Burtscher H, Lutz T, Mayer R et al. Minimizing indoor infection risks with automotive nanofiltration and with laminar vertical flow. Combustion Engines. 2023;194(3):68-77. https://doi.org/10.19206/CE-168141

Jan CZERWIŃSKI
Andreas MAYER
Jörg MAYER
Heinz BURTSCHER
Thomas LUTZ
Rainer MAYER
Barbara ROTHEN-RUTISHAUSER
Joachim FREY
Christian LÄMMLE
Tobias RÜGGEBERG
Patrick SPECHT

Combustion Engines
Polish Scientific Society of Combustion Engines

Minimizing indoor infection risks with automotive nanofiltration and with laminar vertical flow

ARTICLE INFO

Received: 7 April 2023
Revised: 12 May 2023
Accepted: 12 June 2023
Available online: 3 July 2023

The knowledge about nanoaerosols, their potential health effects, their measurement, limitation and administrative-legal treatment has been developed in the last 3 decades in connection with the exhaust gas cleaning of the combustion engines. Nanofiltration, which has thus become known, almost completely eliminates nanoparticles with filters of high durability, high specific filtration areas, and reasonable costs. On the occasion of the Covid pandemic, NanoCleanAir experimentally proved that the viruses in an automotive filter substrate are separated as well as the combustion particles and are also deactivated. To minimize cross exchange of infectious aerosol, new attention must be paid to flow management in ventilated spaces. Digitized flow analysis has also received significant inspiration from engine technology in the past. This paper provides information on some basic investigations and gives valuable advice based on the experimental and numerical results of a retrofitted classroom.

Key words: *ventilation for virus protection, vertical laminar flow, nanoparticle separation, virus deactivation, ceramic honneycomb wall flow filter, nanofiltration*

1. General

A SARS CoV-2 infected person may emit up to 10 million viruses with each m^3 of exhaled air, and on the other hand, the infection dose may be as low as 500–1000 viruses. Given these numbers, the infection risk in a room cannot be sufficiently reduced by periodic window ventilation or by partly cleaning with mobile air cleaners but requires a continuous perfect virus elimination. Furthermore, lateral flow from the infected persons to their direct or distant neighbors must be avoided. This sounds utopic but can indeed be solved by body heat-induced vertical laminar flow and ventilation from floor to the ceiling, extracting the contaminated air at the ceiling and recycling it via a filter back to the floor. Filtration must be very close to 100%. Since the «naket» Corona virus has a size of 60–150 nm, which is the typical size of particles emitted by combustion engines. The diesel particle filter DPF, a honeycomb type ceramic wall-flow filter, was selected for this nanofiltration task. These filters reach > 99% efficiency for soot particles of 10–500 nm and have attractive properties since their filtration surface is > 1 m^2 per liter bulk volume, they can easily be cleaned in situ, if needed thermically disinfected or catalytically coated, and have the life, the quality, low bulk and low cost of an automotive product. To test the bioaerosol filtration properties, bacteriophages MS2, which are non-pathogenic to human, animals and plants and have a viral particle size of 30–40 nm were used for the test as a proxy for SARS-CoV-2 virus. The wall flow filters reached a filtration rate of > 99% for these bacteriophages and the survival test resulted in 1% active viruses after 24 hours, zero after 48 hours. To test the whole system, a classroom was selected as a pilot case. The ventilation was designed to exchange the room's air volume five times per hour. Contaminated air was extracted at the ceiling and recycled to the floor corners after filtration. Fresh air from outside supplied for CO_2-control was also filtered to clean it from ultrafine traffic related carcinogenic particles. The dynamic cleaning process and room distribution was tested with salt nanoparticles simulating the virus source by a cloud concentration of 80,000 particles per cubic centimeter. The lateral flow reaching the neighbor desk of the infected schoolboy contained only 2–300 P/cc, demonstrating that the contaminated air escapes vertically, showing a cross-contamination risk reduction of 2–3 orders of magnitude. This virus protection system is universally applicable, not only for applications in classrooms, but can also be scaled and adapted to industry, hospitals and public transport environments including aircraft cabins.

2. Introduction

Corona viruses, like combustion soot, are among the smallest suspended particles [11, 17, 23]. When exhaled by an infected host, they are usually surrounded by a liquid envelope and reach 500–10,000 nm, but the aqueous envelope evaporates rapidly [8], leaving particles with a thin mucus envelope in the size range of 300–500 nm [9, 20]. Once released as an aerosol in indoor air, they remain suspended for many hours. When they reach surfaces that do not contain host cells, they remain firmly bound there by van der Waals forces, like other fine particles, and lose their

activity after a few hours [4]. Today, it is recognized that only consistent suppression of aerosol transmission in closed rooms, where long periods of residence prevail, can reduce the risk of infection [25, 36]. Thus, ventilation is required.

It is further essential to recognize that the air exhaled by an infected person may contain up to 10 million viruses per m^3 [10, 27]. In contrast, the infectious dose is only 500–1000 viruses, and that infection can occur with a few minutes' exposure [18]. Thus, it makes little sense to aim for dilution by a factor of 2–5 and be satisfied with filter removal efficiencies of 60–80%, which is often considered sufficient for ventilation. Still, much more efficient methods must be sought to ensure adequate protection.

Firstly, the separation efficiency must be high, especially in the diffusion range, i.e., below 1000 nm. Secondly, the ventilation air flow pattern must under no circumstances lead to lateral transport of the virus cloud, which otherwise would favor cross-contamination and accelerate its spread in the course of turbulent dilution of this cloud. Instead, laminar displacement principles are required that reduce cross-contamination by at least two orders of magnitude, and filtration should reach values > 99.9% in the size range < 1000 nm.

Thus periodic window ventilation seems not very suitable because it tolerates a high concentration towards the end of this period, which can be sufficient for contagion and contributes to the rapid expansion of contamination. Also, the use of portable air cleaners by filtration or UV-light, which clean only part of the air but otherwise mix the air in the room by its turbulent flow pattern contribute strongly to the distribution. [7, 21].

If filtration is used, the air supplied from outside should also be filtered efficiently because urban air contains, among others, cancerogenic ultrafine particles from traffic (soot particles and metal oxide particles from exhaust gas, brake abrasion, tire, and road abrasion) in the same size range as the viruses [30, 35] and in much higher concentrations, namely often > 20,000 particles per cubic centimeter, i.e., about one million more than the maximum expected virus concentration.

Both tasks can be solved in combination, which would finally make a significant contribution to mitigating the high mortality risk [12, 34] from traffic-related nanoparticles and avoiding virus infections. In the following, a new technical approach for a sustainable solution to these tasks is presented, which has already been investigated in a classroom as a pilot application by numerical flow simulation and experimentally by salt particle tracing and has fulfilled the requirements mentioned above during a full year of flawless operation [26, 28].

3. Recent developments of ceramic multicell wall flow filters

Over the past thirty years, a filter development has taken place, which, surprisingly, has been completely limited to the application in the exhaust gas of internal combustion engines. From the beginning, the requirements were very high because of the high temperatures in the exhaust tract, the mechanical and thermomechanical demands, the necessity to manage with a very small bulk volume under vehicle floors at low backpressure, and after the introduction of the particle number criterion by Switzerland with a request for high separation efficiency according to VERT [33] of > 98% for particle sizes from 10 nm. 2007 this has been adopted with slight modifications (lower limit 23 nm) by the EU, later by China, India, and many other countries.

Meanwhile, these filters are used in almost all new vehicles, diesel, petrol, and gas. It is estimated that about 300 million vehicles are equipped with particle filters, i.e., a large series product manufactured at comparatively low cost and subject to the stringent quality criteria of the automotive industry. The author team has been involved in developing this technology and the particle metrology required for it from the beginning [2, 5, 19].

In the course of development, the ceramic wall-flow filter design has emerged as the standard solution [13]. Derived from the multicellular structure of a catalyst substrate, but with porous walls (pore size around 10 μm), flow through the walls is forced by alternately plugging the cells (Fig. 1). Since the sum of the wall areas is very large (up to 1.5 m^2 per liter of filter volume), the flow velocity is reduced from an inflow around 50 m/s to a flow of about 5 cm/s through the walls. Thanks to this low velocity, the separation of nanoparticles by diffusion in the pore labyrinth is enabled (Fig. 2), and the pressure drop remains within narrow limits set by the engine.

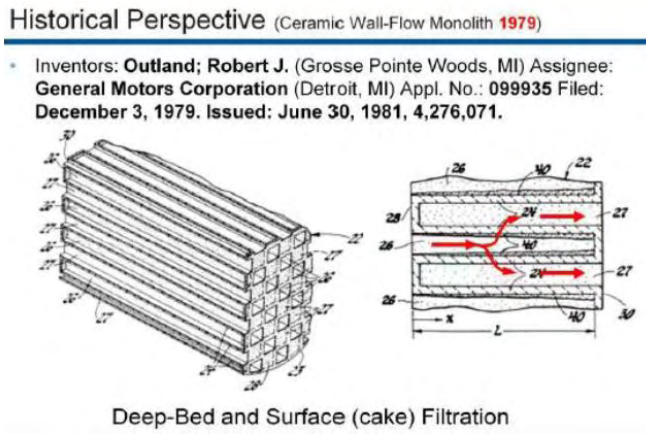

Fig. 1. Ceramic wall flow filter for Diesel application DPF and gasoline application GPF

Starting in the 80's with a cell density of 100 cells per square inch [cpsi], today we are at 300 cpsi and have achieved unprecedented compactness of these filter cells, which allows them to be installed even in small vehicles.

In Diesel engines this filter achieves these high collection efficiencies only after establishing an initial soot layer on the porous filter walls (Fig. 3), which precedes the wall pores with a finer pore structure. This effect of pore gradation can also be achieved by ceramic membrane formation or using hierarchic pore structuring techniques [3] so that filter substrates are available today which reach the high efficiency right from the start and are therefore also suitable for the filtration of viruses, whose concentration in the air is much lower than the concentration of soot particles in the diesel exhaust gas and which would therefore only form a filtering layer after far too long a time.

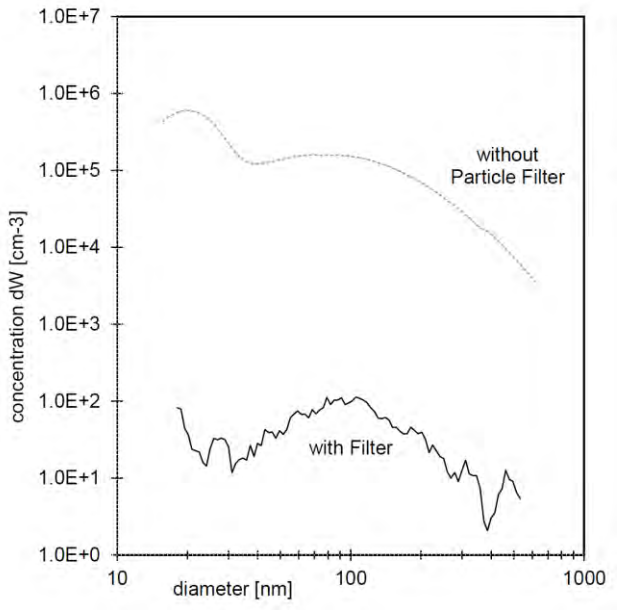

Fig. 2. Diesel soot particle filtration by number > 99% acc. to VERT [33]

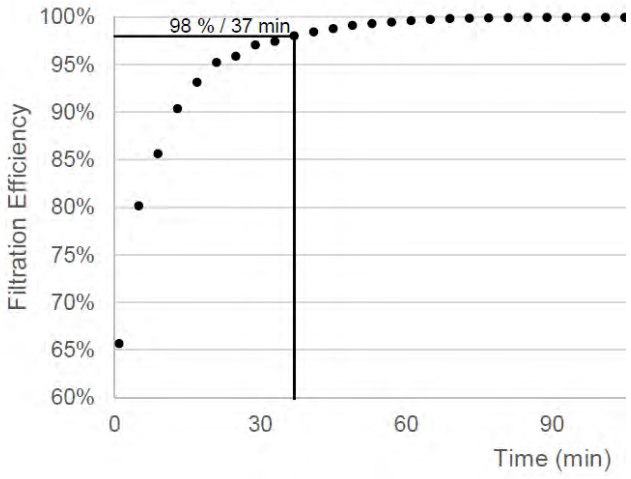

Fig. 3. Filtration efficiency increase by initial soot layer build up on a Diesel engine [33]

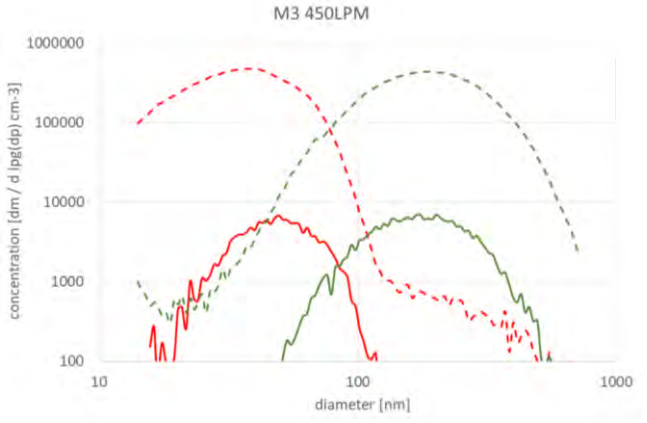

Fig. 4. Filtration of soot generated by two CAST settings [15], measured by SMPS und CNC [31]

These filters have numerous properties which make them suitable for use in exhaust air purification, air conditioning, and, in the present case, for the efficient purification of air from bioaerosols, not only in building services but also in the medical sector and in public transport: low construction volume, light, catalytically coatable, safely heatable for disinfection, easy to clean in situ, do not change their properties due to vibration or wetting or aging and can be easily integrated into a wide variety of geometries and systems.

4. Filtration of infectious bioaerosols

According to the laws of aerosol physics, it may be assumed that viruses behave similarly to soot particles in a filter matrix, i.e. that their flow pattern is determined primarily by mobility, i.e., by size. However, this has to be verified. Therefore, a sensitive test method is needed that provides information on the volumetric concentration of the bioaerosols, and even more precisely, it must provide information on the number of active viruses in the sample volume because the number of deactivated viruses or virus fragments does not make sense for the evaluation of a virus protection filter.

Working with pathogenic viruses, especially highly transmissible ones, poses great health challenges. Due to the high contagiousness (transmissibility) and virulence of SARS viruses in general and SARS-CoV-2 in particular, experiments would have to be carried out under the highest biosafety measures (BSL-3), which makes an experimental facility with aerosols practically impossible.

For these reasons, using bacteriophages as surrogate viruses is state of the art in environmental biology [1, 6, 14, 24, 29]. Bacteriophage MS2 is morphologically, structurally, and genetically similar to human viruses such as SARS-CoV-2, noroviruses, or rotaviruses enabling it to be used as tractable and safe surrogates for human viruses. As a practical surrogate virus, the *Escherichia coli* bacteriophage MS2 can be used together with biological safety laboratory strains of *Escherichia coli* as target cells which are safe for humans and the environment.

MS2 is one of the smallest viruses with a diameter about 2–4 times smaller than SARS-CoV-2. Like SARS-CoV-2, MS2 is a positive-strand RNA bacteriophage. It specifically infects *Escherichia coli* F+ bacteria and can therefore be detected actively (alive) with very high sensitivity in the form of "plaques", which are formed by the multiplication of the viruses in the infected bacterium (up to 1 million viruses in one bacterium) and thus enlarge it to the point where it can be counted visually. In addition, bacteriophage MS2 is highly persistent in aerosols, making it an ideal virus for testing the efficiency of air and water filtration systems; bacteriophage MS2 (ATCC 15597-B1) and its corresponding *Escherichia coli* F+ safety strain C300 (ATCC 15597) are available from the American Type Culture Collection (ATCC).

The following figures show the wind tunnel-like test facility (Fig. 5, 6), sample collection through gelatine filters (Fig. 7), and sample counting the plaques before and after filters (Fig. 8). The equipment and the procedure are described in detail in [28]. Example of result is given in Fig. 9, which illustrates a calculated filtration of > 99.99%.

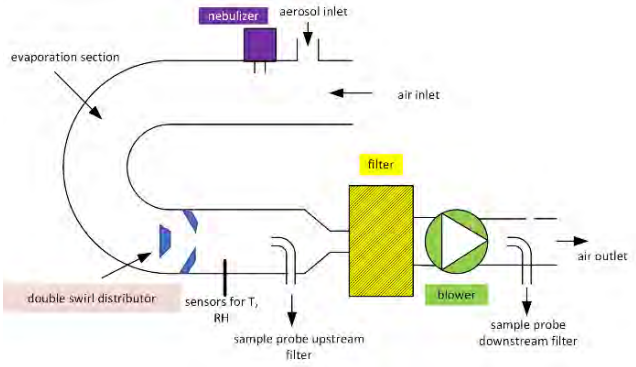

Fig. 5. Flow channel to dry and homogenize salt particles or CAST soot for filter test

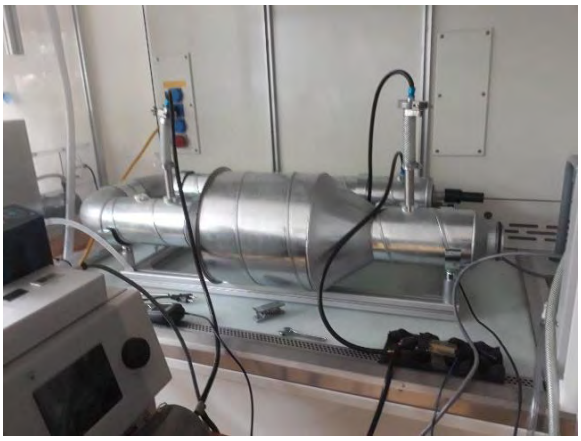

Fig. 6. Actual test installation at FHNW with aerosol sampling points for particle counting

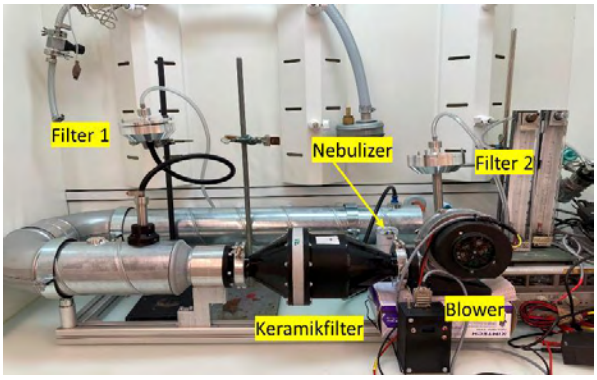

Fig. 7. Test installation at AMI Uni Fribourg for bacteriophage filtration test under the hood

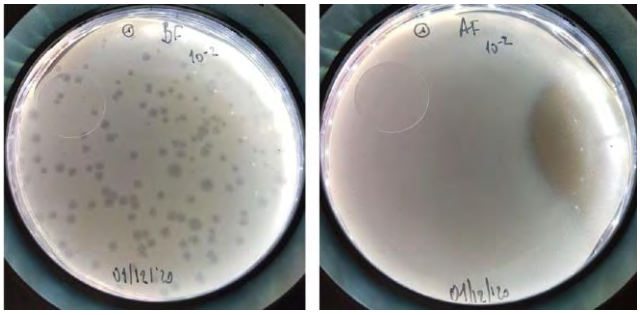

Fig. 8. Agar plates, from which the number of plaques are counted before (left) and after filter (right). The solution was highly diluted to make it countable. Each plaque stays for one original virus

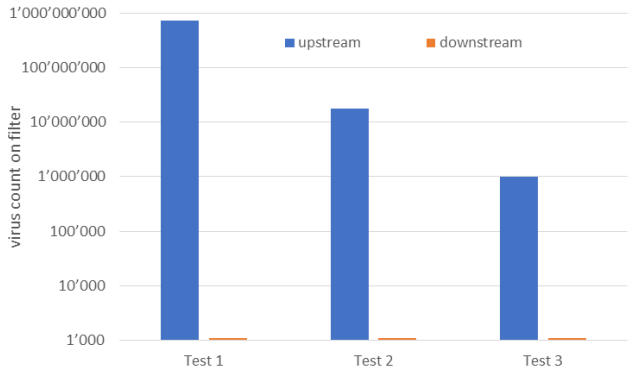

Fig. 9. Typical counting results of « plaques » resulting numerically to values > 99.99%

5. Deactivation of separated viruses in the filter matrix

Filtering alone is not enough because even if the degree of separation is very high, the viruses must be completely deactivated in as short a time as possible, because otherwise there remains an uncertainty as to when, in the course of time, with higher loads or in conjunction with moisture, discharge occurs, so that, as is known with bacteria, the filters themselves could become a dangerous source of pathogenic germs.

In principle, there are many possibilities for disinfection of this type of filter. For example, the filters could be coated with silver or copper or other virucidal substances, or they could be periodically heated to a temperature sufficient for complete desinfection. When used against bacteria, this would certainly be necessary and is basically also provided for this filter design. With viruses, however, the problem may be easier to solve, since viruses are not viable over a long period of time without host cells, they lose their activity or virulence. A detailed report on the loss of activity of SARS CoV-2 viruses deposited on dry solid surfaces is available in [32]. A relatively consistent logarithmic law is shown, although it depends on the materials. After 2–3 days, virulence is hardly detectable. Whether this also applies to the filter materials investigated here had also of course, to be systematically proven.

Paper [28] describes the test shown in Fig. 7: a certain volume of air with a very high concentration of viruses was passed from the test channel in parallel over several small filter samples and analyzed after different times: immediately, after 24 hours, and after 48 hours. Of the 20 million PFU (plaques forming units) that could be counted in the fresh sample, an average of 1–2% were still active after 24 hours at room temperature, and practically none after 48 hours.

Therefore, it can be concluded that, in line with literature, the viruses deposited on the ceramic surfaces rapidly lose their activity even without virucidal coating, i.e., that no active viruses can be discharged. This test should be carried out on all materials used for filtration, and a possible influence of moisture should also be checked.

6. Ventilation to avoid cross contamination in a classroom

It cannot be known who in a group is already infected and can spread the virus through his exhaled air wherever

he goes. Is there a way to avoid infecting people within a distance of 1 m?

Basically there is only one safe place: in the airspace above the heads. This is where the viral cloud must be transported to as soon as possible after exhalation. First and foremost, only body heat can serve this purpose. Every person constantly emits about 100 watts to the environment. Thanks to this heat, a convective movement towards the ceiling takes place in the undisturbed air, which is superimposed by the exhalation speed and slowed down somewhat by the evaporation of moisture (Fig. 10 and 11).

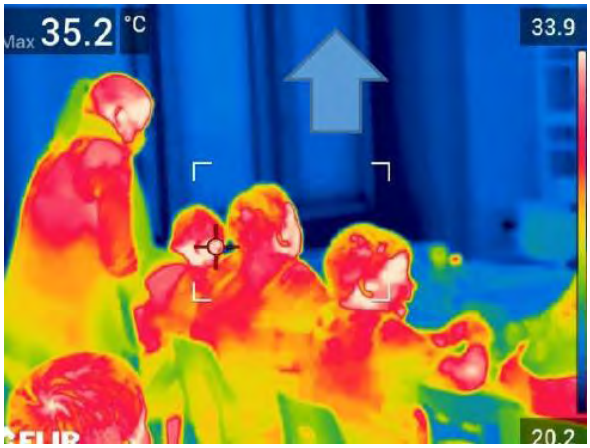

Fig. 10. Infrared camera picture shows the body heat

Fig. 11. Porous textile tubes at the ceiling collect the particles

Fig. 12. Clean air returns to the classroom at the bottom

There is probably only this possibility to quickly remove the viruses from the infection space, and this movement must not be disturbed by turbulence. It must be supported by a laminar displacement of the room air from the bottom to the top.

At the ceiling, the air is extracted without leaving dead-water zones before it would return down along cold walls or windows, then perfectly cleaned in the nanofilter, enriched with fresh air, and returned well-distributed at floor level via skirting boards (Fig. 12). Probably only this approach, derived from the principle of displacement ventilation, can avoid contagion in closed rooms. Even with this method, extreme cases such as coughing and sneezing cannot be controlled, but these will be exceptions that can be controlled by hygienic behavior.

It is clear that this method of transporting the contaminated air by displacement in conjunction with thermal upward drift from the source to the ceiling, where it is collected and extracted, can only serve its purpose if the separation in the filter is very close to 100% because otherwise a part of the viral load would be constantly returned to the room and widely distributed there.

7. The classroom pilot application

The experimental installation shown here does not yet have the character of a finished product but was set up as a laboratory, so to speak, to check the effect of the measures and to carry out an initial optimization. The two figures below (Fig. 13 and Fig. 14) show the room and the installation scheme. The recirculation system is designed for fivefold air exchange per hour and contains a fresh air supply with which the CO_2 level in the fully occupied classroom can be controlled to a setpoint value of around 1200 ppm, i.e., one does not have to accept the large fluctuations of window ventilation. Heat exchange of fresh air and exhaust air supplement the energy balance. The system is deliberately designed to optimize a single room, is compact, and manages with a very low ventilation power.

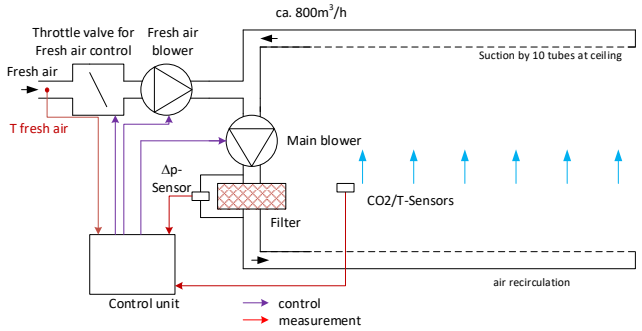

Fig. 13. General arrangement for laminar vertical flow, high nanofiltration, controlled supply of filtered fresh air

The air guidance in textile hoses with well-characterized porosity allows optimum distribution with low turbulence excitation. However, it will still have to be optimized for commercial application, using similar design solutions to those used for displacement ventilation. The principle of avoiding the risk of lateral cross-contamination by capturing emitted viruses overhead and efficiently removing them by nanofiltration can be transferred to many other applica-

tions, especially to applications in the hospital sector and in modes of transport up to aircraft cabins, where the reverse flow direction from top to bottom massively increases the risk of infection today.

Fig. 14. Pilot classroom with hot plates to replace the students body heat

8. Computational flow simulation

Using the SIEMENS STAR-CCM+ software, the schoolroom was digitally simulated to calculate the flow conditions in the entire room in short time steps (Fig. 15). The aim was to represent the three-dimensional flow parameters such as direction and speed in the whole room as a function of the free design parameters such as air exchange rate, flow distribution during suction, backflow as a function of the permeability design of the porous pipes, body temperature, exhaling temperature, filtration efficiency, wall temperature and radiator temperature in their temporal development.

The particles are assumed to be solid particles without post-evaporation using a Lagrangian approach similar to fuel injection in a diesel engine. A two way coupling as an interaction between the particles and the flow and vice versa is used. The 10 students and the teacher realistically exhale and inhale (8 times per minute) and emit 3045 particles per second, which perfectly follow the airflow due to their small size of 100 nm. A particle loss by inhalation is not assumed. Each particle path is tracked and thereby any risk of infection can be detected by marking the particles.

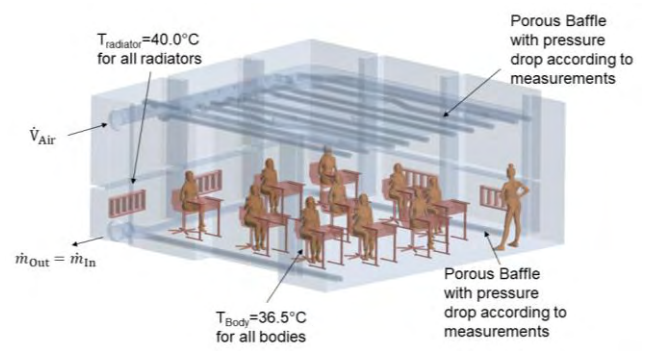

Fig. 15. Digital modelling of the classroom with students and teacher; in the arrangement shown here the flow comes from top to investigate the worst case for virus protection

In the two following illustrations, Fig 16 and Fig 17, it is assumed that the students exhale continuously, and the streamlines starting at the student's mouth and ending at the porous tubes on the ceiling are computed.

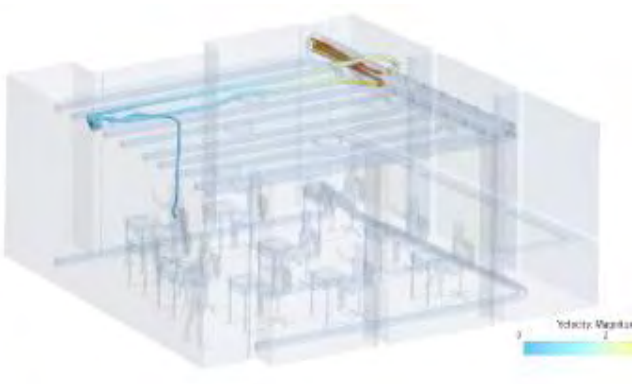

Fig. 16. Ventilation flow from floor to ceiling. Particles are perfectly guided from the infected student to the safe room overhead

This representation is possible for each individual student and also collectively, but then becomes confusing. The protective vertical movement is apparent in all cases, although the current threads form sometimes some unforeseen recirculation zones on the ceiling. These may be suggestions for further optimization of the layout or permeability distribution, which could help to further reduce the flow losses.

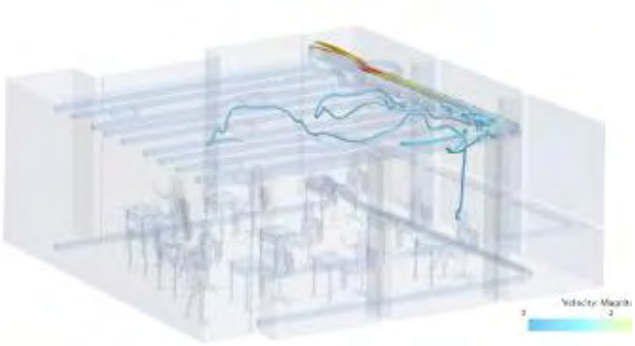

Fig. 17. Same as Fig. 16 but a different student. The virus protection effect is also apparent. Flow pattern is a bit more complex

Suppose we visualize all the particles in the room for a certain time. In that case, we get the following two pictures, where Fig. 18 shows the correct ventilation from bottom to top, Fig. 19 the wrong arrangement with ventilation from top to bottom, which counteracts thermal drift and therefore keeps many more particles in the whole room, although the same amount of air is exchanged and filtered equally efficiently.

One is tempted to consider the total number of particles as a measure of the quality of the process, but this leads to wrong conclusions because the particles collected overhead cannot contribute to the contagion and also cross-contamination is a superimposed local phenomenon.

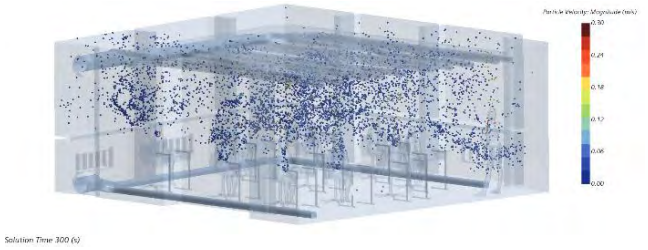

Fig. 18. Flow from floor the ceiling, all students exhaling particles. The lower part of the room stays clean, No cross contamination visible

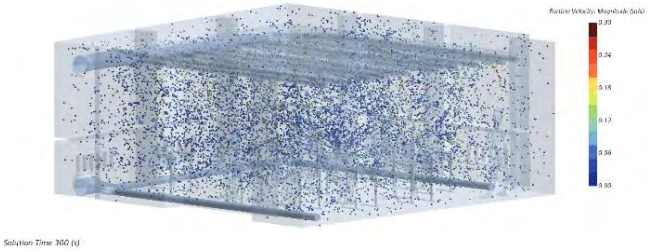

Fig. 19. Ventilation from ceiling to floor against the thermal body heat convection. Heavy cross contamination in the whole room results

It can be investigated by the numeric simulation, whether particles from student X – who may be infected – reach student Y, as was also done in [16, 22] for the contagion ratios in aircraft cabins. The calculation allows to run through this question for all students and to show only the "particle packets" that reach student Y, from each other student and the teacher. In the related overall picture Fig. 18, this "cross-contamination" phenomenon is hardly visible; the numbers in the considered control space are also small in relation to the total number in the space. Finally, Fig. 20 shows the total number of particles in the room during 300 seconds, wherein black represents the ventilation being switched off. In blue, the wrong direction of ventilation from top to bottom is assumed. In red, with the correct ventilation direction from the bottom to the top, a flattening effect quickly appears at low concentration. At the same time, the other two curves will continue to increase over time. For these 300 seconds, the high-performance computer already needs several days. The modeling allows to perform optimizations relatively quickly and agrees reasonably well with the experimental results below.

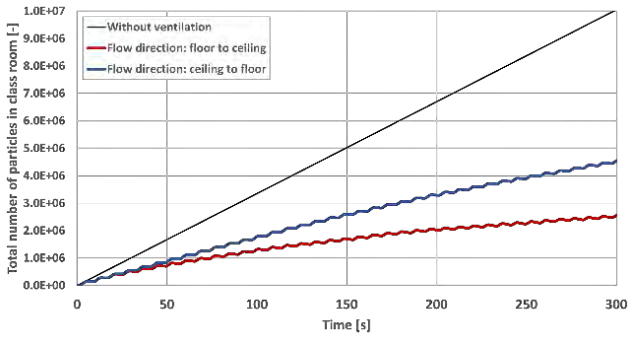

Fig. 20. Total particle number comparing 3 situations: without ventilation (black) ventilation from ceiling (blue) and from floor (red). Calculation for longer time further illustrate the flattening effect

9. Experimental analysis

The most crucial target of the experimental verification of the system functions was the scanning of the entire classroom with respect to nanoparticles released at one point, in order to quantitatively and repeatable verify the risk of infection or the reduction of this risk depending on the control parameters of the system. Since this is not possible in a crowded classroom, the thermal function of the bodies for vertical drift was replaced by adjustable heating plates of appropriate power and temperature (Fig. 21). Instead of a virus source, a nebulizer with a 3% NaCl-solution was placed, which emitted a very regular stream of droplets for 15 minutes (Fig. 22). The water evaporates within fractions of a second, leaving dry salt crystals. Thus, a salt particle cloud of a concentration of about 80,000 particles per cubic centimeter was generated at this location.

Fig. 21. Researcher installs the particle source at one desk, all other desks have particle counters and heated plates to simulate the students

Fig. 22. Nebulizer is used to form a spray of salt solution droplets, drying fast, forming a cloud of 30 nm particles, about 80‘000 per cc

A particle counter was placed on each school desk to measure the particle concentration in the room. The elec-

tronic recording of the signals would provide a synchronous instantaneous picture of the distribution throughout the room in function of time. An optical counter from Sensirion was chosen as the sensor, which, however, only detects particles above 300 nm. The control with a diffusion charging device, which detects all particles above 10 nm, showed that although the Sensirion measurement only counts 1/25 of all particles, this factor remains largely constant so that the relations are detected accurately enough.

Figure 23 is the overall view and shows from these measurements the build-up of particle concentrations as the average value of all 10 sensors in the room over a period of 50 minutes after switching on the salt particle source. The blue curve reflects the case when the ventilation is switched off. The particle concentration in the whole room increases more or less linearly and would continue to increase, so after 2 hours, a concentration of about 4000 P/cc would be reached. In the case of the lower 3 curves, the system is in operation. A plateau is formed after a few minutes, which hardly changes even with a substantial increase in the total number of particles fed in (blue). In the case of green, the fan is running at target speed, in the case of red only at 60%, and in the case of the black curve, the heat sources have been switched on. After a running time of one hour, the entire room has only 10% of the particle concentration that would occur without the system; after two hours, it would be only about 5%, and so on.

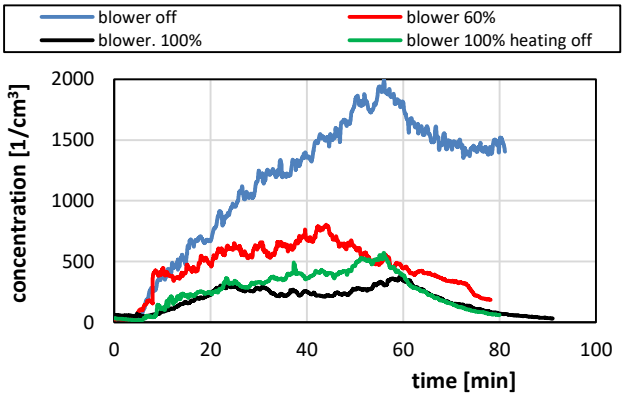

Fig. 23. Development of particle concentration after nebulizer start. Average of all desk counters. Without ventilation (blue), with 60% ventilation (red) with 100% ventilation (green); with body heat in addition (black)

Figure 24 is the single view of the lateral spreading, leading to an infection. Brown is the concentration at the source, repeatedly interrupted by refilling the nebulizer; the other colors show all other sensor locations in the whole room, including the two neighboring tables of the "infected", which are less than one meter away from the source. At first, the extraordinarily uniform distribution in the room is surprising, reaching a level of 2–300 P/cc after only 10 minutes, which hardly seems to change any further. In this case, the fan was running at nominal speed, and the heating plates were switched on, i.e., the case of the lowest curve of Fig. 23. The level of this set of curves is more than two orders of magnitude below the level of the source. The risk of infection is thus reduced by a factor of > 100 even among the immediate neighbors of a potentially infected person.

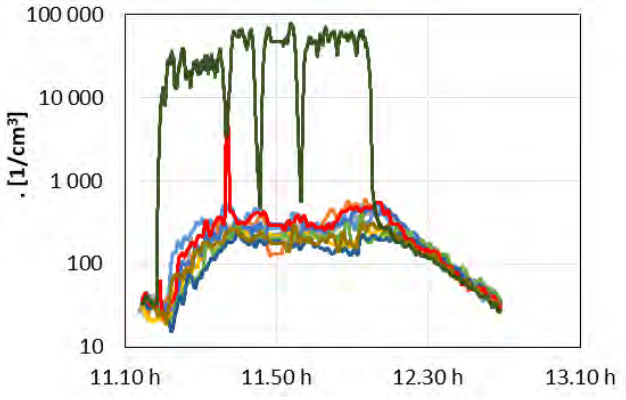

Fig. 24. Cross contamination defined by particle concentration of the source (80,000) compared to number at the desks (2–300), even at the neighbor desks. Distribution over the 10 desks is very uniform. Refill nebulizer four times

10. Conclusions

The use of vertical drift by body heat, combined with laminar ventilation from the floor to the ceiling, extraction of contaminated air from the ceiling, and nanofiltration of contaminated air, makes it possible to sustainably reduce the risk of infection by infectious agents such as corona viruses in closed rooms to a minimum of a few percent. This statement is valid even in case of high occupancy of the rooms, presence of several infected persons, and for a long time. At the same time, the fresh supply air is completely purified from carcinogenic ultrafine dust from traffic, and a CO_2-level is kept at the desired set point of 1000–1200 ppm. This method of leading the contaminated breathing air immediately after exhalation into the safe space "overhead" and removing it from there is not only applicable in buildings but in many other cases. In this way, the risk of virus spread among passengers of commercial airplanes could be virtually eliminated, where today individual ventilation from top to bottom explicitly contributes to a distribution of the viral load.

Acknowledgement

The authors would like to thank all those who contributed to the development of this method: the laboratories of the University of Applied Sciences of Northwestern Switzerland, the AMI-Institute of the University of Fribourg, the Rudolf Steiner Special School in Lenzburg, which made it possible to install the pilot plant in which no corona infections have been observed to date, the FOEN-UTF of the Swiss Federal Office for the Environment for the financial support, the advisory group from several federal offices as well as several private sponsors such as Dr. med. J. Schiltknecht, W. Johann, Dr. J. Mayer and the Swiss Lung Foundation.

Bibliography

[1] Aoyagi Y, Takeuchi M, Yoshida K, Kurouchi M, Yasui N, Kamiko N et al. Inactivation of bacterial viruses in water using deep ultraviolet semiconductor light-emitting diode. J Environ Eng. 2011;137(12):1215-1218. https://doi.org/10.1061/(ASCE)EE.1943-7870.0000442

[2] Bischof OF. Recent developments in the measurement of low particulate emissions from mobile sources: a review of particle number legislations. Emiss Control Sci Technol. 2015;1:203-212. https://doi.org/10.1007/s40825-015-0016-9

[3] Boger T, Glasson T, Rose D, Ingram-Ogunwumi R, Wu H. Next generation gasoline particulate filters for uncatalyzed applications and lowest particulate emissions. SAE Int J Adv & Curr Prac in Mobility. 2021;3(5):2452-2461. https://doi.org/10.4271/2021-01-0584

[4] Brain JD and 200 scientists open letter addressed to WHO; Harvard Public School of Health, 2020.07.06.

[5] Burtscher H, Lutz T, Mayer A. A new periodic technical inspection for particle emissions of vehicles. Emiss Control Sci Technol. 2019;5:279-287. https://doi.org/10.1007/s40825-019-00128-z

[6] Collins KE, Cronin AA, Rueedi J, Pedley S, Joyce E, Humble PJ et al. Fate and transport of bacteriophage in UK aquifers as surrogates for pathogenic viruses. Engineering Geology. 2006;85:33-38. https://doi.org/10.1016/j.enggeo.2005.09.025

[7] Curtius J, Granzin M, Schrod J. Testing mobile air purifiers in a school classroom. Reducig the airborne transmission risk for SARS-CoV-2. Aerosol Sci Tech. 2021;55(5):586-599. https://doi.org/10.1080/02786826.2021.1877257

[8] Drewnick F et al. Abscheideeffizienz von Mund-Nasen-Schutz Masken. Max-Plank-Institut, Mainz 2020.04.30. https://www.mpic.de/4670174/filtermasken_zusammenfassung.pdf

[9] Drossinos Y, Stilianakis NI. What aerosol physics tells us about airborne pathogen transmission, Aerosol Sci Tech. 2020;54(6):639-643. https://doi.org/10.1080/02786826.2020.1751055

[10] Edwards DA, Ausiello D, Salzman J, Devlin T, Langer R, Beddingfield B et al. Exhaled aerosol increases with COVID-19 infection, age and obesity. Biol Sci. 2021;118(8): e2021830118. https://doi.org/10.1073/pnas.202183011

[11] Fernelly KP. Particle sizes of infectious aerosols; implications for infection control. Lancet Respir Med. 2020;8(9):914-924. https://doi.org/10.1016/S2213-2600(20)30323-4

[12] Fuller CH, Brugge D. Ambient combustion ultrafine particles and health. Nova Science Publishers, Inc. New York. ISBN 978-1-53618-831-8.

[13] Handbuch Verbrennungsmotor: Grundlagen, Komponenten, Systeme, Perspektiven. Springer Vieweg Verlag 8. ISBN 978-3-658-10901-1.

[14] Hinds WC. Aerosol Technology: Properties, Behavior, and Measurement of Airborne Particles. John Wiley &Sons 1982, ISBN 0-471-08726-2.

[15] Jing L. Charakterisierung der dieselmotorischen Partikelemissionen. Dissertation der Universität Bern, 1997.

[16] Khanh NC, Thai PQ, Quach HL, Thi NH, Dinh PC, Duong TN et al. Transmission of SARS-CoV 2 during long-haul flight. Emerg Infect Dis. 2020;26(11):2617-2624. https://doi.org/10.3201/eid2611.203299

[17] Klompas M, Baker MA, Rhee C. Airborne transmission of SARS-CoV-2: theoretical considerations and available evidence. JAMA. 2020;324(5):441-442. https://doi.org/10.1001/jama.2020.12458

[18] Lelieveld J, Helleis F, Borrmann S, Cheng Y, Drewnick F, Haug G et al. Model calculations of aerosol transmission and infection risk of COVID-19 in indoor environments. Int J Env Res Pub He. 2020;17(21):8114. https://doi.org/10.3390/ijerph17218114

[19] Lexikon Motorentechnik; A. Mayer zu Partikelfiltern. Verlag Vieweg, ISBN 3-528-03903-5.

[20] Lieber C, Melekidis S, Koch R, Bauer HJ. Insights into the evaporation characteristics of saliva droplets and aerosols: levitation experiments and numerical modeling. J Aerosol Sci. 2021;154:105760. https://doi.org/10.1016/j.jaerosci.2021.105760

[21] Lindsley WG, Derk RC, Coyle JP, Martin SB, Mead KR, Blachere FM et al. Efficacy of portable air cleaners and masking for reducing indoor exposure to simulated exhaled SARS-CoV-2 aerosols. MMWR Morb Mortal Wkly Rep. 2021; 70(27):972-976. https://doi.org/10.15585/mmwr.mm7027e1

[22] Liu J, Huang J, Xiang D. Large SARS-CoV-2 outbreak caused by asymptomatic traveler, China. Emerg Infect Dis. 2020;26(9):2260-2263. https://doi.org/10.3201/eid2609.201798

[23] Marr LC, Tang JW, Mullekom J, Lakdawala SS. Mechanistic insights into the effect of humidity on airborne influenza virus survival, transmission and incidence. J R Soc Interface. 2019; 16(150):201850298. https://doi.org/10.1098/rsif.2018.0298

[24] Miller JH. Experiments in molecular genetics. The Quarterly Review of Biology. 1974;49(2). https://doi.org/10.1086/408025

[25] Morawska L, Cao J. Airborne transmission of SARS-CoV-2: The world should face the reality. Environ Int. 2020;139: 105730. https://doi.org/10.1016/j.envint.2020.105730

[26] NanoCleanAir. www.nanocleanair.ch

[27] Riediker M, Monn C. Simulation of SARS-CoV-2 aerosol emissions in the infected population and resulting airborne exposures in different indoor scenarios; Aerosol Drivers, Impacts and Mitigation. 2021;21(2):20. https://doi.org/10.4209/aaqr.2020.08.0531

[28] Rüggeberg T, Milosevic A, Specht P, Mayer A, Frey J, Petri-Fink A et al. A versatile filter test system to assess removal efficiency for viruses in aerosols. Aerosol Air Qual Res. 2021;21:210224. https://doi.org/10.4209/aaqr.210224

[29] Schmid S, Seiler C, Gerecke AC, Hächler H, Hilbi H, Frey J et al. Studying the fate of non-volatile organic compounds in a commercial plasma air purifier. J Hazard Mater. 2013;256-257:76-83. https://doi.org/10.1016/j.jhazmat.2013.04.021

[30] Silverman DT, Samanic CM, Lubin JH, Blair AE, Stewart PA, Vermeulen R et al. The diesel exhaust in miners study: a nested case-control study of lung cancer and diesel exhaust. J Natl Cancer Inst. 2012;104(11):855-868. https://doi.org/10.1093/jnci/djs034

[31] TSI Incorporated. www.tsi.com

[32] van Doremalen N, Bushmaker T, Morris DH, Holbrook MG, Gamble A, Williamson BN et al. Aerosol and surface stability of SARS-CoV-2. N Engl J Med.2020;382:1564-1567. https://doi.org/10.1056/NEJMc2004973

[33] VERT-Filter List www.vert-certification.eu

[34] Vohra K, Vodonos A, Schwartz J, Marais EA, Sulprizio MP, Mickley LJ. Global mortality from outdoor fine particle pollution generated by fossil fuel combustion: results from GEOS-Chem. Environ Res. 2021;195:110754. https://doi.org/10.1016/j.envres.2021.110754

[35] World Health Organization. https://www.who.int/
[36] Zhang R, Li Y, Zhang AL, Molina MJ. Identifying airborne transmission as the dominant route for the spread of COVID-19. Earth, Atmospheric, and Planetary Sciences. 2020; 117(26):14857-14863. https://doi.org/10.1073/pnas.200963711

Prof. em. Dr. Jan Czerwiński – Nano, NanoCleanAir GmbH, Switzerland.
e-mail: *cjcons19@gmail.com*

Dipl. Ing. Dr. med. h.c. Andreas Mayer – CEO NanoCleanAir GmbH, Switzerland.
e-mail: *a.mayer@nanocleanair.ch*

Dipl. Ing. ETH. Dr. Jörg Mayer – Nano, NanoCleanAir GmbH, Switzerland.
e-mail: *j.mayer@nanocleanair.ch*

Prof. em. Dr. Heinz Burtscher – Institute for Sensors and Electronics, Fachhochschule Nordwestschweiz, Windisch, Switzerland.
e-mail: *h.burtscher@nanocleanair.ch*

Dipl. Ing. ETH Thomas Lutz – Nano, NanoCleanAir GmbH, Switzerland.
e-mail: *t.lutz@nanocleanair.ch*

MSc. BBA Rainer Mayer – Nano, NanoCleanAir GmbH, Switzerland.
e-mail: *r.mayer@nanocleanair.ch*

Prof. Dr. Barbara Rothen-Rutishauser – Adolphe Merkle Institute, University Fribourg, Switzerland.
e-mail: *barbara.rothen@unifr.ch*

Prof. em. Dr. Joachim Frey – Vetsuisse Faculty, University Berne, Switzerland.
e-mail: *joachim.frey@unibe.ch*

Dr. sc. techn., Dipl. Ing. ETH Christian Lämmle – Combustion Flow, Combustion Flow Solutions GmbH, Switzerland.
e-mail: *laemmle@combustion-flow-solutions.ch*

BSc Energy and Environmental Technology (FHNW), Tobias Rüggeberg – Institute for Sensors and Electronics, Fachhochschule Nordwestschweiz, Windisch, Switzerland.
e-mail: *tobias.rueggeberg@fhnw.ch*

Dipl. Ing. Patrick Specht – Institute for Sensors and Electronics, Fachhochschule Nordwestschweiz, Windisch, Switzerland.
e-mail: *patrick.specht@fhnw.ch*

Article citation info:
Trendak M, Czarnigowski J. Influence of oil service life on selected performance parameters of an aircraft piston engine. Combustion Engines. 2023;194(3):78-83. https://doi.org/10.19206/CE-168334

Michał TRENDAK
Jacek CZARNIGOWSKI

Combustion Engines
Polish Scientific Society of Combustion Engines

Influence of oil service life on selected performance parameters of an aircraft piston engine

ARTICLE INFO

Received: 2 June2023
Revised: 14 June 2023
Accepted: 14 June 2023
Available online: 5 July 2023

This article presents an analysis of the influence of oil service life on the performance parameters of an aircraft piston engine lubrication system used in an ultralight aircraft. The ageing of oil between oil changes causes a change in its parameters (such as density, viscosity...). These parameters have a strong influence on the level of protection of the lubricated components. Currently, in aircraft, oil changes are carried out according to a time schedule – oil is changed every fixed period (residual life) regardless of its actual condition. The task of this article is to test the possibility of an indirect assessment of oil condition based on analysis of changes in selected parameters of engine lubrication system operation during normal operation. The oil warm-up speed during the pre-start procedure and the dependence of oil pressure on engine speed were assumed for the analysis. The study was conducted on an ultralight rotorcraft during normal operation. Selected first daily flights directly after oil change, and after 17, 32, 50 and 66 hours of operation were analysed. It was shown that the warm-up rate changes in the samples analyzed, but that this change may also be due to factors other than oil operating time. In the case of the oil pressure vs. speed characteristics, different characteristics were shown for different operating time, but no specific dependencies were found.

Key words: *remaining useful life, engine oil, gyrocopter, gyroplane, exploitation monitoring*

1. Introduction

From the first years of the XXI century, the market of ultralight aircraft mainly gyroplanes, is growing rapidly. On the base of the registry conducted by the Polish Aviation Authority, the number of registered gyroplanes raised from 0 in 2008 [17] up to 105 pcs. in 2022 [15].

These aircraft cover mostly the needs of hobbyists but, since 2013 (the year of the law change in Poland [1]) more and more jobs can be done using this type of aircraft. It is widely used as a platform for power lines or gas pipes scanning. In geodesy [4], it is used to prepare maps and photographs of longitudinal objects. In the agro industry it is used for both biological and chemical crops and forests protection. It is used in the field of surveillance and professional photography. For the last few years, it can be also seen in agro works, in monitoring the state of agrocenosis [5].

According to that, the market for maintenance has grown as well. It can be seen that not all of the owners and operators are careful enough with their aircraft. As safety is the biggest value in aviation, all – the manufacturers, operators, mechanics, owners and pilots are looking for the way how to make it safer. That is why the last decade was the decade of "electronic transformation" in the ultralight aircraft market. Most of the manufacturers moved away from analog avionics in favor of electronic ones. It opened new possibilities for system development. We can now see all kinds of different devices that could be connected to onboard avionics. It is to help the pilot or to modify the aircraft to suit the owner needs. One of these, which can improve safety the most, is a Flight Data Recorder that collects all the data during the flight. It collects air data (e.g. Airspeed) and engine data (e.g. rpm, fuel consumption).

As in modern aircraft Flight Data Recorders are fitted as standard a lot of analysis can be done after or even during every flight. What is common in airlines using QAR [10, 22] (quick access recorder) can be now done in every small aircraft.

It is known from the automotive market [6, 9, 14] that the analysis of the oil degradation based on the record of the engine parameters can be done. Such a system of Remaining Useful Life of engine oil prediction is being onboard of many modern vehicles. The authors of this article think that it is the right time to introduce such a system in ultralight aircraft.

Till now, all of the oil changes were conducted according to total flight/operation time in ultralight aircraft. Most commonly every 100 hours [2, 18]. Such a condition is not optimal in two ways. For the user, it would be best to replace the oil just before the moment that it lubricates the engine not enough, not to lower the expected life time of the engine [8, 21]. It is expected that this point is sometimes earlier than 100 hours – if the pilot uses the aircraft extensively or later if the aircraft is being used gently, e.g. only on long flights with good weather.

The topic of the operation of objects based on condition analysis is widely described in the scientific literature [7, 11, 19, 20, 23]. It has been shown that in the case of internal combustion engines, it is possible to diagnose their condition on the basis of selected parameters of operation, and one of the most important factors determining the operating condition of the engine is the condition of the lubricating oil. These studies have shown a significant link between operating conditions and oil consumption rate. This allows prediction of oil condition degradation in on-board diagnostic systems and, based on this, suggests to the user the moment of oil change. This research work was carried out mainly for engines that powered vehicles or stationary engines. Operating conditions for aircraft engines are sig-

nificantly different, which can significantly affect these correlations.

This article is the first step in developing a method for diagnosing oil condition based on aircraft operating conditions. It will allow assessment of oil condition and prediction its degradation. Authors think that it would be best for the owner of the aircraft and for the environment to replace oil just in the time when it is needed [3, 16].

2. Materials and methods

2.1. Research object

The research object is a Tercel Carbon gyroplane Fig. 1 manufactured by a Polish manufacturer Aviation Artur Trendak. It is an ultralight aircraft made for leisure, professional and training flights. It is a developed version of the Tercel gyrocopter, produced continuously since 2012. The biggest changes compared to the previous model are the change of the supplier of the engine block and the change to a full carbon fiber composite body instead of glass fiber composite.

Fig. 1. Tercel Carbon at flight [12]

Its empty weight is 332 kg, and the MTOW has not changed and is 560 kg. The rest of its performance and technical data is shown in Table 1.

Table 1. Tercel Carbon performance and technical data [2]

Geometric data		
Rotor diameter	8.6	m
Rotor surface	58.06	m^2
Rotor blade chord	0.20	m
Overall length (without rotor)	5.04	m
Fuselage width	2.35	m
Track of wheels	2.20	m
Cockpit width	1.36	m
Overall width	2.35	m
Overall height	2.87	m
Wheel diameter	0.35	m
Weight data		
MTOW	560	kg
Empty weight	332	kg
Load capacity	228	kg
Data of the power unit		
Engine type	AAT 912 RSTi	
Engine power (at 5800 rpm)	140	HP
Reducer ratio	1:2.43	
Propeller	KASPAR AERO 2/3 LT	
Propeller diameter	1.72	m
Capacity of fuel tanks	80	l

2.2. Scope of research

The scope of the research was to analyze the oil temperature and oil pressure records and check if there is any dependence on the total flight time of the gyroplane after the oil change. It was assumed that changes in temperature rise time or differences in the relation between oil temperature and engine rpm could be noticed. The data was collected by the Flight Data Recorder developed by a Polish manufacturer Auto & Aero Technologies Sp. z o.o. It collects 30 different parameters every tenth of a second. The parameters most important for this research are shown in Fig. 2.

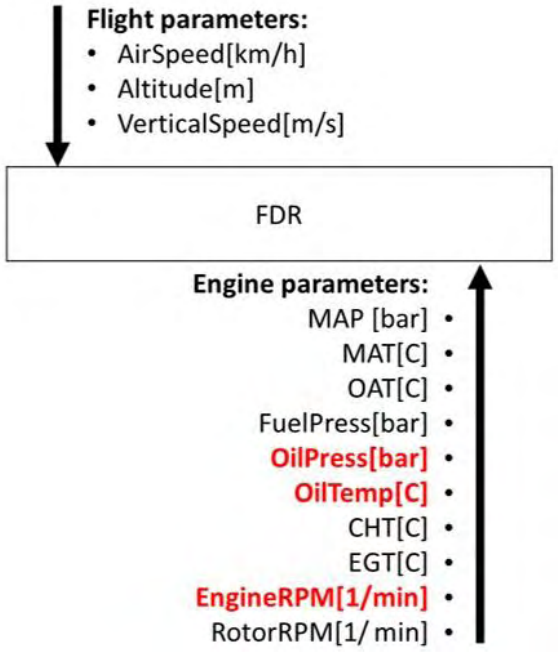

Fig. 2. Parameters collected by Flight Data Recorder

2.3. Methodology

The results were obtained by analyzing data collected from gyroplane's FDR. Data from the time between oil changes was chosen – from 400 to 500 hoobs time (a measure of the total aircraft operation time). The last oil change was done after 400 hours. As a representation for further comparison 5 flights were chosen Table 2.

Table 2. Flights chosen for analysis

	Hoobs time at record start	Duration of operation/flight
1.	405 h 3 min	23 min 25 s
2.	422 h 13 min	19 min 16 s
3.	438 h 34 min	19 min 5 s
4.	455 h 56 min	15 min 28 s
5.	471 h 25 min	10 min 22 s

To determine the changes in the oil parameters, a statistical analysis was performed. The analysis was divided into two parts. The first part was to research in the field of oil temperature rise time. The second part was to research the dependencies between engine rpm and oil pressure. Figure 3 shows the course of these parameters.

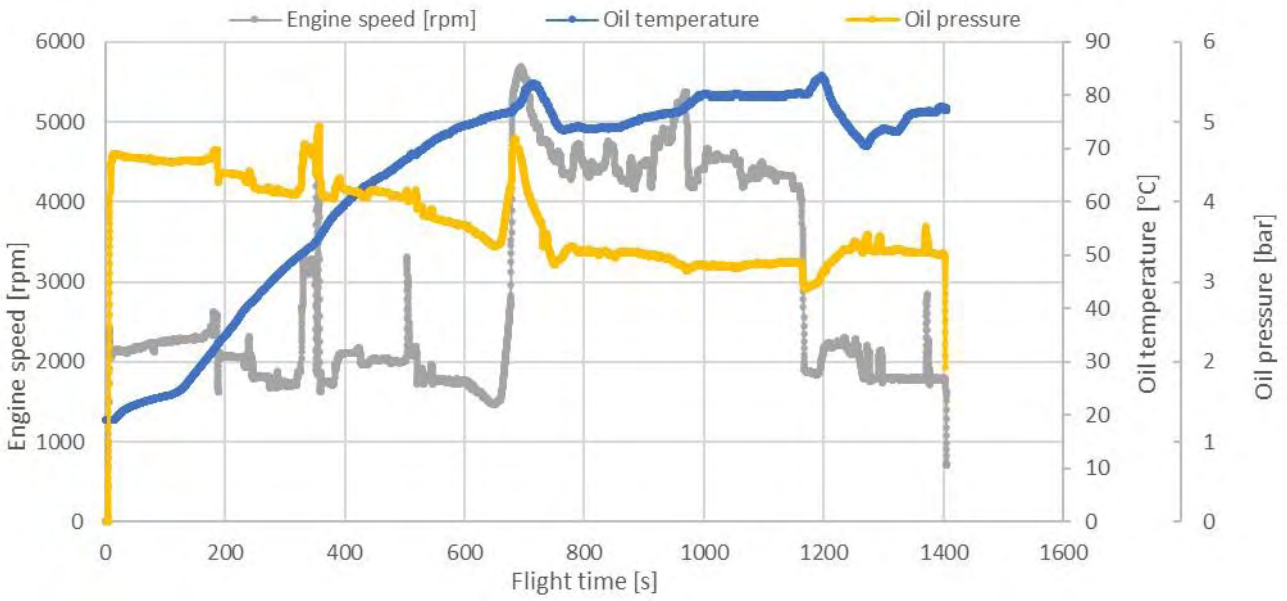

Fig. 3. Course of the parameters from flights at 405.1 hoobs time

3. Analysis of results

3.1. Analysis of oil temperature rise time

The first results were obtained in the scope of oil temperature time rise. Figure 4 shows the oil temperature change during each flight. It can be seen that the starting point depends on the initial temperature – in this case, it is the outside temperature (this was confirmed using another independent sensor – the intake temperature). The slope of the temperature rise up to 60°C can be recognized as similar in every case. Then there is a significant rise in temperature due to the maximum engine rpm achieved at takeoff. Then the temperature decreases and stays at the same average level for the whole flight.

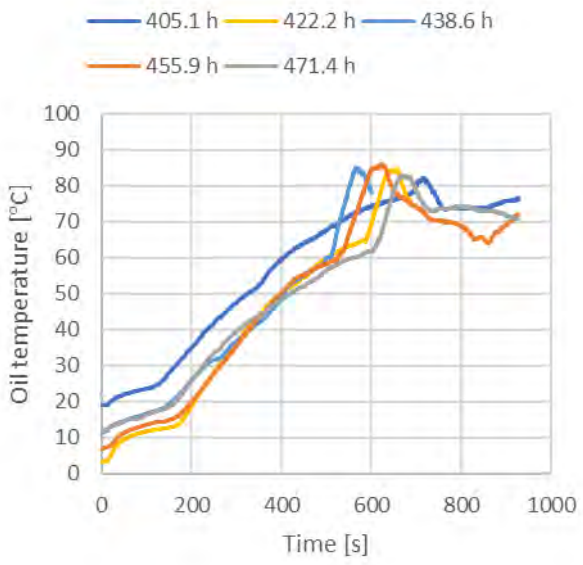

Fig. 4. Oil temperature recorded during every of 5 chosen flights

In the chosen 5 flights oil temperature rise time was measured. Starting from 25°C up to 50°C (minimal temperature needed for operation [2]) – Fig. 5. It can be seen that there are no significant differences between lines in the graph. Every line in the graph starts at 25°C. No characteristic changes with rising hoobs time could be observed. The average temp rise is between 0.112°C/s up to 0.152°C/s.

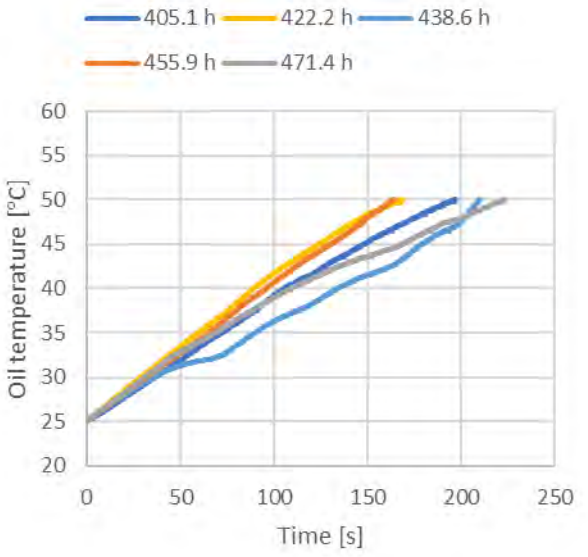

Fig. 5. Oil temperature recorded during every of 5 chosen flights. Rise of oil temperature from 25°C to 50°C

Then the rise time at each flight was shown in the graph Fig. 6. It appears that no significant dependencies could be observed in this field.

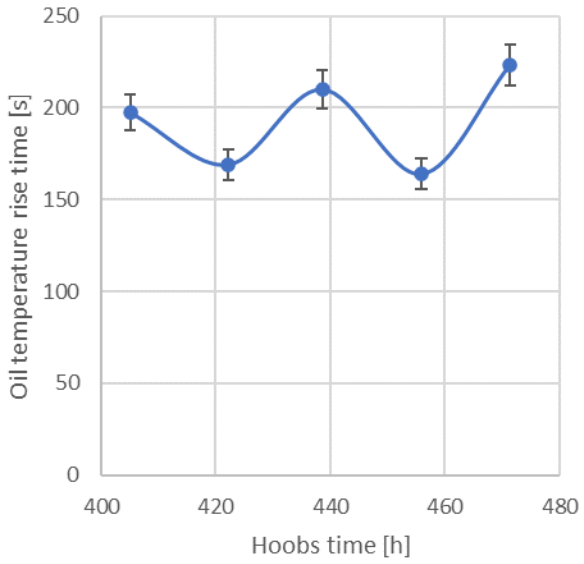

Fig. 6. Oil temperature rise time from 25°C to 50°C

3.2. Analysis of oil pressure record

Many analysis of oil pressure has been performed Fig. 7–9. No dependencies were found when comparing the full record of oil pressure during every flight. Comparing the oil pressures in the state of the rising engine rpm gave no results. This is due to the fact that the distribution of this correlation is heavily affected by the difference in flight parameters (the way the pilot performs the flight). The type and speed of maneuvers significantly affect the dynamics of changes in speed and oil pressure. Thus, it is impossible to draw conclusions from these distributions.

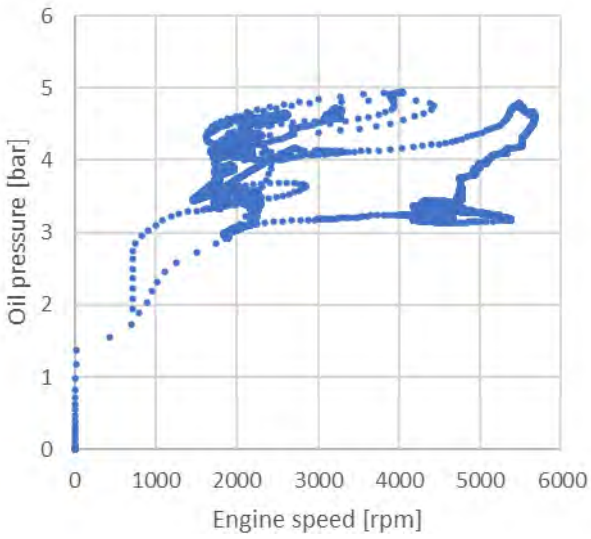

Fig. 7. Oil pressure as a function of engine speed (at 405.1 h)

Therefore, only selected operating points corresponding to steady-state flight and engine operation were analyzed. Figure 10 shows the analysis of the oil pressure in a steady state at about 4300 rpm engine set. With slight variations in engine rpm (±1%) chosen from every flight in the way that it was during a steady flight, not during takeoff, landing, or hard maneuvering. The achieved oil pressures are shown in figure 10. Each record in the graph shows the achieved pressure for a steady engine rpm. Steady states chosen from each flight vary between each other by no more than 10%. There is no upward or downward trend in relation to increasing hoobs time. For 405.1 h hoobs time, the achieved pressure was 3.21 bar at 4419 rpm, then there was 3.52 bar at 4301 rpm and then there was a drop to 3.46 bar at 4195 rpm. After that, there is a drop at 455.9 hoobs time for 3.01 at 4144 rpm, and rise again to 3.19 bar at 4528 rpm after 471.4 h hoobs time. Due to that, no relations could be found in this case.

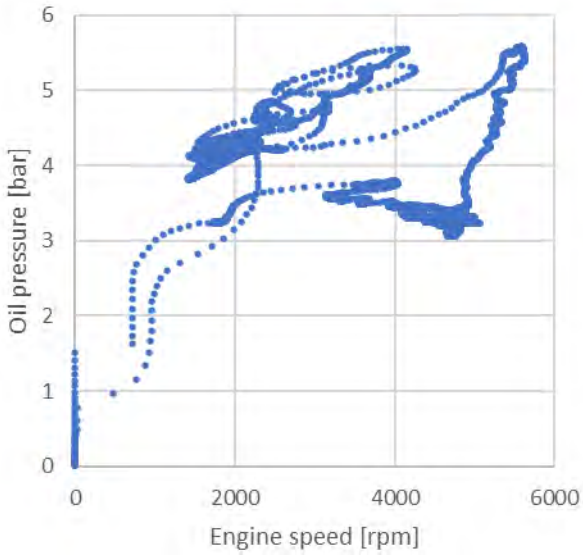

Fig. 8. Oil pressure as a function of engine speed. At 438.6 h

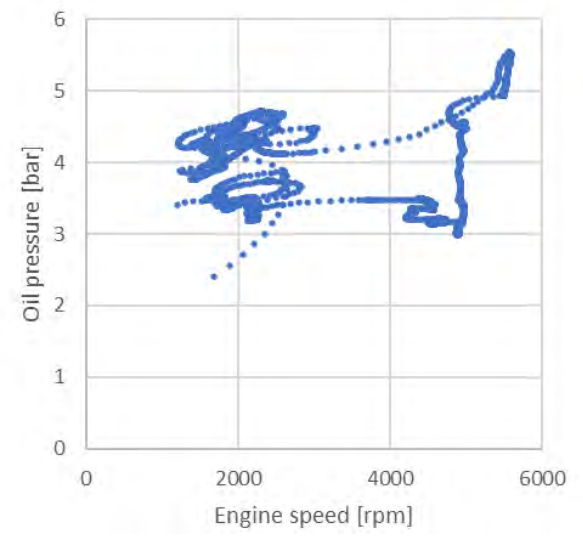

Fig. 9. Oil pressure as a function of engine speed. At 471.4 h

Then another approach was taken. Maximum oil pressure during takeoff at maximum reached rpm was analyzed in Fig. 11. In this case, some dependence could be noticed. Achieved maximum oil pressure during every takeoff raised up to about 5.5 bar. However, in order to recognize this relationship as appropriate, the same analysis should be performed for another aircraft in a similar range of total

flight time. The maximum oil pressure during takeoff is a single point in a record, and it should not be taken as a proof for further inference.

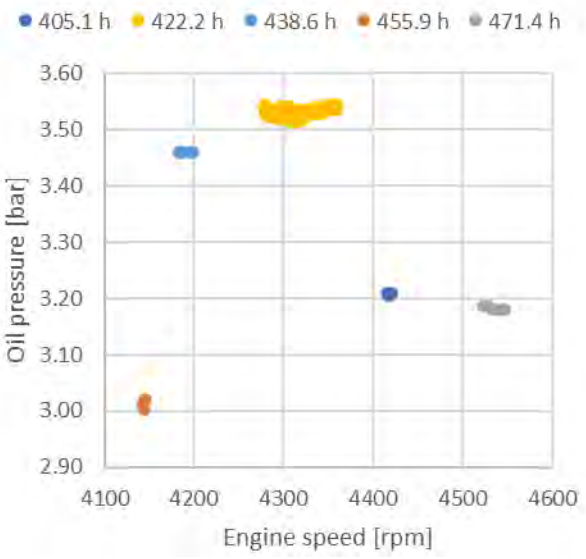

Fig. 10. Oil pressure in a steady state at about 4300 engine rpm set

4. Conclusions

No significant dependencies in the field of this research were found.

1. It is assumed that in the analysis of the oil temperature time rise, outside temperature has a significant impact. Comparing the time rise without taking it in consideration can not give results that could lead to conclusions in the field of oil degeneration.
2. The research in the field of oil pressure shown that the dependence between engine rpm and oil pressure is not changing in any particular way with rising hoobs time. This factor can not be then taken to give any conclusions about oil degeneration as well.
3. In the future, it is planned to conduct research which will take into consideration not only the recorded data but also data obtained during laboratory oil examination [13].
4. The changes in the maximum oil pressure achieved during takeoff have to be checked using records from other aircraft with similar hoobs time.

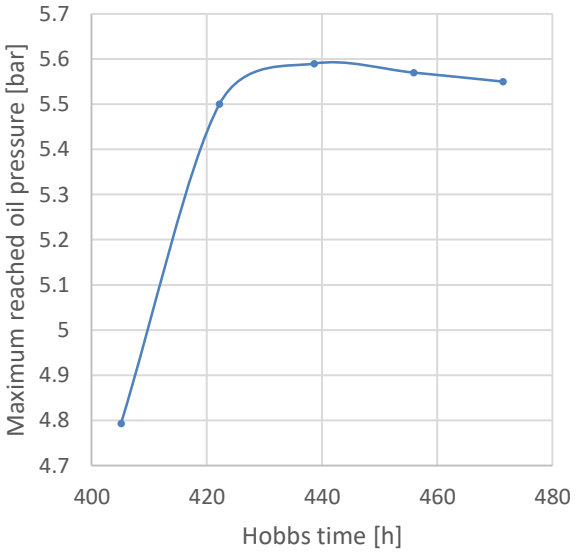

Fig. 11. Maximum oil pressure reached in every chosen flight

Acknowledgements

This work was co-financed under the 6th edition of the Minister's of Education and Science programme entitled "Implementation doctorate".

Nomenclature

CHT	cylinder heat temperature
EGT	exhaust gas temperature
FDR	flight data recorder
MAP	manifold air pressure
MAT	manifold air temperature
MTOW	maximum takeoff weight
OAT	outside air temperature
QAR	quick access recorder

Bibliography

[1] Announcement of the Minister of Infrastructure of July 3, 2019 on the announcement of the consolidated text of the Regulation of the Minister of Transport, Construction and Maritime Economy on the exclusion of the application of certain provisions of the Aviation Law to certain types of aircraft and the determination of the conditions and requirements for the use of these aircraft. (Dz.U. 2019 poz. 1497).

[2] AVIATION ARTUR TRENDAK "Tercel Carbon RSTi Aircraft Maintenance Manual" Tercel-C-AMM-001-EN Edition 1, 28 Oct. 2020.

[3] Balicki W. Przetwarzanie informacji zapisanych w rejestratorze eksploatacyjnym dla celów diagnozowania stanu lotniczego silnika turbinowego, Transactions of the Institute of Aviation. 2011;213:235-244.

[4] Bareth G, Waldhoff G. 2.01 – GIS for mapping vegetation, Comprehensive Geographic Information Systems. 2018:1-27. https://doi.org/10.1016/B978-0-12-409548-9.09636-6

[5] Bzowska-Bakalarz M, Bieganowski A, Bereś P, Dammer KH, Ostroga K, Siekaniec Ł et al. Monitoring the state of agrocenosis with the use of remote-sensing gyro system. IX International Scientific Symposium "Farm machinery and prcesses managment in sustainable agriculture". 2017:64-69. Lublin 22-24.11.2017. https://doi.org/10.24326/fmpmsa.2017.12

[6] Czarnigowski JA, Rękas D, Ścisłowski K, Trendak M, Skiba K. Analysis of operating parameters of the aircraft piston engine in real operating conditions. Combustion Engines. 2021;187(4):83-89. https://doi.org/10.19206/CE-141890

[7] Gajewski J, Vališ D. The determination of combustion engine condition and reliability using oil analysis by MLP and RBF neural networks, Tribol Int. 2017;115:557-572. https://doi.org/10.1016/j.triboint.2017.06.032.

[8] Gołębiowski W, Wolak A, Zając G. Definition of oil change intervals based on the analysis of selected physicochemical

properties of used engine oils. Combustion Engines. 2018;172(1):44-50. https://doi.org/10.19206/CE-2018-105
[9] Jun HB, Kiritsis D, Gambera M, Xirouchakis P. Predictive algorithm to determine the suitable time to change automotive engine oil. Comput Ind Eng. 2006;51(4):671-683. https://doi.org/10.1016/j.cie.2006.06.017
[10] Lewitowicz J. Podstawy eksploatacji statków powietrznych, tom 4. Badania eksploatacyjne statków powietrznych. Wydawnictwo Instytutu Technicznego Wojsk Lotniczych. Warszawa 2008.
[11] Macián V, Tormos B, Olmeda P, Montoro L. Analytical approach to wear rate determination for internal combustion engine condition monitoring based on oil analysis. Tribol Int. 2003;36(10):771-776. https://doi.org/10.1016/S0301-679X(03)00060-4.
[12] Picture of Tercel Carbon provided on demand by Aviation Artur Trendak company.
[13] Piec P. Diagnostics of the wear intensity of engine oil during operation. Tribology. 2012;6:139-145.
[14] Raposo H, Farinha J, Fonseca I, Ferreira L. Condition monitoring with prediction based on diesel engine oil analysis: a case study for urban buses. Actuators. 2019;8(1):14. https://doi.org/10.3390/act8010014
[15] Registry of ultralight gyrocopters. Civil Aviation Authority of the Republic of Poland (accessed 08.04.2022).
[16] Rostek E, Babiak M, Wróblewski E. The influence of oil pressure in the engine lubrication system on friction losses. Procedia Engineer. 2017;192:771-776. https://doi.org/10.1016/j.proeng.2017.06.133
[17] Szczepanik T. Analysis of the state of the gyroplane world market. Transactions of the Institute of Aviation 2016;244(3): 227-238.
[18] Szczepanik T, Łusiak T. The maintenance gyroplanes as aircraft. Transactions of the Institute of Aviation. 2015; 241(4):87-95. https://doi.org/10.5604/05096669.1202197
[19] Wang W. A prognosis model for wear prediction based on oil-based monitoring. J Oper Res Soc. 2007;58(7):887-893. https://doi.org/10.1057/palgrave.jors.2602185
[20] Wang W, Zhang W. A model to predict the residual life of aircraft engines based upon oil analysis data. Nav Res Log. 2005;52:276-284. https://doi.org/10.1002/nav.20072
[21] Wolak A, Zając G, Żółty M. Changes of properties of engine oils diluted with diesel oil under real operating conditions. Combustion Engines. 2018;173(2):34-40. https://doi.org/10.19206/CE-2018-206
[22] Zhang C, Wang N. Aero-engine condition monitoring based on support vector machine. Physcs Proc. 2012;24(B):1546-1552. https://doi.org/10.1016/j.phpro.2012.02.228
[23] Zhu X, Zhong C, Zhe J. Lubricating oil conditioning sensors for online machine health monitoring – a review. Tribol Int. 2017;109:473-484. https://doi.org/10.1016/j.triboint.2017.01.015

Michał Trendak, MEng. – Faculty of Mechanical Engineering, Lublin University of Technology, Poland.
e-mail: *michal@trendak.eu*

Jacek Czarnigowski, DSc., DEng. – Faculty of Mechanical Engineering, Lublin University of Technology, Poland.
e-mail: *j.czarnigowski@pollub.pl*

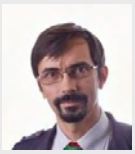

Article citation info:
Rymaniak Ł, Wisniewski S, Woźniak K, Frankowski M. Evaluation of pollutant emissions from a railbus in real operating conditions during transport work. Combustion Engines. 2023;194(3):84-88. https://doi.org/10.19206/CE-169138

Łukasz RYMANIAK
Sławomir WISNIEWSKI
Krystian WOŹNIAK
Maciej FRANKOWSKI

Combustion Engines
Polish Scientific Society of Combustion Engines

Evaluation of pollutant emissions from a railbus in real operating conditions during transport work

ARTICLE INFO

Received: 13 April 2023
Revised: 28 June 2023
Accepted: 1 July 2023
Available online: 21 July 2023

The article discusses issues related to the assessment of pollutant emissions from a railbus during transport work. The test object was a rail vehicle equipped with two diesel engines with a total power of 780 kW, Stage IIIB homologated. Measurements were carried out on the route Poznań–Wągrowiec in two directions. During the tests, the vehicle performed a transport service, where the number of passengers was counted. For the completed cycles, the average number of people was 82 and 18. Based on the obtained data, the vehicle operating conditions and emission indicators were analyzed, which were related to the number of passengers. A dimensionless toxicity index was also determined.

Key words: *emissions, passenger, PEMS, railbus, toxicity indicator*

1. Introduction

In Poland, 342.23 million passengers traveled by rail vehicles in 2022, and the transport performance amounted to 15,882.97 million pkm [22]. Taking into account the data presented by the UTK (Office of Rail Transport), a systematic increase in the above-mentioned values has been visible since 2012. Following the policy of the European Union, actions are being implemented aimed at introducing ecological drives in means of transport. One of such solutions is hybridization or electrification [2, 11, 12], provided that energy is obtained from ecological sources. In recent years, the rolling stock used for passenger transport has seen an increase in the share and development of electric multiple units [4]. There is still a long way to go before complete electrification.

Due to the significant use of passenger vehicles (including railbuses) equipped with internal combustion engines, it becomes necessary to conduct research and considerations regarding their exact impact on the natural environment. This can significantly affect strategic activities related to the development and modernization of infrastructure, as well as the organization of business activities. At the same time, the assessment of emissions from moving vehicles contributes to a deeper understanding of the problem of knowing the local values of air pollution.

For engine rail vehicles, approval tests in the ecological scope are still valid, only on the engine dynamometer. Stand measurements are to simulate the conditions of real engine operation to some extent, but they are far from the actual parameters of their use. This has been proven in many scientific works for various types of vehicles [1, 17]. As presented in publications [5, 8], to obtain reliable ecological indicators for specific machines and vehicles, it is necessary to perform tests in real operating conditions. Preferably while performing normal machine tasks.

The development of technology and test equipment used for the approval and testing of various types of vehicles (including off-road vehicles) made it possible to test vehicle emissions in real operating conditions. This mainly applies to PC (Passenger Car) and HDV (Heavy Duty Vehicles). In recent years, activities have also been carried out for other types of vehicles, primarily belonging to the NRMM (Non Road Mobile Machinery) group [3, 6, 9, 19]. This is possible, among others, by reducing the size of the measuring equipment and reducing its energy consumption [7, 13, 16, 18]. Such devices belong to the PEMS group (Portable Emission Measurement System).

The aim of the work was to determine and compare the operating parameters of the research facility in two tests and to determine ecological indicators in relation to CO_2 and the average number of traveling passengers. The article presents real research that can complement theoretical considerations and modeling of pollutant emissions [10, 15].

2. Research methodology

The assessment of ecological parameters was carried out on a standard-gauge railbus used for passenger transport in Wielkopolska (Fig. 1). Its construction allows for the simultaneous transport of 246 people. The length of the vehicle is 43.73 m, and the total weight of the object ready to drive is 89,000 kg.

Fig. 1. The research object before the start of measurements at the Poznań Główny station

The research object uses two twin compression ignition engines (Table 1). Each of them is turbocharged, has a displacement of 12.8 dm^3 and develops a power of 390

kW at 1800 rpm and a maximum torque of 2200 Nm at 1300 rpm. The engines were homologated according to the Stage IIIB standard, so they were controlled by the NRSC (Non Road Stationary Cycle) and NRTC (Non Road Transient Cycle) tests.

Table 1. Technical data of the powertrain used in the research object

Parameter	Value
Powertrain	2 × CI engines
Layout/number of cylinders	R 6
Displacement volume [dm^3]	12.8
N_{max} [kW] at engine speed [rpm]	390 at 1800
T_{max} [Nm] at engine speed [rpm]	2200 at 1300
Exhaust emission standard	Stage IIIB

In the research work, mobile equipment was used to measure the concentration of harmful compounds from the PEMS group: Axion R/S+. NDIR (Nondispersive Infrared) sensors are used to measure HC, CO and CO_2, E-chem sensors are used to measure NO and O_2, while PM concentration is determined using the Laser Scatter method [20]. The device is characterized by significant miniaturization concerning devices from the PEMS group offered by other manufacturers. It is used e.g. by EPA (Environmental Protection Agency) in the certification process. Information on engine operating parameters and flows in the exhaust system was recorded from the on-board diagnostic system using the Texa Navigator device. The measurement and data acquisition was performed with a frequency of 1 Hz. Based on the recorded data, corrections of the obtained results are made and the road/unit emission of the pollutants tested is calculated.

The tests of the object were carried out on the same route during trips in two directions: Poznań–Wągrowiec (cycle A) and Wągrowiec–Poznań (cycle B, Fig. 2). The total length of individual runs was 56.7 km. The relative height profile varied from 61 to 100 m above sea level, the average slope was 0.7% towards Wągrowiec. In each passage, the rail vehicle served 18 railway stations.

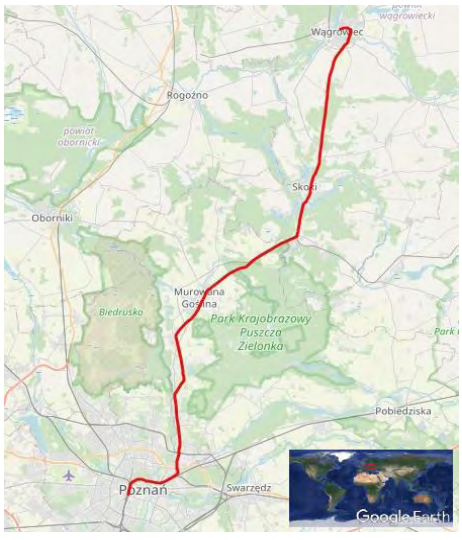

Fig. 2. Research route [21]

The measurements were carried out in real operation, during normal transport service. During the measurements, the number of travelers was acquired based on inspected tickets. In this way, the number of passengers for the Poznań–Wągrowiec route was defined, which was 82. In the second cycle, the value was 18 passengers.

3. Vehicle operating conditions during testing

The tested rail vehicle carried out transport work in real operating conditions. The conditions of its operation are shown in Fig. 3. In both measurement cycles, the object achieved temporary maximum speeds of up to 120 km/h (this is the maximum speed according to the manufacturer). The average speeds were similar and amounted to 43.9 km/h for cycle A and 40.5 km/h for cycle B. Due to the scheduled traffic on the tracks, there was a stoppage of several minutes in each cycle (other rail vehicles were allowed to pass).

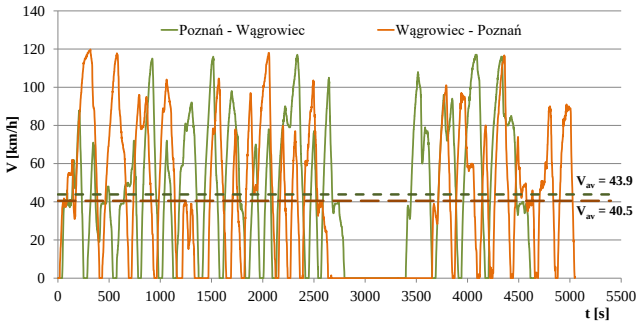

Fig. 3. Velocity characteristics of the research object in cycles A and B

The shares of the working time of the research object in the ranges of speed and acceleration only in cycle A are presented (Fig. 4). This was due to the similar nature of the journeys on the same route in two directions. The largest share of working time, 26.6%, was obtained for standstill. For driving at constant speed (a = 0 m/s^2) 19.4% was achieved. The highest shares of accelerations were obtained for the ranges (0 m/s^2; 0.8 m/s^2⟩ – 28.7% and ⟨–0.8 m/s^2; 0 m/s^2) – 17.8%. In the other acceleration ranges, the share for single speed ranges was less than 1%.

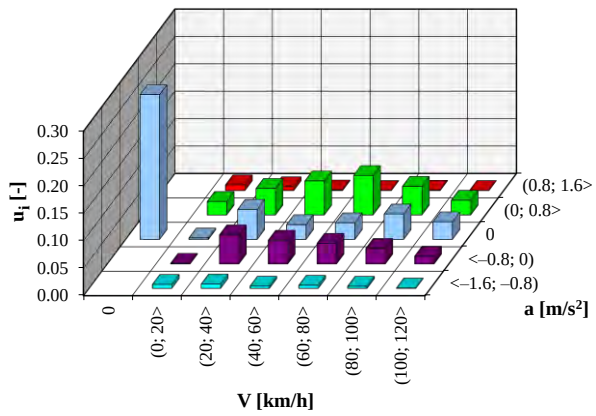

Fig. 4. Shares of research object work time in the speed and acceleration ranges during tests in cycle A

The shares of working time in the speed and acceleration ranges recorded during the tests in cycles A and B were compared (Fig. 5).

This was a supplement to the analyzes of vehicle operation conditions. The characteristics show the differences between route A (minuend) and route B (subtrahend). The size of the circles refers to the obtained difference, for positive values they are full, while for negative results they have not been filled in. This allowed to indicate how the characteristics obtained in subsequent cycles differ.

The greatest differences occurred during standstill 4.69% and driving at constant speed, e.g. in the range (20 km/h; 40 km/h⟩, where 4.04% was obtained. For the considered accelerations and decelerations ($a \neq 0$ m/s^2) in the individual speed ranges, the differences were less than 1% (excluding one point for $V \in$ (80 km/h; 100 km/h⟩). The obtained results prove that the trips were similar, especially in terms of driving style. Therefore, the parameter of a different mode of operation in individual cycles is excluded.

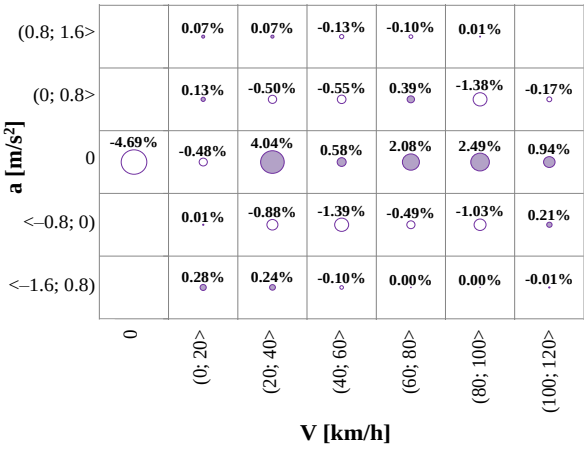

Fig. 5. The difference in the share of the research object's working time during measurements in the speed and acceleration ranges

4. Analysis of test results

Based on recorded data on the vehicle operating conditions and the concentrations of chemical compounds in the exhaust system, the emission intensity of individual harmful compounds was determined. On this basis, it was possible to integrate CO_2 emissions during the implementation of cycles A and B (Fig. 6).

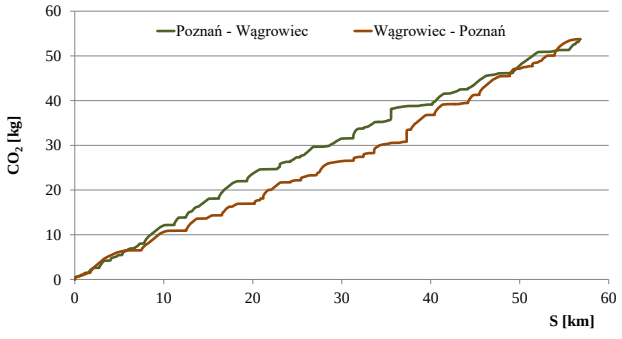

Fig. 6. Total CO_2 emissions during tests in cycles A (Poznań–Wągrowiec) and B (Wągrowiec–Poznań)

The presented characteristics about the speed of the vehicle indicate that the greatest increase of the considered harmful compound occurs during acceleration. Due to the implementation of the same driving style by the driver and driving on the same route, very similar results of the total CO_2 emissions were obtained. It was 53.5 kg for the A cycle and 56.8 kg for the B cycle. The cumulative emissions from two internal combustion engines downstream of the after-treatment systems were taken into account.

Taking into account all the analyzed harmful components, the road emission in cycles A and B was determined (Fig. 7). The obtained results indicate that similar values were achieved during the measurements, the largest differences occurred for CO – respectively 6.46 g/km (cycle A) and 5.22 g/km (cycle B). For CO_2 and NO_x, the determined values differ by less than 1%. Specific emissions are used to assess rail vehicles, but for the purposes of the article reference was made to the cited indicators. It also did not affect the determination of toxicity indicators presented in the further part of the paper.

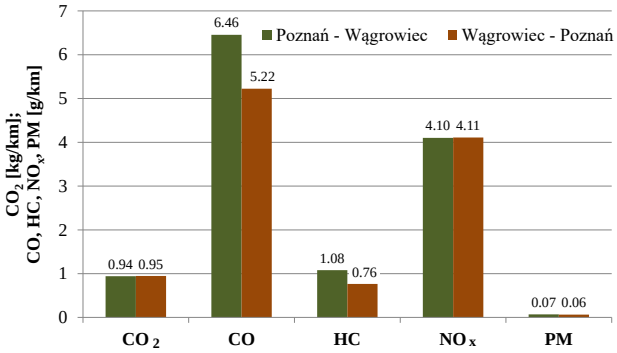

Fig. 7. Summary of road emissions during tests in cycles A (Poznań–Wągrowiec) and B (Wągrowiec–Poznań)

Based on the collected data, fuel consumption was determined using the carbon balance method. Road emission of CO_2 has the greatest impact on the results of calculations, because it has the largest mass in harmful gases. Therefore, fuel consumption reached similar values: 35.49 dm^3/100 km was obtained in cycle A and 35.57 dm^3/100 km in cycle B.

Comparing road emission or unit emission indicators for different groups of vehicles can be difficult. This is related to the nature of the work of the facility and its intended use. This is especially true for the NRMM vehicle group. The basic combustion product in engines is CO_2. Its weight is directly related to fuel consumption, but also to the quality of the combustion process and the operation of engine exhaust gas treatment systems.

Toxic compounds such as CO, HC, NO_x or PM are products of incomplete or imperfect combustion and combustion at high temperature and pressure. It is therefore possible to compare CO_2 emission to other emitted toxic compounds and on this basis to determine the toxicity indicator M_j. Index j means the toxic compound to which it relates [14]. The structure of the M_j indicator allows for dimensionless expression of values, described e.g. in [14]. Its structure is as follows:

$$M_j = b \cdot \frac{e_{real,j}}{e_{CO_2}} \quad (1)$$

The universal constant b makes it possible to reduce the results to a range of quantities greater than hundredths or thousandths (CO, HC, NO_x = 10^3, PM = 10^5). Whereas the $e_{real,}$j and e_{CO2} components mean the specific emission, road emission or mass of the compound j determined during the tests [g/kWh; g/km; g]. The numerator and denominator units must always be the same. According to the recommendations of the European Commission, such an indicator should be introduced into the emission assessment of vehicles and work should be conducted on its recognition.

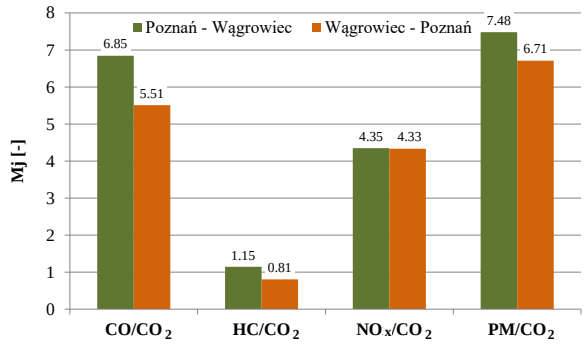

Fig. 8. Summary of dimensionless toxicity indicators during tests in cycles A (Poznań–Wągrowiec) and B (Wągrowiec–Poznań)

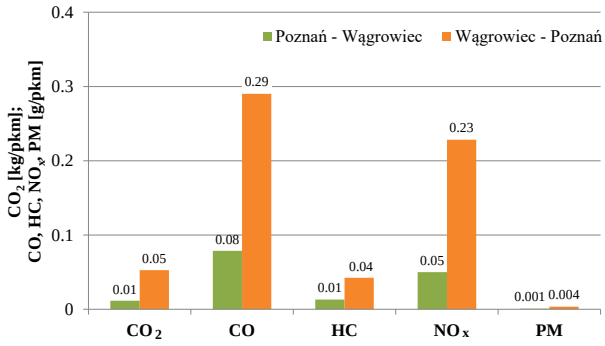

Fig. 9. Summary of road emissions per passenger during tests in cycles A (Poznań–Wągrowiec) and B (Wągrowiec–Poznań)

Values ranging from 0.81 to 7.48 were obtained for the defined dimensionless toxicity indicators (Fig. 8). The highest indices were obtained for CO and PM. This means that greater efforts must be made to reduce emissions of this compound, e.g. by improving fuel atomization during injection, changing the fuel injection strategy, or improving off-engine exhaust aftertreatment systems. Based on the data collected in work [14], it can be concluded that the obtained indicators are the closest to those of a small passenger car equipped with a petrol engine (CO and HC). However, in the NO_x range, the greatest similarity was obtained to an off-road vehicle with a CI engine.

The last stage of the evaluation of pollutant emission results is to compare them per 1 passenger (Fig. 9). The most favorable values were obtained for cycle A, where a larger number of passengers traveled.

Based on such a shape of the results, it can be concluded that the mass of the traveling passengers has little impact on the emission of toxic compounds during transport work. Assuming that each passenger weighs 70 kg (there were also children on board), the difference in subsequent cycles was about 4500 kg. This accounted for 5% of the total weight of the facility ready for service.

5. Summary

The assessment of the real emission of pollutants from vehicles is very important for the implementation of remedial actions in the field of environmental degradation. In rail vehicles used for passenger transport, more and more new solutions in drive systems are used – engines with newer emission standards, electrification, as well as the introduction of hydrogen structures. However, a significant group of about 25% is still combustion engines traction units.

The article presents the results of pollutant emission tests from a rail vehicle in real operating conditions. Tests carried out on the same route in two directions, show very similar results. However, during the implementation of individual cycles, a different number of passengers traveled. Calculated per person, it was proven that the emissions are much lower in the A cycle. This was mainly due to the low weight of these passengers in relation to the total weight of the vehicle.

The obtained values of toxicity indicators M prove the validity of its use to assess vehicles with internal combustion engines. It makes it possible to compare various groups of vehicles, regardless of the type of emissions taken into account for the calculations. In the next stage of scientific work, it is expected that rail vehicles of other emission standards will be subjected to the emission assessment, rather than greater diversification of the load using the principles of ecodriving.

Acknowledgements

The research was funded by European Union from European Regional Development Fund through the National Centre for Research and Development (Narodowe Centrum Badań i Rozwoju) – research project within the Smart Growth Programme (contract No. POIR.04.01.02-00-0002/18).

Nomenclature

a	acceleration
CI	compression ignition
EPA	Environmental Protection Agency
HDV	heavy duty vehicles
M	toxicity indicator
NDIR	nondispersive infrared
NRMM	Non Road Mobile Machinery
NRSC	Non Road Stationary Cycle
NRTC	Non Road Transient Cycle
PC	passenger cars
PEMS	Portable Emission Measurement System
V	velocity

Bibliography

[1] Bodisco T, Zare A. Practicalities and driving dynamics of a real driving emissions (RDE) Euro 6 regulation homologation test. Energies. 2019;12(12):2306. https://doi.org/10.3390/en12122306

[2] Cieslik W, Szwajca F, Zawartowski J, Pietrzak K, Rosolski S, Szkarlat K et al. Capabilities of nearly zero energy building (NZEB) electricity generation to charge electric vehicle (EV) operating in real driving conditions (RDC). Energies. 2021;14(22):7591. https://doi.org/10.3390/en14227591

[3] Daszkiewicz P, Andrzejewski M, Urbański P, Woch A, Stefańska N. Analysis of the exhaust emissions of toxic compounds from a special purpose rail machine PŁT-500 during profiling the ballast cess. Journal of Ecological Engineering. 2021;22(7):80-88. https://doi.org/10.12911/22998993/139214

[4] Far M, Gallas D, Urbański P, Woch A, Mieżowiec K. Modern combustion-electric PowerPack drive system design solutions for a hybrid two-unit rail vehicle. Combustion Engines. 2022;190(3):80-87. https://doi.org/10.19206/CE-144724

[5] Fu M, Ge Y, Tan J, Zeng T, Liang B. Characteristics of typical non-road machinery emissions in China by using portable emission measurement system. Sci Total Environ. 2012;437:255-61. https://doi.org/10.1016/j.scitotenv.2012.07.095

[6] Kamińska M, Kołodziejek D, Szymlet N, Fuć P, Grzeszczyk R. Measurement of rail vehicles exhaust emissions. Combustion Engines. 2022;61(2). https://doi.org/10.19206/CE-142526

[7] Kim MK, Park D, Kim M, Heo J, Park S, Chong H. A study on characteristic emission factors of exhaust gas from diesel locomotives. Int J Environ Res Pub He. 2020;17(11):3788. https://doi.org/10.3390/ijerph17113788

[8] Merkisz J, Fuc P. The exhaust emission from light duty vehicles in road test in urban traffic. SAE Int J Fuels Lubr. 2010;3(2):467-475. https://doi.org/10.4271/2010-01-1558

[9] Merkisz J, Lijewski P, Fuc P, Siedlecki M, Weymann S. The use of the PEMS equipment for the assessment of farm fieldwork energy consumption. Appl Eng Agric. 2015;31(6): 875-879. https://doi.org/10.13031/aea.31.11225

[10] Murakami K, Haga I, Nakamura H, Maehashi S, Yamashita O. Development of a system to calculate energy consumed by diesel railcars. Quarterly Report of RTRI. 2009;50(2):76-80. https://doi.org/10.2219/rtriqr.50.76

[11] Pielecha I, Pielecha J. Simulation analysis of electric vehicles energy consumption in driving tests. Eksploat Niezawodn. 2020;22(1):130-137. https://doi.org/10.17531/ein.2020.1.15

[12] Pielecha I. Control algorithms for a Range Extender vehicle with an combustion engine. Combustion Engines. 2020; 183(4):3-10. https://doi.org/10.19206/CE-2020-401

[13] Rymaniak Ł, Kamińska M, Szymlet N, Grzeszczyk R. Analysis of harmful exhaust gas concentrations in cloud behind a vehicle with a spark ignition engine. Energies. 2021; 14(6):1769. https://doi.org/10.3390/en14061769

[14] Rymaniak Ł, Ziętara B, Szymlet N, Kołodziejek D. Use of toxicity indexes in reference to carbon dioxide for a vehicle equipped with a two-stroke engine without an exhaust aftertreatment system. Journal of Ecological Engineering. 2023; 24(4):228-236. https://doi.org/10.12911/22998993/159721

[15] Shang B, Zhang X. Study of emission reduction: Benefits of urban rail transit. Procedia-Social and Behavioral Sciences. 2013;96:557-564. https://doi.org/10.1016/j.sbspro.2013.08.065

[16] Szymlet N, Lijewski P, Kurc B. Road tests of a two-wheeled vehicle with the use of various urban road infrastructure solutions. Journal of Ecological Engineering. 2020;21(7):152-159. https://doi.org/10.12911/22998993/125503

[17] Szymlet N, Lijewski P, Sokolnicka B, Siedlecki M, Domowicz A. Analysis of research method, results and regulations regarding the exhaust emissions from two-wheeled vehicles under actual operating conditions. Journal of Ecological Engineering. 2020;21(1):128-139. https://doi.org/10.12911/22998993/113077

[18] Vojtisek-Lom M, Jirků J, Pechout M. Real-world exhaust emissions of diesel locomotives and motorized railcars during scheduled passenger train runs on Czech railroads. Atmosphere. 2020;11(6):582. https://doi.org/10.3390/atmos11060582

[19] Warguła Ł, Kukla M, Lijewski P, Dobrzyński M, Markiewicz F. Impact of compressed natural gas (CNG) fuel systems in small engine wood chippers on exhaust emissions and fuel consumption. Energies. 2020;13(24):6709. https://doi.org/10.3390/en13246709

[20] https://www.globalmrv.com/axion-rs-2/ (accessed on 03.2023).

[21] https://www.gpsvisualizer.com (accessed on 03.2023).

[22] https://dane.utk.gov.pl/sts/ (accessed on 03.2023).

Prof. Łukasz Rymaniak, DSc., DEng. – Faculty of Civil and Transport Engineering, Poznan University of Technology, Poland.
e-mail: *lukasz.rymaniak@put.poznan.pl*

Sławomir Wiśniewski, MEng. – Doctoral School of Poznan University of Technology, Faculty of Civil and Transport Engineering, Poland.
e-mail:
slawomir.wisniewski@doctorate.put.poznan.pl

Krystian Woźniak, MEng. – Doctoral School of Poznan University of Technology, Faculty of Civil and Transport Engineering, Poland.
e-mail: *krystian.wozniak@doctorate.put.poznan.pl*

Maciej Frankowski, MEng. – Doctoral School of Poznan University of Technology, Faculty of Civil and Transport Engineering, Poland.
e-mail: *maciej.frankowski@doctorate.put.poznan.pl*

Article citation info:
Fuć P, Sokolnicka-Popis B, Ziółkowski A, Bednarek M, Jagielski A, Michałowska A. Technology for manufacturing catalytic systems using a pilot line for precious metal recovery. Combustion Engines. 2023;194(3):89-96. https://doi.org/10.19206/CE-169332

Paweł FUĆ
Barbara SOKOLNICKA-POPIS
Andrzej ZIÓŁKOWSKI
Maciej BEDNAREK
Aleks JAGIELSKI
Anna MICHAŁOWSKA

Combustion Engines
Polish Scientific Society of Combustion Engines

Technology for manufacturing catalytic systems using a pilot line for precious metal recovery

ARTICLE INFO

Received: 2 June 2023
Revised: 6 July 2023
Accepted: 6 July 2023
Available online: 5 August 2023

The subject of this article is to compare the effectiveness of commercial exhaust gas aftertreatment systems such as TWC and GPF with their prototype variant, which is produced on a pilot line that allows the recovery of precious metals. What's more, the said production line allows the manufacture of components compliant with Euro IV, V and VI standards. Depending on the model of the monolith made, it is possible to reduce the consumption of precious metal raw materials by up to 20%, which should be considered a significant result. The article describes in detail the manufacturing process of metal carriers using the mentioned technology. A dynamic engine dynamometer was used for tests verifying the effectiveness of particulate filters, on which the RDE test route covering the area of the Poznan agglomeration was mapped. The tests performed are particularly important, as it should be borne in mind that according to the forecast in 2025, internal combustion engines powered by conventional fuels will account for 85% of all propulsion sources. In addition, the increasing environmental awareness of vehicle users and manufacturers requires solutions to reduce PM emissions into the atmosphere in both mass and number.

Key words: *DPF, TWC, PM, catalytic systems*

1. Introduction

One of the environmental problems, especially visible in large metropolitan areas, is smog. Its source is, among other things, emissions of harmful compounds from vehicles. Emitted hydrocarbons, nitrogen oxides or particulates, which undergo photo-technical reactions under the influence of sunlight, create photo-technical smog, commonly known as California smog. Reducing emissions from combustion engine units is an essential way to reduce the negative impact of road transport on the environment. Among the components of exhaust gases, particulate matter is the most dangerous to humans. Particularly small particles, which are not filtered by the human respiratory system, are the etiological factors causing disease. The problem of particulate emissions affects both diesel and gasoline-powered internal combustion vehicles. The use of direct gasoline injection contributes to the formation of PM with small diameters (less than 100 nm) [8, 11]. Ultra-fine particles (UFP), despite their small mass and diameter, dominate in number in the ambient air. Significant effects of air pollution by particles with diameters smaller than 100 nm on the occurrence of cardiovascular and respiratory diseases (especially asthma and lung cancer) have been proven [1, 2, 12, 17, 24]. The issue of emissions from dual-fuel vehicles additionally fueled with alternative fuels such as CNG as presented in [27], is discussed. The issue of reducing emissions as a result of replacing conventionally fueled vehicles with alternative vehicles was, in turn, addressed in [25]. Analyzing the literature, it can be noted that researchers focus on analyzing emissions from conventional and alternative vehicles as well as engines for other uses. This may be due, perhaps, to the fact that legislators around the world are systematically reducing emission limits from internal combustion engines [26]. Nowadays, in order to reduce emissions of individual components of exhaust gases, advanced exhaust gas cleaning systems are used [15, 16].

To reduce PM emissions, particulate filters are mainly used. Built on a ceramic or metal support, the filter resembles a honeycomb structure [10]. The inside of the channels are covered with intermediate and catalytic layers. The active layer is made up of Precious Group Metals (PGMs) [20]. These are mainly platinum Pt, palladium Pd and/or rhodium Rh [14]. Oxide catalysts have also found application. The aforementioned active and intermediate layers are applied to the support. Currently, there are two main types of supports – ceramic and metal. The advantages of the first type of carrier are low mass, repeatability of channel shape and limited heat loss. However, the ceramic solution is characterized by high thermal inertia and lower resistance to mechanical damage. Metal carriers, on the other hand, are characterized by high resistance to high temperatures, ease of fabrication of large-diameter components, resistance to sudden temperature changes and, above all, short time to reach light-off temperature. Its disadvantages include high manufacturing cost, significant heat loss during part-load engine operation, the possibility of corrosion, and reduced mechanical strength due to soldering and welding [7]. It is worth noting that the automotive industry is characterized by a very high demand for precious metals. In the case of palladium, the largest amount of this raw material is consumed in the production of catalytic systems used in motor vehicles [22]. As indicated in [22], in 2011, the demand for palladium used in the production of catalytic reactors amounted to 66% of the total demand for this element. One catalytic reactor used in passenger vehicles contains between 3–7 grams of platinum [18]. Over the past five years, a fivefold increase in the price of palladium has been observed. Price increases have also been observed for rhodi-

um and platinum [19]. This directly affects the price of a catalytic reactor, which is a component of the manufacturing price of a new vehicle. In order to optimize the cost and manufacturing process of catalytic systems, an innovative production line was created to recover precious metals. The purpose of this is to reduce the manufacturing costs of these components. This article foretells the results of performance verification tests of prototypes created on a pilot production line.

2. Technology for manufacturing metal carriers

2.1. Manufacturing of metal carriers

Metal carriers are formed by rolling flat and corrugated/perforated metal foil. The thin walls provide a small increase in backpressure at the gas inlet to the carrier and a large OFA surface area. The use of metal foil facilitates the creation of these large-diameter components, which have applications in exhaust gas purification of stationary operating engines (e.g., power generators) and NRMM (Non-Road Mobile Machinery). The manufacture of metal-backed filters is characterized by shorter production times and reduced processes compared to ceramic carriers. The carriers are produced by rolling 0.05 mm thick film. The material undergoes a degreasing process at the beginning of production to maximize surface adhesion properties. Degreasing is carried out in ultrasonic washers (Fig. 1).

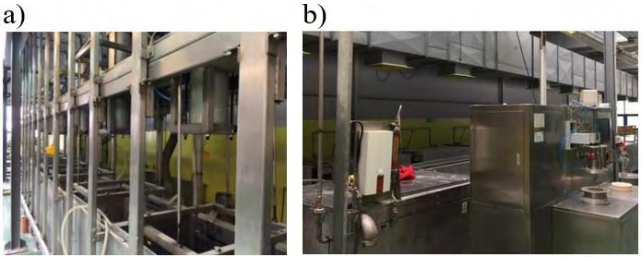

Fig. 1. Treatment of metal film at the beginning of production: a) degreasing in ultrasonic washers, b) coating with catalytic layers together with intermediate layer by bath method

The next stage in the production of the carrier is the spinning process (Fig. 2). Using a feeder with a guide, the metal film is directed to a machine that forms the target shape of the carrier. The film of the required width is then wound onto a spool of a defined diameter and secured with tape before returning to its previous shape (Fig. 3a). The prepared film is coated with catalytic layers together with an intermediate layer by the bath method, less often by spraying. For particulate filters, a coating containing oxidizing elements, mainly platinum, is used. The catalytic layer should be applied uniformly over the entire surface of the carrier. In the filters being developed, the exact composition of the catalytic layer is part of the manufacturer's patent, which determines the proportion of oxidizing or oxidation-reducing elements applied. The catalytic coating varies depending on the type of element produced.

In the case of motor vehicles, the most common shape of the carrier is a cylinder (Fig. 3b). The next stage of production is the manufacture of the housing. The outer part of the carrier and the housing are joined by welding or soldering. This process is carried out manually due to the large differences in the filters and reactors produced. The final stage is the addition of a diffuser at the inlet and a confuser at the outlet of the carrier, depending on the requirements of the customer and the application for a specific use (Fig. 3c).

Fig. 2. Spinning process of metal foil

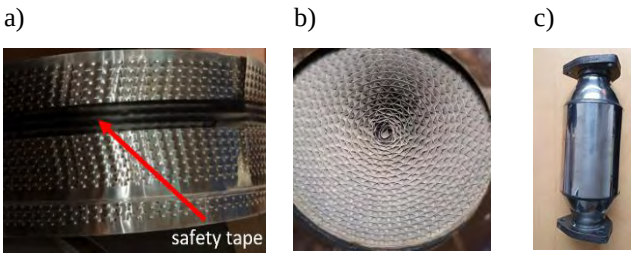

Fig. 3. View of selected stages of metal carrier manufacturing: a) securing the film with tape before restoring the original shape b) cross-section of the finished carrier, c) view of the complete particulate filter

2.2. Recovery of catalytic materials from metal carriers

In the world literature, examples of the application of recycling methods for catalytic reactor carriers and particulate filters made of ceramic materials constitute the vast majority compared to metal carriers. The End-of-Life Vehicles Directive 2000/53/EC sets the general framework for the operation of a country's recycling system, which leaves freedom in the choice of methods and tools used to process vehicles and their components [3, 4]. Pyrometallurgical and hydrometallurgical methods are widely used in the processing of ceramic monoliths. In the case of metal carriers, the recovery of platinides can be carried out using a device equipped with a magnetohydrodynamic pump. Analogous to ceramic monoliths, metal carriers are crushed using dedicated shredders and grinders until a dust with the appropriate grain diameter is obtained. The illustration shows a corrugated film metal carrier for X-ray analysis and recycling (Fig. 4).

Fig. 4. Catalytic reactor metal support used for X-ray analysis and recycling [6]

An analysis of the application of this technology by various research centers indicates that the grinding step of the

carrier is not always carried out. The monolith is placed in a liquid metal moving at a certain speed. Two types of pumps are used in the devices. The combination of a magnetic field and current flow creates a force that directs the liquid metal along the axis of the channel (in the case of a conduction pump). In an induction pump, eddy currents are created, which induce a pressure difference at the inlet and outlet of the filter, so that a suction-pressure force is created [5].

According to research conducted by the laboratory of the Institute of Metal Technology of the Silesian University of Technology, the effectiveness of the method was demonstrated by proving the depletion of platinum content in the processed carriers. In Poland, there are more than a dozen plants for the purchase and disposal of all types of carriers. In order to ensure the cost-effectiveness of the process, many companies declare a minimum number of carriers/weights of elements to be delivered for disposal [21]. While processes for ceramic carriers are already fully industrialized and standardized, for their metal counterparts, work is underway to improve the efficiency and effectiveness of the methods used. The undeniable advantage of recycling metal carriers is the degree of material reuse. Fragments of both housing and carrier that no longer contain precious metals are separated and recycled [11]. In recent years, environmental contamination with platinum group metals has been discovered. One likely source is catalytic reactors and particulate filters used in automotive applications. Ceramic supports are subjected to high temperatures, changes in oxidation-reduction conditions and mechanical abrasion. This results in violation of the monolithic structure and leakage of carrier fragments along with exhaust gases into the environment [23]. It is possible to partially eliminate the ingress of PGM metals into the environment by using metallic catalytic supports, which have greater mechanical strength and resistance to rapid temperature changes in the outlet system.

2.3. Innovative technology for manufacturing metal carriers with 20% recovery of precious metals

AWG Polonez has developed an innovative line for manufacturing catalytic systems that meet Euro V and VI standards, which allows the use of 20% recycled precious metals (Fig. 5). The construction of commercial catalytic monoliths consists of spirally coiled or otherwise two types of strips: smooth and corrugated, 0.05 mm thick, bonded together using a binder – hard solder. Such a structure, which resembles a honeycomb in structure, results in a certain number of channels (on average 400 cpsi – the number of holes per 1 cal^2). The exhaust gases flowing through them come into contact with a catalytic layer applied to their surface, which ensures the conversion of CO, HC or NO_x. In the case of AWG Polonez, a catalytic cartridge with a hole density per 1 cal^2 of up to 700 cpsi (600 on average) has been achieved, and the use of hard solder developed at laboratory scale has enabled the use of 0.04 mm thick strips. Washcoat is a porous developed surface containing mainly Al_2O_3, and precious metals derived from the active layer of the catalytic monolith. The active layer contains catalytic substances: palladium, platinum, rhodium or ruthenium. In the technological process of the innovative line, washcoat waste is ground in mills until the desired grain size is achieved, then grain size control is performed. The next step is to produce a homogeneous slurry containing washcoat, precious metals and washcoat from the recovery process. With the use of braze providing sufficiently strong joints, it was possible to use a thinner coil strip to fill the monolith. Braze is a nickel-based eutectic alloy with the addition of phosphorus and boron and chromium. The solder also offers economic advantages due to its reduced melting point compared to current alloys. The fabrication of the catalytic system is divided into 3 stages: preparation of the raw materials needed to make the catalytic monolith and ultimately the finished product-catalyst, physical and chemical processes of the monolith taking into account recycled materials, incorporation of the monolith into the finished product. A key element of monolith manufacturing is the brazing of monolith components. Due to the requirements of the process, it is carried out under a 10-3Tr vacuum. A nickel-based alloy with the addition of phosphorus and boron will be used as the binder for brazing. The alloy has a liquidus temperature below 900^{o}C. This will make it possible to reduce the temperature of the process, which is beneficial for economic as well as environmental reasons. A laboratory tube furnace was used to carry out tests on joining stainless steel layers with brazing. Observations of the structure of the brazed joint were carried out on an X-ray microanalyzer. The obtained joints were characterized by about 90% gap filling by the solder material, while the American Welding Society for responsible joints considers 85% coverage of the bonded surfaces sufficient. The evaluation of the quality of the solder joints, made on the basis of macroscopic observations of the shapes of the solder outflows, also made it possible to describe them as correct. In most of the connections, correct concave-shaped efflorescences were observed, proving good adhesion of the solder to the parent material. In all samples, regardless of the soldering parameters used, the joint structures were qualitatively similar. The native material and the zone of the actual joint could be distinguished in the tested joints. Strength tests confirmed that the tested binder in the form of an amorphous strip meets the requirements for solder joints in catalytic monoliths. The very good performance of the used braze allowed for saving 20% of material in the actual process.

Fig. 5. Innovative metal carrier production line with 20% precious metal recovery

3. GPF filter testing

3.1. Description of the manufactured filter

The metal-backed particulate filter made on the innovative production line was a flow-through filter. It consisted of 50 filter channels with a height of 2 mm, which translated into 200 cpsi. One of the basic geometrical parameters of the filter media is the angle of perforation of the metal film. The prototype filter was characterized by dividing the length of the carrier channel into 3 sections (Fig. 6). Each with a length of 50 mm, but variable perforation angle: 20°, 25°, 30°. The use of perforations of the carrier's metol film forced the flow of exhaust gases on the outer radii of the carrier's longitudinal axis, which increased the efficiency of the filter (Fig. 7a). The diameter of the carrier was 100 mm, the length was 150 mm (Fig. 7a and 7b). These dimensions are close to the solutions used in series for the tested engines by manufacturers of catalytic reactors and particulate filters in the vast majority of solutions. The angle of inclination of the diffuser and confuser (30°) was adjusted to the diameter of the exhaust system pipe.

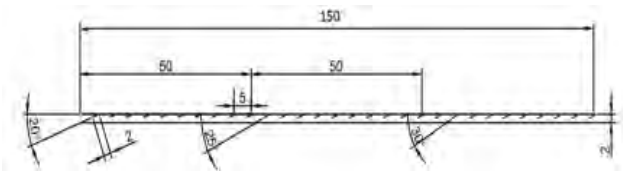

Fig. 6. Geometry of the channel of the prototype filter

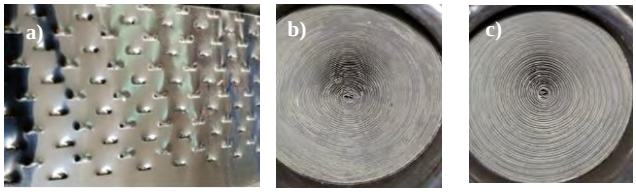

Fig. 7. Prototype filter: a) perforations of metal sheet, b) filter inlet, c) filter outlet

3.2. Methodology

Verification of the efficiency of the manufactured filter was carried out by measuring the emission of harmful exhaust gas compounds downstream of the exhaust gas aftertreatment system. The subjects of the study were 4 components of the exhaust gas cleaning system. Two commercial solutions were used in the study – a TWC catalytic reactor and a GPF/TWC particle filter, as well as a prototype catalytic coated particle filter manufactured on the innovative production line described earlier. The prototype solution was juxtaposed with the TWC 400 CPSI reactor (Fig. 8). Data on the individual research configurations are summarized in Table 1.

Table 1. Configurations of exhaust gas purification systems used for testing

No	Number of elements	Distribution of elements	Number cpsi	Type configurations	Material carrier
1	1	TWC	200	commercial	ceramics
2	1	GPF/TWC	400		
3	2	TWC + GPF/TWC	400 + 200	prototype	metal
GPF/TWC – catalytic coated particulate filter					

The test was carried out using an engine dynamometer. The tested configurations of exhaust gas treatment systems were mounted behind an engine meeting the Euro 5 emission standard. The location of the various components on the bench is shown in Fig. 9.

A dynamic braking stand was used to load the engine. The measurement was carried out on the basis of the author's test, which reflected the test in real operating conditions. The premise of the test was to simplify and shorten the test procedure performed under real conditions to tests using an engine dynamometer. The test was divided into 3 cycles corresponding to the division considered in the RDE procedure. The dynamometer used is characterized by a short overdrive (load change) time, making it possible to reproduce a previously recorded test, as well as to reproduce the braking of an engine that is driven by an electric unit. The simulated speed of the vehicle is shown in Fig. 10. According to the standard, the parameters in each of the three cycles are strictly defined by the time the vehicle travels at a speed equal to or less than 60 km/h for the urban cycle, between 60 and 90 km/h for the extra-urban cycle, and between 90 and 140 km/h for the highway cycle. A mobile apparatus from the Portable Emission Measurement Systems (PEMS) family was used to measure exhaust emissions of harmful compounds. Emission rates of gas compounds (CO, CO_2, NO_x, HC and O_2) and exhaust mass flow rates were measured using the SEMTECH DS apparatus. PM_m concentration was measured using AVL's MSS (Micro Soot Sensor) analyzer. The method of operation and parameters of the measurement apparatus used are described in detail in other publications by the authors [9, 13, 28, 29].

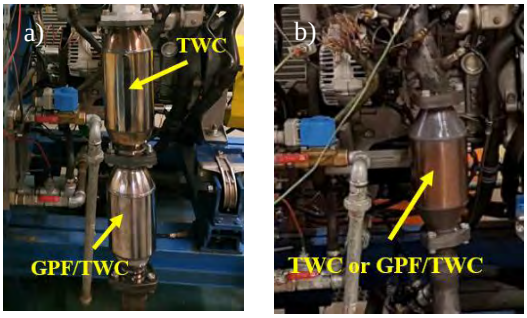

Fig. 8. Arrangement of the outlet system components depending on the tested configuration: a) TWC+ prototype GPF/TWC reactor, b) commercial TWC or GPF/TWC

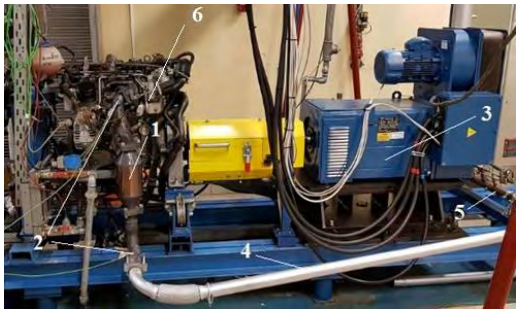

Fig. 9. Test stand: 1 – particulate filter, 2 – temperature measuring points, 3 – electric motor of dynamic dynamometer, 4 – exhaust system, 5 – exhaust gas flow meter, 6 – internal combustion engine

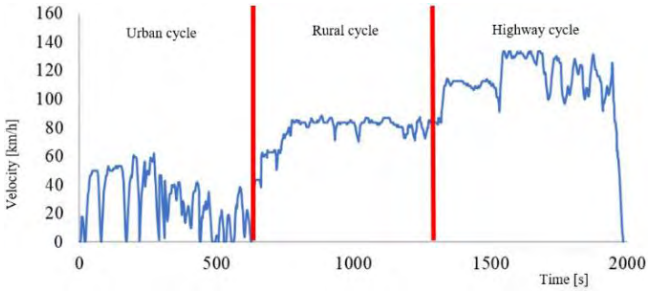

Fig. 10. Vehicle speed in the author's engine dynamometer test

4. Research results

4.1. Configuration 1

The choice of test methodology is based on the need to develop a solution that combines the advantages of on-road and laboratory testing. The first exhaust aftertreatment system configuration tested consisted solely of a commercial TWC (Fig. 11).

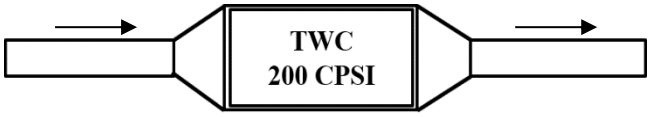

Fig. 11. Schematic of test system with commercial ceramic carrier

Characteristics of PM_m emission intensity over a range of load and crankshaft speed illustrate ranges with increased emission intensity: a load of 5% for speeds in the 1000–1250 rpm range, loads of 10 and 20% for speeds in the 3000–3250 rpm range, and a load of 30% for speeds in the 2250–2750 rpm range. In addition to the large value observed for the engine's idling points, particle emissions under conditions corresponding to the entire load range and higher speeds account for the largest share of the entire test (Fig. 12). Most PN were emitted during engine operation at medium and high speeds in the partial load range (Fig. 13).

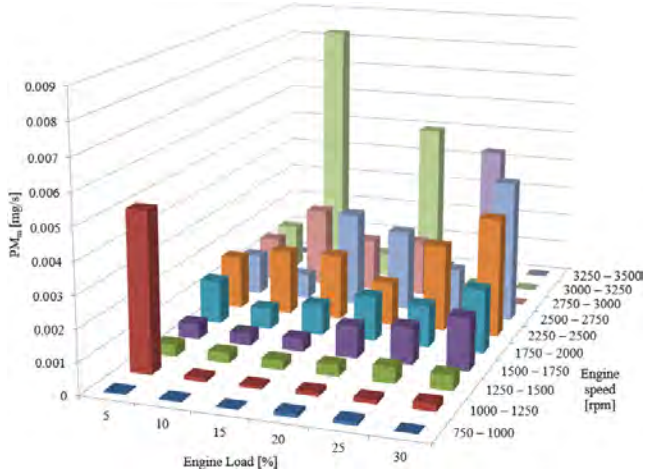

Fig. 12. PM_m emission intensity in the range of engine speed and engine load for configuration 1 of the exhaust system in the rendered test

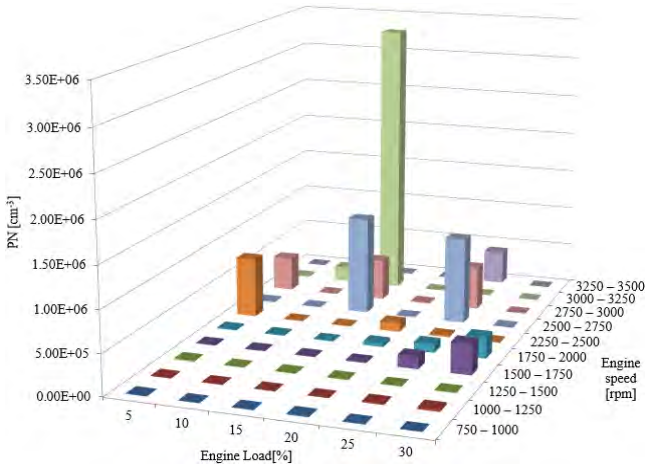

Fig. 13. PN concentration in the range of engine speed and engine load for configuration 1 of the exhaust system in the rendered test

4.2. Configuration 2

Another configuration tested was a commercial GPF/TWC filter in series on the engine accepted for research (Fig. 14).

Fig. 14. Schematic of the test system with commercial *wall-through* ceramic carrier

The intensity of PM_m emissions over a range of load and crankshaft speed is divided into three ranges. The first reflects engine operation with a load of 5–30% and an engine speed of 750–1250 rpm (Fig. 15). The highest value in this range was registered for the lowest value of engine load and speed corresponding to idling. The other values are several times lower, indicating the effect of increasing the load on increasing the efficiency of the particulate filter. In the second interval of 1250–2750 rpm, emissions are uniform. There is a several-fold increase in the recorded values in the third interval, 2750–3250 rpm.

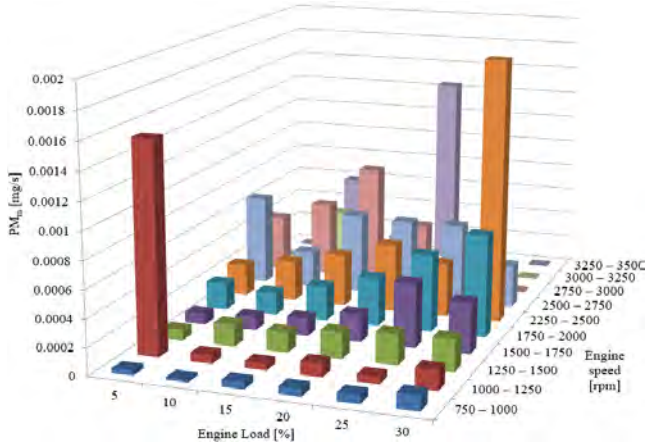

Fig. 15. PM_m emission intensity in the range of engine speed and engine load for configuration 2 of the exhaust system in the rendered test

PN concentration is highest in the speed range above 2000 rpm and load above 20% (Fig. 16). From the characteristics, it can be seen that low rotational speeds have an aggregately smaller effect on PN emissions compared to near-maximum speed values.

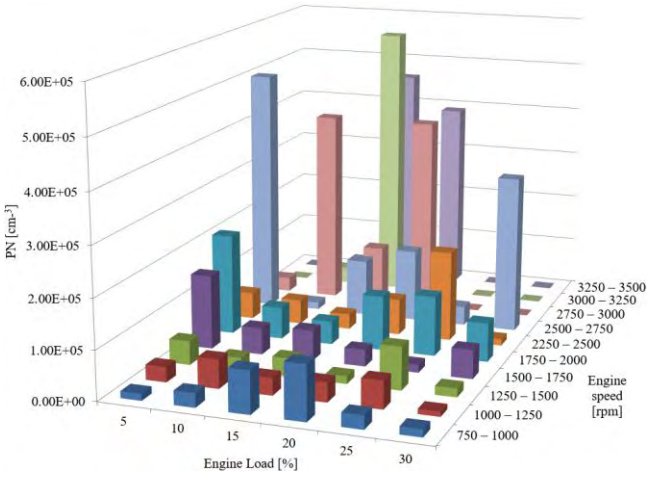

Fig. 16. PN concentration in the range of engine speed and engine load for configuration 2 of the exhaust system in the rendered test

4.3. Configuration 3

The premise of Configuration 3 was to place two elements made with metal carriers in the exhaust system. The first was a TWC 400 CPSI reactor supporting CO, HC oxidation and NO_x reduction reactions. The second element was a prototype GPF/TWC acting as a filter (Fig. 17).

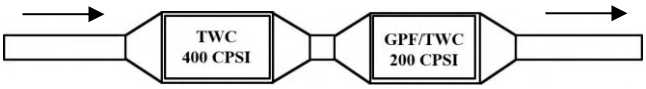

Fig. 17. Schematic of exhaust gas purification system with TWC 400 CPSI reactor and prototype GPF/TWC 200 CPSI metal carrier

The maximum value of PM_m emission intensity differs from the other results by about ten times. This result was obtained for a load of 5% and a rotational speed in the range of 1250–1500 rpm (Fig. 18).

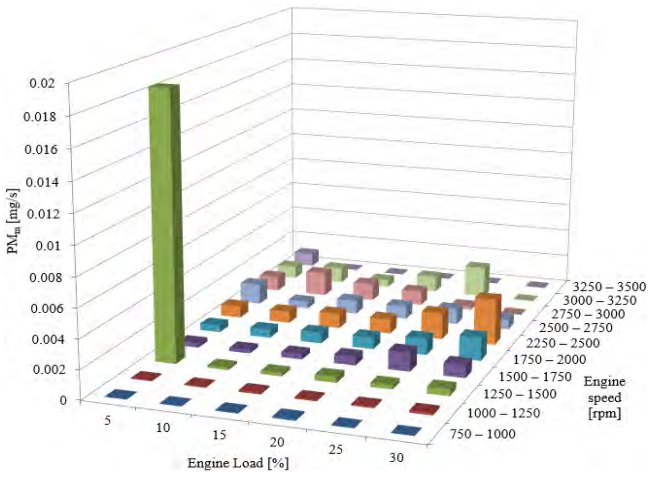

Fig. 18. PM_m emission intensity in the range of engine speed and engine load for configuration 3 of the exhaust system in the rendered test

These values correspond to operation in urban conditions during congestion. The intensity of PM_m emissions in such a case is particularly undesirable due to the exposure of people near the roadway. PM_m emission intensities above 1500 rpm reach similar values for the entire load range. The highest PN was measured during low-load operation in the crankshaft speed range from 1500–1700 rpm (Fig. 19). Apart from this case, the effect of simultaneously increasing speed and load resulted in a gradual increase in PN until it reached values corresponding to engine operation at the highest vehicle speeds.

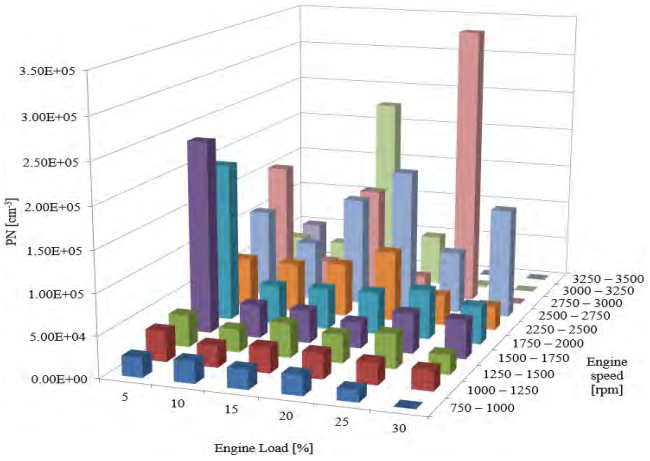

Fig. 19. PN concentration in the range of engine speed and engine load for configuration 3 of the exhaust system in the rendered test

In order to summarize the results obtained, graphs were made showing the measured values for the various configurations that were tested (Fig. 20).

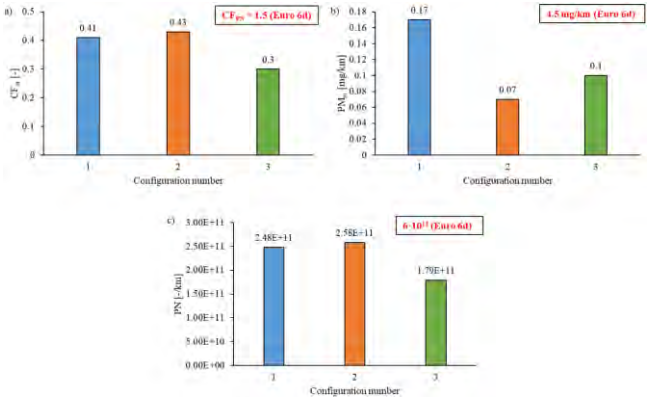

Fig. 20. Summary of the results obtained for each configuration: a) CF_{PN}, b) PM_m, c) PN

Based on the Conformity Factor for PN, it can be concluded that all test facilities did not exceed the limits assumed for the Euro 6d standard. The particulate filter manufactured on a state-of-the-art assembly line allowing recovery of precious metals had the lowest value, which means that among the tested configurations it was the most effective. Analyzing the measured values of particulate mass analogously to the first chart also, none of the configurations exceeded the limits. Both the second and third variants reached values close to each other. The highest

value was recorded for configuration number 1, in which a commercial trifunctional catalytic reactor was installed. In the case of the third graph showing the number of particles emitted, the prototype particulate filter was also the most effective. Analyzing the other commercial solutions, there is an increase in particle number emissions of about 30% than for configuration number 3.

5. Conclusion

Three configurations of the exhaust gas treatment system were tested, and their effectiveness was compared in a test that replicated a real-world run complying with the requirements of the RDE procedure. All configurations met the requirements of the Euro 6d standard for PM_m and PN emissions. In configuration 3 used, the measured CF and PN values are about 30% lower than those of commercial exhaust aftertreatment systems. This is directly related to the construction of the described filter and the solutions used in it. Therefore, the manufactured prototype particulate filter in a state-of-the-art pilot line enabling precious metal recovery has better particulate filtering properties than commercial solutions. What's more, the innovative manufacturing technology makes it possible to use metal carriers with 20% precious metal recovery, while meeting the respective guidelines for Euro V and Euro VI standards. Tests of commercial carriers were carried out to compare performance in reducing gaseous components of exhaust gases and filtration efficiency with prototype configurations made. Based on the test results, it is clear that the use of metallic media as replacements for commonly used ceramic media filters will be a more effective solution.

Acknowledgements

This work was supported by project: Launch of a pilot line of the production of ecological catalytic systems, taking into account the sustainable recycling of critical raw materials POIR.01.01.02-00-0033/16-00 10.2018-09.2019.

Nomenclature

CF	conformity factor
CO	carbon monoxide
CO_2	carbon dioxide
GPF	gasoline particulate filter
HC	hydrocarbon
NO_x	nitrogen dioxide
O_2	oxygen
PEMS	portable emission measurement system
PM_m	particulate matter mass
PN	particulate number
RDE	Real Drive Emission
SI	spark ignition
TWC	three way catalysts

Bibliography

[1] Awad OI, Ma X, Kamil M, Ali OM, Zhang Z, Shuai S. Particulate emissions from gasoline direct injection engines: a review of how current emission regulations are being met by automobile manufacturers. Sci Total Environ. 2020;718: 137302. https://doi.org/10.1016/j.scitotenv.2020.137302

[2] Baldauf RW, Devlin RB, Gehr P, Gianelli R, Hassett-Sipple B, Jung H et al. Ultrafine particle metrics and research considerations: review of the 2015 UFP Workshop. Int J Environ Res Public Health. 2015;13(11):1054. https://doi.org/10.3390/ijerph13111054

[3] Blažek M, Žalud M, Kočí P, York A, Schlepütz C, Stampanoni M et al. Washcoating of catalytic particulate filters studied by time-resolved X-ray tomography. Chem Eng J. 2021;409:128057. https://doi.org/10.1016/j.cej.2020.128057

[4] Directive 2000/53/EC of the European Parliament and of the Council of 18 September 2000 on end-of-life vehicles (OJ L 269, 21.10.2000, p. 34).

[5] Drzewiecki P. Device for recovering platinum from spent automotive catalysts using a magnetohydrodynamic pump. Materiały Śląskiego Środowiskowego Studium Doktoranckiego 2013.

[6] Fornalczyk A, Kraszewski M, Willner J, Kaduková J, Mrážiková A, Marcinčáková R et al. Dissolution of metal supported spent auto catalyst in acids. Arch Metall Mater. 2015;61(1):233-236. https://doi.org/10.1515/amm-2016-0043

[7] Fuć P. Influence of the composition and parameters of the catalytic bed modified with nanoparticle ruthenium on the emission of harmful exhaust components from a compression-ignition engine. Doctoral dissertation, Poznań 2002.

[8] Fuć P, Kamińska M, Kołodziejek D, Szymlet N, Grzeszczyk R. Measurement of rail vehicles exhaust emissions. Combustion Engines. 2022;189(2):10-17. https://doi.org/10.19206/CE-142526

[9] Fuć P, Rymaniak Ł, Ziółkowski A. The correlation of distribution of PM number emitted under actual conditions of operation PC and HDV vehicle. Air Pollution XXI, WIT Press 2013;174:207-218. https://doi.org/10.2495/AIR130181

[10] Hensel C, Konieczny R, Brück R. Recycling technology for metallic substrates: a closed cycle. SAE Technical Paper 2000-01-0596. 2000. https://doi.org/10.4271/2000-01-0596

[11] Imaoka Y, Hashizume Y, Inoue T, Shiraishi T. A study of particulate emission formation mechanism from injector tip in direct-injection gasoline engines. SAE Int J Adv & Curr Prac in Mobility. 2020;2(1):376-384. https://doi.org/10.4271/2019-01-2244

[12] Kim HJ, Choi MG, Park MK, Seo YR. Predictive and prognostic biomarkers of respiratory diseases due to particulate matter exposure. J Cancer Prev. 2017;22(1):6-15. https://doi.org/10.15430/JCP.2017.22.1.6

[13] Lijewski P, Kozak M, Fuć P, Rymaniak Ł, Ziółkowski A. Exhaust emissions generated under actual operating conditions from a hybrid vehicle and an electric one fitted with a range extender, Transport Res D-Tr E. 2020;78:102183. https://doi.org/10.1016/j.trd.2019.11.012

[14] Merkisz J, Fuć P, Lijewski P. Physicochemical aspects of the construction and operation of particulate filters. Publishing House of Poznan University of Technology, Poznań 2016.

[15] Merkisz J, Pielecha J. Particulate emissions from automotive sources, Publishig House of Poznan University of Technology, Poznań 2014.
[16] Merkisz J, Siedlecki M, Ziółkowski A, Fuć P, Lijewski P. Methods of reducing emission from HDV Euro VI engines. Combustion Engines. 2015,162(3):480-486.
[17] Ohlwein S, Kappeler R, Joss MK, Künzli N, Hoffmann B. Health effects of ultrafine particles: a systematic literature review update of epidemiological evidence. Int J Public Health. 2019;64(4):547-559. https://doi.org/10.1007/s00038-019-01202-7
[18] Specialty Metals. https://specialtymetals.com (accessed on 19.01.2021).
[19] Trading Economics. https://tradingeconomics.com (accessed on 07.04.2021).
[20] Trębacz H, Michno P. The evaluation of platinum group metals (PGMs) and their recovery from car catalytic converters, Structure and Environment. 2017;9(2):133-147.
[21] Umicore. Precious Metals Refining: https://pmr.umicore.com (accessed on 31.01.2021).
[22] Wołowicz A. Use of palladium and its compounds with particular emphasis on catalysis. Przem Chem. 2013;92(7): 1237.
[23] Xun D, Hao H, Sun X, Liu Z, Zhao F. End-of-life recycling rates of platinum group metals in the automotive industry: Insight into regional disparities. J Clean Prod. 2020;266: 121942. https://doi.org/10.1016/j.jclepro.2020.121942
[24] Yang J, Stewart M, Maupin G, Herling D, Zelenyuk A. Single wall diesel particulate filter (DPF) filtration efficiency studies using laboratory generated particles. Chem Eng Sci. 2009;64(8):1625-1634. https://doi.org/10.1016/j.ces.2008.12.011
[25] Zamboni G, Dressino L, Boileau H, A tool for the assessment of the potential benefits of electric and hybrid cars for emissions reduction in urban areas. Int J Environ Stud. 2020;77(4):703-723. https://doi.org/10.1080/00207233.2020.1736845
[26] Zhang Z, Zhao J, Man H, Qi L, Yin H, Lv Z et al. Updating emission inventories for vehicular organic gases: indications from cold-start and temperature effects on advanced technology cars. Sci Total Environ. 2023;882:163544. https://doi.org/10.1016/j.scitotenv.2023.163544
[27] Zhiliang Y, Xinyue C, Xianbao S, Yingzhi Z, Xintong W, Kebin H. On-road emission characteristics of CNG-fueled bi-fuel taxis. Atmos Environ. 2014;94:198-204. https://doi.org/10.1016/j.atmosenv.2014.05.027
[28] Ziółkowski A, Fuć P, Jagielski A, Bednarek M. Analysis of emissions and fuel consumption in freight transport. Energies. 2022;15:4706. https://doi.org/10.3390/en15134706
[29] Ziółkowski A, Fuć P, Lijewski P, Rymaniak Ł, Daszkiewicz P, Kamińska M et al. Analysis of exhaust emission measurements in rural conditions from heavy-duty vehicle. Combustion Engines. 2020;182(3):54-58. https://doi.org/10.19206/CE-2020-309

Prof. Paweł Fuć, DSc., DEng. – Faculty of Civil and Transport Engineering, Poznan University of Technology, Poland.
e-mail: *pawel.fuc@put.poznan.pl*

Barbara Sokolnicka-Popis, DEng. – Customer Support Representative, John Deere, Poland.
e-mail: *sokolnicka-popisbarbara@johndeere.com*

Andrzej Ziółkowski, DSc., DEng. – Faculty of Civil and Transport Engineering, Poznan University of Technology, Poland.
e-mail: *andrzej.j.ziolkowski@put.poznan.pl*

Maciej Bednarek, MEng. – Faculty of Civil and Transport Engineering, Poznan University of Technology, Poland.
e-mail: *maciej.bednarek@doctorate.put.poznan.pl*

Aleks Jagielski, MEng. – Faculty of Civil and Transport Engineering, Poznan University of Technology, Poland.
e-mail: *aleks.jagielski@doctorate.put.poznan.pl*

Anna Michałowska Eng. – AWG Polonez, Poland.
e-mail: *polonez@polonez-kat.com.pl*

Article citation info:
Korczewski Z. Research on the effect of low-sulfur marine fuels on the dynamic characteristics of a CI engine. Combustion Engines. 2023;194(3):97-103. https://doi.org/10.19206/CE-168390

Zbigniew KORCZEWSKI

Combustion Engines
Polish Scientific Society of Combustion Engines

Research on the effect of low-sulphur marine fuels on the dynamic characteristics of a CI engine

ARTICLE INFO

Received: 2 May 2023
Revised: 13 June 2023
Accepted: 15 June 2023
Available online: 3 July 2023

The implementation of low-sulphur, so-called modified marine fuels into operation requires prior laboratory engine tests to assess the energy, emission and structural effects of their usage. This type of research are carried out on the test bed of a diesel engine as a small-scale physical model that reproduces the adequate design and process (parametric) features of a full-size marine engine. Their key stage is to determine the energy characteristics of the engine in the steady state of operation determined on the basis of the analysis of the developed indicator diagram and the dynamic characteristics of the transient processes from idling to the reference steady state of load – and vice versa. In this way, the basic diagnostic parameters of the fuel usable quality are determined: the rate of pressure increase in the cylinder and the average deceleration of the engine crankshaft within the strenuous transient process. This article presents representative results of this type of research carried out on six different, low-sulphur marine fuels used to feed marine engines.

Key words: *low-sulphur marine fuels, engine tests, dynamic features*

1. Introduction

Experimental assessment of the impact of newly produced, low-sulphur marine fuels on the energy state of a diesel engine in terms of its performance, efficiency, dynamic characteristics and chemical emissivity of exhaust gases is a complex process [1, 2, 13]. It is the basis for making an operational decision regarding their further usage to feed full-size marine engines. It involves the need to carry out engine tests on specially adapted laboratory test beds in accordance with the developed methodology, as well as to perform a multi-criteria assessment of this impact using appropriate operations research tools [4–6]. As a result, it gives the possibility to build a ranking of the usable quality of the tested marine fuels according to the established diagnostic criteria (diagnostic parameters) [7, 14]. This type of research has been carried out for several years at the Marine Power Plant Department of the Gdańsk University of Technology on the test bed of a research CI engine as a small-scale physical model that maps adequate design and process (parametric) features of a full-size marine engine [7]. So far, six different low-sulphur marine fuels have been tested, the basic physical and chemical properties of which are listed in Table 1.

The key stage of the program of experimental research of a laboratory CI engine in the conditions of non-standard marine fuel feeding is the determination of dynamic features characterizing the combustion process, as well as transient processes enforced in a strictly defined alteration range of load and crankshaft rotational speed. In this way, two diagnostic parameters are determined (out of the ten criterion parameters of the ranking of marine fuels in usage quality), which are characterized by the greatest sensitivity to changes in the marine fuel used: the rate of in-cylinder pressure increase and the average engine crankshaft rotation delay in the transient process.

2. A rate of the in-cylinder pressure increase

A measurement of the pressure of the working medium in the cylinder in terms of an angle of the crankshaft rotation stands for a basis for the analysis and evaluation of energy processes worked out in the research engine Farymann Diesel D10, in the conditions of supply with various types of marine fuels. This is carried out in the states of steady engine load, using specialized measuring equipment (Fig. 1):

– Optrand Incorporated optical pressure sensor: AutoPSI-TC Sensor, 0–200 bar, 0.1 Hz to 20 kHz;
– two proximity (inductive) sensors, type PNP NO 5 mm: angular position and rotational speed of the crankshaft;
– DT9816 measurement card by Data Translation – for simultaneous recording control parameters (sampling frequency 10 kHz, resolution 16 bit), together with the QuickDAQ ver. 3.7.0.46 – for the direct acquisition of measurement data in online mode.

Computer application programs, developed in the MATLAB R2015b environment, for processing and analyzing the obtained results represent an important supplement to the measurement system. They enable averaging the recorded indicator charts, as well as determination of the magnitudes characterizing the working process worked out in the engine cylinder: average indicated pressure p_i, indicated power P_i, the maximum combustion pressure p_{max} and the rate of in-cylinder pressure increase $dp/d\alpha$.

The latter parameter, determined from the developed indicator diagram, makes it possible to evaluate the dynamic characteristics of the fuel combustion process in a diesel engine, in accordance with the known calculation

Table 1. Measurement results of elemental composition as well as energy and ignition properties of the considered low-sulphur marine fuels

Parameter	MGO	MDO	RMD 80/L	RMD 80/S	RME 180	RMG 380
The content of carbon C, % m/m	86.20	86.63	86.14	86.54	86.12	86.10
The content of hydrogen H, % m/m	11.10	11.20	11.72	11.75	11.80	11.90
The content of nitrogen N, % m/m	0.05	0.04	0.027	0.02	0.02	0.02
The content of sulfur S, % m/m	0.09	0.008	0.028	0.10	0.01	0.01
Gross calorific value, MJ/kg	46.20	45.68	46.01	45.41	46.19	46.03
Net calorific value, MJ/kg	43.23	42.70	43.04	42.44	43.20	43.08
Cetane number (CN)/calculated carbon aromaticity index (CCAI)	57.2	51	755	791	750	747
Density at 15°C, kg/m^3	827.1	820	872.7	885	878.7	884.5
Kinematic viscosity at 40°C (dist.)/50°C (res.), mm/s	2.99	2.37	77.83	16.48	165.30	308

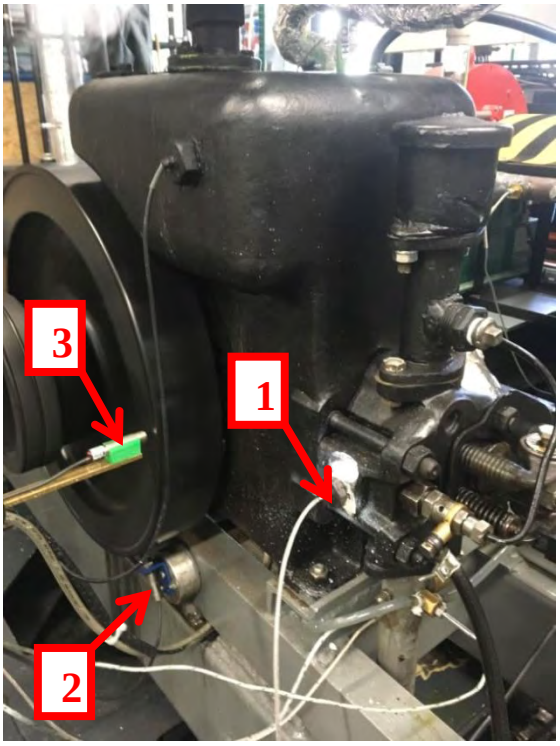

Fig. 1. Measuring sensors on the Farymann Diesel D10 research engine: 1 – in-cylinder pressure, mounted in the side wall of the cylinder head, 2 – proximity sensor, crankshaft angle position (TDC), mounted in a plane perpendicular to the flywheel, 3 – proximity sensor, crankshaft rotational speed, mounted in a plane parallel to the flywheel

formula for the intensity of heat release in the combustion chamber dQ/dα [11, 12][1]:

$$\frac{dQ}{d\alpha} = \frac{1}{\kappa-1} \cdot V \cdot \frac{dp}{d\alpha} + \cdot \frac{\kappa}{\kappa-1} \cdot p \cdot \frac{dV}{d\alpha}, \frac{kJ}{^oCA} \quad (1)$$

where: κ – specific heat ratio of the working medium c_p/c_v, V – combustion chamber volume, p – in-cylinder pressure, α – angle of the crankshaft rotation.

The above equation, after appropriate transformation, can be used to determine the formula on the rate of in-cylinder pressure increase dp/dα in the form:

$$\frac{dp}{d\alpha} = \frac{\kappa-1}{V} \cdot \frac{dQ}{d\alpha} - \kappa \cdot \frac{p}{V} \cdot \frac{dV}{d\alpha}, \frac{MPa}{^oCA} \quad (2)$$

In turn, knowing that the total amount of heat released in the process of complete combustion Q depends on the injected fuel dose m_{fuel} and its net calorific value NCV:

$$Q = m_{fuel} \cdot NCV, kJ \quad (3)$$

equation (1) can be written in the expanded form:

$$\frac{dp}{d\alpha} = \frac{\kappa-1}{V} \cdot NCV \cdot \frac{dm_{fuel}}{d\alpha} - \kappa \cdot \frac{p}{V} \cdot \frac{dV}{d\alpha}, \frac{MPa}{^oCA} \quad (4)$$

where: NCV – fuel calorific value, kJ/kg, m_{fuel} – fuel dose for one engine work cycle, kg/cycle.

The first component of the right-hand side of equation (4) takes into account the time (angular) characteristics of the injection of a specific fuel dose $dm_{fuel}/d\alpha$ and its calorific properties NCV. That means that the direction of changes in the rate of in-cylinder pressure increase is consistent with the direction of changes in the energy potential of the applied type of feeding fuel. The second component of the right-hand side of equation (4) characterizes the work of compression performed by the thermodynamic system, which can be proved using the general isentrope equation [10, 12].

Electronic cylinder indication brings a completely new information quality in the aspect of assessing the dynamic characteristics of the fuel combustion process in a research diesel engine, despite the known metrological weaknesses of this method[2], used mainly in the diagnostics of high-power engines – land and marine. On the basis of a properly smoothed (e.g. by synchronous averaging) course of variation of the working medium in-cylinder pressure as

[1] Since it is not possible to directly (by measurement) determine the course of heat release in the process of fuel combustion in the cylinder of a diesel engine, it is recreated by calculation, by means of an analytic-empirical model derived from the first law of thermodynamics. A course of the in-cylinder pressure alteration during the valves closing period stands for the input parameter of this model. It is recorded during the experimental tests of the engine. But the rate of net heat release (amount of heat released as a result of combustion reduced by heat losses penetrating the walls of the combustion chamber, heat for fuel heating and evaporation, as well as the heat of thermal dissociation of the fuel vapor) constitutes the model output parameter.

[2] They result from the following problems:
- the need for the manufacturer to ensure sufficient exam susceptibility of the engine, in the sense of its standard equipment with cylinder indicator valves (most modern high-speed and even medium-speed engines do not meet this condition);
- the need to ensure a steady, nominal load during the engine testing (this is easy to fulfill for engines driving generating sets, while for engines of the ship's main propulsion system it is difficult because their cylinders indication requires constant sailing conditions);
- significant measurement uncertainty resulting from errors in determining the piston TDC and fluctuation rotational speed of the crankshaft;
- deformations of the working medium in-cylinder pressure course caused by changes in the geometry of the indicator cock passage as a consequence of its contamination or wear, as well as imperfection of the measuring transducers used (temperature drift).

a function of an angle of the crankshaft rotation p = f(α), it is possible to determine the courses of the first and second-order derivatives (Fig. 2). They provide key diagnostic information regarding the quality of the working process (combustion):

- the angular position of the crankshaft at which the pressure in the cylinder reaches its maximum value – the zero point of the first-order derivative dp/dα;
- the angular position of the crankshaft at which fuel self-ignition occurs – the zero point of the second-order derivative $d^2p/d\alpha^2$;
- dynamics of the combustion process – maximum of the first-order derivative $(dp/d\alpha)_{max}$.

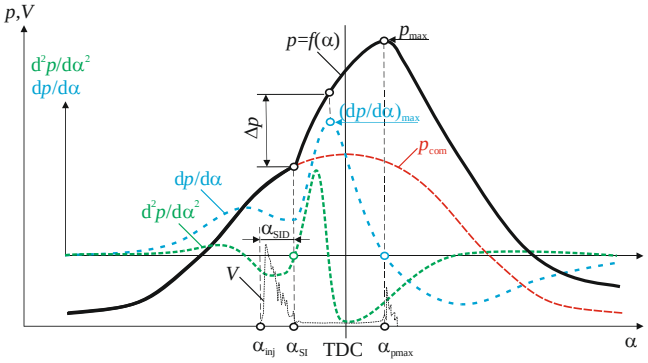

Fig. 2. The method of using the 1st and 2nd order derivative of the cylinder pressure function p = f(α) to evaluate the dynamic features of the fuel combustion process in a diesel engine: p – working medium in-cylinder pressure, p_{com} – air in-cylinder pressure during the "clean" compression process (without self-ignition), V – vibration signal forced by the injector, generated from the cylinder head (vibration acceleration envelope), α – angle of the crankshaft rotation (°CA), α_{inj} – angle of the fuel injection beginning, α_{SI} – fuel self-ignition angle, α_{max} – angle of the maximal combustion pressure

In assessing of the combustion process dynamics, more complex indicators are also applied. For example, Kozaczewski proposed in his monograph the so-called dynamic impulse D_{comb}, defined as a product of the maximum of the first-order derivative $(dp/d\alpha)_{max}$ and the pressure increase until this maximum Δp [8]:

$$D_{comb} = \Delta p \cdot \left(\frac{dp}{d\alpha}\right)_{max} \quad (5)$$

While analyzing the impact of the rate of in-cylinder pressure in a diesel engine, its two aspects should be considered: the efficiency of the realised working process and the strength of the engine structure. In general, the compromise principle of maintaining the highest possible dp/dα values while preventing excessive pressure pulsations in the cylinder space and the so-called knocking combustion, with all the further effects of this negative phenomenon on the engine reliability [8].

An average rate of the in-cylinder pressure increase of the engine with a pre-combustion chamber is much lower than in the engine with direct fuel injection [6]. However, regardless of the engine construction, the limit value of dp/dα should not exceed 0.8–1.0 MPa/°CA in the entire range of the load alterations. Hence, this is recommend to apply a calculation formula that takes into account the need to maintain appropriate proportions of pressure increase in the cylinder during the period of fuel self-ignition delay and the period of kinetic combustion [6]:

$$\left(\frac{dp}{d\alpha}\right)_{\alpha_{SI}-\alpha_{pmax}} - \left(\frac{dp}{d\alpha}\right)_{\alpha_{inj}-\alpha_{SI}} \leq 0.25 \text{ MPa/ }^{o}\text{CA} \quad (6)$$

A different approach to the issue of determining a rate of the in-cylinder working medium pressure of the research engine was adopted, treating this value as a diagnostic parameter characterizing the usable quality of marine fuels. It was assumed that the most destructive for the mechanical system of the engine are the local maxima of the first-order derivative of the pressure in the cylinder, occurring during the period of kinetic combustion $\alpha_{SI} - \alpha_{pmax}$. Hence, only the highest instantaneous value of the pressure increase of the working medium in this period was adopted for further diagnostic evaluation (Fig. 3):

$$\sup\left(\frac{dp}{d\alpha}\right)_{\alpha_{SI}-\alpha_{pmax}} = \sup\left(\lim_{\Delta\alpha\to 0}\frac{p(\alpha+\Delta\alpha)-p(\alpha)}{\Delta\alpha}\right) \quad (7)$$

Table 2 lists numerical values of a rate of the in-cylinder pressure increase of the engine fed with the tested marine fuels.

Table 2. Calculation results of a rate of the in-cylinder pressure increase of the engine fed with the tested marine fuels

Parameter	**MGO**	MDO	RMD 80/L	RMD 80/S	RME 180	**RMG 380**
dp/dα MPa/°CA	**0.6406**	0.6130	0.4947	0.5600	0.4817	**0.4693**

Analyzing the numerical data presented in Table 1, it can be concluded that the most favorable course of the combustion process in the dynamic aspect ("soft" engine operation) was obtained when the engine had been fed with RMG380 fuel, for which the rate of in-cylinder pressure increase was equal dp/dα = 0.4693 MPa/°CA. The most unfavorable combustion course ("hard" engine operation) – when powered by MGO fuel, for which dp/dα = 0.6406.

3. Angular acceleration and deceleration of the crankshaft in transient processes

In the second stage of testing marine fuels, examinations of research diesel engine dynamics are carried out in transient processes. They are worked out within the established range of the engine load variability [6]. These processes are initiated (enforced) by changes in the armature current intensity of the generator loading the engine. The processes are forcedly carried out in about 1–2 s (of a course similar to a unit stroke). In this way, further diagnostic parameters are determined: angular acceleration within the process of the engine crankshaft acceleration and angular deceleration in the process of its deceleration as observable effects, respectively: accumulation and dissipation of kinetic energy stored in the rotary power train unit.

These parameters primarily reflect the inertia of the accelerated and decelerated mechanical system of the entire power train unit, which results from moments of the masses inertia within the engine reciprocating and rotational motion and the rotating masses of the drive line along with the power receiver.

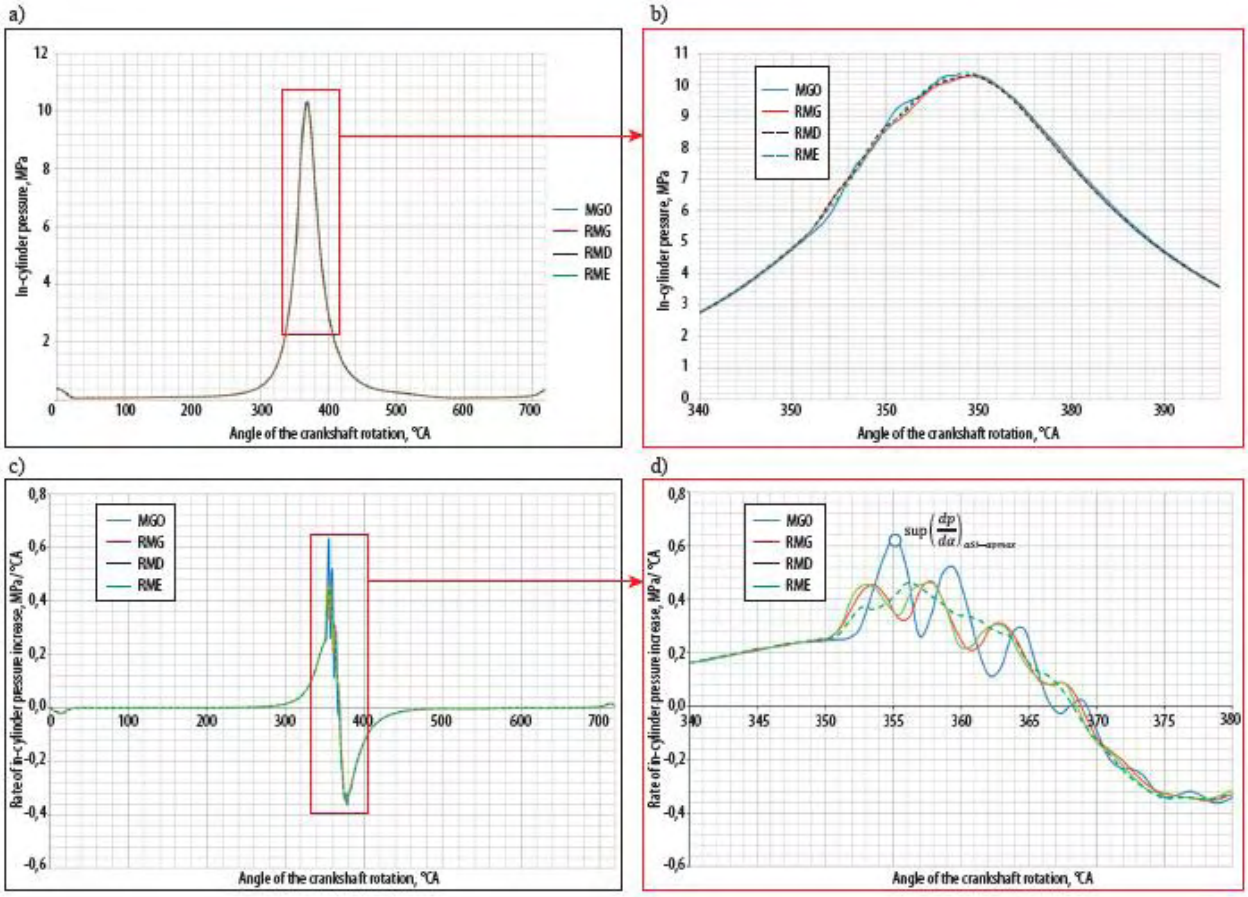

Fig. 3. Developed indicator diagram p = f(α) of the Farymann Diesel D10 research engine in the conditions of feeding with the tested marine fuels: a) assembly diagram; b) magnification of the graph p = f(α) in the area of the piston TDC; c) the course of the derivative dp/dα for the entire engine cycle; d) magnification of the derivative dp/dα for the period of kinetic combustion [6]

It also results from dynamic features of the power supply and control system engine, including the calorific properties of the feeding fuel used.

According to Newton's second law of dynamics, in the transient operating states of the considered power train unit with a CI engine, there are specific alterations in the kinetic energy of the rotating masses, which result from the following relationship [3, 9]:

$$\pm J \cdot \frac{d\omega}{d\tau} = M_e - M_{load} = M_i - M_m - M_{load} \tag{8}$$

where: J – mass polar moment of inertia of the rotating masses of the engine and generator, ω – angular velocity of the propulsion unit, M_e – effective (useful) torque of the engine, M_i – indicated torque developed by the engine, M_m – torque of the mechanical losses within the whole power train unit, M_{load} – load torque (DC generator).

On the other hand, the indicated torque M_i, which is directly proportional to the mass flow rate of the feeding fuel $\dot{m}_{fuel}$, its net calorific value NCV and thermal efficiency of the engine thermodynamic cycle η_{th}, and inversely proportional to the rotational speed of the crankshaft n, can be calculated from the following formula:

$$M_i = \dot{m}_{fuel} \cdot NCV \cdot \eta_{th} \cdot \frac{1}{2 \cdot \pi \cdot n} \tag{9}$$

while the indicated engine power – from the formula:

$$P_i = 2 \cdot \pi \cdot n \cdot M_i = \dot{m}_{fuel} \cdot NCV \cdot \eta_{th} \tag{10}$$

Thus, in order to increase or decrease the engine power, the mass flow rate of the feeding fuel to the combustion chamber for each transient rotational speed of the crankshaft must be, respectively: greater or lesser than during the operation of the power train unit, with the same rotational speed over a fixed range.

As a result, while analyzing dynamic characteristics of the engine in the transient process, the dependence on the acceleration (deceleration) time of the crankshaft from the rotational speed n_1 to n_2 (and vice versa) can be expressed in the form:

$$\tau_{a(d)} = \frac{\pi}{30} \cdot J \cdot \int_{n_1}^{n_2} \frac{dn}{|M_d|} \tag{11}$$

where: $M_d = M_i - M_m - M_{load}$ – dynamic torque (accelerating or decelerating) on the engine output shaft.

The greater the value of the dynamic torque M_d and the smaller the value of the mass polar moment of inertia of the rotating masses J and the smaller the range of changes in the crankshaft rotational speed $n_2 - n_1$, the shorter the time of the transition process $\tau_{a(d)}$. The dynamic torque, positive or negative, can also be generated during the transient process enforced by changes in the engine load torque (generator driving torque). In such a situation, there are two options for implementing this process:

– during engine running on the external speed characteristics (line A-B in Fig. 4), while maintaining a constant fuel dose per engine work cycle m_{fuel} (constant fuel rail setting l_{fuel}), taking into account its correction, which results from the speed characteristics of the injection unit. Deceleration or acceleration is caused, respectively: by increasing or decreasing the load torque M_{load};
– during the running of the engine on the regulator characteristics with the rotational speed changing in the range of the regulator's astatic operation[3] (line B-C in Fig. 4). The fuel dose is changed as a result of an impact of the rotational speed controller on the fuel rail of the injection pump. Deceleration represents a result of the simultaneous increase in the load torque M_{load} and the fuel dose per cycle m_{fuel}, while acceleration – a simultaneous decrease in M_{load} and m_{fuel}.

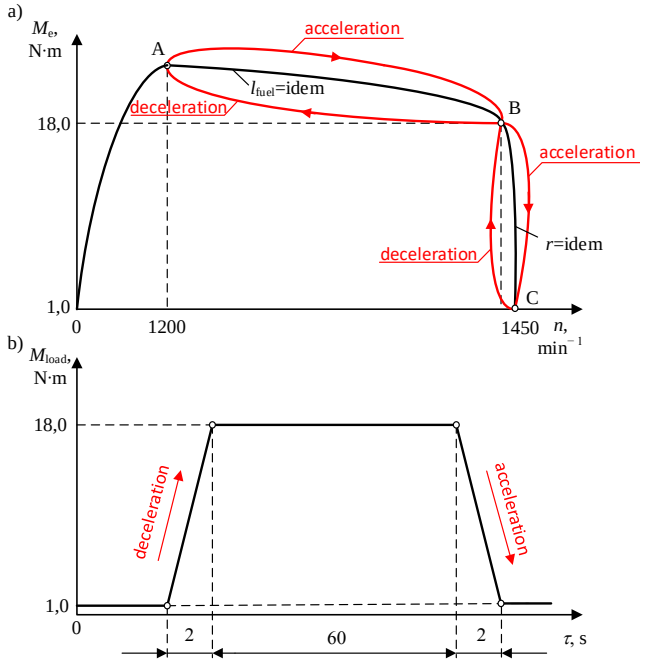

Fig. 4. Characteristics of the realised transient processes of the research engine: a) alteration of the effective torque of the engine in the process of acceleration and deceleration; b) the nature of the applied excitation: A-B – external speed characteristics (fuel rail setting – the amount of injected fuel per one engine cycle, l_{fuel} = idem), B-C – control characteristic (setting the rotational speed controller, r = idem)

The formulas (8)–(10) also result in an important methodological conclusion in the field of testing marine fuels. Well, the time of acceleration and deceleration of the engine crankshaft depends additionally on the net calorific value of the feeding fuel NCV. The higher the NCV value, the shorter the engine crankshaft acceleration time and the longer the deceleration time. Thus, by registering the rotational speed of the engine crankshaft in a given range and the nature of the load variation, it is possible to determine the average value of the angular acceleration (deceleration) $\Delta\omega_{a(d)} = |\Delta\omega|/\Delta\tau$ in the transient process and, on this basis, to assess the impact of the marine fuel applied on the dynamic characteristics engine and the entire powertrain.

[3] The so-called "slip" of the rotational speed controller.

Figure 5 shows the representative time courses of the research engine load (power of the generator), enforcing the process of acceleration and deceleration of the power train unit, and the corresponding time courses of the crankshaft rotational speed as a response to the applied inputs of the dynamic process. The method of determining the angular acceleration and deceleration of the crankshaft in the considered transient processes is graphically illustrated in Fig. 6. First, the recorded courses of rotational speed of the engine crankshaft should be smoothed and averaged[4], and then the differential quotients $\Delta\omega/\Delta\tau$ should be calculated for successive instantaneous time values implementation of the transition process. In the next step of the calculations, it is necessary to determine the beginning and ending times of the transient process τ_b and τ_e. It is assumed that these are the characteristic zero points of the $\Delta\omega/\Delta\tau$ course, for which limit values of the crankshaft rotational speed n_b and n_e are determined. On this basis, it is possible to calculate the average values of the engine crankshaft angular acceleration and deceleration in the specified time interval of the acceleration and deceleration process:

$$\left(\frac{d\omega}{d\tau}\right)_{a(d)} \approx \left(\frac{\Delta\omega}{\Delta\tau}\right)_{a(d)} = \left(\frac{\Delta n}{\Delta\tau}\right)_{a(d)} = \frac{|n_b - n_e|}{\tau_e - \tau_b} \qquad (11)$$

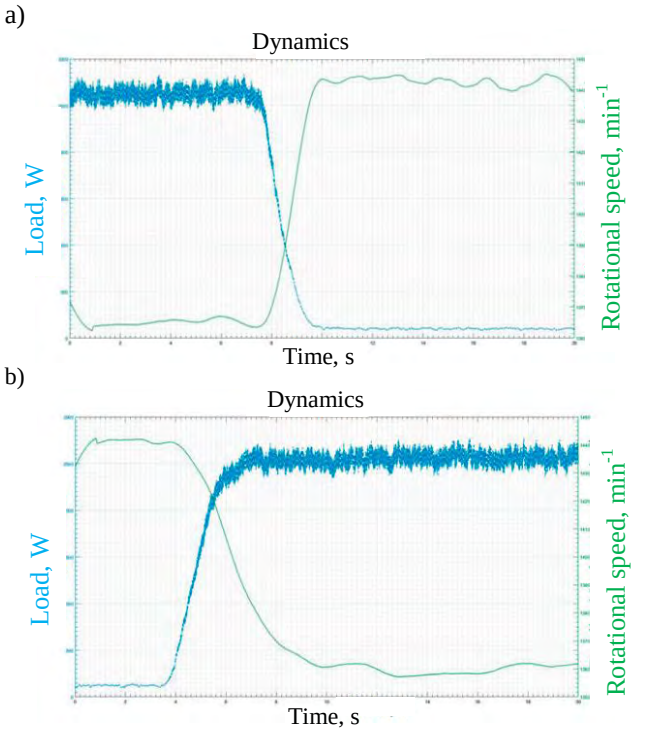

Fig. 5. Time courses of the load and crankshaft rotational speed of the research engine in the acceleration (a) and deceleration (b) processes [6]

Table 3 lists the numerical values of diagnostic parameters determined by this method. Since the direction of their changes is the same, only the average angular deceleration of the engine crankshaft $(\Delta\omega/d\tau)_d$ was selected for further analyzes of the usable quality of the tested marine fuels.

[4] Repetition of the transient process at least 4–5 times under the same thermal conditions.

Table 3. Calculation results of the angular acceleration and deceleration of the engine crankshaft fed with the tested marine fuels in the transient processes of acceleration and deceleration

Parame-ter	MGO	MDO	RMD 80/L	RMD 80/S	RME 180	RMG 380
$(\Delta\omega/\Delta\tau)_a$ $1/s^2$	0.210	**0.420**	0.021	0.032	0.042	**0.025**
$(\Delta\omega/\Delta\tau)_d$ $1/s^2$	0.095	**0.165**	0.033	0.043	0.032	**0.030**

The numerical data presented in Table 3 show that a much more advantageous solution, from the point of view of the marine engine motion dynamics, is the application of distillation fuels for its feeding, which is in line with the expectations. The best dynamic features in the transient process were shown by the engine being fed with MDO distillate fuel, for which the average angular deceleration of the crankshaft was $(\Delta\omega/\Delta\tau)d = 0.165\ 1/s^2$, and the worst – by the engine fed with residual fuel RMG380, for which $(\Delta\omega/\Delta\tau)d = 0.030\ 1/s^2$.

4. Final remarks and conclusions

By comprehensively analyzing the obtained numerical values of diagnostic parameters characterizing the usable quality of low-sulphur marine fuels in terms of the dynamic characteristics of the diesel engine powered by them, it can be generally concluded that while distillate fuels have a beneficial effect on the dynamics of transient processes, their impact on the dynamics of the combustion process is already definitely less favourable ("hard" engine running).

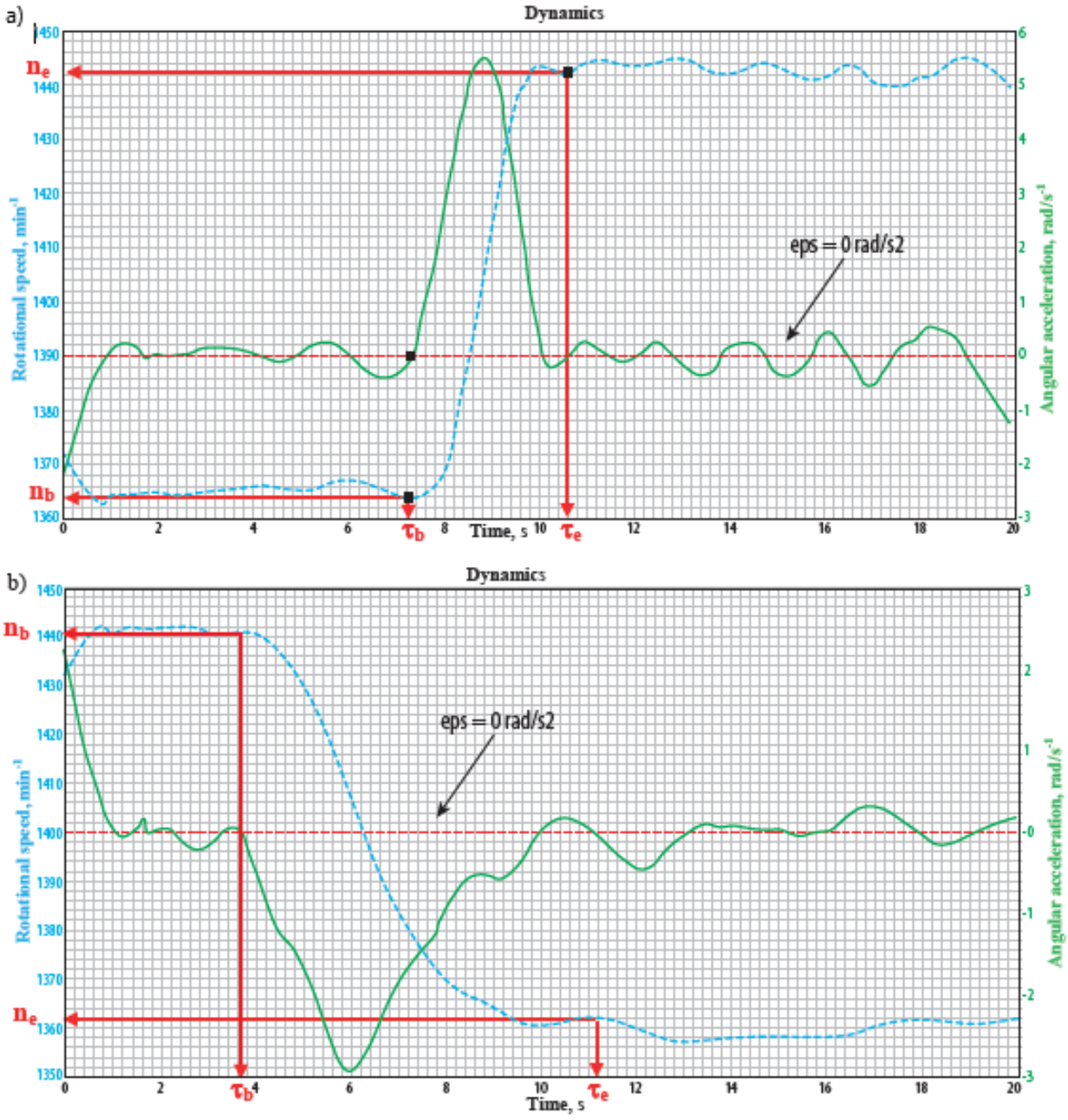

Fig. 6. Time courses of the research engine rotational speed and crankshaft acceleration in the acceleration (a) and deceleration (b) processes – the method of determining the limit values of the crankshaft rotational speed n_b and n_e [6]

The opposite is true for residual fuels. It turns out that the combustion process is milder for them ("soft" engine running), with a slightly slower response of the engine's mechanical system to the given load alterations. In the case of marine main propulsion engines, this kind of inertia is not of great importance in practice.

Moreover, considering the obtained results of the conducted examination of the engine dynamic features in the context of the currently built ranking of the usable quality of newly produced, modified marine fuels, additional methodological conclusions can be drawn:

– The type of feeding fuel has a significant impact on the considered dynamic parameters of the IC engine, that stands for the basis for treating them as key diagnostic parameters in a multi-criteria ranking of the usable quality of the tested fuels, not only marine ones;
– The engine crankshaft angular acceleration and deceleration might represent stimulant parameters of such a ranking, in which the increase or decrease of their values is perceived as, respectively: an increase or a decrease in the evaluation of the fuel usable quality;
– The attitude to similar classification the rate of in-cylinder pressure is more complex. Taking into account the marine engine durability it should be treated as a destimulant of the ranking. But, in more in-depth and detailed analyses, should be treated as the ranking nominant. It can be assumed that the optimal value of this parameter should be in the range of, for example, 0.2–0.8 MPa/°CA In such a situation, exceeding both the lower limit of the range, which means a reduction in the working process efficiency, and the upper one, indicating too “hard” engine work that leads to excessive loads on its mechanical system, means a reduction of the fuel usable quality rating. It has been established that in treating this parameter as a destimulant, it is assumed that the same marine engine power is achieved with its “softer” running – which is more desired.

Bibliography

[1] Abedin MJ, Masjuki HH, Kalam MA, Sanjid A, Rahman SM Ashrafur, Masum BM. Energy balance of internal combustion engines using alternative fuels. Renew Sust Energ Rev. 2013;26(C):20-33. https://doi.org/10.1016/j.rser.2013.05.049

[2] Andersson K, Brynolf S, Fridell E, Magnusson M. Compliance possibilities for the future ECA regulations through the use of abatement technologies or change of fuels. Transport Res D-Tr E. 2014;28:6-18. https://doi.org/10.1016/j.trd.2013.12.001

[3] Cannon RH. Dynamics of physical systems. Dover Publication, New York 2003.

[4] Evans GW. Multiple criteria decision analysis for industrial engineering: methodology and application. CRC Press Taylor & Francis Group 2017.

[5] Hillier FS, Lieberman GJ. Introduction to operations research. New York: McGraw-Hill Higher Education 2010.

[6] Korczewski Z. Methodology of testing marine fuels in real operating conditions of the compression-ignition engine. Gdansk University of Technology, Gdansk 2022 (in Polish).

[7] Korczewski Z. Energy and emission quality ranking of newly produced low-sulphur marine fuels. Pol Marit Res. 2022;4(116):77-87. https://doi.org/10.2478/pomr-2022-0045

[8] Kozaczewski W. Construction of the piston-cylinder group of internal combustion engines. Transport and Communication Publishers. Warsaw 2004 (in Polish).

[9] Natke HG. Cempel C. Model-aided diagnosis of mechanical systems: fundamentals, detection, localization, assessment. Springer Science & Business Media 2012.

[10] Polanowski S. Determination of location of top dead centre and compression ratio value on the basis of ship engine indicator diagram. Pol Marit Res. 2008;2(56):77-87. https://doi.org/10.2478/v10012-007-0065-2

[11] Rosłanowski J. Identification of technical state of fuel engine apparatus on the grounds of mechanical operation speed in piston-connecting rod system. Journal of Polish CIMAC. 2011;6(1):163-170.

[12] Rychter T, Teodorczyk A. Mathematical modeling of the engine working cycle. Polish Scientific Publisher. Warsaw 1990 (in Polish).

[13] Zacharewicz M, Kniaziewicz T. Model tests of a marine diesel engine powered by a fuel-alcohol mixture. Combustion Engines. 2022;2(189):83-88. https://doi.org/10.19206/CE-143486

[14] Zadrąg R, Kniaziewicz T. Utilization of the zero unitarization method for the building of a ranking for diagnostic marine engine parameters. Combustion Engines. 2017;4(171): 44-50. https://doi.org/10.19206/CE-2017-408

Prof. Zbigniew Korczewski, DSc., DEng. – Faculty of Mechanical Engineering and Ship Technology, Gdańsk University of Technology, Poland.
e-mail: *zbikorcz@pg.edu.pl*

Article citation info:
Sidorowicz M. An example of adoption of the model-based design (MBD) methodology in the development process of an LPG fuelling system. Combustion Engines. 2023;194(3):104-108. https://doi.org/10.19206/CE-168387

Maciej SIDOROWICZ

Combustion Engines
Polish Scientific Society of Combustion Engines

An example of adoption of the model-based design (MBD) methodology in the development process of an LPG fuelling system

ARTICLE INFO

Received: 31 May 2023
Revised: 12 June 2023
Accepted: 15 June 2023
Available online: 7 July 2023

The research aims to recognize the potential of adopting the model-based design methodology to the development process of an LPG (liquefied petroleum gas) fuelling system. Changing regulations often force the modern development of internal combustion engines (Euro 7, CO_2 reduction measures, etc.). With the definitive ban on new registrations of vehicles powered by internal combustion engines in Europe (planned for 2035), there is still ongoing development of the adaptation of the fuelling system to LPG. There is still market potential in adapting new internal combustion engines, usually equipped with direct injection systems, to reduce customers' cost of ownership of a vehicle. As the engineering process should be accelerated in the face of the variety of direct injection systems offered by OEMs (original equipment manufacturers), the model-based design methodology is proposed to make the development more effective. The article presents the SWOT analysis of this approach in the engineering process and the potential of the method in an LPG system development is concluded.

Key words: *model-based design, LPG, SWOT analysis, direct injection, automotive software development*

1. Introduction

Combustion engines are still the most popular power source in passenger cars globally. For about a decade, the market share of ICE-powered (internal combustion engine) passenger cars has been decreasing in favor of alternative powertrains (hybrid, battery electric, and others). This trend is becoming clearly visible in recent years, as it was presented in the chart in Fig. 1 for the EU (European Union) market.

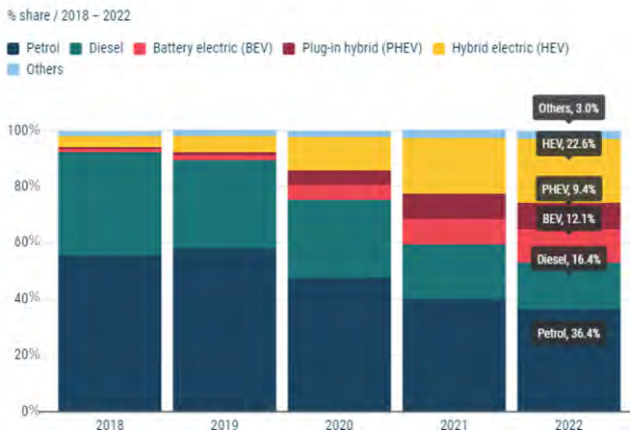

Fig. 1. New cars in EU by the fuel type [10]

The changing situation in the passenger car market globally is mainly caused by the efforts to decrease CO_2 emission reduction from the transportation sector.

Despite the fact, that only around of the 50% passenger cars are powered by the classical powertrains (ICE only, petrol or diesel), the ICE remains a component of the powertrain of almost 85% of new cars (petrol, diesel, HEV – hybrid electric vehicle, and PHEV – plug-in hybrid electric vehicle). The majority of these ICEs can be easily converted to be partially or completely LPG-powered.

LPG, as a fuel to power vehicles, is regarded not only as a cheaper alternative to petrol or diesel fuel but also as a more environmentally friendly combustion [2]. It is also the most widely used alternative fuel in Europe, although other alternative fuels are present in the market. Theoretically, the engines which can be fuelled by the LPG can also be fuelled by the CNG (compressed natural gas), with small modifications to the conversion system. However, due to the still limited network of CNG filling stations [25], it is not as popular as the LPG.

Stelmasiak et al. [26] presented the potential of utilizing methanol as an alternative fuel. However its high toxicity prevents ~~the~~ further study on expanding the supply network of this fuel, especially in the current legislative situation in Europe.

Ethanol is another alternative fuel, which can replace petrol in powering ICEs [5]. Currently, it is used as an addition to petrol, since its ability to form a homogeneous mixture. The engine control algorithms provided by OEMs already take into consideration the addition of ethanol, thus no conversion kit is needed for ethanol combustion in ICEs.

LPG conversion kits are being manufactured by many automotive companies. Most of them are based in Europe and offer conversions of engines powered by petrol, diesel and those included in a hybrid powertrain.

The development of an LPG conversion kit dedicated to modern ICEs mostly consists of software modification to control the LPG dosage by reducing or switching off the original fuel supply. To keep pace with OEM powertrain development, the manufacturers of LPG kits need to invest in engineering resources. One of the means to improve productivity in software development is to adopt the model-based design methodology (MBD). This article focuses on recognizing the potential of adopting MBD in software development for an LPG conversion kit.

1.1. Current situation of a passenger vehicle powered by an ICE

The current development of the automotive industry struggles with many issues related to economic, ecological, political, legal, and technical aspects. Some of them are:

– banning new fossil fuel vehicles (planned on 2035 on leading markets and 2040 globally [5, 17])
– introducing more stringent emission standards, such as Euro 7 in EU [24]
– weak supply chains affected by events with the global range, such as the war in Ukraine or COVID-19 pandemic
– high engineering costs and long development time of projects in the automotive industry.

The ever-changing environment around the development of ~~the~~ new passenger vehicles enforces changes in the operation of all automotive companies. It concerns the OEMs, Tier 1-3 suppliers, and the aftermarket equipment producers.

Manufacturers of automotive LPG kits enable with their products the means to convert the powertrains powered with petrol to use the LPG as a partial or a complete replacement fuel. LPG is considered cheaper and more environmentally friendly fuel than gasoline [2].

Currently (2022), 36.4% of new cars in the EU are powered with gasoline [10]. For around a decade, there has been a visible rising trend of equipping the engines in new petrol cars with a DI system [19].

The modern LPG conversion kits allow applications on the new ICEs with sophisticated DI systems. However, the variety of the combustion systems and features applied in the currently available DI engines (SPCCI – spark-controlled compression ignition, VVT – variable valve timing, SCE – stratified charge engine, etc.) enforces the individual approach in the development of the LPG fuelling system for each engine application.

This paper introduces the potential approach of accelerating the development of the software of a modern LPG system with the deployment of the model-based design.

1.2. Model-based design

Model-based design is an established approach to developing efficient solutions to complex engineering problems. In this method, complicated systems can be created ~~by~~ using mathematical models representing system components and their interactions with their surrounding environment [1]. The modeled phenomena can be simulated by system engineers and applied in the production software code by the automatic code generation toolchain. The behaviour of the model can be easily validated and verified on various testing benches (MiL – Model-in-the-Loop, SiL – Software-in-the-Loop, HiL – Hardware-in-the-Loop).

Embedded software development is a continuously developing engineering branch. The progress made in the field of control algorithms include the adoption of modern applications, such as artificial intelligence (neural networks, machine, deep, reinforced learning, etc.) [21], digital twins [13], Internet of Things (IoT) [27]. The specific feature of the MBD is the significant improvement of ~~the~~ software development efficiency.

The main advantages of MBD are that modelling and simulation enable engineers to quickly try many ideas without the need for expensive prototypes, testing and validation are done early and continuously rather than at the end of the process so that errors are found and corrected before hardware testing, and software source code can be generated from the system models, which reduces effort and eliminates hand-coding errors [11].

In general, the MBD approach in automotive software development is applied due to its positive impact on the development time, which influences the engineering cost significantly. An example of the implementation of a system in the MBD methodology applied in the MATLAB/Simulink environment is shown in Fig. 2.

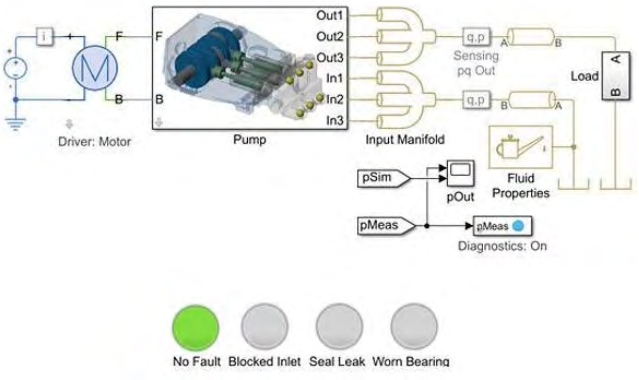

Fig. 2. Example of the MBD model in MATLAB/Simulink [15]

The main content in the MBD is the mathematical model of the system for which the software is being developed. The literature proves that an LPG system has been successfully modelled mathematically [7, 12, 20]. An example of a top-level model for software architecture for an LPG system is presented in Fig. 3.

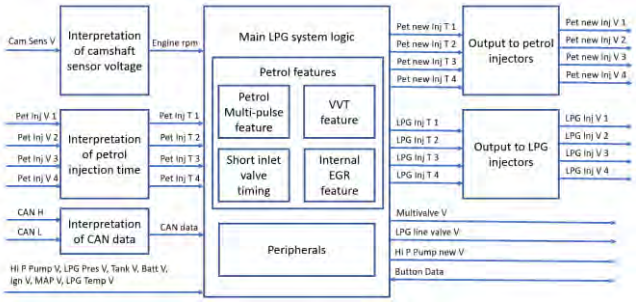

Fig. 3. An example of a top-level architecture model for an LPG system software

1.3. Novel autogas systems

Although petrol engines are currently considered as the legacy constructions, with limited focus on development from the OEMs' side, they are still the most frequent chosen powertrain type in the new passenger cars in Europe [10]. Many car owners choose to convert the classical, petrol powered engines to bi-fuel ones, which can be powered with LPG. Their decision is made mainly due to lower fuel costs.

LPG vapor phase injection systems utilize the signals from the gasoline system controller, where they intercept

the gasoline injector control signal at the start of the injection and its duration [23].

Modern SI engines often utilize DI (direct injection) systems in combination with advanced features in the mixture formation and combustion processes, such as SPCCI, VVT, Miller cycle, internal EGR (exhaust gas recirculation), charge stratification, etc. These features are possible to apply to a high extent, mainly due to the deployment of DI. However, most ~~of~~ modern LPG systems still use LPG vapor injection into the intake manifold. The issues related to the dependency of the LPG injection on the intake timing (which direct petrol injection does not meet) are resolved by influencing the petrol-LPG composition for individual combustion cycles, depending on the engine operating range and its power demand. Schematics of the Prins LPG vapor injection system applied on a DI engine is presented in Fig. 4.

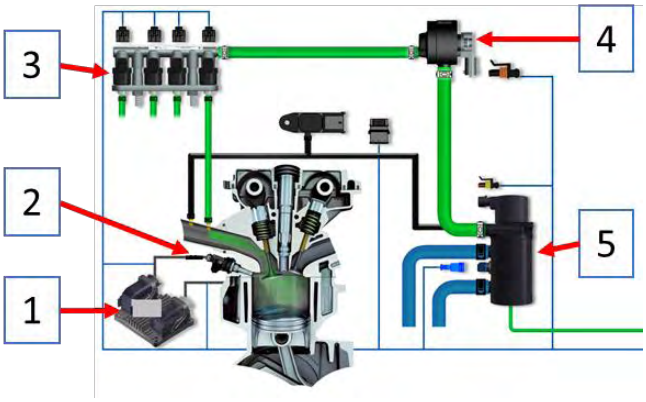

Fig. 4. Schematics of the LPG vapor injection system applied on a DI engine [28]: 1 – petrol engine ECU, 2 – ICE equipped with DI, 3 – LPG injectors, 4 – LPG filter, 5 – LPG evaporator

Controlling both fuel dosages is difficult in terms of software and hardware. The controller needs to take into consideration rapidly changing engine operation points, measurement of original petrol dosages, and adapt to the current petrol direct injection accordingly. Each OEM applies different strategies to meet the power demand in various engines, whereas the LPG kit manufacturers are focused on covering ~~the~~ most of the engine applications on the market. This creates a high demand for engineering resources, which are costly.

2. Analysis aim and goal

The aim of the analysis is to assess the potential of applying the MBD methodology for software development of the modern LPG conversion systems.

The automotive industry knows many success stories related to the deployment of the MBD approach in developing the production software code. Toyota claims that the MBD is a measure to deliver more complex systems with quality and improved productivity [18]. Stellantis developed the new generation of its gasoline Engine Control System using MBD [8]. VW and MathWorks successfully collaborated to craft an MBD process that is targeted towards reaching compliance with important industry quality standards [4]. MAN successfully applies the MBD approach in the embedded software development for more than 15 years [7].

This valuable experience in the development of the software controlling the functionality of automotive powertrain systems can possibly be transferred to companies manufacturing LPG conversion kits.

The goal of the analysis is to prove the above argument by analyzing the strengths, weaknesses, opportunities, and threats of adopting the MBD processes into the embedded software development for LPG system controllers.

3. SWOT analysis

The SWOT analysis is a simple method that can provide a realistic interpretation of the strengths and weaknesses of a business [3]. Mostly, organizations carry out SWOT analysis at a strategic planning stage, try to identify and examine the existing resources, both internally and externally, investigating their trends and patterns that may have either positive or negative impacts on businesses [16]. The presented analysis focuses on the aspect of adopting the MBD in the development process of ~~a~~ modern LPG system software.

3.1. Strengths

Rapid development of software: MBD process is highly efficient compared to the classical embedded software development. The addition of model-based systems engineering to the traditional approach delivers a 55% reduction in total development cost [14]. Not only does it concern the LPG kit manufacturers, but all the companies developing the control algorithms for complex systems.

Advantage over the competition: deployment of MBD is not a common practice among manufacturers of LPG conversion kits. Implementing the MBD process can enable releasing the applications more often than other competitors on the market.

Potential of the development of the new technology products: due to its ease of use, MBD can shift the engineering focus on the system development instead of being put on mundane implementation details. MBD also enables fast simulation and validation techniques with convenient integration of the measurement data.

3.2. Weaknesses

High initial cost: implementing MBD can be costly, especially in the initial phase, when the results are not yet visible. The costs include framework licenses, consulting, and support.

Foreseen limited growth in the particular product range: MBD applied only to the LPG kit development process is risky in the face of the threats related to the internal combustion engines mentioned in the introduction. However, this risk can be mitigated by extending the product range, where MBD can also be successfully adopted (companies like AC or ALEX already extend their product portfolio with photovoltaic systems).

3.3. Opportunities

Quick expansion on the market: applying MBD to the engineering process can provide a chance to cover a broad range of engine applications, not only petrol powered with DI, but also PFI-DI or diesel.

Satisfying "here and now" demand: until the complete removal of internal combustion engines from the streets, there are decades of their presence. Converting as many engines as possible to be LPG-powered can be regarded as environmentally friendly, with the means currently available. MBD can be a way of reducing air pollution in the near future.

3.4. Threats

Changes in legislation: investing in the further development of LPG conversion systems can be risky in the face of the continuous change of the regulations. Even the rules defining the installation of LPG systems in cars are not free from the changes (vide new project of changes in R115 homologation proceeded in Poland [22]).

Variability of fuel prices: uncertainty of profitability of an LPG system installation influences the customers' decisions. Currently, the fuel prices are not forecastable long term.

3.5. Interpretation of the SWOT analysis

In the SWOT analysis process it was recognized, that adopting the MBD methodology to the software development process of an LPG conversion system has more strengths than weaknesses. However, the analysis did not take into consideration the individual business development plan of an LPG kit manufacturer. Provided the company focuses on the further development of its products in order to cover the most of the ICE applications, adopting the MBD is a reasonable step to take.

Introducing the MBD is not free from risks. However, they can be mitigated in the following ways:

– high initial cost can be reduced by applying for external funding (e.g. from the EU) or hire external freelancers or consultants
– limited growth in the LPG conversion kit's market is inevitable, regardless of the adoption of MBD. However, if a company adopts ~~the~~ MBD for the currently offered product range (LPG kits), the methodology can be easily applied to other technology products offered in the future.

Table 1. SWOT analysis of the potential of adopting the MBD methodology in the software of LPG powering system

Strengths	Weaknesses
1) Rapid development of software 2) Advantage over the competition 3) Potential of the development of new technology products	1) High initial cost 2) Foreseen limited growth in the particular product range
Opportunities	**Threats**
1) Quick expansion on the market 2) Satisfying "here and now" demand	1) Changes in legislation 2) Variability of fuel prices

Despite the potential drawbacks of adopting the MBD, it ~~is~~ cannot be forgotten that this methodology is a modern process to develop software for automotive applications, and its advantages outweigh the threats. The detailed calculation of the profitability of introducing MBD cannot be performed within this article due to the individual situation of each company.

4. Conclusion

Adopting the MBD methodology in the development process of the embedded software used to control a modern LPG conversion system can be advantageous for the company, which would decide to do so. The biggest strength of this method is its potential for cost savings. The decision to introduce MBD in the company is not free from risks, ~~which were~~ described in the SWOT analysis.

The decision to adopt the MBD process in the development of the software to control the LPG system is to be made individually by a company, however in the face of an ever-changing situation with ICEs, it can be a decent starting point to modernize the development process for future products.

Nomenclature

CNG	compressed natural gas
DI	direct injection
ECU	electronic control unit
EGR	exhaust gas recirculation
EU	European Union
HEV	hybrid electric vehicle
HiL	Hardware-in-the-Loop
ICE	internal combustion engine
IoT	Internet of things
LPG	liquified petroleum gas
MBD	model-based design
MiL	Model-in-the-Loop
OEM	original equipment manufacturer
PHEV	plug-in hybrid electric vehicle
SCE	stratified charge engine
SiL	Software-in-the-Loop
SI	spark ignition
SPCCI	spark-controlled compression ignition
SWOT	strengths, weaknesses, opportunities, threats
VVT	variable valve timing

Bibliography

[1] Ahmadian M, Nazari ZJ, Nakhaee N, Kostic Z. Model based design and SDR. 2005. https://doi.org/10.1049/ic:20050389
[2] Beik Y, Dziewiątkowski M, Szpica D. Exhaust emissions of an engine fuelled by petrol and liquefied petroleum gas with control algorithm adjustment. SAE Int J Engines. 2020; 13(5):739-759. https://doi.org/10.4271/03-13-05-0047
[3] Benzaghta MA, Elwalda A, Mousa M, Erkan I, Rahman M. SWOT analysis applications: an integrative literature review. JGBI. 2021;6(1):55-73. https://doi.org/10.5038/2640-6489.6.1.1148
[4] Bermas D. Software detailed design for model-based development – obligatory or superfluous? Mathworks.com. 2016. https://www.mathworks.com/content/dam/mathworks/mathworks-dot-com/company/events/conferences/automotive-

conference-stuttgart/2016/proceedings/software-detailed-design-for-model-based-development-obligatory-or-superfluous.pdf
[5] Bielaczyc P, Woodburn J, Gandyk M, Szczotka A. Ethanol as an automotive fuel – a review. Combustion Engines. 2016;166(3):39-45. https://doi.org/10.19206/CE-2016-338
[6] Brand C, Anable J. "Disruption" and "continuity" in transport energy systems: the case of the ban on new conventional fossil fuel vehicles. European Council for an Energy Efficient Economy (ECEEE) Summer Study 2019 Proceedings. 2019. https://eprints.whiterose.ac.uk/147678/
[7] Cipollone R, Villante C. A dynamical model for the design of LPG liquid-phase injection systems. ICE Technical Conference ASME 2000. https://www.researchgate.net/profile/Carlo-Villante/publication/235248936_A_dynamical_model_for_the_design_of_LPG_liquid-phase_injection_systems/links/0deec53177d7a0864e000000/A-dynamical-model-for-the-design-of-LPG-liquid-phase-injection-systems.pdf
[8] Deissenboeck F, Hummel B, Jürgens E, Schätz B, Wagner S, Girard J-F et al. Clone detection in automotive model-based development. Proceedings of the 13th international conference on Software engineering – ICSE '08. ACM Press, New York 2008. https://doi.org/10.1145/1368088.1368172
[9] FCA develops AUTOSAR-compliant Engine Control System with model-based design. Mathworks.com. 2018. https://www.mathworks.com/company/user_stories/case-studies/fca-develops-autosar-compliant-engine-control-system-with-model-based-design.html
[10] Fuel types of new passenger cars in the EU – ACEA – European Automobile Manufacturers' Association. ACEA – European Automobile Manufacturers' Association. 2021. https://www.acea.auto/figure/fuel-types-of-new-passenger-cars-in-eu/
[11] How Engineering Teams Adopt Model-Based Design. www.mathworks.com. 2021. https://www.mathworks.com/campaigns/offers/next/how-engineering-teams-adopt-model-based-design.html
[12] IAV Develops Mass-Production Gaseous-Fuel ECUs Using Model-Based Design. www.mathworks.com. 2009. https://www.mathworks.com/company/newsletters/articles/iav-develops-mass-production-gaseous-fuel-ecus-using-model-based-design.html
[13] Ibrahim M, Rjabtšikov V, Gilbert R. Overview of digital twin platforms for EV applications. Sensors. 2023;23(3):1414. https://doi.org/10.3390/s23031414
[14] Krasner J. How product development organizations can achieve long-term cost savings using model-based systems engineering (MBSE). 2015. https://www.omgwiki.org/MBSE/lib/exe/fetch.php?media=mbse:how_product_development_organizations_can_achieve_long-term_savings_1_.pdf
[15] Model-Based Design. Mathworks.com. 2019. https://www.mathworks.com/solutions/model-based-design.html
[16] Namugenyi C, Nimmagadda SL, Reiners T. Design of a SWOT analysis model and its evaluation in diverse digital business ecosystem contexts. Procedia Computer Science. 2019;159:1145-54. https://doi.org/10.1016/j.procs.2019.09.283
[17] Nóvoa GPAS da. The adaptability of companies in the automotive sector to the ban on internal combustion vehicles in Europe from 2035. 2022. https://repositorio.iscte-iul.pt/handle/10071/27306
[18] Ohata A, Butts KR. Improving model-based design for automotive control systems development. IFAC Proceedings. 2008;41(2):1062-5. https://doi.org/10.3182/20080706-5-KR-1001.00182
[19] Pielecha I. Diagnostics of stratified charge combustion under the conditions of multiple gasoline direct injection. J Therm Anal Calorim. 2014;118(1):217-25. https://doi.org/10.1007/s10973-014-3956-3
[20] Pulawski G, Szpica D. The modelling of the compression ignition engine powered with diesel fuel with LPG admixture. Mechanika. 2016;21(6):500-505. https://doi.org/10.5755/j01.mech.21.6.11147
[21] Rai A, Kumar NS, Pai SP, Rao BS. Fuzzy logic based prediction of performance and emission parameters of a LPG-diesel dual fuel engine. Procedia Engineering. 2012;38:280-292. https://doi.org/10.1016/j.proeng.2012.06.036
[22] Rządowy projekt ustawy skierowany do Sejmu (Government bill submitted to the Sejm). Gov.pl. https://www.sejm.gov.pl/sejm9.nsf/agent.xsp?symbol=RPL&Id=RM-0610-1-23
[23] Szpica D. The influence of selected adjustment parameters on the operation of LPG vapor phase pulse injectors. J Nat Gas Sci Eng. 2016;34:1127-1136. https://doi.org/10.1016/j.jngse.2016.08.014
[24] Samaras ZC, Kontses A, Dimaratos A, Kontses D, Balazs A, Hausberger S et al. A European regulatory perspective towards a Euro 7 proposal. SAE Technical Paper. 2022-37-0032. 2022. https://doi.org/10.4271/2022-37-0032
[25] Stelmasiak Z, Larisch J, Pietras D. Issues related to naturally aspirated and supercharged CI engines fueled with diesel oil and CNG gas. Combustion Engines. 2017;169(2):24-31. https://doi.org/10.19206/CE-2017-205
[26] Stelmasiak Z, Semikow J. The possibilities of improvement of spark ignition engine efficiency through dual fueling of methanol and gasoline. Combustion Engines. 2010;142(3):59-67. https://doi.org/10.19206/CE-117136
[27] Venkatesh B, Babu JC, Mathivanan SK, Jayagopal P, Prasanna S, Uddin MS. Influences of aqueous nanofluid emulsion on diesel engine performance, combustion, and emission: IoT (Emission Monitoring System). Adv Mater Sci Eng. 2022;2022:1-9. https://doi.org/10.1155/2022/8470743
[28] VSI-DI system. Prinsautogas.com. 2013. https://www.prinsautogas.com/en/vsi-di-system

Maciej Sidorowicz, DEng. – MSeng, Białystok, Poland.
e-mail: *maciej.sidorowicz.pb@gmail.com*

Article citation info:
Brzozowski M, Parczewski K. Problems related to the operation of autonomous vehicles in adverse weather conditions. Combustion Engines. 2023;194(3):109-115. https://doi.org/10.19206/CE-168805

Michał BRZOZOWSKI
Krzysztof PARCZEWSKI

Combustion Engines
Polish Scientific Society of Combustion Engines

Problems related to the operation of autonomous vehicles in adverse weather conditions

ARTICLE INFO

Received: 23 May 2023
Revised: 19 June 2023
Accepted: 26 June 2023
Available online: 22 July 2023

The article introduces and discusses the sensors used in autonomous cars. The reliability of these devices is crucial for the proper operation of autonomous driving systems. The research works related to the issue of the performance of autonomous sensors in adverse weather conditions is discussed and critically analysed. The negative effects caused by bad weather conditions are characterised. The paper presents the result of author's own research concern on the effects of rain, snow and fog on lidar measurements. The results obtained are presented, detailing the most important threats from each weather phenomenon. Attempts currently being made to address these issues are presented as well. The paper concludes with a summary of the research results, the current state of knowledge and suggestions for future developments.

Key words: *lidar, autonomous vehicle, adverse weather, rain, detection*

1. Introduction

Technologies related to autonomous cars are currently being widely developed. Selected autonomous driving systems are increasingly appearing in new cars. The aim of using these technologies, is primarily to improve road safety and assist the driver. The overall name for this system is used ADAS (Advanced Driving Assist Systems). System ADAS consist of elements:

- partly autonomous driving:
- lane keep assist
- lane change assistant
- active cruise control
- emergency braking
- traffic sign reading (and automatic vehicle speed correction)
- driver fatigue assessment
- automatic parking
- cross traffic warning, etc.

There are six levels of autonomy according to the widely accepted classification developed by the SAE (Society of Automotive Engineers). The highest, fifth level, assumes that autonomous driving takes place without driver involvement, regardless of weather conditions [31]. Some of the cars can be classified as, being on the borderline of levels 3 and 4. This means that in favourable weather and road conditions, the car takes complete control of the steering, leaving the driver as an observer. Before bringing in vehicles on level 5, it is necessary to solve a number of technical problems, taking into account both the structure of the vehicle itself and its mobility[26].

2. Sensors used in autonomous cars

2.1. Sensor characteristics

When an autonomous car moves, it uses data from sensors installed in the vehicle. The simplest division of sensors can be made them as internal and external. Internal sensors provide information on the state of the vehicle. These include among others: speed sensor, accelerometer or gyroscope. These sensors are not affected by adverse weather conditions.

External sensors are responsible for analysing the environment. Nearby objects are analysed by sonar, those at medium distances by lidar and cameras, and by radar those objects that are far away. In addition, data obtained from the car's communication with the environment (V to X) are used. The external sensors may be strongly affected by adverse weather conditions.

A prerequisite for safe driving of an autonomous car is the acquisition of reliable data regardless of the traffic and weather situation. Based on the information from the sensors, the car driving system: creates a map of the environment, identifies and classifies objects, and finally creates a complete parametric model to determine the trajectory of movement [3, 27, 36]. These tasks include detection and tracking of moving objects, hereinafter referred to as DATMO and simultaneous localization and positioning on the map (mapping) referred as SLAM. The basic characteristics of the sensors used in autonomous cars are shown in Table 1.

Table 1. Basic characteristics of sensors used in autonomous cars

	Tasks	Range	Weather vulnerability
Radar	DATMO	medium and long	minor
Sonar	DATMO	short	minor
Lidar	SLAM, DATMO	short and medium	significant
Cameras	SLAM, DATMO	short	critical
Internal sensors	SLAM	n/a	minor

Radar is an acronym for Radio Detecting and Ranging. It is one of the most commonly used sensors among road-approved vehicles. It is relatively inexpensive, easy to implement in a vehicle, and weather-resistant. It performs well in measuring distances over both short and long distances. It enables quick determination of the speed of an object. The biggest disadvantage of radar is its low accuracy in determining the shape of objects, which greatly limits its usefulness in object identification and classification tasks.

Sonar is a specific type of radar used for object detection at very short distances, e.g. during a parking manoeuvre or driving in heavy traffic. Experiments are being conducted on its use in lane change warning or pedestrian detection systems [22]. The biggest disadvantage of sonar is its short range – usually below 5 meters. In addition, it can be susceptible to interference from other objects generating sounds such as the noise of the wheels or of a passing train [34].

Lidar is an acronym for Light Detection and Ranging. It is a remote sensing technology that creates a three-dimensional image of the environment by illuminating objects with a laser beam and analysing the energy of the reflected beam. In the automotive industry, pulsed lidar is most commonly used. The device consists of a transmitter, a mirror and a receiver. The laser beam, upon encountering an object in space, is reflected from its surface and returns to the light-sensitive diode. The time from emission to reception and the reflection intensity indicator allow the position of a given point in space to be determined. Each point is defined by four parameters: x,y,z coordinates, and the reflection intensity index [10]. Lidar has a wide range of applications in autonomous driving systems, as it is used both as a tool to identify and track objects and to detect environmental features (e.g. kerbs) [6, 13, 29]. It is considered to be one of the most important sensors used in autonomous cars and is also used in currently new road-approved vehicles (e.g. Mercedes-Benz EQS 2022). Lidar prices are decreasing year on year and the technology is being developed intensively. The disadvantage of lidar is that the information obtained does not allow the exact nature of the object to be determined, e.g. lidar does not provide colour information. The problem worsens as the distance from the object increases. Lidar is susceptible to interference from adverse weather conditions.

Camera as well as camera systems (stereovision) are commonly used in autonomous vehicles. Cameras have a very wide range of applications, being effective in detecting road signs and signals. It is used to locate the vehicle in its surroundings, because it allows you to detect the edges of individual objects and their colours. Cameras are a good source of data for object identification systems, as the video image is detailed and easy to analyse. The biggest disadvantages include: susceptibility to processing errors, low resolution at longer distances and, above all, high susceptibility to adverse weather and light conditions.

2.2. Impact of adverse weather conditions on the performance of sensors used in autonomous cars

It is believed that it is currently impossible to build an autonomous vehicle that can navigate in all conditions (SAE level 5), because weather conditions affect the data received from sensors of such a vehicle too much [2, 24, 25, 33, 38]. A single drop of water on a camera lens can scatter light blurring the camera's field of view. Most algorithms used in vision systems based on cameras, assume that light intensity is proportional to the brightness of the scene. However, dynamically changing weather conditions introduce sharp fluctuations in light intensity that reduce picture quality. Raindrops in the air reduce the intensity of the image and blur the edges of analysed objects [40]. An experiment conducted by Ferreira and Martins [12] showed that when performing the task of detecting a vehicle in the rain, the quality of the image obtained from the camera deteriorates due to poor colour gradient saturation which, at a later stage of image processing, results in problems in creating the envelope of the detected vehicle – the algorithm has a problem when restricting the images field in which the vehicle is visible [12]. Based on experimental studies in rain conditions, a decrease in object detection quality of 20 to 65% was reported. Another experiment showed a decrease in detection performance of up to 65% during rain-fall and up to 45% during thunderstorms (results obtained with clear skies were taken as 100%) [41]. Fog, although less frequent than rain, is very disruptive to camera operation. First of all, it causes the effective range of vision of the camera to shrink considerably, so that detection of the rear lights of the vehicle ahead or the edge of the road becomes very difficult. The same problems can be applied to snowfall, relatively they are much more frequent. The snowfall conditions are a serious problem, because even if the autonomous car uses additional localization methods (e.g. GPS), snow accumulation can lead to serious localization errors [38].

Radar shows little susceptibility to bad weather conditions. Part of the radio wave can be absorbed by water droplets in the air (attenuation effect), the wave can also be depolarized or scattered by rain [12]. The most disruptive effect on radar operation is the occurrence of backscattering. This effect occurs because the size of the water droplet is comparable to the radio (millimetre) wavelength. The attenuation effect reduces the received power of the signals and the backscattering effect increases interference to the receiver [38]. Rain also causes a decrease in the effective radar range. For 50 mm/h intensity of rain, the range decreases by 11%, and a more significant reduction in range is caused by 150 mm/h rain [39]. At the same time, it should be remembered that rainfall of 150 mm/h is already a true tropical typhoon. In rainy conditions, the smaller the object is, the faster the distance from which it can be detected decreases. This is particularly important for pedestrian detection [35]. Studies show that for obstacles at ranges of up to 25 m, even dense fog has a negligible effect on radar performance. However, in the case of heavy snowfall, the effective radar range decreases up to 25% [19].

Rain poses a threat to lidar on many levels [37]. It can lead to a number of adverse effects such as: deterioration of reflectivity, decrease in effective range, and distortion of the shape of the identified object [41]. The more intense the rain, the more these effects increase – rain intensity of 15 mm/h does not cause significant interference, but already intensive rain of 30 mm/h reduces the effective range of lidar operation by 50% [16].

In the authors' own research, it was found that during heavy rainfall, when measuring at a distance of 10 meters, the quality of detection drops by several percent. The shape and size of the droplets are also important as larger droplets distort the laser beam more [39]. On the other hand, a decreasing number of generated points on the picture, not only results in a decreasing range but also reduces the amount of data available for analysis [4]. In addition, splashes from other vehicles can result in the detection of

falsely existing points and consequently the generation of phantom (unreal) objects [29]. This effect leads to an enlargement of the real object by non-existent points which affects the detection process. This is because the falsely curvature of the shape of analysed object, can result in a poor match of the object class. Points of phantom objects (unreal) generally have a low reflection intensity index, however, as a result of precipitation, the intensity of points resulting from reflection from real objects also decreases. According to a study by Hesper Riviere et al. [18], for the emitted by lidar wavelengths of 905 nanometres (95% of the devices currently use this wavelengths), fog is more challenging to analyse than rain. This is due to the scattering of light by the fog particles. At the same time, the denser the fog, the more problems the sensor has in providing reliable information. Tests in the chamber show that target detection at a distance of 10.5 m in 10 m visibility is impossible for most lidars [19]. Where visibility is understood as a parameter subjectively assessed. Similar conclusions were obtained by conducting the Authors' own studies on the effects of fog on lidar performance. Similar effects to fog are also caused by dust – especially PM10 particles [4].

3. Studies on the effects of atmospheric conditions on lidar

As part of the in-house research, a series of experiments were conducted to determine the susceptibility of the lidar to adverse weather conditions. For this purpose, special test rigs were built, consisting of the Livox Horizon lidar and reflective targets – road signs of different diameters. The basic parameters of the equipment used are shown in Table 2.

Table 2. Basic parameters of Lidar Livox Horizon

Wavelength	905 nm
Maximum range	260 m @ 80% reflectivity
Point of View	81.7° vertically× 25.1° horizontally
Beam divergence	0.28° vertically × 0.03° horizontally
Number of points generated	240,000 points/s (first or strongest reflected signal) 480,000 points/s (both signals)

As part of the research carried out, an attempt was made to establish the effect of rainfall on lidar performance. The study was an extension of earlier tests conducted by authors [7]. The work was divided into two stages. Firstly, the interference that rain causes when identifying objects was measured, and then the phenomenon of unreal points – resulting from the reflection of the laser beam from water droplets in the air – was investigated. To perform the tests, a special test rig – a rain gauge – was constructed. A major problem was to ensure, by all time, high water pressure in the system, which was achieved by using an 850 W pump and a hydrophore tank. Uniform and controllable water distribution was achieved by using ¼" diameter pipes. A section of the point cloud image generated by the lidar during the high intensity rain impact study (> 25 mm/h) was shown in Fig. 1.

The blue points visible in the figure are the result of the laser beam reflecting off water droplets floating in the air. These points are blue in colour because the reflection intensity factor of water drops is low. The traffic sign shield visible in the centre, made of reflective material, is bright red. In spite of this, even on the background of the sign, blue dots appear which directly indicates that the number of dots generated for the sign face has been reduced caused by the beam reflection from the water droplets. Studies have shown a decrease in overall object detection quality and blurring contours as a result of rain-induced interference.

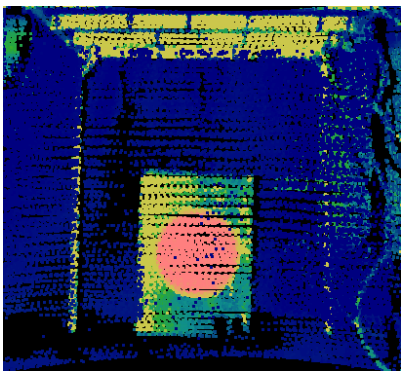

Fig. 1. A section of a point cloud generated by lidar during a study of the impact of high-intensity rain

As part of the second part of the study, the effects on the point cloud generated by the lidar were investigated which has been created by a splash of water is observed behind a vehicle travelling on wet pavement. An existing test rig was modified to capture by lidar the water cloud formed behind one of the rear wheels of the vehicle. A driving speed of approximately 36 km/h was simulated. In the tests, the movement of the air masses surrounding the vehicle (using a blower) were assumed too. Figure 2 shows a section of the point cloud generated by the lidar.

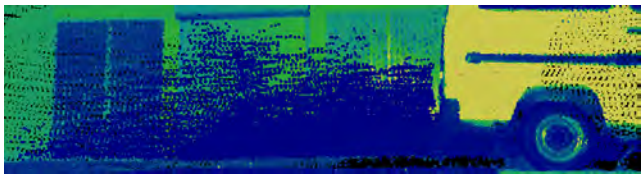

Fig. 2. A section of the point cloud generated by the lidar during the investigation of the water splash by the wheel

The cloud of blue points visible behind the vehicle is the result of the laser beam reflecting off the water droplets. This cloud significantly obscures objects behind it.

The study of the effect of fog on lidar performance, was carried out on a test stand located inside a building. Some limitation for the tests was the small size of the room; however, even under such specific conditions, it was possible to observe the effect of fog on sensor performance. Targets with high reflection index were positioned at a distance of 6 m from the sensor, and reference posts allowed the level of visibility to be determined. The view of the targets which was beam-illuminated of the lidar is shown in Fig. 3.

As part of the tests carried out, visibility was progressively reduced, to the point of complete absence, by fog. As the opacity was gradually increased (for this purpose, steam from heating the water-glycol mixture was sprayed), a decrease in the visibility level of observed objects. The reflectivity index has been measured. The maximum achievable

reflectivity index was 255, and the lowest was 10. The differences in the measured index value, for the different levels of visibility (smoke), are shown in Fig. 4.

Fig. 3. Test stand for measuring the effects of fog on lidar performance

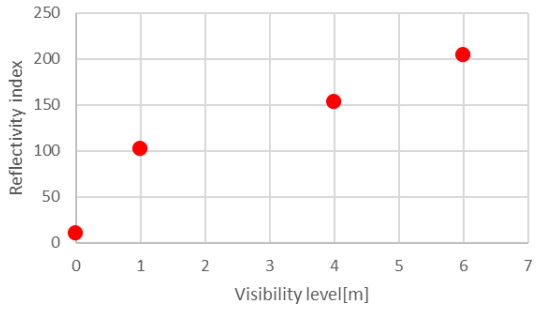

Fig. 4. Dependence of reflectivity on visibility level

Reflection index readings were taken at irregular intervals as it proved very difficult to obtain a specific level of visibility under the conditions of the actual experiment. Maintaining an evenly distributed artificial fog on a test rig is a challenge in itself.

The study showed that the decrease in reflectivity as a function of distance is nonlinear. However, it can be assumed that the greater the opacity, the steeper the drop in the reflectivity value. During the almost completely smoke-filled room (visibility less than 1 m), the lidar could still see the target, although the reflectivity index of them has dropped to a level of 10.

When investigating the effect of snowfall on lidar performance, it was decided to use naturally occurring atmospheric conditions, the falling snow had an intensity of about 5 mm/h with visibility below 800 meters. Such conditions, are considered high intensity precipitation [9]. A series of experiments were conducted with targets placed at different distances from the lidar (5, 10, 15 m). As the distance increased, an increase in snow-induced interference was observed. The effect caused by snow is very similar to that generated by rain – the laser beam reflects off snow-flakes swirling in the air, causing unreal points obscuring the target. The characteristic blue points caused by falling snow are shown in Fig. 5. The picture shows a large disturbance caused by snowflakes.

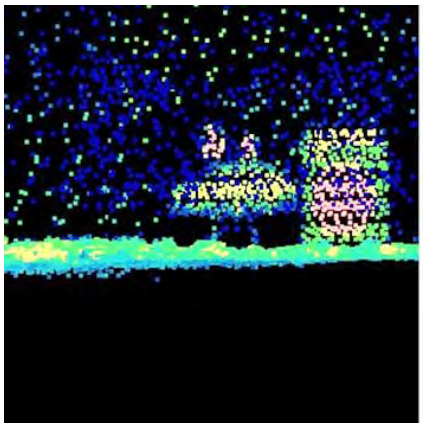

Fig. 5. A section of a point cloud generated by lidar during a snowfall impact study

4. Analysis of the measurement results

Developing a methodology to accurately assess the impact of changing atmospheric conditions on lidar is difficult because the difficulty is in repeating exactly the same conditions for each experiment. This is because it is necessary to take into account not only the repeatability of the distance, but also the position of targets, relative to the sensor, the angle of incidence of the laser beam, the height of the targets, interference from, wind and other disturbances. Despite these difficulties, efforts have been made to develop an in-house detection algorithm that can be used to assess the magnitude of interference. This algorithm has already been used successfully in previous work [7]. It works on the basis of a two-dimensional point cloud image, and uses information from lidar about the reflectivity index of a given object points. Objects with a high reflectivity index are displayed as red, while those at the other end of the scale (objects that reflect the laser beam poorly) are shown as blue. Once the survey area has been delineated, the program analyses the image for the presence of the specified pixel colour – this colour must first be read from an image sample or otherwise determined. The bright red colour of the sign shield read from the image has RGB components of 255. 97. 89. The program allows a colour selection tolerance to be set, e.g. by setting a tolerance of 10, the program will label the pixels not only with the RGB colour 255.97.89, but also e.g. 245.105.95 or 250.87.79. After the initial identification of the pixels meeting the colour criterion, the program applies a mask filter. This filter increases the area to be analysed from one pixel (1 × 1) to a three-by-three pixels area (3 × 3). A field is marked as it fulfil the colour criterion if at least half of the pixels in it fulfil this criterion. The mask filter was introduced to improve detection quality, which has been confirmed by tests. The operation of the algorithm can be described by the following formula. A given pixel is marked if it meets the condition:

$$W(i) = \begin{cases} 1 \text{ when } R\mp < T, G\mp < T, B\mp < T \\ 0 \text{ when } R\mp > T, G\mp > T, B\mp > T \end{cases} \quad (1)$$

where T is the colour selection tolerance. Area O (3 × 3 pixels) is then highlighted in red if:

$$\sum_{i=1}^{9} W(i) \geq 5;\ i = 1, \ldots 9 \quad (2)$$

When testing the effect of rain, for the reference measurement 1640 pixels have been matched to the object surface. Comparing the number of identified pixels to the reference number, tests carried out for rain intensities ranging from about 5 mm/h to more than 30 mm/h have shown the interference rate was between 11% and 25%. It should be noted that the rain not only reduced the total number of identified pixels, but also distorted the image of the targets. Potentially, this effect could also hinder object identification. However, it is difficult to measure.

Investigations of the splash of water from under the wheels showed that, for an air speed around the car of about 36 km/h, the water cloud assumes a size of ~ 2.23 m × 1.10 m, and the number of points formed by the reflection of the laser beam from the water droplets was 68446. Which accounts for almost 30% of all generated points by lidar. Thus, the water cloud formed behind the vehicle when driving on wet pavement (or during rainfall) represents a significant disturbance in the picture, somewhat resembling very high-intensity rain.

The falling snow caused a very noticeable reduction in the number of identified pixels on the lidar picture. As the distance increased, the visibility of the targets decreased. There is an overlap between two phenomena: a general decrease in the number of points generated for objects further away from the sensor and an accumulation of disruption caused by snow-flakes. Changing the measurement distance from 10 to 15 m with snow intensity of about 5 mm/h resulted in a 22% decrease in visibility level. The effect caused by snow is essentially similar to that caused by rain.

When examining the effect of fog on the lidar operation, the number of pixels visible to the sign face did not change, Thus, it is impossible to determine the impact of disturbances. The effect that fog causes on lidar performance is different from that caused by rain or snow. While raindrops or snowflakes reflect the laser beam and cause unreal points, fine fog droplets do not reflect the beam but cause a decrease in its energy. This effect was very evident in the tests carried out.

Table 3 summarizes the impact of the different weather conditions on lidar performance. As shown in Table 3, heavy rain and snow have the most negative effects on the lidar operation.

Table 3. Impact of the different weather conditions on lidar performance

Phenomenon	Effect
Light rain	Decrease in reflectivity index
Heavy rain	Decrease in reflectivity index, Formation of phantom points, deformation of the shape of objects
Light snow	Decrease in reflectivity index, deformation of the shape of objects
Heavy snow	Decrease in reflectivity index, Formation of phantom points, deformation of the shape of objects
Rare fog	Decrease in reflectivity index
Dense fog	Almost total lack of visibility of targets

5. Counteracting the effects of adverse weather conditions on lidar operation

Based on research into the impact of weather conditions on lidar operation, it was found that the effect can be both an overall decrease in the reflectivity index and the formation of unreal low-intensity points on the lidar picture. Methods to counteract the effect of adverse weather conditions on lidar performance can be divided into:

– equipment optimization which is general improvement of the technical performance of the equipment
– use of advanced filtering algorithms, aimed primarily at removing low intensity points.

An example of optimizing lidar technical parameters could be: selecting the optimal wavelength, adjusting possible power levels and optimizing optical and electronic components [21]. For example, a way to solve the problem of lidar operation in fog, could be to use lidars with a wavelength of 1550 nm. According to this, the longer wavelength scatters less in the fog with less loss of beam energy, resulting in an increased reflectivity index [20].

A much more developed group of methods are filtration algorithms. In order to apply an additional algorithm to facilitate image analysis, it is necessary to first correctly identify the atmospheric phenomenon in question, which is a difficulty in itself [4]. An example of a filtering algorithm is an algorithm that restores the reflectivity index [1]. This uses different types of filters (e.g. particle filters) optimizing lidar performance for wet surfaces [40]. As an example of another method, a system comparing the position of a given point on successive scans can be used. Authors Hahner et al [17], on the other hand, propose their own filtering algorithm to improve object detection quality during snowfall. The authors used point clouds on which they had independently simulated snow for their study.

Also, camera operation during adverse weather conditions can be improved. Examples of optimization for greater reliability include the use of polarization filters in cameras and other techniques based on polarimetry [11, 32]. According to Blin and Ainouz, the use of polarimetry increases the quality of object detection in difficult conditions by up to 20% [5]. Another method is the use of infrared cameras or cameras whose operation is combined with the action of a laser (gated camera) [4, 38]. An example of an algorithm that improves the quality of the camera image can be the method of determinants. An experiment shows that this method actually works and increases object detection accuracy by more than 2% [15]. Other methods involve removing rain from the image. Examples of algorithms working in this way are: DDN [14], DeRaindrop [28], PreNet [30], UNIT [23]. Algorithms of this type are designed to remove the effects of rain and restore the image to a version undisturbed by drops and streams, thereby increasing image quality and the amount of visible detail.

As part of the research work, some researchers are proposing combining data obtained from different sensors as a solution to problems arising from bad weather conditions. This work deliberately does not approximate such research. In the authors' opinion, combining data from different sensors is not a solution, just a way around the problem. Though, such methods, have been presented in an earlier paper on autonomous cars [7, 8].

6. Conclusions

Studies reported within the literature show that the extent to which adverse weather affects objects detection quality varies. This is due to both the nature of the atmos-

pheric phenomenon in question and the detection algorithm used, and finally the parameters of the device itself. Although an official methodology for testing such types of sensors has not yet been developed, this paper compiles the results of Authors' own tests, carried out using the same sensor (Livox Horizon Lidar), in an attempt to replicate actual conditions as accurately as possible. Both the results obtained from our own research and information from other researchers show that the impact of adverse weather conditions on the performance of autonomous car sensors is significant and needs to be addressed. Work on minimizing this impact, comes down primarily to hardware optimization and the use of filtering algorithms. Based on the – Solving the problems associated with the operation of ambient sensors in harsh atmospheric conditions, is necessary for the introduction of vehicles to level 4 autonomy.

- The correct identification of an atmospheric phenomenon is crucial not only for the sensors of an autonomous car, but also for its control system, as it makes it possible to take into account, for example, the decreasing grip coefficient of the tires when planning the traffic path.
- Low-intensity rain poses little disruption to the lidar, while medium and heavy rain reduces the number of detected pixels by up to 24.6%.
- The reflection of the laser beam from water droplets in the air creates unreal points with a low reflection intensity index. This effect also occurs during snowfall.
- The water cloud formed behind the wheels of a vehicle travelling on wet pavement, at urban speeds, assumes a size of more than 4 m^2.
- Water in the form of rain or snow on surfaces negatively affects the reflectivity of the laser beam, which can lead to blurred shapes. Largely accumulated snow can strongly alter the shape of an object, making it impossible to identify.
- During heavy snowfall, a road sign with a diameter of 50 cm at a distance of 15 m from the sensor is already poorly visible. This applies to both the camera and the lidar (when viewed straight ahead in two-dimensional space). This clearly impedes the movement of the autonomous vehicle.
- Snow and rain cause formation of unreal (phantom) points, while fog causes a reduction in the reflectivity index from objects. This decrease is nonlinear. In fog, when the observer or camera is no longer able to see the targets, the laser beam continues to reflect off them. Although the reflectivity index of such points is low, the lidar still sees the targets, which gives a considerable advantage over the camera, which is by then completely ineffective.
- Various attempts are being made to counteract the effects of atmospheric conditions on the sensors of an autonomous car. These methods are divided into hardware optimization and the use of filter algorithms.
- Selecting the right filter algorithm for each weather phenomenon can have the effect of negating part of the negative effect caused by bad weather.

Ongoing research shows the importance of the problem of how weather conditions affect the performance of autonomous vehicle sensors. Without solving this problem with fast filtering algorithms, it is not possible to reach SAE Level 4 of autonomous vehicle traffic. In the authors opinion of the authors, further activities should focus primarily on a thorough understanding of individual atmospheric phenomena and the preparation of appropriate correction algorithms.

Acknowledgements

This work was done in Department of Internal Combustion Engines and Vehicles of Bielsko-Biala University.

Nomenclature

DATMO	Detection and Tracking of Moving Objects	ADAS	Advanced Driving Assist Systems
SLAM	Simultaneous Localization and Mapping		

Bibliography

[1] Aldibaja M, Suganuma N, Yoneda K. Improving localization accuracy for autonomous driving in snow-rain environments, International Symposium on System Integration. 2016:212-217. https://doi.org/10.1109/SII.2016.7844000

[2] Anderson J, Kalra N, Stanley K, Sorensen P, Samaras C, Oluwatola T. Autonomous vehicle technology a guide for policymakers. Publisher Rand Corporation 2014.

[3] Bertolazzi E, Frego M, Biral F. Point data reconstruction and smoothing using cubic splines and clusterization. Math Comput Simulat. 2020;176:36-56. https://doi.org/10.1016/j.matcom.2020.04.002

[4] Bijelic M, Gruber T, Ritter W. Benchmarking image sensors under adverse weather conditions for autonomous driving. IEEE Int Veh Sym. 2018:1773-1779. https://doi.org/10.1109/IVS.2018.8500659

[5] Blin R, Ainouz S, Canu S, Meriaudeau F. Road scenes analysis in adverse weather conditions by polarization-encoded images and adapted deep learning, IEEE Int C Intell Tr. 2019:27-32. https://doi.org/10.1109/ITSC.2019.8916853

[6] Brummelen J, O'Brien M, Gruyer D, Najjaran H. Autonomous vehicle perception: the technology of today and tomorrow, transport. Res. C-Emer. 2018;89:384-40. https://doi.org/10.1016/j.trc.2018.02.012

[7] Brzozowski M, Parczewski K. Validating adverse weather influence on LiDAR with an outdoor rain simulator. TRANSBALTICA XIII: Transportation Science and Technology. 2023:12-22. https://doi.org/10.1007/978-3-031-25863-3

[8] Brzozowski M. Autonomous cars, environmental sensors and problems of perception. Publisher House in ATH Bielsko-Biała. Bielsko-Biala 2023 (in Polish).

[9] Colomb M, Duthon P, Laukkanen S. Characteristics of adverse weather conditions. DENSE 2021. https://www.dense247.eu/fileadmin/user_upload/PDF/DENSE_D2.1_Characteristics_of_Adverse_Weather_Conditions.pdf (accessed on 2023.04.07)

[10] Druml N, Maksymova I, Thurner T, Lierop D, Hannecke M, Foroutan A. 1D MEMS micro-scanning Lidar. International

Conference on Sensor Device Technologies and Applications, Italy. 2018. https://www.researchgate.net/publication/326632441_1D_MEMS_MicroScanning_Lidar#fullTextFileContent
[11] Farahnakian F, Heikkonen J. Deep learning based multi-modal fusion architectures for maritime vessel detection. Rem Sens. 2020:2509. https://doi.org/10.3390/rs12162509
[12] Ferreira J, Martins A, Monteiro V. Intelligent transport systems, from research and development to the market uptake, Challenges in Object Detection Under Rainy Weather Conditions. Publisher Springer 2018.
[13] Filgueira A, González-Jorge H, Lagüela S, Díaz-Vilariño L, Arias P. Quantifying the influence of rain in Lidar performance. Measurement. 2017;95:143-148. https://doi.org/10.1016/j.measurement.2016.10.009
[14] Fu X, Huang J, Zeng D, Huang Y, Ding X, Paisley J. Removing rain from single images via a deep detail network. Proc Cvpr IEEE. 2017:3855-3863. https://doi.org/10.1109/CVPR.2017.186
[15] Gehriga S, Schneidera N, Stalderb R, Franke U. Stereo vision during adverse weather – using priors to increase robustness in real-time stereo vision. Image Vision Comput. 2017;68:28-39. https://doi.org/10.1016/j.imavis.2017.07.008
[16] Hadj-Bachir M, de Souza P. LIDAR sensor simulation in adverse weather condition for driving assistance development. 2019. https://hal.archives-ouvertes.fr/hal-01998668/document (accesed on 2023.04.17).
[17] Hahner M, Sakaridis C, Bijelic M, Heide F, Yu F, Dai D et al. LiDAR snowfall simulation for robust 3D object detection, CVF. arXiv. 2203:15118. https://doi.org/10.48550/arXiv.2203.15118
[18] Hespel L, Riviere N, Huet T, Tanguy B, Ceolato R. Performance evaluation of laser scanners through the atmosphere with adverse condition. The International Society for Optical Engineering. 2011. https://doi.org/10.1117/12.898010
[19] Jokela M, Kutila M, Pyykönen P. Testing and validation of automotive point-cloud sensors in adverse weather conditions, Appl. Sci. 2019;9:2341. https://doi.org/10.3390/app9112341
[20] Kutila M, Pyykonen P, Holzhuter H, Colomb M, Duthon P. Automotive Lidar performance verification in fog and rain. IIEEE Int C Intell Tr. 2018:1695-1701. https://doi.org/10.1109/ITSC.2018.8569624
[21] Kutila M, Pyykönen P, Ritter W, Sawade O, Schaufele B. Automotive LIDAR sensor development scenarios for harsh weather conditions. IIEEE Int C Intell Tr. 2016:265-270. https://doi.org/10.1109/ITSC.2016.7795565
[22] Li S, Li G, Yu J, Liu C, Cheng B, Wang J et al. Kalman filter-based tracking of moving objects using linear ultrasonic sensor array for road vehicles. Mech Syst Signal Pr. 2018;98:173-189. https://doi.org/10.1016/j.ymssp.2017.04.041
[23] Liu M-Y, Breuel T, Kautz J. Unsupervised image-to-image translation networks. Adv Neur In. 2017:700-708. https://doi.org/10.48550/arXiv.1703.00848
[24] Maurer M, Gerdes J, Lenz B, Winner H. Autonomous driving technical, legal and social aspects. Publisher Springer 2016.
[25] Ondruš J, Kolla E, Vertaľ P, Šarić Z. How do autonomous cars work? Transp Res Proc. 2020;44:226-233. https://doi.org/10.1016/j.trpro.2020.02.049
[26] Parczewski K, Romaniszyn K, Wnęk H. Influence of electric motors assembly in hubs of vehicle wheels on the dynamics of movement, especially on surfaces with different adhesion coefficient. Combustion Engines. 2019;179(4):58-64. https://doi.org/10.19206/CE-2019-409
[27] Porębski J, Kogut K, Markiewicz P, Skruch P. Occupancy grid for static environment perception in series automotive applications, IFAC PapersOnLine. 2019;52:148-153. https://doi.org/10.1016/j.ifacol.2019.08.063
[28] Qian R, Tan RT, Yang W, Su J, Liu J. Attentive generative adversarial network for raindrop removal from a single image. Proc Cvpr IEEE. 2018:2482-2491. https://doi.org/10.48550/arXiv.1711.10098
[29] Rasshofer RH, Spies M, Spies H. Influences of weather phenomena on automotive laser radar systems. Adv Radio Sci. 2011;9:49-60. https://doi.org/10.5194/ars-9-49-2011
[30] Ren D, Zuo W, Hu Q, Zhu P, Meng D. Progressive image deraining networks: a better and simpler baseline. Proceedings of the Proc Cvpr IEEE. 2019:3937-3946. https://doi.org/10.48550/arXiv.1901.09221
[31] SAE International. 2021. Last accessed: 2023-05-08. https://www.sae.org/news/press-room/2018/12/sae-international-releases-updated-visual-chart-for-its-%E2%80%9Clevels-of-driving-automation%E2%80%9D-standard-for-self-driving-vehicles
[32] Schechner Y, Narasimhan S, Nayar S. Instant dehazing of images using polarization. Proc Cvpr IEEE. 2001;1:325-332. https://doi.org/10.1109/CVPR.2001.990493
[33] Shit R. Precise localization for achieving next-generation autonomous navigation: state-of-the-art, taxonomy and future prospects. Computer Communications. 2020;160:351-374. https://doi.org/10.1016/j.comcom.2020.06.007
[34] Sjafire H. Introduction to self-driving vehicle technology. Publisher Chapman and Hall 2020.
[35] Slutsky M, Dobkin D. Dual inverse sensor model for radar occupancy grids. IEEE Int Veh Sym. 2019:1550-1557. https://doi.org/10.1109/IVS.2019.8813772
[36] Wang X, Wang W, Yin X, Xiang C, Zhang Y. A new grid map construction method for autonomous vehicles. IFAC PapersOnLine. 2018:377-382. https://doi.org/10.1016/j.ifacol.2018.10.077
[37] Wojtanowski J, Zygmunt M, Kaszczuk M, Mierczyk Z, Muzal M. Comparison of 905 nm and 1550 nm semiconductor laser rangefinders' performance deterioration due to adverse environmental conditions. Opto-Electron Rev. 2014;22(3): 183-190. https://doi.org/10.2478/s11772-014-0190-2
[38] Yoneda K, Suganuma N, Yanase R, Aldibaja M. Automated driving recognition technologies for adverse weather conditions. IATSS Research. 2019;43:253-262. https://doi.org/10.1016/j.iatssr.2019.11.005
[39] Zang S, Ding M. The impact of adverse weather conditions on autonomous vehicles: examining how rain, snow, fog, and hail affect the performance of a self-driving car. Vehicular Technology Magazine. 2019;99:1. https://doi.org/10.1109/MVT.2019.2892497
[40] Zhang C, Ang MH, Rus D. Robust LIDAR localization for autonomous driving in rain. IEEE Int C Int Robot. 2018:3409-3415. https://doi.org/10.1109/IROS.2018.8593703
[41] Zimmermann M, Wotawa F. An adaptive system for autonomous driving. Software Qual J. 2020;28:1189-1212. https://doi.org/10.1007/s11219-020-09519-w

Michał Brzozowski, MEng. – Faculty of Mechanical Engineering and Computer Science, University of Bielsko-Biała, Poland.
e-mail: *mbrzozowski@ath.bielsko.pl*

Krzysztof Parczewski, DSc., DEng. – Faculty of Mechanical Engineering and Computer Science, University of Bielsko-Biała, Poland.
e-mail: *kparczewski@ath.bielsko*

Article citation info:
Samoilenko D, Savchenko A, Kravchenko S. Improving the performance of diesel engines fueled with water-fuel emulsion. Combustion Engines. 2023;194(3):116-122. https://doi.org/10.19206/CE-169139

Dmytro SAMOILENKO
Anatolii SAVCHENKO
Serhii KRAVCHENKO

Combustion Engines
Polish Scientific Society of Combustion Engines

Improving the performance of diesel engines fueled with water-fuel emulsion

ARTICLE INFO

Received: 31 May 2023
Revised: 27 June 2023
Accepted: 1 July 2023
Available online: 20 July 2023

Due to unique properties, production and operation features, water-fuel emulsion (WFE) could be considered as one of the most promising type of alternative fuels for diesel engines. Experimental research showed that compared to traditional diesel fuel, application of water-fuel emulsion allows to reduce nitrogen oxides and soot emissions, which is due primarily to a decrease in the level of maximum temperatures in the engine cylinder, as well as a more uniform distribution of fuel over the combustion chamber volume thanks to its secondary dispersion (micro-explosion phenomena). To control the stability of water-fuel emulsion properties during engine operation it is recommended to install water content sensor in the fuel supply system.

Key words: *diesel, water-fuel emulsion, combustion process, micro-explosion, water particles size distribution*

1. Introduction

Over a long period of time, internal combustion engines have become widespread in all spheres of human activity, which is explained by their numerous advantages. However, it is the extremely wide application of ICE has caused a number of global problems, related to the depletion of world oil reserves, atmospheric pollution with toxic substances, global warming etc. There is a solution that allows to partially solve the mentioned problems through application of alternative fuels in internal combustion engines [3, 7, 10, 13, 15]. In this content a water-fuel emulsion (WFE) could be treated as one of the most promising type of alternative fuels due to the combination of the unique properties, characteristics, production and operation features [1, 2, 5, 14]. The main advantages of WFE are as follows: reduction of average effective fuel consumption, a significant reduction in emissions of soot and nitrogen oxides in exhaust gases of diesel engines [2, 4, 5, 14], the absence of the need to make changes in the engine design, the possibility of large-scale fuel production and relative simplicity of its production [9, 14].

There is a number of theoretical research on numerical simulations of spark ignition and diesel engines fueled with water-fuel emulsion using AVL Boost simulation software that are shown in [6, 11, 12]. According to numerous studies, the use of WFE makes it possible to reduce emissions of nitrogen oxides by up to 50...80%, reduce soot emissions by up to 35%, and improve diesel fuel efficiency by 3...5% [1, 2, 5].

Experimental studies indicate a noticeable decrease in the temperature of exhaust gases when water-fuel emulsion is used [4, 14]. This is mainly due to additional heat consumed for heating and evaporation of water contained in the WFE (compared to original diesel fuel), as well as an increase in the mass and specific heat capacity of the combustible fluid inside of the cylinder. Decrease in the exhaust gas temperature at the inlet to the turbine of the turbocharger can potentially cause a drop in air pressure in the intake manifold of the diesel engine. As a result, the air excess factor should decrease as well, which in turn has a strong influence on the combustion process. However, experimental studies showed improvement in fuel combustion characteristics when WFE with a moderate water content (no more than 20...25%) is used. Thus, the potential reduction in the amount of fresh air delivered (due to the decrease in boost pressure) is fully compensated by the improvement in uniformity of liquid fuel distribution over the volume of the combustion chamber thanks to the micro-explosion phenomenon [8].

2. The influence of the properties of the water-fuel emulsion on the performance of the diesel engine

To determine the effect of WFE on diesel engine performance, experiments were conducted on compression ignition engine fueled with standard diesel fuel and water-fuel emulsions. WFE was characterized by 15 % of water content (by mass units). The specification of the experimental diesel engine is given in Table 1. The properties of diesel fuel and WFE, that were used in the study, are shown in Table 2.

Table 1. Technical characteristics of the experimental engine

Engine parameter	Value
Number of cylinders	4 (in-line)
Cylinder diameter, mm	120
Piston stroke, mm	140
Compression ratio	15.5
Nominal power, kW	100
Nominal crankshaft rotational speed, rpm	2000
Maximum torque, N·m	632

Table 2. Physical, chemical properties of DF and WFE used in the study

Parameter	Diesel Fuel	Water-fuel emulsion
Density at temperature of 15ºC, kg/m^3	829	857
Heat capacity, kJ/kg·K	2.02	2.37
Low calorific value of the fuel, kJ/kg	42,500	35,100
The ignition temperature in a closed crucible (no lower than), ºC	70.5	ignition is missing
Water content by mass, %	0	15
Kinematic viscosity at temperature of 20ºC, mm^2/s	5.15	6.19

The results of experimental study where the effect of using WFE on fuel efficiency and toxic substances emissions were established are given in Table 3 and Table 4. Effective efficiency of the engine was chosen as a criterion of fuel efficiency in this study.

Table 3. Indices of the CI engine fueled with a standard diesel fuel

n, rpm	P_e, MPa	η_e	W_{NOx}, ppm	W_{CO}, ppm	W_{CH}, ppm	Soot, opacity in %
2000	0.95	0.3873	850	260	90	16.90
	0.7	0.3687	520	240	100	13.7
	0.474	0.3359	350	250	120	10.8
	0.24	0.2611	210	300	135	5.5
	0.099	0.1541	145	430	170	3.4
1500	1.076	0.4117	1380	300	90	24.2
	0.809	0.4088	1255	170	115	13.8
	0.544	0.3791	840	130	140	9.4
	0.279	0.3099	365	200	175	5.1
	0.14	0.2223	190	320	210	2.6
1000	0.752	0.3962	1410	620	105	40
	0.558	0.3892	1180	430	120	27.5
	0.377	0.3642	940	330	150	11
	0.181	0.291	305	440	195	4.5
	0.098	0.2138	175	570	240	2.2

Table 4. Indices of the CI engine fueled with WFE

n, rpm	P_e, MPa	η_e	W_{NOx}, ppm	W_{CO}, ppm	W_{CH}, ppm	Soot, opacity in %
2000	0.95	0.4072	725	180	100	11.9
	0.7	0.4025	425	150	105	7.7
	0.474	0.3615	270	170	120	5.1
	0.24	0.2731	120	240	140	2.6
	0.099	0.1611	70	330	180	1.5
1500	1.076	0.4414	1145	220	90	16.1
	0.809	0.433	995	140	100	10.1
	0.544	0.4108	697	110	135	5.2
	0.279	0.3393	257	160	175	1.9
	0.14	0.2416	128	250	200	1.2
1000	0.752	0.4188	845	490	125	29.5
	0.558	0.4168	690	350	135	16.5
	0.377	0.3906	514	250	160	8.4
	0.181	0.3105	160	400	210	3.6
	0.098	0.218	60	490	265	1.8

As it can be seen from Table 3 and Table 4 application of WFE makes it possible to reduce soot from exhaust gases by 18...56%. Moreover, at a high crankshaft rotation speed, the positive effect of WFE application on soot emission is greater than at a low crankshaft rotation speed.

At all investigated modes, the concentration of nitrogen oxides decreased by 14...66% when WFE was used. The maximum reduction in nitrogen oxide emissions refers to low-load modes. It can be also seen that the use of water-fuel emulsion helps to increase the effective efficiency from 0,7 to 3,4% depending on the load and crankshaft rotation speed.

3. The influence of the application of the water-fuel emulsion on mixture formation and combustion process in diesel engine

The influence of application of WFE on the processes of mixture formation, combustion and exploitation of the diesel engine was evaluated by comparing a number of indicators of the engine cycle in ICE running on WFE and traditional diesel fuel at the same operating modes.

As it can be seen from the indicator diagrams (Fig. 1) the maximum pressure in the cycle is greater for diesel running on traditional DF when compared to WFE. At the same time, there are differences in pressure increase rate that could be observed from the moment of the start of combustion till the moment of reaching the maximum pressure. To identify the reasons for these differences, the processes of fuel injection and combustion were analyzed. From the given dependences of the change in fuel pressure at the injector inlet on the crankshaft rotation angle (Fig. 2), it can be seen that the start of injection for WFE and DF is almost the same. A little earlier start of DF injection could be explained by its lower compressibility. Injection of WFE lasts longer for 3…5 degrees of crank angle. It could be explained by increased fuel supply per cycle for the same power. As a result of increased fuel supply in one cycle and higher fuel viscosity, the maximum injection pressure of WFE increases by 14–18%, which can lead to an improvement in the fuel atomization process.

In-cylinder temperature dependences for diesel engine running on DF and WFE are shown in Fig. 3. It can be seen that the maximum temperature in the cylinder decreases by 15–30 K when WFE is used. The specified decrease in temperature level is explained by the increased heat capacity of the water-fuel emulsion (Table 2) which will be resulted in the increased amount of heat consumed for fuel heating and its evaporation. Reduction in the maximum temperature of the cycle has a positive effect on nitrogen oxide emissions that was confirmed by the previous experimental studies where WFE was used as a fuel for diesel engines.

Further analysis was conducted based on heat release rate dependences that are shown in Fig. 4. As it can be seen from the Fig, the release of heat in the engine cylinder starts with a 3..5 crank angle delay when WFE is used. Taking into account the almost identical moment of the start of injection for both types of fuels, the increase in the ignition delay period by 2…4 crank angles can be explained by an increase in activation energy of fuel combustion and a decrease in temperature and pressure inside of the cylinder at the beginning of fuel injection process when WFE is used.

According to Fig. 4, the heat release rate as well as the area under the heat release curve at the second combustion phase (premixed combustion) is greater for WFE. It can be explained by the fact that a larger amount of diesel-water emulsion fuel will evaporate during a comparatively longer ignition delay period. Accordingly, the share of fuel burning during the second combustion phase and the rate of heat release during this phase increases.

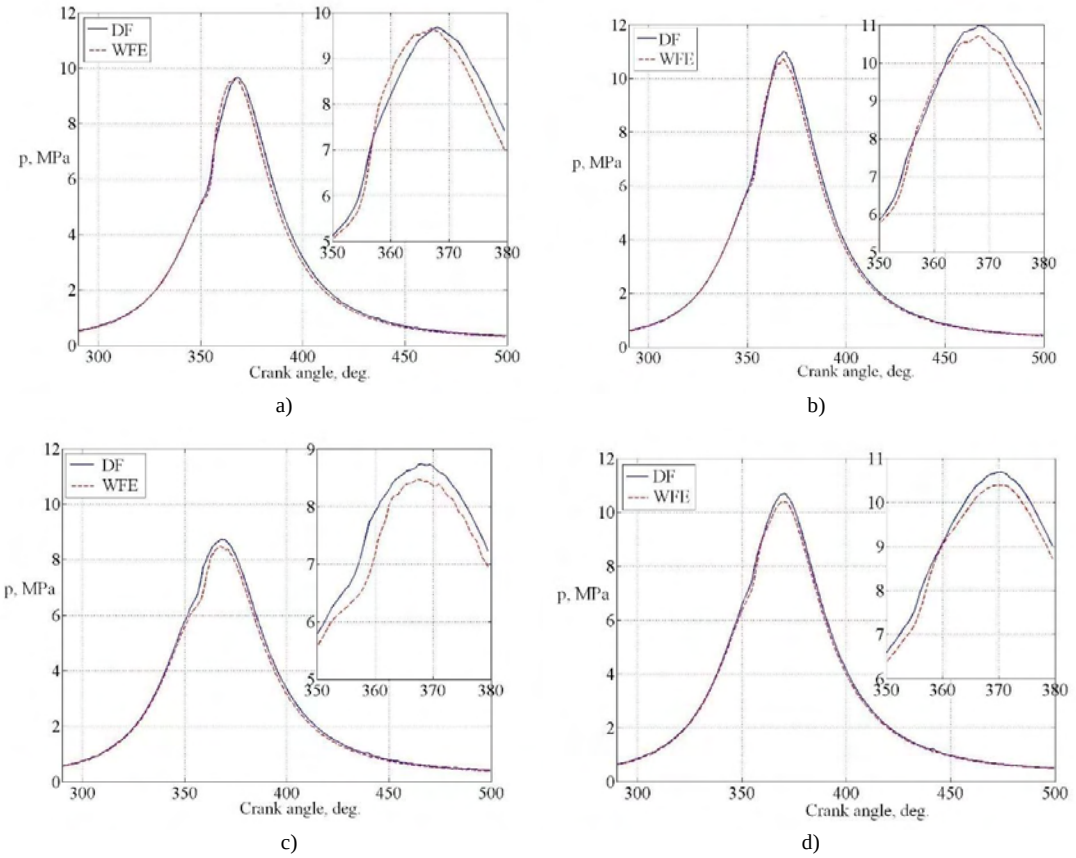

Fig. 1. Indicator diagrams of a diesel engine running on DF and WFE: a) n = 1500 rpm, P_e = 0.809 MPa; b) n = 1500 rpm, P_e = 1.076 MPa; c) n = 2000 rpm, P_e = 0.71 MPa; d) n = 2000 rpm, P_e = 0.95 MPa

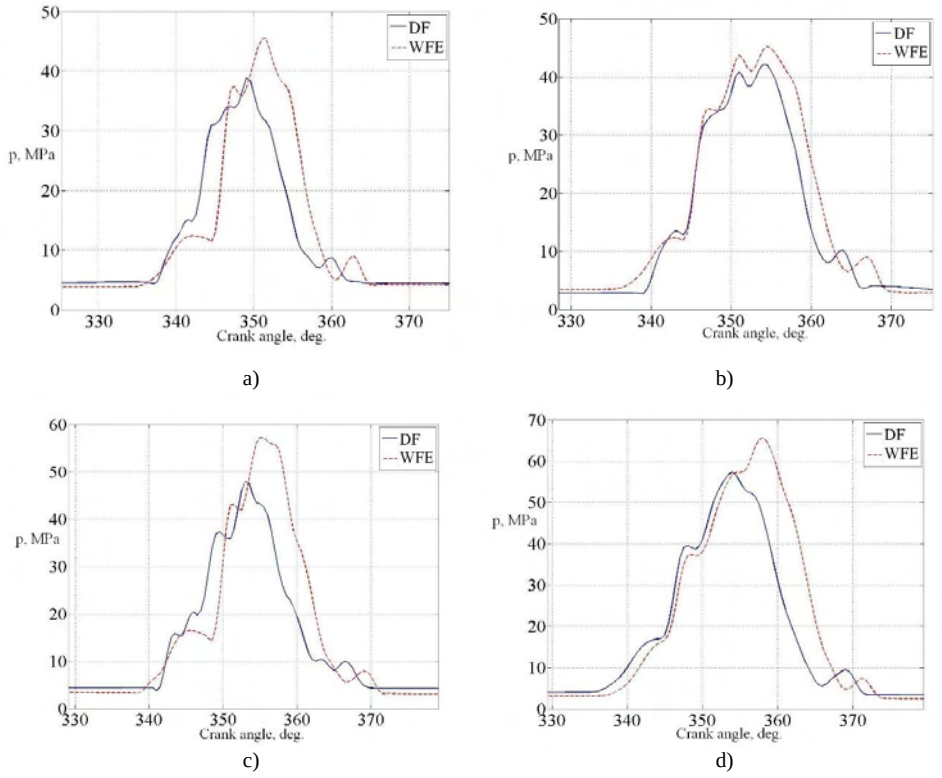

Fig. 2. Fuel pressure at the injector inlet for diesel engine running on DF and WFE: a) n = 1500 rpm, P_e = 0.809 MPa; b) n = 1500 rpm, P_e = 1.076 MPa; c) n = 2000 rpm, P_e = 0.71 MPa; d) n = 2000 rpm, P_e = 0.95 MPa

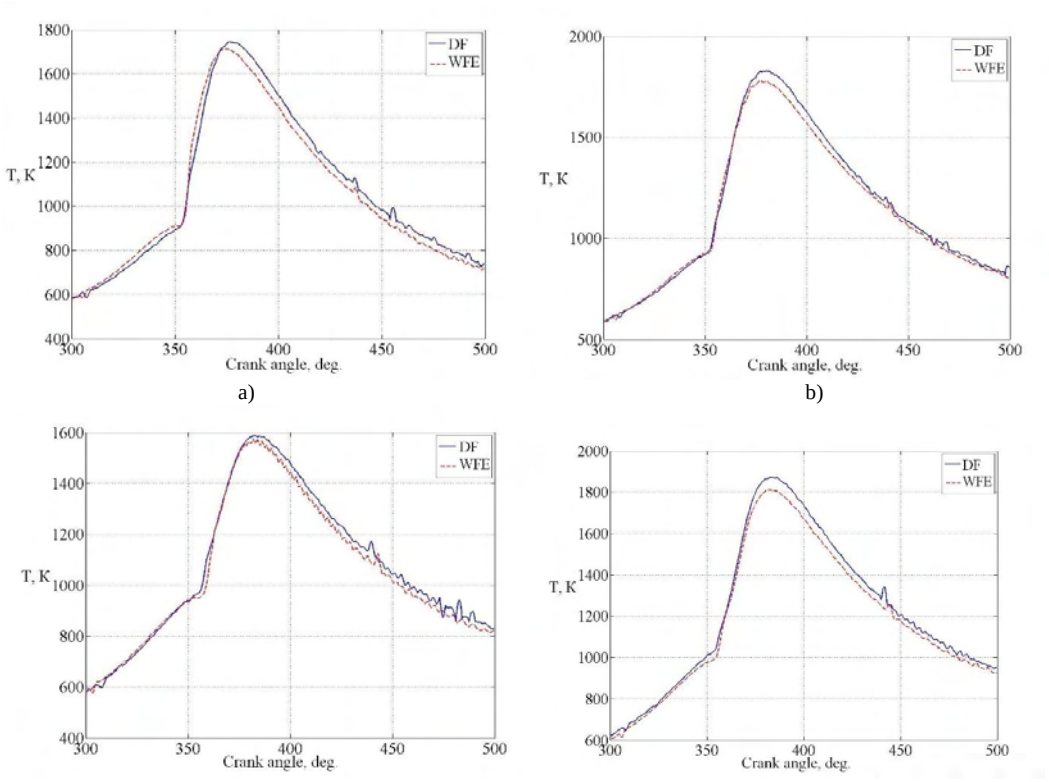

Fig. 3. In-cylinder temperature for diesel engine running on DF and WFE: a) n = 1500 rpm, P_e = 0.809 MPa; b) n = 1500 rpm, P_e = 1.076 MPa; c) n = 2000 rpm, P_e = 0.71 MPa; d) n = 2000 rpm, P_e = 0.95 MPa

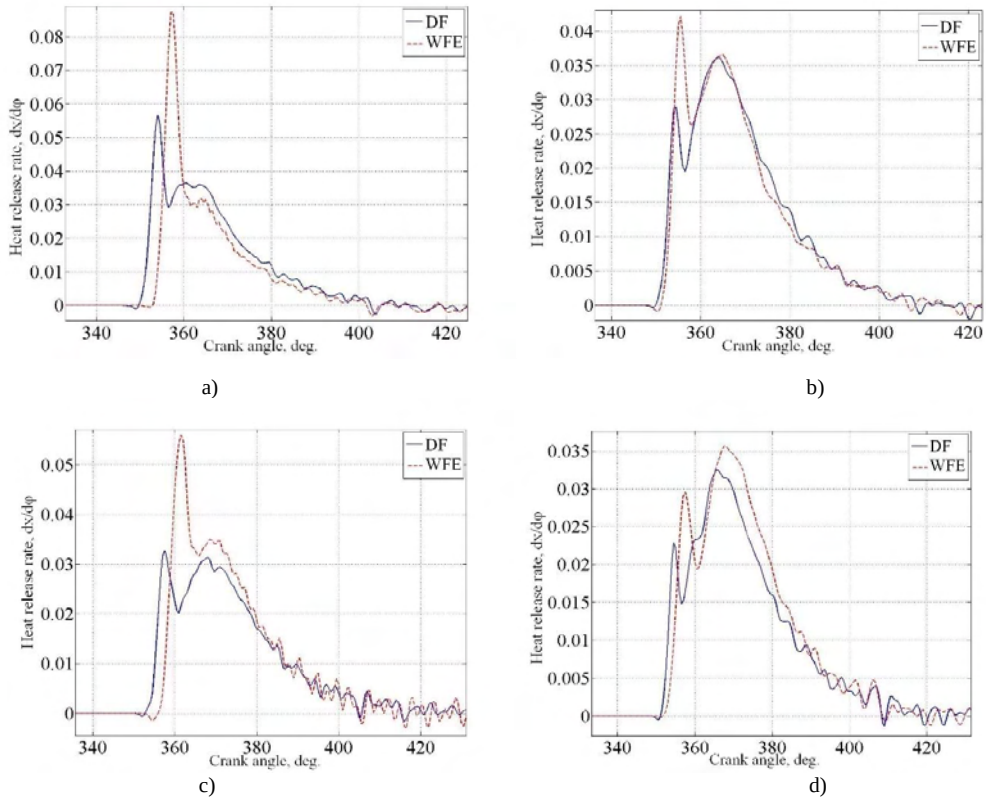

Fig. 4. Dependences of heat release rate on crank angle for diesel engine running on DF and WFE: a) n = 1500 rpm, P_e = 0.809 MPa; b) n = 1500 rpm, P_e = 1.076 MPa; c) n = 2000 rpm, P_e = 0.71 MPa; d) n = 2000 rpm, P_e = 0.95 MPa

The analysis of the mixing-controlled combustion phase shows that the rate of heat release during the combustion of WFE is greater than during the DF combustion in this phase and it is evident for the higher crankshaft rotation speeds.

The moment of the end of combustion (the moment when the rate of heat release is equal to zero) for DF and WFE is approximately the same. Taking into account the later start of heat release in the premixed combustion phase (for WFE), it can be concluded that the duration of the combustion of WFE is shorter than the diesel fuel combustion duration despite the fact that the heat capacity of WFE is greater than that of DF. Thus, an increased combustion rate of WFE could be observed compared to DF combustion.

There are several theories that explain the influence of WFE on combustion processes in compression ignition engines. For example, in one theory the influence of WFE is primarily explained by the catalytic effect of water dissociation products on the fuel combustion process. Under high temperature conditions in the combustion chamber of a diesel engine, water vapor dissociates into hydrogen and oxygen, as well as into hydrogen radicals and hydroxyl groups. The presence of hydrogen radicals in the combustion chamber accelerates chemical reactions and results in a more complete combustion of hydrocarbons.

Another theory suggests that there is a secondary atomization of fuel in the combustion chamber due to the boiling of water (micro-explosions phenomena) stored inside a water-fuel emulsion droplet.

Based on analysis of heat release rate dependences shown in Fig.4 it could be assumed that both mechanisms occur during water-fuel emulsion combustion in CI engine. Thus, the micro-explosion phenomenon can have a significant impact on the combustion processes at its initial stage because the high dispersity of fuel atomization has the greatest positive effect on the initiation of the combustion process, and secondary atomization of fuel due to the micro-explosion phenomenon can contribute to the improvement of fuel atomization characteristics. From another point, the catalytic effect of hydrogen radicals and hydroxyl groups (water dissociation products) presented in WFE allows to increase in combustion rate during the mixing-controlled combustion phase and even in the late combustion phase. During these combustion stages, the local concentration of active radicals is significant in the immediate vicinity to unburned fuel droplets and it contributes to its rapid combustion. Thus, application of WFE in diesel engines makes it possible to simultaneously improve fuel efficiency and environmental characteristics of the ICE.

Considering the above-mentioned differences in the combustion process for CI engine running on diesel fuel and water-fuel emulsion, and in order to achieve maximum efficiency when WFE is used, special attention should be paid to the stability of water-fuel emulsion. In order to ensure the reliable operation of the diesel engine fueled with WFE, a study on the stability behavior of WFE samples with different water content was conducted. The Zeta-Sizer device was used to determine the size of water particles in the water-fuel emulsion. For this experiment, a number of WFE samples were produced with the water content from 0 to 15% (by mass).

4. Study on the stability behavior of water-fuel emulsion

To study the stability behavior of the WFE, a number of measurements of the size distribution of water particles in the fuel for specified time intervals were performed. Based on the results of these measurements, the relative change in the average size of water particles as a function of time was plotted (Fig. 5).

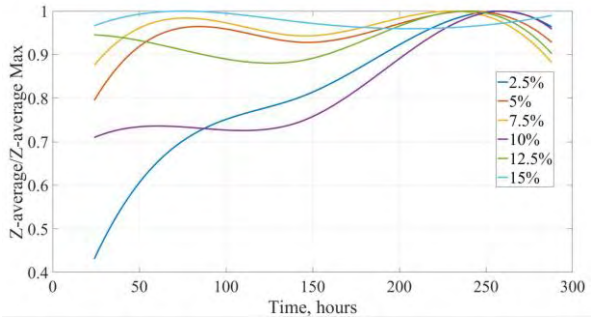

Fig. 5. The relative change in the average size of water particles depending on the time since the sample was made

It can be seen from the chart that the size of water particles increases during the first 200 hours after WFE production, and then it stabilizes. The size distribution of water particles in WFE with different water content is shown in Fig. 6. It can be seen from the Fig.6 that the size of water particles in the emulsified fuel increases with an increase in water content. In this content the risk of loss of WFE stability increases and fuel stratification problems could arise as well.

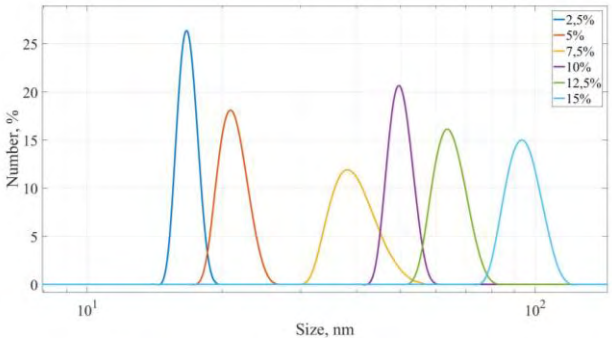

Fig. 6. Size distribution of water particles in water-fuel emulsion for samples with different water contents

The currently mentioned problem is mostly solved through the proper manufacturing technology and specified storage conditions applied to emulsified fuels. But, in order to minimize the risk of WFE stratification during engine exploitation it is recommended to introduce a water content sensor in the fuel delivery system for real-time control of water-fuel emulsion stability. The main requirements for the sensor are sufficiently high precision, high response, compactness, reliability, and relatively low price. Sensors based on absorption spectroscopy meet these requirements to the greatest extent. Such a sensor was used in the research. The results of the study of WFE samples with different water content are shown in Fig. 7. It can be seen

from Fig.7 that in several wavelength ranges, the correlation between absorption by the WFE sample and water content in it is clearly traced. Thus, the specified regularity can be used to determine the water content in WFE. In commercial applications, the sensor must determine absorption in one or several relatively narrow wavelength ranges. This will help to simplify and reduce the price of solution without any loss of accuracy of the obtained data on the emulsified fuel composition.

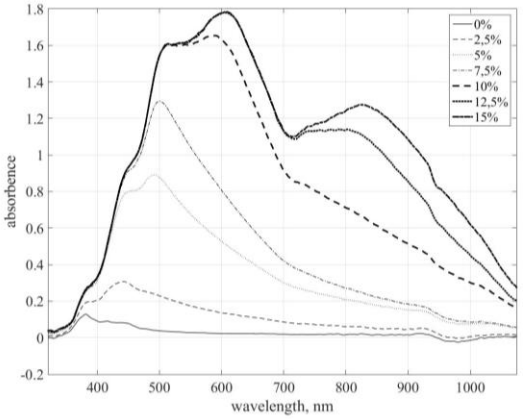

Fig. 7. Results of the study with WFE samples at different water content using absorption spectroscopy method

The use of a water content sensor in the fuel delivery system will make it possible to increase the reliability of operation in diesel engines running on WFE. It can be achieved by analyzing the dynamics of changes in the fuel absorption characteristic over time. Laboratory tests showed that water-fuel emulsion with high homogeneity of the volume structure is characterized by high stability of absorption in each range of wavelength. In the event of a loss of WFE stability (fuel stratification), the absorption value will change rapidly that will be detected by the sensor. Thus, it is possible to implement an algorithm where in emergency mode fuel delivery system will be switched from WFE fuel supply to the traditional diesel fuel supply. The engine should have the reserve fuel tank filled with traditional diesel fuel in this case.

Thus, the implementation of the above-mentioned concept of the adaptive management system with the water content sensor for diesel engine running on WFE would improve not only its reliability but also increase its fuel and environmental performance.

5. Conclusion

1. Application of water-fuel emulsion in diesel engines is a promising solution that could accelerate transformation from traditional fuels to alternative ones accompanied by reduction in engine NO_x and soot emissions.

2. Experimental studies on the influence of the physical and chemical properties of water-fuel emulsions on the environmental and fuel performance of diesel engine were carried out. It was established that concentration of `nitrogen oxides decreased by 14...66% when WFE was used. The maximum reduction in nitrogen oxide emissions refers to low-load modes. At the same time, application of WFE makes it possible to reduce soot formation in exhaust gases by 18...56%. Moreover, at high crankshaft rotation speed, the positive effect of WFE application on soot is greater than at a low crankshaft rotation speeds. The use of water-fuel emulsion helps to increase the effective efficiency from 0.7 to 3.4% depending on the load and crankshaft rotation speed as well.

3. The maximum temperature in the cylinder decreases by 15–30 K when WFE is used. The specified decrease in temperature level is explained by the increased heat capacity of the water-fuel emulsion that will be resulted in increased amount of heat consumed for fuel heating and its evaporation during the combustion process. Reduction in the maximum temperature of the cycle has a positive effect on nitrogen oxide emissions.

4. Based on experimental research results it was established that the ignition delay period and the intensity of combustion during the premixed combustion phase slightly increase for CI engine running on WFE (compare to diesel fuel). At the same time, the moment of the end of the combustion for both types of fuel is the same, despite the longer duration of the water-fuel emulsion fuel supply and increased ignition delay period. It can be explained by the intensification of combustion in mixing-controlled phase when WFE is used.

5. Based on analysis of heat release rate dependences it could assumed that the micro-explosion phenomenon can have a significant impact on the combustion processes at its initial stage when WFE is used. In this case, a high dispersity of fuel atomization has the greatest positive effect on the initiation of combustion, and secondary atomization of fuel due to the micro-explosion phenomenon can contribute to the improvement of fuel atomization characteristics. From another point, the catalytic effect of hydrogen radicals and hydroxyl groups (water dissociation products) presented in WFE allows to increase in combustion rate during mixing-controlled combustion phase and even in the late combustion phase. During these combustion stages, the local concentration of active radicals in the immediate vicinity to unburned fuel droplets is significant and it contributes to its rapid combustion. Thus, the application of WFE in diesel engines makes it possible to simultaneously improve fuel efficiency and environmental characteristics of the ICE.

6. In order to ensure the reliable operation of the diesel engine running on WFE, a study on the stability behavior of WFE samples with different water content (from 0 to 15% by mass) was conducted. It was established that the size of water particles gradually increasing during the first 200 hours after WFE production, and then it stabilizes. Moreover, the size of water particles in the emulsified fuel increases with an increase in water content.

7. It is recommended to use a water content sensor in the fuel delivery system of CI engines running on WFE because it will increase the reliability of its operation. The sensor should analyze the dynamics of changes in the fuel absorption characteristic over time. In the scenario of fuel stratification, the absorption value will change rapidly. In this case, it will be possible to implement an algorithm where fuel delivery system is switched from WFE fuel supply to the traditional diesel fuel supply.

Nomenclature

CI	compression ignition	ICE	internal combustion engine
DF	diesel fuel	WFE	water-fuel emulsion

Bibliography

[1] Al-lwayzy SH, Yusaf T, Saleh K, Yousif B. The Influence of emulsified water fuel containing fresh water microalgae on diesel engine performance, combustion, vibration and emission. Energies. 2019;12(13):2546. https://doi.org/10.3390/en12132546

[2] Badran O, Emeish S, Abu-Zaid M, Abu-Rahmaa T, Al-Hasana M, Al-Ragheba M. Impact of emulsified water/diesel mixture on engine performance and environment. International Journal of Thermal and Environmental Engineering. 2011; 3:1-7. https://doi.org/10.5383/ijtee.03.01.001

[3] Belousov E, Marchenko A, Gritsuk I, Savchuk V, Mitienkova V, Bulgakov N et al. Research of the gas fuel supply process on the compression stroke in ship's low-speed gas-diesel engines. SAE Technical Paper 2020-01-2107. 2020. https://doi.org/10.4271/2020-01-2107

[4] Bukkarapu KR, Jyothi Y, Raju L, Babu G, Narayanan K. A review on current trends in water in oil emulsions. International Journal of Mechanical Engineering and Technology. 2017;8:359-371.

[5] Chaichan MT. Enhancement of DI compression ignition engine performance and emission using diesel-water emulsion as fuel. Al-Rafidain Engineering. 2013;4:29-41. https://doi.org/10.33899/rengj.2013.77216

[6] Choi I, Lee C. Feasibility study of emission reduction on marine engine with variation of emulsified water concentration and turbocharger compression ratio. Appl Sci. 2020;10: 1215. https://doi.org/10.3390/app10041215

[7] Marchenko AP, Semenov VG. Alternative biofuel from rape oil derivatives. Chem Tech Fuels Oil+. 2001;37(3):183-185. https://doi.org/10.1023/A:1017976722355

[8] Nissar Z, Rybdylova O, Sazhin SS, Heikal M, Rashid A, Ismael M. A model for puffing/microexplosions in water/fuel emulsion droplets. Int J Heat Mass Tran. 2020;149:119208. https://doi.org/10.1016/j.ijheatmasstransfer.2019.119208

[9] Oo YM, Legwiriyakul A, Thawornprasert J, Somnuk K. Production of diesel–biodiesel–water fuel nanoemulsions using three-dimensional printed rotor–stator hydrodynamic cavitation. Fuel. 2022;317:123445. https://doi.org/10.1016/j.fuel.2022.123445

[10] Parsadanov I, Marchenko A, Tkachuk M, Kravchenko S, Bulgakov N, Tkachuk M et al. Complex assessment of fuel efficiency and diesel exhaust toxicity. SAE Technical Paper 2020-01-2182. 2020. https://doi.org/10.4271/2020-01-2182

[11] Qadiri U, AlFantazi A. Numerical 1-D simulations on single-cylinder stationary spark ignition engine using micro-emulsions, gasoline, and hydrogen in dual fuel mode. Cleaner Chemical Engineering. 2022;2:100009. https://doi.org/10.1016/j.clce.2022.100009

[12] Qadiri U, Pasha AA, Rahman MM, Raheem MA, Abdul Jameel AG, Pillai SN. Parametric investigation on single cylinder spark ignition engine fueled methanol blends; water-based micro emulsions and conventional gasoline. International Journal of Heat and Technology. 2021;39(3):919-924. https://doi.org/10.18280/ijht.390327

[13] Stępień Z. Synthetic automotive fuels. Combustion Engines. 2023;192(1):78-90. https://doi.org/10.19206/CE-152526

[14] Sugeng DA, Zahari MH, Ithnin AM, Yahya WJ. Diesel engine fuel consumption and emission analysis using steam generated non-surfactant water-in-diesel emulsion fuel. International Conference on Mechanical Engineering Research. 2017;4:1-10. https://doi.org/10.1088/1757-899X/257/1/012036

[15] Zacharewicz M, Kniaziewicz T. Model tests of a marine diesel engine powered by a fuel-alcohol mixture. Combustion Engines. 2022;189(2):83-88. https://doi:10.19206/CE-143486

Prof. Dmytro Samoilenko, DSc., DEng. – Faculty of Automotive and Construction Machinery Engineering, Warsaw University of Technology, Poland.
e-mail: *dmytro.samoilenko@pw.edu.pl*

Serhii Kravchenko, DEng. – Department of Engines and Hybrid Power Plants, National Technical University "Kharkiv Polytechnic Institute", Ukraine.
e-mail: *serhii.kravchenko@khpi.edu.ua*

Anatolii Savchenko, DEng. – Department of Engines and Hybrid Power Plants, National Technical University "Kharkiv Polytechnic Institute", Ukraine.
e-mail: *anatolii.savchenko@khpi.edu.ua*

Article citation info:
Magryta P, Pietrykowski K. Crankshaft geometry modification and strength simulations for a new design of diesel opposed-piston engine. Combustion Engines. 2023;194(3):123-128. https://doi.org/10.19206/CE-169371

Paweł MAGRYTA
Konrad PIETRYKOWSKI

Combustion Engines
Polish Scientific Society of Combustion Engines

Crankshaft geometry modification and strength simulations for a new design of diesel opposed-piston engine

ARTICLE INFO

Received: 31 May 2023
Revised: 6 July 2023
Accepted: 7 July 2023
Available online: 8 August 2023

The article presents simulation strength calculations of a newly designed crankshaft for a PZL 100 engine with a reciprocating piston design. This engine is the subject of a research and development project co-financed by NCBR. The article presents four successive versions of the crankshaft geometric changes which underwent strength calculations. Such elements as the outer and inner parts of the crankshaft arm were changed in these geometric versions. The geometry of the shaft was changed using Catia v5 software, while strength calculations were carried out in Abaqus software. In summary, one of the presented models was selected for further work due to the possible simplification of the manufacturing process and the reduction of mass and stresses. This model was further investigated in the project.

Key words: *crankshaft, FEM, diesel, opposed-piston engine, strength*

1. Introduction

The crankshaft is one of the main components of an internal combustion engine. Its task is to convert reciprocating motion into rotary motion. Crankshafts in internal combustion engines are subjected to high load indirectly resulting from piston force. In most cases, research into crankshaft strength is limited to checking crankshaft wear resistance to bending and twisting conditions. Increasingly, simulation tools based on FEM analysis are being used for such calculations. [19]. This approach saves time during the pro-design of a new engine structural component such as the crankshaft.

The authors of the article used computer-aided design software and wear resistance simulation software to study the effect of changing the external geometry of the crankshaft on its strength. It should be noted that the geometric solutions presented in the article are new designs, and the crankshaft itself was subjected to a design process for the new PZL-100 aircraft diesel engine developed by WSK "PZL-Kalisz" S.A. The goal of the project was to develop a two-stroke supercharged diesel engine for aircraft propulsion. The engine will feature reduced unit weight, fuel consumption and CO_2 emissions thanks to supercharging, a uniflow charge exchange system and direct fuel injection into the central combustion chamber. This will result in shorter combustion times, reduced heat loss and high efficiency. The two-stroke nature of the operation, increased speed (no valvetrain) and increased supercharging will increase specific power compared to current aircraft engines. Aircraft diesel engines including opposed piston engines were analyzed in [7]. Opposed piston engines are currently in use, for example the Achates Power engine for powering trucks and military vehicles [15, 18].

If you look more closely at the market, you can notice that the main competing solutions that exist on the drawing board include such engine designs as Motors Rotax 912 and 914 (BRP-Powertrain GmbH & Co KG), Lycoming O-235 (Lycoming Engines) or Continental O-200 (Continental Motors, Inc.). It should be added that the Rotax 912 engine is used in the majority of manufactured windjammers. Similarly, the ultralight recreational aircraft market commonly used a Rotax engine that allows refueling with standard automotive gasoline. Another competitive solution is the Avco Lycoming O-235 engine which belongs to a family of air-cooled four-cylinder aircraft engines. Similar engines are offered by Continental. In summary, the engine under design is expected to provide power and weight at the level of competing engines, with a reduction in operating costs and CO_2 emissions due to Diesel fuel.

The engineering design process of the crankshaft consisted in developing a new crankshaft geometry for an aircraft diesel engine with opposite pistons. Thus, the design process was a multi-stage one, and the presented article contains a description of part of the work carried out under the project. The work on the above-mentioned engine also included issues related to the construction of the piston [17] or modeling of dynamic phenomena [9]. It is worth mentioning that earlier geometric versions of the designed crankshaft were subjected to both strength calculations and checking their natural frequency [8]. There are also publications examining opposite piston engines in terms of the thermodynamic process [20] or numerical analysis of the impact of crank mechanism design on engine efficiency [16].

The results of the simulation studies presented in the article are the same as those currently being conducted all over the world. Similar research issues include the methodology of testing in ANSYS [21] or the effect of changing the crankshaft material on its strength [11]. There are also publications whose authors use the same simulation software as in this article. The authors of the publication [12] presented a comprehensive approach to the influence of dynamic loads calculated in Adams and load-bearing loads in Abaqus. An equally important issue currently under study is strength analysis for residual stress during shaft bending [4, 5]. In addition to strength analysis, some of the works preface a comprehensive approach to fatigue life analysis and the evaluation of crankshaft life [3] or analyze the cause of critical shaft damage [2, 23]. The above publi-

cations indicate that preliminary strength calculations of the new crankshaft to estimate its strength are therefore crucial.

2. Model description

The geometry of the shaft was prepared using Catia v5 software which is commonly used for such a design of crankshaft geometry [22], while strength calculations were carried out in Abaqus software. The finite element method that was used is one of the most effective and widely used numerical methods, based on the discretization of a continuous model.

Using the FEM, we can consider the process of approximating a continuous medium (real object), having an infinite number of degrees of freedom, with a set of sub-areas (discrete model) and a finite number of degrees of freedom. The calculations that have been performed in Abaqus use the incremental method combined with iterative algorithms or the so-called Newton-Raphson (NR) method. It is the most typical incremental-iterative algorithm used in displacement methods, giving accurate results and ensuring rapid convergence in most cases encountered in practice in structural mechanics.

Each change in geometry was analyzed in terms of balancing the rotating masses, which is extremely significant for the crankshaft of the two-stroke engine [14]. The basic design assumptions of the crankshaft were mostly directly derived from the geometry of the newly developed engine which specifies that the shaft should have three cranks offset from each other successively by an angle of 120° with 100 mm spacing along the axis of rotation. In addition, the radius of the crank should provide 72 mm of piston travel. Only the central section of the crankshaft which is exposed to the highest external forces was subjected to strength testing. This is because the central section of the crankshaft is exposed to the maximum values of forces. For all four simulation cases, the same (verified) design mesh density was established with a single element size of 1.1 mm. Before the original simulation, the size of the mesh was checked with the pre-simulation studies. It was proven that a mesh smaller than 1.1 mm would give no significant changes in the results. Consequently, it was decided not to make the mesh dense at any part of the model. Normally, if the mesh size is not correct, you should making the mesh dense in critical spots of geometry as presented in [13].

All models presented were calculated for two conditions, i.e. bending and twisting. The force loading conditions were implemented from the previous simulation calculations performed in MCS Adams. According to the earlier calculations, the highest piston force acting on the crankshaft occurs for the values of 0 CAD and 14.5 CAD, as shown schematically in Fig. 1. The same method was used by the authors of [12] who determined the maximum forces for bending and twisting.

A material for the crankshaft defined as cast iron was assumed for the simulation calculations. The material properties adopted for the calculations are shown in Table 1.

The conditions of immobilization at one side and the possibility of free rotation on the other side were imposed on the crankshaft. Additionally, to reflect the restraint conditions, it was decided to immobilize the crankshaft by using an intermediate element as a bushing. Otherwise, when restraining directly the surfaces the shaft was supported on, local maximum stresses occurred. This happened because high stresses were created at the edge between the restrained and moving surfaces, resulting mainly from the local shear stresses. Such a situation does not occur when the crankshaft operates in an internal combustion engine, so it was decided to immobilize the crankshaft by an intermediate element, i.e. a bushing. Additional elements like bushings imposed the need to define the contact conditions between the crankshaft and additional bushings. These conditions were defined as "normal contact", which reflects the contact of components across their entire surface. The bushings were made of 40H steel whose properties are specified in Table 1.

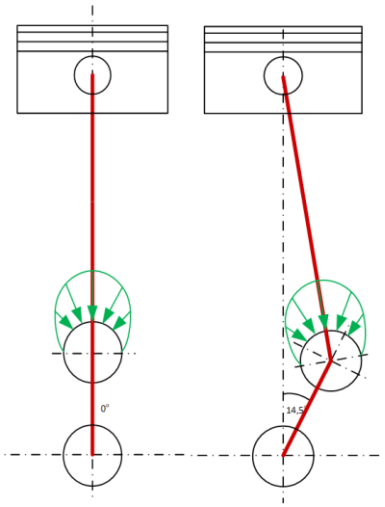

Fig. 1. Boundary conditions as forces acting on the model

Table 1. Material properties adopted for the calculation

Properties	Crankshaft	Bushing
Poisson's number	0.3	0.3
Density	7197 kg/m^3	7850 kg/m^3
Young's modulus	178 GPa	207 GPa

3. Geometry change in models 1–4

3.1. Geometry of model 1

The geometry of the crankshaft developed for the research engine was designed based on the analyzed literature [6] and the design solutions used in modern OPOS engines The basic design assumptions of the crankshaft are mostly directly derived from the geometry of the newly developed engine which was initially described in the first section of this article. In addition, it was also assumed that the shaft at the air intake side will be made similarly to the crankshaft at the exhaust side although it carries lower loads. The solid model shown in Fig. 3 shows a crankshaft designed along the lines of the crankshaft of the Gemini 100 engine (Fig. 2) and follows the above guidelines.

3.2. Geometry of model 2

The second geometric model of the crankshaft was slightly modified in relation to the first model. The outer part of the crankshaft arm was modified by introducing an undercut with a radius of 60 mm instead of the rounding with a radius of 220 mm, mainly aimed at conducting strength tests with reduced mass.

Fig. 2. View of the Gemini 100 engine crankshaft [1]

3.3. Geometry of model 3

The third geometric model of the crankshaft analogously to model 2 has reduced weight. This time, however, it was less than 5 kg. This was only possible by modifying the inner part of the crankshaft arm by introducing an undercut with a radius of 60 mm in place of the 220 mm radius rounding. The project was mainly aimed at carrying out strength analysis of the crankshaft structure at the maximum reduced weight.

3.4. Geometry of model 4

The fourth geometric model of the crankshaft, unlike the previous versions, was designed to simplify the structure as much as possible. To this end, the geometries forming the outer and inner shapes of the radial arms were replaced by straight sections equidistant from each other. This will reduce their manufacturing time and the manner of the complexity of the machining process of the crankshaft. A beneficial aspect of the modification is the fact that the weight of the component is reduced compared to the first model.

The changes in the geometry of a single crankshaft compared to previous models are presented in Table 2 (the changes are marked in orange).

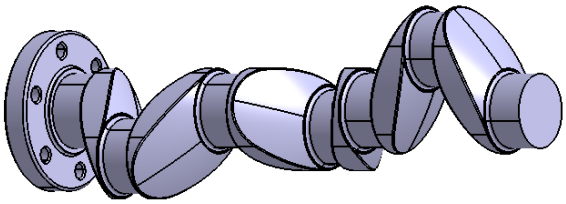

Fig. 3. Geometry of model 1

4. Results

The results present 4 geometrical models of the crankshaft. The results are grouped into 4 groups to sequentially represent the results of the bending and twisting strength calculations. In each model, the results of the strength tests were presented as stress maps on the external surface of the shafts during both the bending and twisting simulations. In addition, the mass of the entire crankshaft was calculated for each case. All the presented results refer to the identical range from 0 to 120 MPa so they can be compared.

Table 2. Geometry compared to model 1

Model number	Geometry view
1	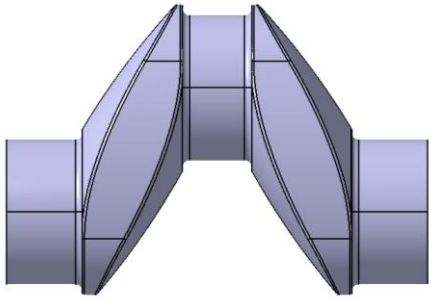
2	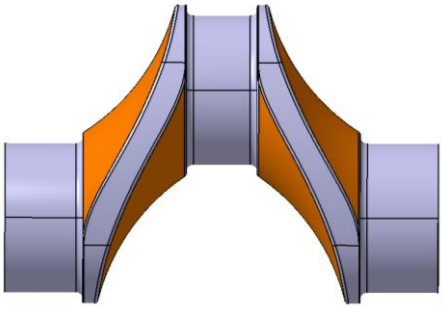
3	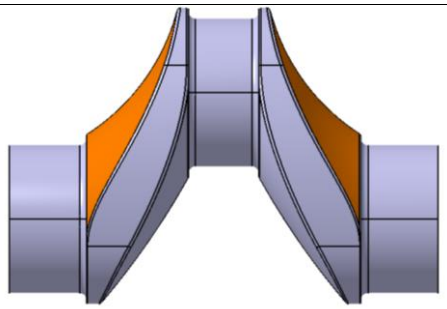
4	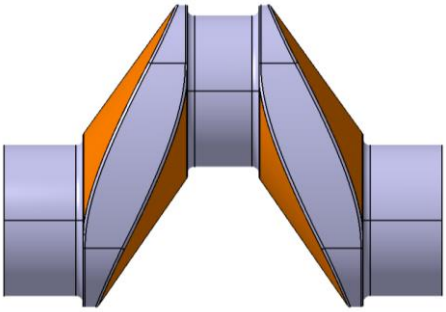

4.1. Bending results in model 1-4

As can be seen in the figures below, the highest stresses occur at the rounded point between the surface of the crankshaft and the side surface of the counterweight. The maximum values that occur there were observed for model 3 and reached 122.9 MPa, while the lowest stress concentration was observed for model 4 and reached 107.8 MPa. The results for all models are compared in Table 3 and Fig. 4. On the other hand, at the center of the bottom surface of the crankshaft, the maximum stresses vary between 60–70 MPa for models 1, 2 and 4 and 70–80 MPa for model 3.

However, it should be noted that the stress distribution in the crankshaft section is uniform and shows a typical distribution for bending.

The stress distributions are symmetrical with respect to the connecting rod placement because of to the symmetrical load on both sides of the crankshaft.

The influence of the crankshaft geometry on the distribution of stresses is well shown in Table 3. The zone of stress concentration on the side surfaces of the crankshafts is the larger, the smaller the cross-section of the crankshaft is.

4.2. Twisting results in model 1-4

The figures show that the highest stresses are at the rounded point between the surface of the main bearings and the side surface of the counterweight, particularly on the left. This is the side where the crankshaft surface was immobilized for the direction of movement along the main axis of the crankshaft. The maximum values that occur there were observed for model 3 and reached 132.7 MPa, while the lowest stress concentration, i.e. 126.8 MPa was observed for model 2. The results for all models are compared in Table 4 and Fig. 4. On the other hand, at the center of the bottom surface of the crankshaft, the maximum stresses vary between 70–80 MPa for models 1 and 2 and 60–70 MPa for models 3 and 4.

However, it should be noted that the distribution of stresses in the crankshaft section is uniform and shows a typical distribution for twisting. The stress distributions are almost symmetrical concerning the connecting rod bearing, however, it is clear that the left crankshaft arm is subjected to greater stress than the right one. This is due to the accumulation of torque on this crank.

5. Discussion of the results

The maximum stresses that occurred in all models during bending and torsion simulations are compared Table 5 and Fig. 4. Different types of support for the crankshaft during the simulations enable us to compare the values of the maximum stresses in all models. In addition, the table presents the mass of the entire crankshaft. The mass was calculated from the density of the material used.

The data in the table show that each version of the crankshaft has its positive and negative aspects. It is worth mentioning that the maximum stress for bending and twisting does not exceed 135 MPa, which can be considered an acceptable value for the material used. For comparison purposes, the authors of a similar solution obtained values above 300 MPa in dynamic tests [10]. In this research, dynamic loads were not analyzed as this was not the final geometric version of the crankshaft.

To sum up, model 1 has a reduced mass but increased stresses for bending and compression. Model 2, despite its reduced mass, has reduced stresses compared to its predecessor. Model 3 has the lowest mass but shows the highest bending stresses. Model 4 has a mass comparable to its predecessors, its bending stresses are low, and its compressive stresses are medium. The authors conclude that model 4 should be selected for further work due to a possible simplification of its manufacturing process and the reduction of its mass and stresses. This model was further studied in the project.

Table 3. Stress simulation results for bending

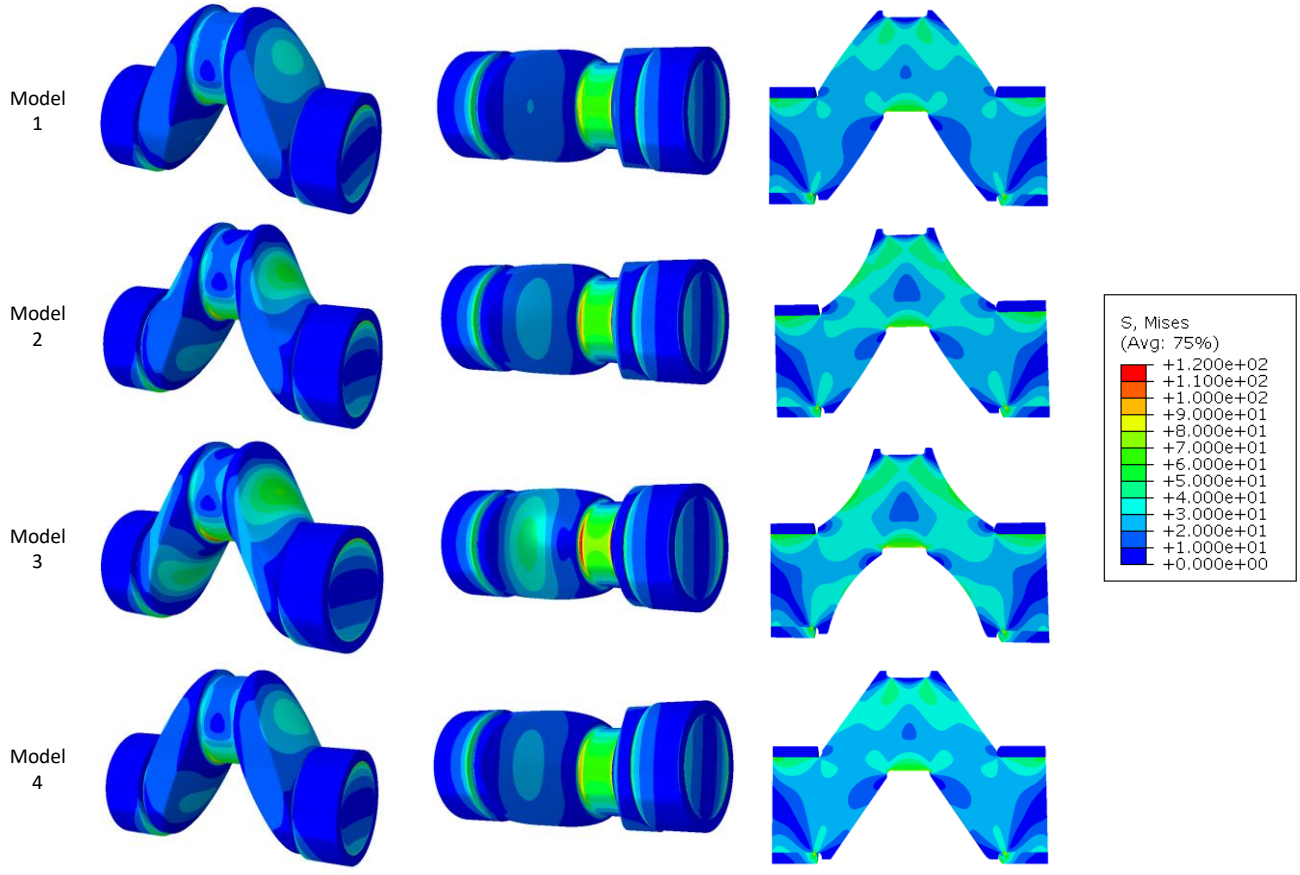

Table 4. Stress simulation results for twisting

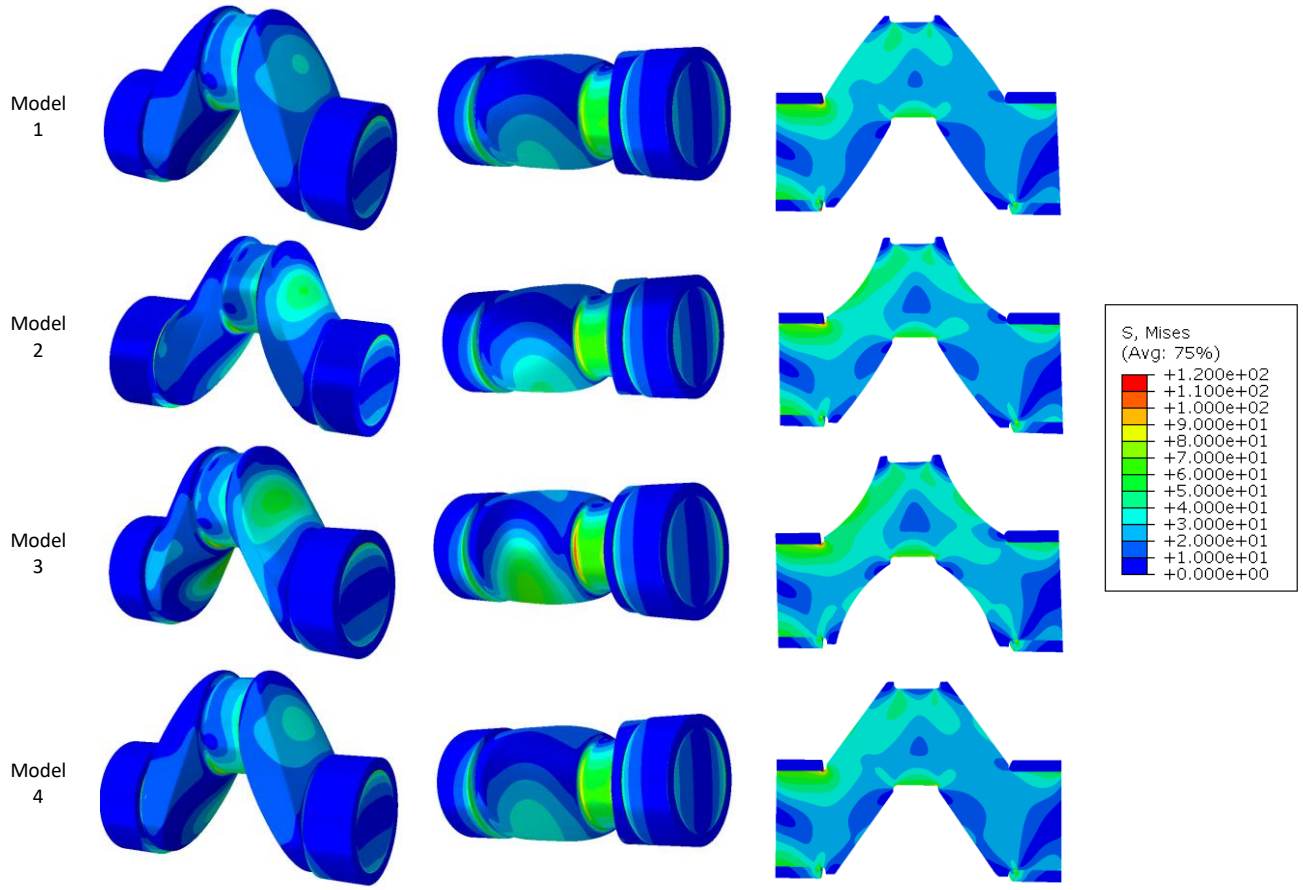

Table 5. Stress for bending and twisting

Model number	Bending [MPa]	Twisting [MPa]	Mass of crankshaft [kg]
Model 1	119.2	128.6	5.65
Model 2	113.7	126.8	5.30
Model 3	122.9	132.2	4.94
Model 4	107.8	132.4	5.53

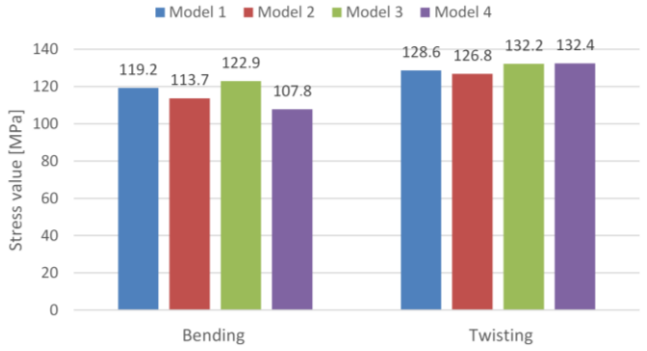

Fig. 4. Stress for bending and twisting

6. Conclusions

The conclusions that can be drawn from the presented results are as follows:

- modern design and simulation methods allow for improving the design of processors of crankshafts of internal combustion engines
- at the stage of designing new engine elements, it is possible to assess the strength of a given part
- the authors of this paper analyzed the strength of four different geometric versions of the crankshaft and selected the model for further design work
- the same material was adopted in all models, but its change can affect strength
- the material density and volume of the geometric model of the crankshaft enabled us to estimate its mass, which also influenced the selection of the target model for further work because the designed crankshaft will potentially be used in an aircraft engine
- the conducted research is part of the worldwide trend of using modern simulation methods for fatigue calculations of engine parts.

Acknowledgements

This work has been realized in cooperation with The Construction Office of WSK "PZL-KALISZ" S.A." and is part of Grant Agreement No. POIR.01.02.00-00-0002/15 financed by the Polish National Centre for Research and Development.

Nomenclature

CAD	crank angle degree
FEM	finite element method
NCBR	Polish National Centre for Research and Development
OPOS	opposed-piston
PZL	Polskie Zakłady Lotnicze
WSK	Wytwórnia Sprzętu Komunikacyjnego

Bibliography

[1] Anderson T. Superior's New Gemini Diesel (posted on 28.06.2015). http://www.dieselarmy.com/news/video-superiors-new-gemini-diesel/

[2] Ang YZ, Ku PX. Study on failure analysis of crankshaft using finite element analysis. MATEC Web Conf. 2021;335: 03001. https://doi.org/10.1051/matecconf/202133503001

[3] Bulut M, Cihan O, Temizer I. Fatigue life and stress analysis of the crankshaft of a single cylinder diesel engine under variable forces and speeds. Mater Test. 2021;63(8):770-777. https://doi.org/10.1515/mt-2020-0122

[4] Chien WY, Pan J, Close D, Ho S. Fatigue analysis of crankshaft sections under bending with consideration of residual stresses. Int J Fatigue. 2005;1(27):1-19. https://doi.org/10.1016/j.ijfatigue.2004.06.009

[5] Choi KS, Pan J. Simulations of stress distributions in crankshaft sections under fillet rolling and bending fatigue tests. Int J Fatigue. 2009.31(3):544-557. https://doi.org/10.1016/j.ijfatigue.2008.03.035

[6] Flint M, Pirault J-P. Opposed piston engines: evolution, use, and future applications. SAE International 2009.

[7] Gęca M, Czyz Z, Sułek M. Diesel engine for aircraft propulsion system. Combustion Engines. 2017;169(2):7-13. https://doi.org/10.19206/CE-2017-202

[8] Grabowski Ł, Pietrykowski K, Karpiński P. FEM simulation research of natural frequency vibration of crankshaft from internal combustion engine. ITM Web Conf. 2017;15: 07004. https://doi.org/10.1051/itmconf/20171507004

[9] Grabowski Ł, Pietrykowski K, Karpiński P. The zero-dimensional model of the scavenging process in the opposed-piston two-stroke aircraft diesel engine. Propulsion and Power Research. 2019;8(4):300-309. https://doi.org/10.1016/j.jppr.2019.11.003

[10] He CM, Xu SC. Opposed-piston crankshaft system dynamics simulation and durability analysis in a neotype two-stroke diesel engine. American Journal of Mechanical and Industrial Engineering. 2017;2(2):54-63 https://doi.org/10.11648/j.ajmie.20170202.11

[11] Karthick L, Stephen Leon J, Ravi R, Michel J, Mallireddy N, Vadivukarasi L. Modelling and analysis of an EN8 crankshaft in comparison with AISI 4130 crankshaft material. Mater Today-Proc. 2022;52(3):1036-1040. https://doi.org/10.1016/j.matpr.2021.10.484

[12] Montazersadgh FH, Fatemi A. Dynamic load and stress analysis of a crankshaft. SAE Technical Paper 2007-01-0258. 2007. https://doi.org/10.4271/2007-01-0258

[13] Montazersadgh FH, Fatemi A. Stress analysis and optimization of crankshafts subject to dynamic loading. A Final Project Report Submitted to the Forging Industry Educational Research Foundation (FIERF) and American Iron and Steel Institute (AISI). 2007.

[14] Mosakowski R. Analysis of balancing of six-cylinder in-line two-stroke internal combustion engines. Combustion Engines. 2009;139(4):22-33. https://doi.org/10.19206/CE-117165

[15] Naik S, Johnson D, Fromm L, Koszewnik J, Redon F, Regner G et al. Achieving Bharat Stage VI emissions regulations while improving fuel economy with the opposed-piston engine. SAE Int J Engines. 2017;10(1):17-26. https://doi.org/10.4271/2017-26-0056

[16] Opaliński M, Teodorczyk A, Kalke J. The closed-cycle model numerical analysis of the impact of crank mechanism design on engine efficiency. Combustion Engines. 2017; 168(1):153-160. https://doi.org/10.19206/CE-2017-125

[17] Pietrykowski K, Magryta P, Skiba K. Finite element analysis of a composite piston for a diesel aircraft engine. Combustion Engines. 2019;179(4):107-111. https://doi.org/10.19206/CE-2019-417

[18] Regner G, Johnson D, Koszewnik J, Dion E, Redon F, Fromm L. Modernizing the opposed piston, two stroke engine for clean, efficient transportation. SAE Technical Paper 2013-26-0114. 2013. https://doi.org/10.4271/2013-26-0114

[19] Sandya K, Keerthi M, Srinivas K. Modeling and stress analysis of crankshaft using FEM package Ansys. International Research Journal of Engineering and Technology. 2016;3(1):687-693. https://www.irjet.net/archives/V3/i1/IRJET-V3I1119.pdf

[20] Shokrollahihassanbarough F. Alqahtani A, Wyszynski ML, Thermodynamic simulation comparison of opposed two-stroke and conventional four-stroke engines. Combustion Engines. 2015;162(3):78-84. https://doi.org/10.19206/CE-116867

[21] Thejasree P, Dileep Kumar G, Leela Prasanna Lakshmi S. Modelling and analysis of crankshaft for passenger car using ANSYS. Mater Today-Proc. 2017;4(10):11292-11299. https://doi.org/10.1016/j.matpr.2017.09.053

[22] Vinay AV, Shankar MU, Satya LP, Kumar YS, Srikanth M. Modelling and analysis of crankshaft for four stroke diesel engine by using composite materials. Bachelor Thesis in Anil Neerukonda Institute of Technology and Sciences. India 2021.

[23] Witek L, Sikora M, Stachowicz F, Trzepiecinski T. Stress and failure analysis of the crankshaft of diesel engine. Eng Fail Anal. 2017;82:703-712. https://doi.org/10.1016/j.engfailanal.2017.06.001

Paweł Magryta, MEng. – Faculty of Mechanical Engineering, Lublin University of Technology, Poland.
e-mail: *p.magryta@pollub.pl*

Konrad Pietrykowski, DSc., DEng. – Faculty of Mechanical Engineering, Lublin University of Technology, Poland.
e-mail: *k.pietrykowski@pollub.pl*

Article citation info:
Pietras D, Stelmasiak Z, Pietras P. Comparison of operational parameters and stability of performance of an automotive SI engine powered by methyl and ethyl alcohols. Combustion Engines. 2023;194(3):129-140. https://doi.org/10.19206/CE-169136

Dariusz PIETRAS
Zdzisław STELMASIAK
Piotr PIETRAS

Combustion Engines
Polish Scientific Society of Combustion Engines

Comparison of operational parameters and stability of performance of an automotive SI engine powered by methyl and ethyl alcohols

ARTICLE INFO

Received: 25 May 2023
Revised: 27 June 2023
Accepted: 1 July 2023
Available online: 19 August 2023

The article presents research results performed using automotive spark ignition engine run on methyl and ethyl alcohols as well as gasoline as a reference fuel. The research was performed on automotive engine of Fiat 1100 MPI type. The aim of the conducted analysis was to compare the operational parameters of the engine. These parameters included engine power output, overall efficiency, emissions of toxic components in exhaust gases, and a comparison of the combustion process course. This comparison was conducted based on recorded and averaged indicator diagrams, as well as individual combustion cycles. The averaged diagrams were used in analysis of the pressure course during combustion, in analysis of pressure growth rate and heat release rate. Diagrams of individual combustion served for assessment of operational smoothness of the engine when fuelled with alcohols. As the reference, parameters measured in case of gasoline fuelling were used.

Key words: *methyl and ethyl alcohols, operational parameters, overall efficiency, indicated pressure, smoothness of engine operation*

1. Introduction

For nearly two decades, intensive research has been carried out worldwide on the gradual substitution of traditional petroleum-derived fuels with alternative fuels [2, 3, 5, 13**,** 14, 17, 19, 20, 21, 23–25]. Diversification of energy sources and ecological aspects are the main objectives of this research. Parallel to the research, in many countries regulations imposing an obligation to use biofuels as admixtures to gasoline and diesel oil, but also as homogenous fuels were introduced [4, 7, 10]. The basic biofuels include (used mainly in spark ignition engines) and esters of unsaturated fatty acids, used mainly to feed compression ignition engines. The biofuels are produced from biomass, an annually reproducible source of energy, obtainable in large quantities [1, 12–14, 16]. The biomass is created in the process of photosynthesis, using carbon dioxide from the atmosphere and solar energy. Under natural conditions, the biomass undergoes biological decomposition, which is accompanied by the emission of carbon dioxide and methane. As a result of the combustion of biofuels in combustion engines carbon dioxide is produced only, without emission of methane CH_4, having a considerably stronger greenhouse effect, compared with CO_2. Considering circulation of carbon dioxide in atmosphere, the process taking place in the engine is therefore much more advantageous than process of natural decomposition of the biomass. Some authors even believe that aggregated process of biomass formation, production, and combustion of biofuels, is close to zero emission in terms of carbon dioxide [1, 18]. Taking the above into consideration as well as unlimited resources of biomass, it can be assumed that importance of biofuels should increase in the future.

The obligation to use biofuels in Poland is due to the accomplishment of the National Indicator Targets (NCW in short), which assume a gradual increase in share of renewable fuels in the total amount of consumed engine fuels. Following the Regulation of the Polish Council of Ministers on the NCW of July 20th 2013, energetic share of biofuels in the year 2020 should reach the level of 10.0% [5, 22].

Legal regulations in the area of toxicity of exhaust gases mean that the share of compression ignition engines will decrease in the future. This will particularly apply to power systems of passenger cars driven mainly in the cities. It is anticipated that spark ignition engines will dominate in the future, while some of them will be powered with biofuels. From the point of view of the benefits of alcohol fuelling and the easiness of production, primary alcohols, like methylene and ethylene, will be of the greatest importance [8, 11].

Primary alcohols due to their perfect properties, mainly high octane number, high evaporation heat and high combustion rate, can be successfully used both in spark ignition engines (as homogenous fuels or as additives to traditional fuels), and in compression ignition engines as additives combusted simultaneously with diesel oil [9, 15, 17]. The advantages of alcohols cause that research on alcohol fuelling of engines is carried out presently in many research centres around the world.

The ethyl alcohol is produced in process of fermentation of plant materials (sugar cane, cassava, cereals, potatoes) and cellulose from timber waste. Production of ethanol from cellulose, which is intensively developed in Sweden and other Scandinavian countries, seems to be particularly attractive [20]. It allows for obtaining a significant amount of fuel without reduction of grocery products, which is an issue often raised by environmentalists. It seems that methyl alcohol produced from coal or natural gas may also play an important role in the future [1]. New technology for synthesis of methanol from carbon dioxide and hydrogen, which was developed in the recent years, also promises a certain future.

Both methyl and ethyl alcohols are fuels containing significant amount of oxygen in their molecule, and thus in combustion process in engine conditions, leading to reduction in emissions of toxic exhaust components, mainly nitrogen oxides and particulate matter.

Table 1. Properties of the fuels [1, 4, 11, 18]

Properties	Gasoline	Diesel oil	Methanol	Ethanol
Molecular formula	C_7H_{16}	$C_{14}H_{25}$	CH_3OH	C_2H_5OH
Octane/cetane number	95/~22	~15/51	115/~3	/~11
Lower heating value, MJ/kg	42–44	42.5	19.5	26.9
Density at 20°C, kg/m^3	720–760	820–845	792	789.5
Viscosity at 40°C, mPa s	1.07	3.11	0.57	1.1
Kinematic viscosity, mm^2/s	0.57	2.419	0.75	1.51
Heat of evaporation, kJ/kg	315–350	250	1101	841.5
Stoichiometric air fuel ratio	14.9	14.5	6.52	9.0
Explosion limits: lower, %vol upper, %vol			 5.5 44	 3.3 19
Flash point, °C	36	78/56	11.0	18.3
Auto-ignition temperature, °C	280/480–550	250/330–350	455	425
Flame speed, m/s		0.86		~3
Flame temperature, °C		2054	1890	2120
Carbon content, %wt	85.5	87	37.5	52.2
Hydrogen content, %wt	14.5	13	12.5	13
Oxygen content, %wt	0	0	50.0	34.8

Carbon dioxide and water are the products of the combustion of methyl and ethyl alcohol, while such a process takes place according to the following reaction:

$$CH_3OH + \frac{3}{2}O_2 \rightarrow CO_2 + 2H_2O + 29.7\frac{MJ}{kg} \quad (1)$$

$$C_2H_5OH + 3O_2 \rightarrow 2CO_2 + 3H_2O + 22.68\frac{MJ}{kg} \quad (2)$$

The mass fraction of carbon atoms in molecules of alcohol is lower compared to traditional fuels, and amounts to 0.375 for methyl alcohol, and 0.520 for ethyl alcohol, while for gasoline and diesel oil this ratio is approximately 0.845–0.850. However, taking into account differences in calorific values, the generation of the same unit of energy from alcohol results in only a slight, within 2%, reduction of CO_2 emissions in relation to gasoline.

The spark ignition engines are most commonly powered by mixtures of anhydrous alcohol, its esters, and gasoline. Due to the tendency for delamination of alcohol-gasoline mixtures at low temperatures and in the presence of water, the total content of alcohol and application time of the mixtures are limited. For this reason, it seems beneficial to feed the spark ignition engines with alcohols as homogenous fuels. Consequently, it is possible to use water-logged alcohols obtained directly from the distillery, which considerably reduces the costs of their production. Moreover, fuelling with homogenous alcohol makes it possible to take full advantage of the high anti-knocking resistance of alcohols through the increase in compression ratio. This results in an increase in overall efficiency and unit power output of the engine [2, 9]. The alcohol, as homogenous fuel, can be used in fleets of vehicles like taxis, post office cars, delivery vehicles or others. For example, a large number of cars powered by ethyl alcohol produced from cassava and sugar cane have been operated in Brazil for a long time [5], their number is around 2 million.

Currently, new possibilities to use alcohol additives to gasoline, or alternating usage of gasoline and alcohol are created by the common use of multipoint injection of light fuels in engine fuelling systems. With small modifications in the fuel supply system, engine start-up and its heating-up can be performed with gasoline alone, while further operation of the engine goes with alcohol fuelling [20]. In such engines, the compression ratio may be increased by 2.0–3.0 units, which should increase the power output and thermal efficiency of the engine. Research shows that also in the area of partial engine loads, the efficiency of the engine powered by alcohol only is higher, which is of the highest importance in the case of automotive spark ignition engines operated in cities.

In this study the test results of the FIAT 1100 MPI engine, powered alternately with gasoline, methyl alcohol and ethyl alcohol, were presented. The subject of the research was to assess operational parameters of the engine, to compare some selected combustion parameters and assessment of stability of the engine operated on alcohol. Parameters of combustion process were calculated based on registered indicator diagrams, averaged for 50 successive cycles. Smoothness of engine operation was assessed based on an analysis of 50 successive cycles of individual combustion. Parameters from individual combustion diagrams were processed using mathematical statistical analysis. On this basis, stability of engine operation, so-called – *cycle by cycle* – was evaluated. The same parameters obtained in the case of gasoline fuelling were used as reference values.

Performed bench tests indicate stable operation of the engine powered by both methyl and ethyl alcohol, which enables usage of both alcohols in normal engine operation. Performance parameters, such as power output, overall efficiency, emissions of nitrogen oxides and hydrocarbons, as well as exhaust gas temperature, have clearly undergone improvement.

2. Test bench

The bench tests were performed on four cylinders, spark ignition, multipoint injection engine of Fiat 1100 MPI type. Technical data of the engine are specified in Table 2.

For the purpose of engine indication, a hole was drilled for an adapter of a non-cooled GH13 sensor in the second cylinder of the cylinder head. The INDIMETER 619 system from AVL was used to register the quick-changing pressures in the combustion chamber.

Table 2. Technical data of Fiat 1100 MPI engine

Engine type	Fiat 1100 MPI
Bore × stroke	70 × 72 mm
Swept capacity	1108 ccm
Compression ratio	9.6
Rated power/rotational speed	40 kW/5000 rpm
Max torque/rotational speed	88 Nm/3000 rpm

A system for automatic acquisition of measurement data to the Excel calculation sheet was installed on the test bench. For the particular requirements of the testing, a dual system of fuelling for alcohol and for gasoline was installed in the test bench. Each of the systems was equipped with an individual fuel pump and pressure stabilization system, and a system to measure the fuel consumption. The fuelling system enabled control of instantaneous consumption of the fuels, which considerably facilitated selection of engine adjustment and recording of time of consumption of a determined dose of fuel. A view of the test bench is presented in Fig. 1.

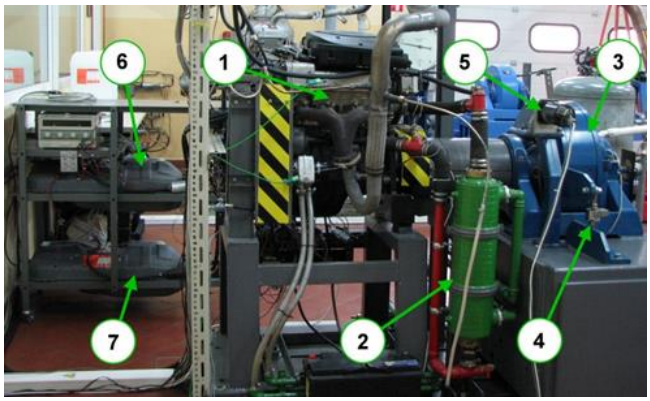

Fig. 2. Test bench – general view: 1 – research engine of Fiat 1100 MPI type, 2 – radiator, 3 – eddy-current engine brake made by Schenck, 4 – transducer of engine load, 5 – engine speed sensor, 6 – alcohol tank, 7 – gasoline tank

3. Analysis of the results of the research

3.1. Operational parameters of the engine running on methanol and ethanol

The use of alcohols has a positive effect on maximal power output, which is shown in Fig. 2. In the complete range of the investigated rotational speeds of the engine of 2000–3500 rpm the increase of the power output for alcohol feeding can be seen. This can be evaluated based on the relative increase of the power output, calculated from the following formula:

$$\mathrm{DNe_{Alc}} = \frac{\mathrm{Ne_{Alc}} - \mathrm{Ne_{G95}}}{\mathrm{Ne_{G95}}} \cdot 100\% \tag{3}$$

where: $\mathrm{DNe_{Alc}}$ – relative increase of the power output when supplied with methyl or ethyl alcohol, $\mathrm{Ne_{Alc}}$ – power output when supplied with alcohol, $\mathrm{Ne_{G95}}$ – power output when supplied with G 95 gasoline.

Relative increase in the power output reached 1.7–3.3% when the engine was run on ethyl alcohol and 3.8–7.7% in case of methyl alcohol. A higher growth of the power output, when fuelled with methanol, could be caused by a higher combustion rate of combustible mixture and effect of a higher value of vaporization heat of methanol injected near the inlet valve, which resulted in better filling and smaller losses of the heat to cylinder walls during compression. It is worth underlying that these parameters were achieved for an unchanged compression ratio and without optimization of ignition advance angle. It can therefore be assumed that the engine performance when fuelled with alcohols may be even higher due to optimization of compression ratio and adjustment of ignition angle.

Conclusions about the beneficial effect of alcohols on the combustion of fuel charge can be confirmed by comparison of the overall efficiency of the engine shown in Fig. 3. This indicates that in the complete range of changes in the engine load, the efficiency when the engine was supplied with alcohols was higher than the efficiency when it was supplied with gasoline:

– with 1.2–2.5% for ethyl alcohol
– with 1.5–7.5% for methyl alcohol.

a)

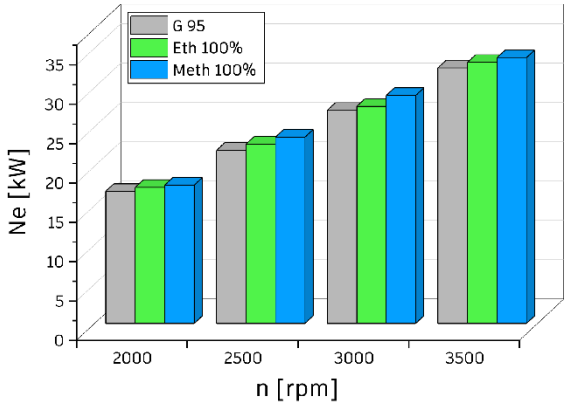

b)

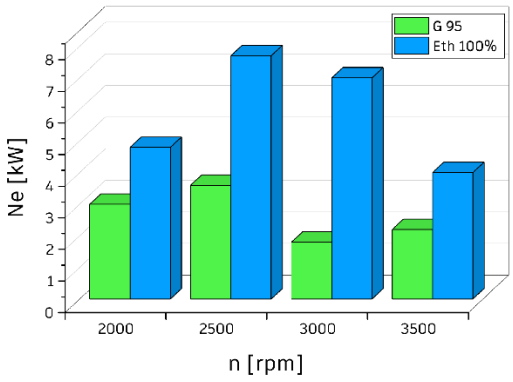

Fig. 2. Comparison of the power output and relative change of the power output in Fiat 1100 MPI engine run on G 95 gasoline and Eth ethyl alcohol and Meth methyl alcohol

A distinct increase in the efficiency when the engine was run on methanol was observed in the entire range of engine load changes, and the difference increased with increasing load. For ethyl alcohol, significant differences occurred in the range of medium and maximum engine loads, when an increase in the efficiency of 1.5–2.5% in absolute values was observed. For lower engine loads, gasoline and ethanol fuelling efficiency was comparable, especially for higher rotational speeds. Bigger changes in the efficiency as the engine load increases may be caused by the increase of temperature in the combustion chamber and of the temperature of fuel charge during compression, which promotes faster evaporation of alcohols, improves homogeneity of combustible mixture and promotes acceleration of combustion rate in the initial stages of the process.

It seems that both increase in maximum power output, as well as in the engine efficiency, when fuelled with methanol, is caused by a higher combustion rate of methanol in relation to ethanol and gasoline, which results in lower thermal losses in the cycle. Simultaneously, higher evaporation heat of methanol reduces the charge temperature during compression and at the beginning of combustions, which can lead to reduced mechanical losses during compression stroke. Both the above mentioned factors increase thermal efficiency of the engine.

A comparison of concentrations of nitrogen oxides NO_x and Total Hydrocarbons Content THC is presented in Fig. 4. From the point of view of ecology, it is especially important to reduce concentration of NO_x in the exhaust gases when fuelling with both alcohols, occurring in the entire range of engine load changes, as shown in Fig. 4a and 4b. Differences in concentrations of NO_x were respectively 15–0% for methyl alcohol and 35–75% for ethyl alcohol. Compared to gasoline, differences in concentrations of NO_x for both alcohols were growing as the engine load increased, and the biggest differences were observed in the area of medium and maximal engine loads. A greater reduction in the concentration of NO_x, observed for ethanol is particularly important, because this alcohol is used in some regions of the world as admixture to gasoline or as homogenous fuel.

The fact of NO_x emissions reduction when fuelling with alcohols was also signalled in some previous reports found in the literature [1, 9, 18], while the analysis of the obtained results of the research indicates a considerable scale of such phenomenon. Due to huge difficulties in the reduction of nitrogen oxides by catalytic converters, the advantageous feature of the combustion of alcohols, especially ethanol, described here requires special emphasis.

It seems that shorter combustion time of methanol-air and ethanol-air mixtures, and lower temperatures of the flame of alcohol vapours are the reasons for the reduction of NO_x quantities generated in the combustion process of alcohols. Temperatures of the working medium behind the front of the flame, which are lower in the case of alcohol vapours, have an especially important effect [8, 11]. This is due to the fact that the effect of time on quantities of generated NO, the main constituent of nitrogen oxides in exhaust gases of the spark ignition engine, is linear. In contrast, the effect of temperature is exponential, which considerably influences quantities of generated NO.

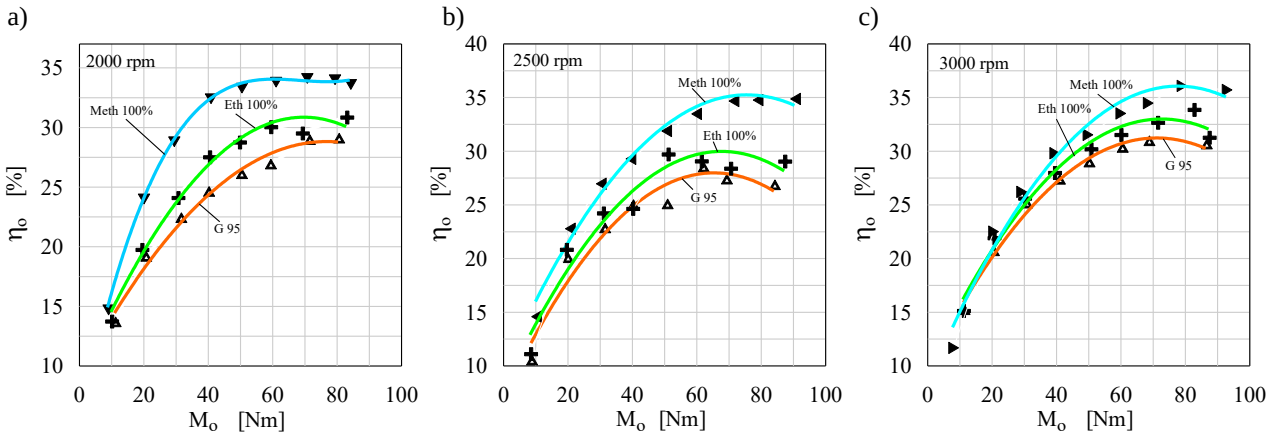

Fig. 3. Comparison of overall efficiency of Fiat 1100 MPI engine fuelled with G 95 gasoline and Eth 100% ethyl alcohol and Meth 100% methyl alcohol

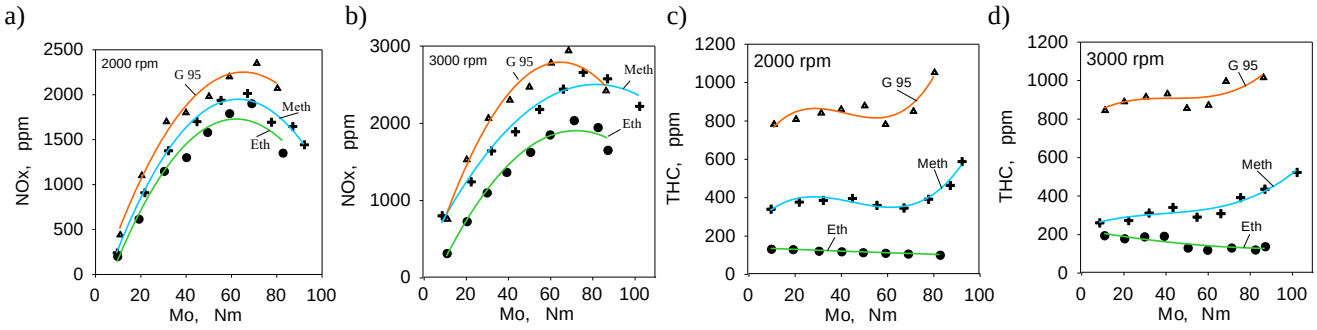

Fig. 4. Comparison of concentration of toxic components of exhaust gases from Fiat 1100 MPI engine run on G 95 gasoline and ethyl alcohol Eth and methyl alcohol Meth

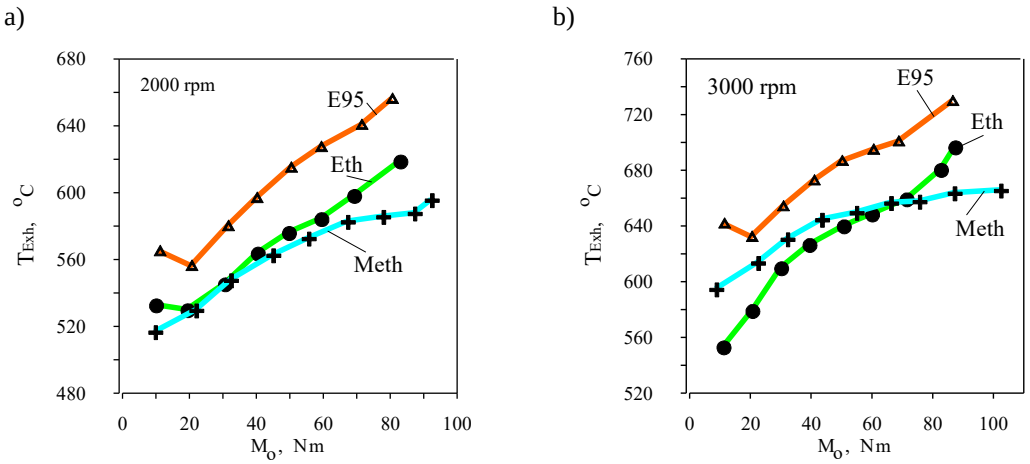

Fig. 5. Comparison of the exhaust gases temperature in Fiat 110 MPI engine run on gasoline and methyl and ethyl alcohols

The combustion of alcohols has advantageous effects on emissions of THC, as shown in Fig. 4c and 4d. At methanol fuelling, concentrations of THC in a complete range of change of engine loads were nearly 2–3 times lower than gasoline fuelling. Even greater differences in concentration of THC were observed at ethanol fuelling, where the reduction was 4.5–8.2 times.

Such significant changes in THC concentration can be explained by the different chemical composition of methanol, CH_3OH, and ethanol, C_2H_5OH, compared to gasoline that is a mixture of different hydrocarbons with complex chemical composition. Simple chemical structure and the presence of oxygen in molecule of alcohols contribute to rapid and complete oxidation of these fuels. Oxygen contained in the molecules of alcohols is released in the combustion process directly in zones of the reaction, which considerably accelerates oxidation of carbon and hydrogen atoms. The additional factors contributing to the rapid oxidation of alcohols are the higher combustion rates of alcohol vapours and thus, higher temperatures of the entire load during the initial stages of combustion compared to the ones occurring in the case of fuelling with gasoline. In the case of gasoline combustion, the oxidation time of higher hydrocarbons increases as the number of carbon and hydrogen atoms increases, which in high-speed spark ignition engines may affect concentrations of total hydrocarbons in the exhaust gases.

Faster combustion of alcohol vapours causes that temperatures of the exhaust gases downstream of the exhaust valve are lower than the ones observed in the case of gasoline fuelling, as in Fig. 5. The temperature differences are present in the entire range of load variations and increase with the increase of the engine load. Depending on engine load and rotational speed, the observed temperature differences amounted to 45–90°C for methanol and 30–60°C for ethanol. It can be assumed, that lower temperatures of exhaust gases have an advantageous effect on the durability of the engine fuelled with alcohols.

3.2. Comparison of combustion parameters for methanol and ethanol fuelling

The pressure trace in the second cylinder was recorded using a piezoelectric sensor type GH13 made by AVL mounted in the engine's cylinder head. Average indicator diagrams for 50 successive cycles of engine operation and pressure runs of 50 individual and successive cycles of engine operation were the subject of the analysis.

Figure 6 presents a comparison of average cylinder pressure during combustion for two selected rotational speeds and different loads of the engine running on methanol and gasoline. From this comparison, it can be concluded that considerably higher maximal pressures are present during the combustion of methanol. The heat release process for methanol is greater at the beginning of combustion, which increases rate of pressure rise compared to gasoline. Such a tendency is noticeable for all engine loads and for all rotational speeds. It was also ascertained that for medium and maximum engine loads, when methanol is combusted, the maximal pressures are reached faster than gasoline feeding, thus approaching TDC. This is one of the reasons for increasing engine power output and efficiency [9, 20]. A different tendency was observed for the lowest engine loads (green colour), where in the case of methanol, the maximum pressures were reached slightly later than for gasoline.

In the case of ethanol supply (Fig. 7), similar tendencies to those discussed earlier for methanol occur for lower rotational speeds of 2000 rpm, where for the engine load of 30–80 Nm, both maximal pressures and pressure growths at the beginning of combustion are higher comparing to gasoline. For higher rotational speeds of 2500–3000 rpm, the values of the average pressures in the course of combustion for ethanol and gasoline are similar. It is worth emphasizing, however, that also for rotational speeds discussed here, in the range of medium engine loads, a tendency to slightly higher pressures occurring when feeding with ethanol can be noticed.

In a spark-ignition engine, there is a significant uniqueness of work from cycle to cycle. This is caused by changes in the quality of the fuel charge in subsequent suction cycles but mainly by changes in the delay time of combustion and the formation of a stable flame around the spark plug. To check courses of the pressure in individual cycles for the combustion of ethanol and gasoline, the indicator diagrams of individual combustion for rotational speed of 3000 rpm and for two engine loads, minimal 10 Nm and maximal 86

Nm, were compared in Fig. 8. In the Figures, the courses with the maximum pressure close to the average value, calculated from 50 consecutive cycles of engine operation are depicted in black, and two courses with the maximum pressures lower are depicted with coloured dashed lines while the ones with the maximal pressure higher than the average are presented with continuous lines.

The comparison shows that lower maximal combustion pressures are accompanied by later angles of termination of the kinetic combustion phase (reaching the maximal pressure), depicted with dashed lines. This phenomenon is more clearly visible for low engine loads, such as in Fig. 8c and 8d. Protracted combustion is visible for the minimal engine load of Mo = 10 Nm in cycles with low maximal pressures, as illustrated in Fig. 7a and 7b. This is due to a longer ignition delay, which causes active combustion to shift towards later angles after TDC, accompanied by higher pressures in the latter stages of combustion and expansion.

The comparison outlined in Fig. 8 shows that for both tested fuels, ethanol and gasoline, both the combustion courses at high pressures p_{max} and at low pressures are similar. The heat release rate dQ/dα can be a measure of the rate of fuel combustion. Its value was calculated based on the recorded indicator diagrams. To perform the calculations, an author's proprietary computer program designed to analyse indicator diagrams was used, which was developed by the Combustion Engines and Automobiles Department of Bielsko-Biala University, described in detail in the publications [20]. The averaged diagrams from 50 consecutive cycles were used as representative cycles for engine operation in a selected points defined by n-Mo (rotational speed and torque). As a result of the calculations, the courses of combustion parameters were obtained, such as: pressure increase rate, heat release rate, the temperature of the working medium, composition of the charge as a function of crank angle, as well as aggregated and maximal values of selected parameters. An analysis of only some of the calculated parameters is presented in this paper.

Comparison of values of maximal heat release rates $(dQ/d\alpha)_{max}$ for the investigated fuels confirms greater dynamics of the heat release during the combustion of alcohols, and especially of methanol. In the complete range of changes of the engine load, for both analysed rotational speeds, values of $(dQ/d\alpha)_{max}$ are higher for alcohol than the ones calculated for gasoline. It is worth emphasizing at this point that the differences in the heat release rate for

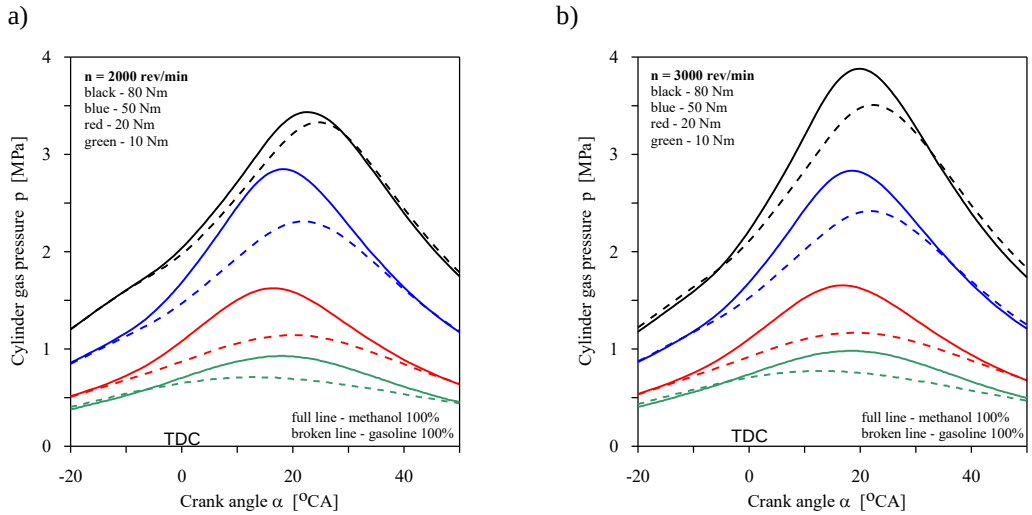

Fig. 6. Comparison of cylinder pressure in function of crank angle in Fiat 1100 MPI engine run on gasoline and methanol for a various engine loads

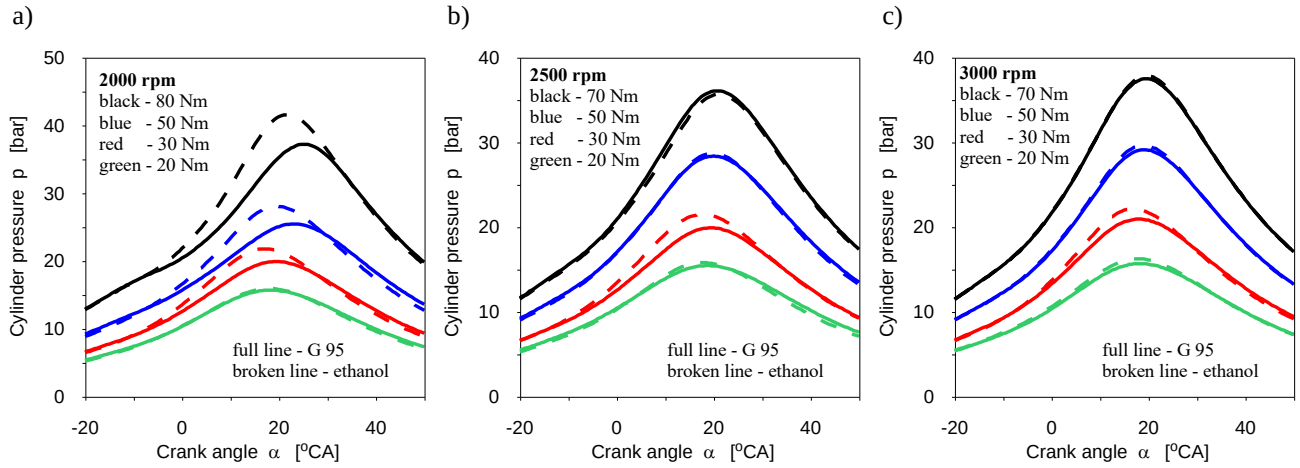

Fig. 7. Comparison of cylinder pressure in function of crank angle in Fiat 1100 MPI engine run on gasoline and ethanol for a various engine loads

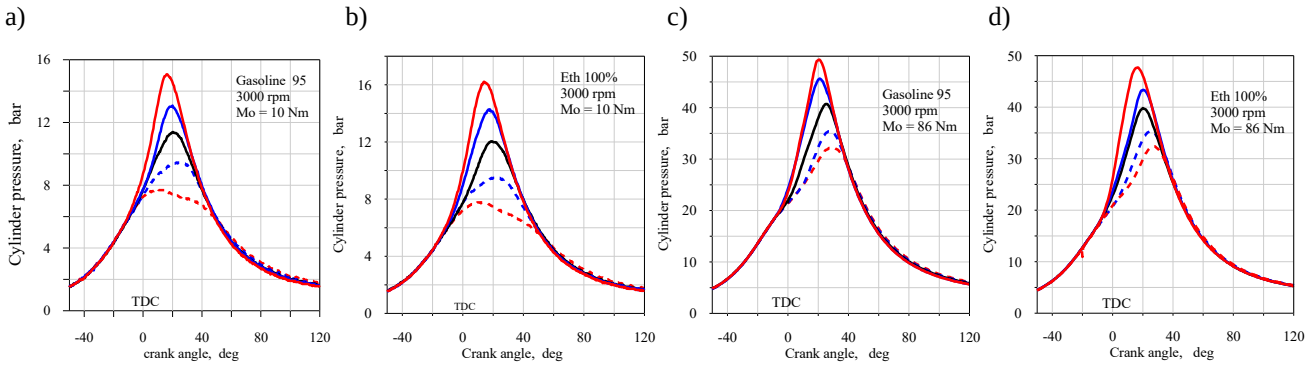

Fig. 8. Comparison of cylinder pressure in function of crank angle in Fiat 1100 MPI engine run on gasoline and methanol for a various engine loads

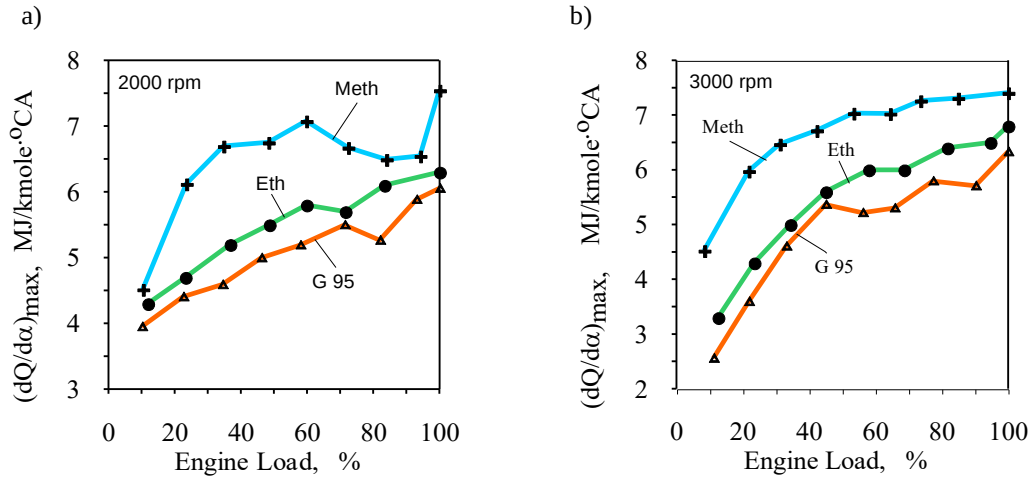

Fig. 9. Maximal heat release rate in Fiat 1100 MPI engine fuelled with gasoline, ethanol and methanol, for various rotational speeds and engine loads

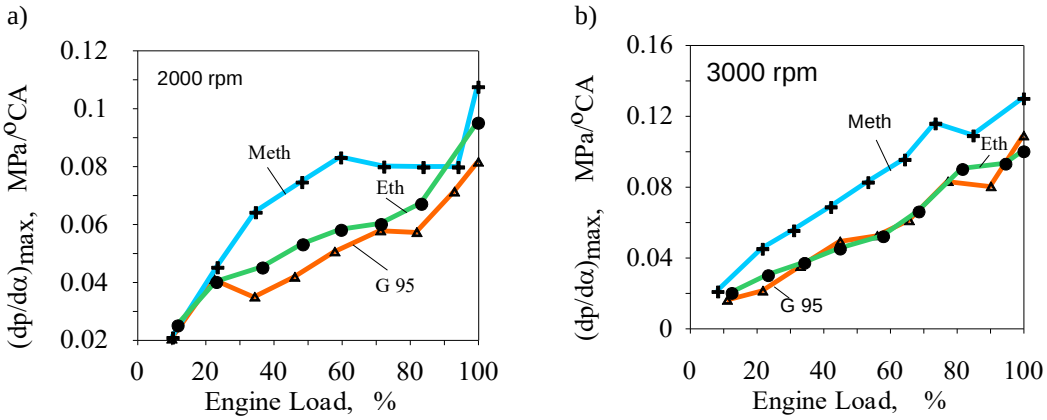

Fig. 10. Maximal rates of pressure growth in Fiat 1100 MPI engine run on gasoline and methanol for various rotational speeds and engine loads

ethanol are only slightly greater within the range of 10–18%, while for methanol are clearly greater by 50–80% compared to those recorded when fuelling with gasoline (Fig. 9).

As a measure of engine operational noise, the value of the maximal pressure increase rate $(dp/d\alpha)_{max}$ may be used, in the interval from the beginning of the combustion to the moment when the maximal pressure is reached. The analysis of this parameter, presented in Fig. 10, shows that operation of the engine fuelled with methanol is characterized by rougher run of the engine, which is evidenced by higher values of $(dp/d\alpha)_{max}$. Value of $(dp/d\alpha)_{max}$ for maximal engine loads exceeds 0.1 MPa/°CA and is higher with about 0.025 MPa/°CA in relation to gasoline fuelling. Also, in the range of medium engine loads, the values of $(dp/d\alpha)_{max}$ for methanol are distinctly higher compared to gasoline. However, due to the fact that they are lower than 0.9 MPa/°CA, this should not have any significant effect on the operational roughness of the engine run on methanol.

Higher values of $(dp/d\alpha)_{max}$ for methanol are connected with higher combustion rate of methanol-air mixture in the first stage of kinetic combustion, which results in a faster growth of pressure and heat release rate $(dQ/d\alpha)_{max}$ as presented in Fig. 7 and Fig. 9.

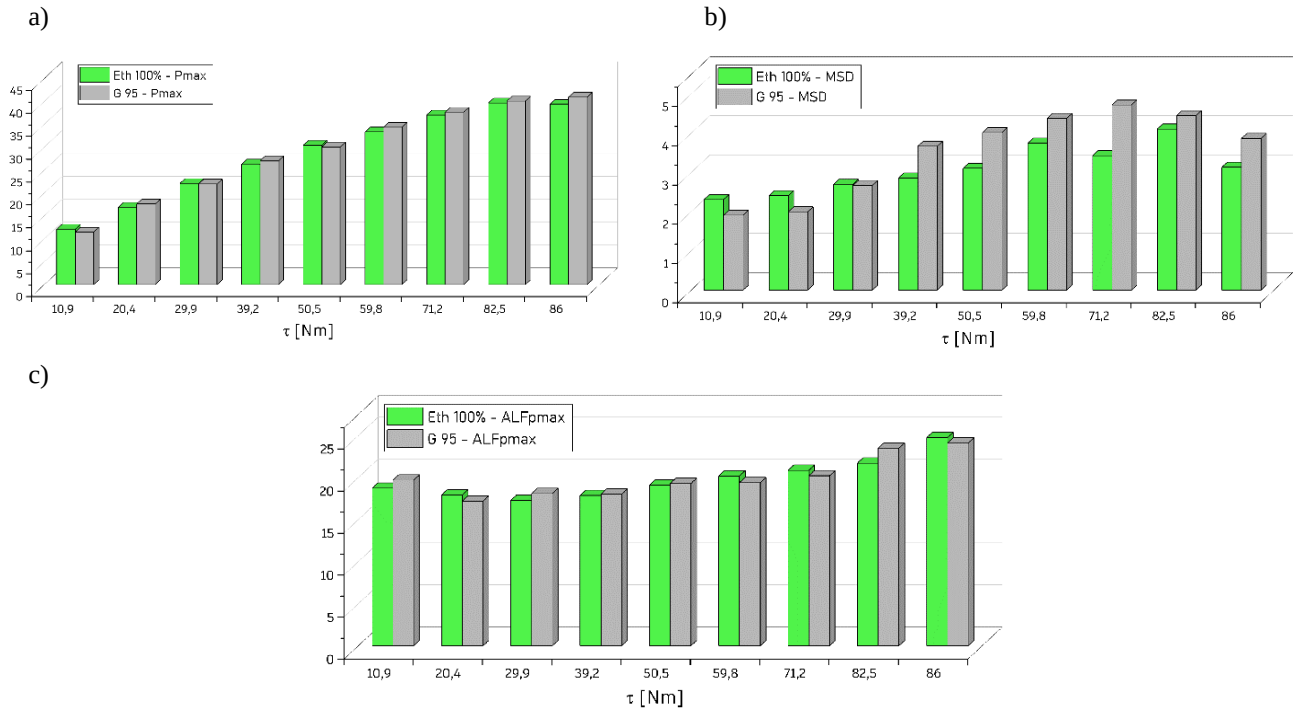

Fig. 11. Comparison of parameters calculated from diagrams of individual combustion for the engine fuelled with ethanol and gasoline: a) mean value of maximal combustion pressure, b) mean standard deviation $\sigma_{p_{max}}$ of the maximal combustion pressures, c) maximal pressure variation coefficient s_p

The values of $(dp/d\alpha)_{max}$ for supply with gasoline and ethyl alcohol are similar, especially in the case of the higher rotational speed of 3000 rpm, as presented in Fig. 9. Therefore, it can be assumed that supply of the engine with ethyl alcohol will not affect the noise levels of its operation.

3.3. Smoothness of the operation of the engine powered by alcohol

The spark ignition engines are characterized by greater operational smoothness cycle by cycle in relation to the compression ignition engines. This is due to cyclical changes in mass of the intake air, the course of the ignition spark, changes in the ignition delay time, the time of a stable front flame formation, and changes in the combustion rate depending on the composition of the homogeneous combustible mixture. The majority of fuels for the spark ignition engines is characterized by narrow flammability limits and a large change in combustion rate, dependent on excess air coefficient λ. Due to ecological reasons, modern spark ignition engines operate on stoichiometric mixtures and the excess air coefficient λ = 1.0 is controlled precisely by the oxygen sensor (λ sensor). With stochastic changes in amount of the air sucked in, the oxygen sensors can act with some delay, causing that for a number of cycles, changes in the excess air coefficient can occur around the value of λ = 1.0. It is also worth mentioning here that the lambda sensors available on the market were developed for petroleum-derived fuels. When using alcohols, i.e. fuels with molecules significantly different than gasoline hydrocarbons, there is a need to investigate the impact of fuel on the repeatability of cycles of engine operation. It is also important to check if there is no misfiring during the combustion of alcohols. This was the basis to undertake research in this area.

The assessment of smoothness of engine operation for gasoline and alcohol fuelling was performed based on recorded diagrams of individual combustion for 50 successive cycles of engine operation. The following parameters were used for the assessment:

$$\bar{p}_{max} = \frac{\sum p_{max-i}}{n} \tag{4}$$

$$\sigma_{p_{max}} = \sqrt{\frac{\sum (p_{max-i} - \bar{p}_{max})^2}{n-1}} \tag{5}$$

$$s_p = \frac{\sigma_{p_{max}}}{\bar{p}_{max}} \cdot 100\% \tag{6}$$

where: $\bar{p}_{max}$ – mean value of maximal pressure for n successive cycles, p_{max-i} – maximal pressure of the next cycle, n – number of analysed cycles, $\sigma_{p_{max}}$ – mean standard deviation, s_p – PVC – pressure variation coefficient.

Figure 11a presents a comparison of the average maximal pressures calculated on the basis of indicator diagrams of individual combustion for 50 successive cycles of engine operation. The engine was operated at rotational speed of 3000 rpm and variable engine loads from the minimal of 10.9 Nm to the maximal of 86.0 Nm. This comparison shows that over the entire range of engine loads, the values of the mean pressures for gasoline and alcohol were similar. Also, in the case of other investigated rotational speeds of 2500 rpm and 3500 rpm, maximal pressures for the both fuels were similar.

The comparison of the values of the standard deviation $\sigma_{p_{max}}$ and maximal combustion pressures shown in Fig. 11b indicates that for engine loads higher than 30 Nm, the engine operated on ethanol is characterized with bigger operational repeatability, cycle by cycle. This is evidenced by significantly lower values of $\sigma_{p_{max}}$. Only in the area of low-

er engine loads, higher values of σ_{pmax} are present in the case of ethanol fuelling, which proves that there are greater fluctuations of maximal pressures. Greater fluctuations of the pressures at low engine loads can be caused by a reduction in the charge temperature associated with higher vaporization heat of alcohol, and prolonged stabilization time of the flame after ignition.

The pressure variation coefficient s_p shown in Fig. 11c can prove the effect of pressure fluctuations on the stable operation of the engine. This coefficient decreases with increasing engine load, suggesting pressure fluctuations' diminishing effect on stable engine operation. A comparison of the s_p coefficient for both investigated fuels shows that the engine fuelled with ethanol in the range of mean and maximum loads is characterized by greater repeatability cycle by cycle. It demonstrates that this type of fuel supply brings about smoother and more stable operation comparing to standard operation on gasoline.

Fluctuations of the maximal pressures for individual combustion of gasoline and ethanol are presented in Fig. 12. From the comparison, it can be found that at the engine load close to the maximal M_o = 86 Nm, in successive cycles of engine operation, there are significant absolute differences in the pressures for both fuels. At the same time, slightly higher fluctuations of the maximum pressures for gasoline can be observed, Fig. 12a.

For the quantitative assessment of the fluctuations of combustion pressure, the absolute differences and relative differences of the maximal pressures related to the medium value of the maximal pressure calculated for 50 successive cycles of engine operation are presented in Fig. 13.

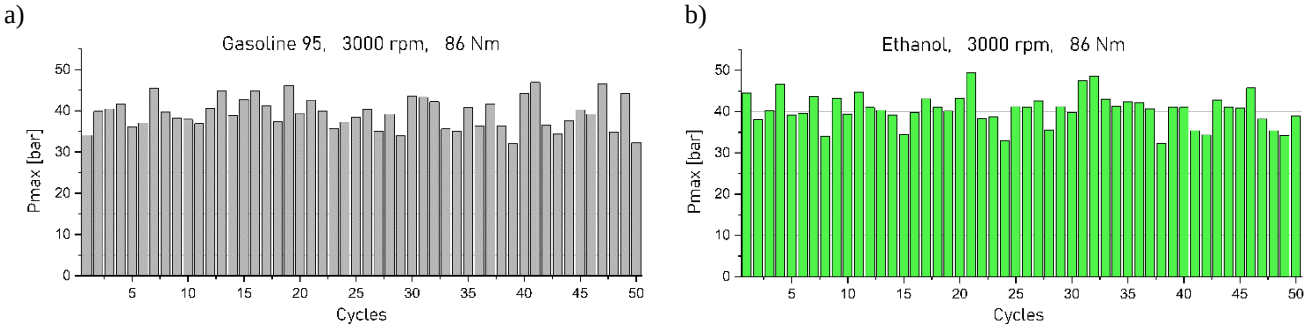

Fig. 12. Fluctuations of the maximum combustion pressures in successive operational cycles of Fiat 1100 MPI engine fuelled with gasoline and ethyl alcohol

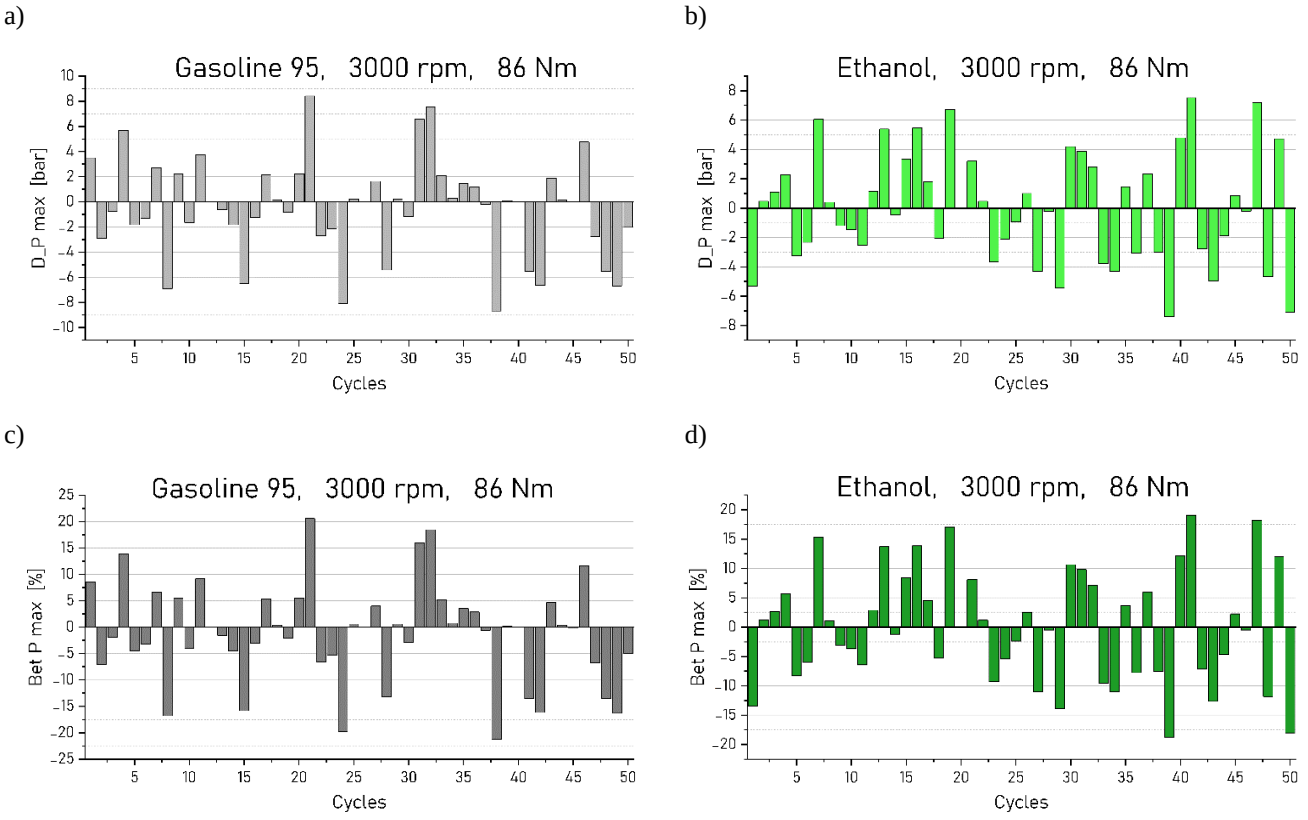

Fig. 13. Absolute and relative differences of maximal combustion pressures in successive operational cycles of Fiat 1100 MPI engine run on gasoline and ethyl alcohol

The differences were calculated from the following equations:

$$AD_{p_{max}} = p_{max-i} - \bar{p}_{max} \quad (7)$$

$$RD_{p_{max}} = \frac{Ap_{max}}{\bar{p}_{max}} \cdot 100\% \quad (8)$$

where: $AD_{p_{max}}$ – absolute difference of maximal pressure, $RD_{p_{max}}$ – relative difference of maximal pressure, $\bar{p}_{max}$ – medium value of maximal pressure calculated from 50 successive cycles of individual combustion.

The absolute differences of the maximal pressures for gasoline are high. The maximal value of $AD_{p_{max}}$ for the highest pressures exceeds +8 bar, and the minimal ones more than –8 bar, which results in maximal fluctuations of the pressures of about 17 bar, as depicted in Fig. 13a. For ethanol feeding, the values of $AD_{p_{max}}$ are slightly lower and fluctuate within the range of –7.2 to 7.4 bar, and hence, maximal fluctuations of the pressures are equal to 14.6 bar, as illustrated in Fig. 13b.

The relative values of pressure changes for gasoline amount to $RD_{p_{max}}$ = –21.5–20.5% (Fig. 13c), while for ethanol fuelling to $RD_{p_{max}}$ = –18.5–19.0% (Fig. 13d). Such changes should be evaluated as quite high. However, it seems that they should not have any adverse effect on loading of the crank system and the durability of the engine.

Both indicators, $AD_{p_{max}}$ and $RD_{p_{max}}$, are a little lower for ethanol, which proves the beneficial effect of ethanol fuelling on the smoothness of engine operation.

Regarding the conversion of chemical energy into mechanical work, not only the value of maximum combustion pressure is important, but so is the angle at which the p_{max} which respect to TDC is reached.

Both changes in the p_{max} as well as the value of the angle at which the p_{max} is reached in successive cycles of the operation cause fluctuations of the mean indicated pressure and the torque, having adverse effect on the cooperation of the engine with the receiver. High fluctuations in the cycles result in accelerated wear of bearings, clutches and transmissions. For this reason, smoothness of engine operation is of utmost significance and should be carefully evaluated when fuelling systems or fuel type is to be changed.

In Figure 14 a comparison of average values of the p_{max} angle for gasoline and ethanol fuelling is presented. The comparison was performed for the rotational speed of 3000 rpm and variable engine load. From the analysis of Fig. 14a, it can be perceived that the maximum p_{max} angles initially decrease, and then increase, as the engine load increases. This is connected with changes in the combustion course and fluctuations in successive cycles of the engine operation. At minimal loads of the spark ignition engine, a small amount of the charge is burnt in the combustion chamber at lower temperatures of the walls of the chamber and the working medium. It results in the prolongation of the first stage of kinetic combustion. At the same time, due to the lower energetic density of the charge, fluctuations in the course of combustion are more pronounced. As a result, at minimal engine loads, the time to reach the p_{max} is extended. With increasing engine load, amount of the sucked charge increases, and so does its energetic density, which increases the combustion speed and shortens the time to reach the p_{max}. However, a further increase in the engine load is related to an increase in the angle to reach the p_{max}, which is induced by the longer time of kinetic combustion of the growing quantity of the mixture.

From the comparison presented in Fig. 14a it may be inferred, that for the majority of the cycles, the maximal combustion pressures for both fuels were reached for the angles of 18–24°CR after TDC. Average values of these angles for alcohols and gasoline are similar, and the difference can be neglected.

Figure 14b presents a comparison of the variation coefficient of occurrence of the maximal combustion pressure angle calculated from the following formula:

$$s_{\alpha p_{max}} = \frac{\sigma_{\alpha p_{max}}}{\bar{\alpha}_{p_{max}}} \cdot 100\% \quad (9)$$

where: $s_{\alpha p_{max}}$ – coefficient of variation of the maximal combustion pressure angle, $\sigma_{\alpha p_{max}}$ – mean standard deviation of the p_{max} angle, $\bar{\alpha}_{p_{max}}$ – average value of the p_{max} angle calculated from 50 successive cycles of engine operation.

From the analysis of Fig. 13b, it may be concluded, that the effect of the changes in the $\alpha_{p_{max}}$ angle of individual cycles on the value of the coefficient of variation $s_{\alpha p_{max}}$ decreases with the increase of engine load. At the same time, in the range of average engine loads, the values of the $s_{\alpha p_{max}}$ for ethanol are lower than for gasoline. Only at the lowest and the maximal engine loads, the values of the $s_{\alpha p_{max}}$ for ethanol are higher than values for gasoline. The reason for this phenomenon in the case of the lowest engine load may be greater fluctuations in the combustion rate of ethanol caused by an excessive decrease in temperature of the charge due to the higher evaporation heat of alcohol, as mentioned before. On the other hand, in the case of maximal engine loads, different air excess coefficients of the

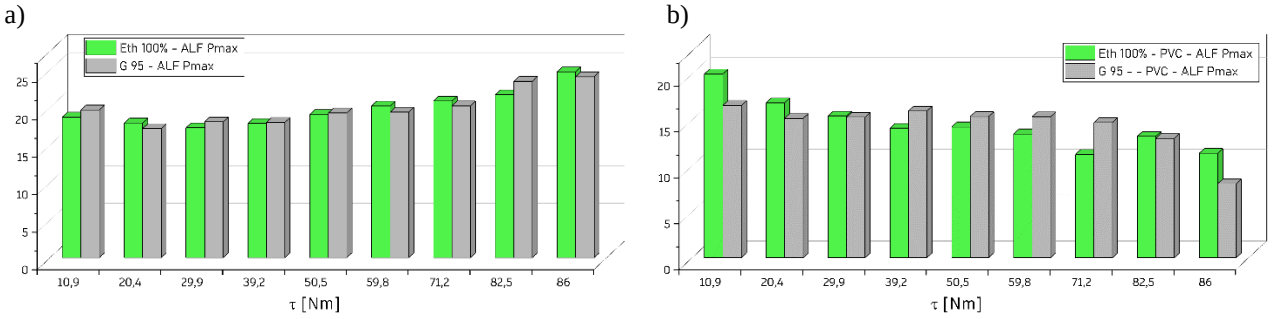

Fig. 14. Comparison of the angles of occurrence of the maximal pressures and the coefficient of angle variations $\sigma_{\alpha p_{max}}$ in course of combustion in Fiat 1100 MPI engine run on gasoline and ethyl alcohol

sucked mixture were found. A lower air excess coefficient for the gasoline-air mixture could cause a faster combustion of the mixture and smaller fluctuations of the angle.

Changes in the course of the combustion process during successive cycles of engine operation, manifested by fluctuations in maximum combustion pressure p_{max} and its angle α_{pmax} affect the changes in the crankshaft torque and the values of the mean indicated pressure pi for individual cycles of engine operation.

However, as demonstrated by the previous research of the authors, described in [23], the fluctuations of pi in subsequent cycles of engine operation are small at constant engine load, and they are similar for both fuels. The analysis of the relative coefficient of variability of the mean indicated pressure s_{pi} (calculated similarly as for the maximal pressure angle according to the formula 9) indicates that in the range of mean and maximal engine loads, the fluctuations of the p_i in individual cycles for both fuels are similar, while their values are lower than 2%, which should be considered irrelevant for the spark ignition engine, see Fig. 15.

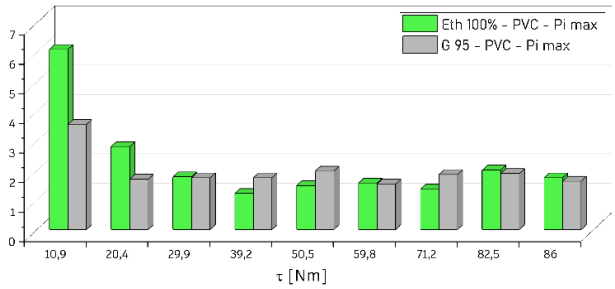

Fig. 15. Comparison of variability coefficient s_{pi} of the mean indicated pressure in Fiat 1100 MPI engine fuelled with gasoline and ethyl alcohol

4. Summary

In this paper, the results of the research performed on the engine fuelled with two kinds of primary alcohols. i.e. ethanol and methanol, as homogenous fuels, are presented. Gasoline was the reference fuel, and all the analysed parameters obtained from alcohol fuelling were compared to gasoline. Using alcohol as a homogenous fuel allows the application of water-logged ethanol obtained directly from the distillery, considerably reducing production costs.

The research performed in this paper has shown that using methyl and ethyl alcohols in a spark ignition engine improves its performance and ecological parameters with simultaneous improvement of smoothness of engine operation.

In relation to gasoline fuelling, the following parameters were found to be improved in the tested car engine of the passenger model of Fiat 1100 MPI:

- increase of maximal output power of the engine within the range of rotational speeds of 2000–3500 rpm, by 3.8–7.5% for methanol fuelling and by 1.7–3.3% for ethanol fuelling
- increase the overall efficiency of the engine by 1.5–7.5% for methanol and by 1.2–2.5% for ethanol
- reduction in the concentration of toxic components of exhaust gases: nitrogen oxides NO_x by 15–60% for methanol and by 35–75% for ethanol, total hydrocarbons content THC by 2–4 times for methanol and 4.5–8.2 times for ethanol.

The increase in efficiency was observed in the entire range of changes in engine load and its rotational speed, with higher values of the changes occurring as the engine load increased.

The increase in the performance parameters was obtained with the unchanged compression ratio and the unchanged ignition advance angle. Both these parameters were optimized in the tested engine for gasoline fuelling. It seems that a further increase in the power output and efficiency can be achieved by increasing the compression ratio, which will allow better utilization of high anti-knock resistance of alcohols.

Feeding the engine with alcohol reduces the exhaust gas temperature behind the exhaust valve in the range of 45–90°C for methanol and 30–60°C for ethanol. This should lead to an increase in the durability of the engine.

The combustion of methanol vapours proceeds faster than gasoline, which is accompanied by higher maximum pressures in the cylinder p_{max}, higher heat release rate $(dQ/d\alpha)_{max}$ and higher maximal rate of pressure growth $(dp/d\alpha)_{max}$. As a result, the kinetic combustion phase of methanol is shorter, and the maximum pressure of the process is achieved faster than for gasoline. This explains the significant increase in the maximum power output and overall efficiency of the methanol-supplied engine. The increase in the maximum pressures is not high, and it seems that it should not change the engine's durability.

The analysed parameters, like pressure p, heat release rate $(dQ/d\alpha)_{max}$ and $(dp/d\alpha)_{max}$ during the course of combustion of ethyl alcohol, are similar to gasoline. As a result, the engine's operational noise and its durability should not change when the engine is run on ethanol as homogenous fuel.

The analysis of 50 successive cycles of individual combustion of alcohol and gasoline has shown that changes in the maximum pressure p_{max} in subsequent cycles of engine operation are stochastic and typical for the spark ignition engine. The character of changes of the p_{max} is similar for ethanol and gasoline.

The quantitative assessment of fluctuations of the maximal pressure defined by the mean value of the maximal pressure, mean standard deviation σ_{pmax} and coefficient of variability of pressures s_p indicates that in the range of engine loads higher than 20 Nm, fluctuations of the maximal pressure for ethanol are lower comparing to gasoline. It proves the improvement of smoothness of the engine powered by ethyl alcohol. Only for the lowest engine loads below 20 Nm, when the engine is fed with ethyl alcohol, an increase in the pressure fluctuations p_{max} and deterioration in smoothness of engine operation from cycle to cycle were observed. This can cause start-up difficulties and rough engine operation in warm-up phase during winter time.

This is probably due to excessive reduction in temperature of the fuel charge triggered by the greater heat of evaporation of ethanol in relation to gasoline, which affect the time of stabilization of the flame after ignition of the combustible mixture.

The research conducted for this paper fully confirms the possibility of using alcohols as homogenous fuels to feed the engines. It is especially recommended to use ethyl alcohol as a less aggressive fuel to the materials used in construction of the engines and less toxic to the environment.

Nomenclature

CI	compression ignition
CNG	compressed natural gas
DI	direct injection
LPG	liquefied petroleum gas
Ne	power output
NO_x	nitrogen oxides
SI	spark ignition
THC	total hydrocarbons
η_o	overall efficiency

Bibliography

[1] Baczewski K, Koldonski T. Fuels for a SI engines. Publishing House WKiL, Warsaw 2005.

[2] Borychowski M. Production and consumption of liquid biofuels in Poland and in the world – opportunities, threats, controversies. Roczniki Ekonomiczne Kujawsko-Pomorskiej Szkoły Wyższej w Bydgoszczy. 2012;5:39-59.

[3] Bulletin of the Energy Regulatory Office. 2010;2.

[4] Ethanol Internal Combustion Engines. ETSAP energy technology system analysis programme. Technology Brief, June 2010.

[5] Gmyrek J. Bioethanol in progress NCW w PKN ORLEN S.A. Conference „FUEL'S ZOOM – BIOETANOL" Kraków 27-28.04.2010.

[6] Gruca M, Pyrc M, Szwaja M, Szwaja S. Effective combustion of glycerol in the compression ignition engine equipped with a double direct fuel injection. Energies. 2020;13:6349. https://doi.org/10.20944/preprints202010.0096.v1

[7] Kelly KJ, Bailey BK, Coburn TC, Clark W, Lissiuk P. Federal test procedure emisssion test results from ethanol variable-fuel vehicle Chevrolet Luminas. Technical Paper 961092. 1996. https://doi.org/10.4271/961092

[8] Kowalewicz A. Efficiency of the SI engine fuelled with methanol-gasoline blends. P I Mech Eng D-J Aut. 1994; 208(2):123-128. https://doi.org/10.1243/PIME_PROC_1994_208_170_02

[9] Kowalewicz A. Emission characteristics of compression ignition engines fuelled with RME/DF and ethanol. Journal of KONES. 2004;11(1-2).

[10] Kowalewicz A. Methanol as a fuels for combustion engines. Combustion Engines. 1992;3-4.

[11] Kowalewicz A. Metanol as a fuel for spark ignitron engines: a review and analysis. P I Mech Eng D-J Aut. 1993;207(1): 43-52. https://doi.org/10.1243/PIME_PROC_1993_207_158_02

[12] Kowalewicz A, Pajączek Z. Eco-diesel engine with additional injection of ethanol. Archives Combustionis. 2003; 23(3-4):169-183.

[13] Kozak M. Ethyl alcohol as a fuel for contemporary internal combustion engines. Diagnostyka. 2019;20(2):27-32. https://doi.org/10.29354/diag/109173

[14] Kozak M. Exhaust emissions from a diesel passenger car fuelled with a diesel fuel-butanol blend. SAE Technical Paper 2011-28-0017. 2011. https://doi.org/10.4271/2011-28-0017

[15] Lábaj J, Barta D, Lenhard R. CFD simulation of glycerol combustion in diesel engine. Institute of Thermomechanics. 2008:35-50.

[16] McNeil J, Day P, Sirovski F. Glycerine from biodiesel: the perfect diesel fuel. Process Saf Environ. 2012;90(3):180-188. https://doi.org/10.1016/j.psep.2011.09.006

[17] McNeil J. Efficient combustion of glycerol and other low cetane fuels in the diesel engine. The Institution of Diesel and Gas Turbine Engineers publication. Power Eng. 2011, 15.

[18] Merkisz J, Pielecha I. Alternative automobiles drives. Publishing House Poznan University of Technology. Poznan 2006.

[19] Pańczyszyn T. Energy crops forum. Production of liquid biofuels – raw material potential. Poznan 12.02.2010.

[20] Semikow J. Study of a dual-fuel spark-ignition engine powered by gasoline and alcohol. PhD thesis, ATH Bielsko-Biała 2012 (in Polish).

[21] Stelmasiak Z. Applications of alcohols to dual-fuel feeding the spark-ignition and self-ignition engines. Pol Marit Res. 2014;3(83):86-94. https://doi.org/10.2478/pomr-2014-0034

[22] Stelmasiak Z, Larisch J, Semikow J. Some aspects of dual fuelling SI engine with gasoline and alcohol 12th EAEC European Congress Bratislava EAEC 2009, June 29-July 1, 2009.

[23] Stelmasiak Z, Pietras D. The evaluation of the regularity of the combustion process in the SI engine fuelled with petrol and ethanol. Combustion Engines. 2017;168(1):94-102. https://doi.org/10.19206/CE-2017-115

[24] Wang X, Gao J, Chen Z, Chen H, Zhao Y, Huang Y et al. Evaluation of hydrous ethanol as a fuel for internal combustion engines: a review. Renew Energ. 2022;194:504-525. https://doi.org/10.1016/j.renene.2022.05.132

[25] Yusuf AA, Inambao FL, Farooq AA. Impact of n-butanol-gasoline-hydrogen blends on combustion reactivity, performance and tailpipe emissions using TGDI engine parameters variation. Sustainable Energy Technologies and Assessments. 2020;40:100773. https://doi.org/10.1016/j.seta.2020.100773

Prof. Dariusz Pietras, DSc., DEng. – Faculty of Mechanical Engineering and Computer Science, University of Bielsko-Biala, Poland.
e-mail: *pietras@ath.bielsko.pl*

Prof. Zdzislaw Stelmasiak, DSc., DEng. – Faculty of Mechanical Engineering and Computer Science, University of Bielsko-Biala, Poland.
e-mail: *zstelmasiak@ath.bielsko.pl*

Piotr Pietras – student at Faculty of Mechanical Engineering, Wroclaw University of Science and Technology, Poland.
e-mail: *ppietras675@gmail.com*

Article citation info:
Kneba Z. Fuel systems of high power stationary engine. Combustion Engines. 2023;194(3):141-146. https://doi.org/10.19206/CE-169151

Zbigniew KNEBA

Combustion Engines
Polish Scientific Society of Combustion Engines

Fuel systems of high power stationary engine

ARTICLE INFO

Received: 30 May 2023
Revised: 28 June 2023
Accepted: 2 July 2023
Available online: 4 August 2023

The use of alternative fuels and, in the future, synthetic fuels has forced changes in the design of fuel supply systems in internal combustion engines. When operating a stationary engine at constant load, the possibility of using lean fuel mixtures appears. The selection of a precise operating mixture ignition system requires changes in traditional fuel systems. The article presents the current designs of fuel supply systems and their properties. Attention was paid to operating parameters resulting in acceptable emissions of toxic exhaust gas components.

Key words: *marine engine, stationary engine, engine fuel system, engine load, exhaust emission limits*

1. Introduction

Engines used on ships and stationary combustion engines in power plants have very similar fuel supply systems. This is due to the common pedigree of these engines. Manufacturers of high-power engines used them at the beginning as marine ones and later adopted them for land applications. Following the introduction of limits on the emission of other toxic components in marine and land-based engine applications, a distinction should be made between these designs. Because those were the times when the electronic control previously known from the automotive industry was adapted to marine engines, it was enough to diversify the software for main propulsion engines and power generators. However, because of certain differences between the fuel equipment of high-power engines and car engines, it is worth realizing these differences. This article is devoted to presenting the principles of operation of fuel supply systems in high-power engines.

2. Limitations of exhaust gas toxicity

Restrictions on the emission of toxic components in the exhaust gases of stationary engines apply to NO_x, CO, NMHC and particulate matter. Emissions are converted to g/kWh. The exhaust gas purity standards for stationary applications are derived directly from those applicable to marine engines. They take into account the size of the engine, taking into account the displacement and power (Table 1). Engines with a displacement of up to 10 dm^3 have relatively high requirements compared to larger engines. Such stationary engines serve as backup power generators and can provide power in the event of a power outage. They often work in urbanized areas. In the US, stationary power plants with multiple high-power generators operating near wind farms or photovoltaics as a backup energy source are also common. Because they are often far from cities, the exhaust gas purity requirements are lower. Requirements introduced for 2007 model year engines. Before this year there were no restrictions and at that time, not the manufacturer but the owner was responsible for the emissions when the technical condition deteriorated.

Table 1. Emission requirements for non-emergency stationary engines [3]

Displacement	Power	Year	Emission certification
< 10 dm^3/cyl	<= 3000 hp	2007–	Tier 2/3/4
	> 3000 hp	2007–2010	Tier I
		2010–	Tier II/IV
10–30 dm^3/cyl.	all	2007–	Marine Cat. 2 Tier III/IV
> 30 dm^3/cyl.	all	2010–2011	Marine Cat. 3 Tier I
		2012–	Marine Cat. 3 Tier II/III

In marine applications, limits for the emission of toxic exhaust components apply only to engines with a power of more than 130 kW. Regulation 13 of MARPOL Annex VI then applies. Offshore watercraft engines and emergency engines are not subject to this convention.

The limits of the permissible emission of toxins in exhaust gases depend on the sailing area of the vessel. Tier I and Tier II are applicable in all international seas, while Tier III is only in Emission Control Areas. The main parameter on which the permissible value depends is the engine speed.

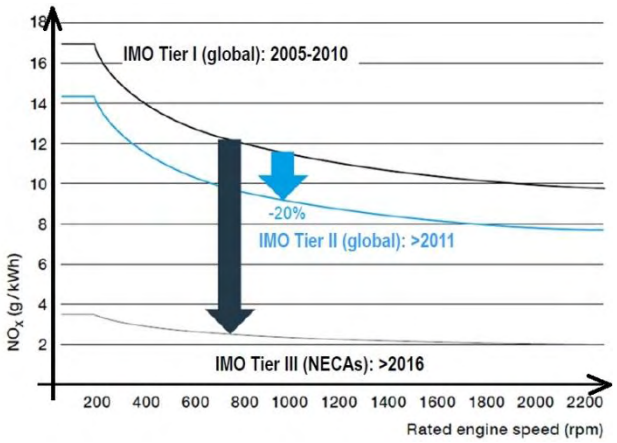

Fig. 1. Allowable NO_x emissions in exhaust gases [3]

3. Stationary and marine engine loads

Unlike engines used in vehicles and working machines, the rotational speed and often the load remain constant over long periods of operation of stationary and marine engines. The stability of parameters facilitates the design and testing of motors.

The studies presented in [1] indicate significant differences between the operating conditions and the valid tests that are used to measure engine emissions. These differences are shown in the graphs in Fig. 2 and 3. Load distributions differ a lot between electricity production – auxiliary engines and main engine.

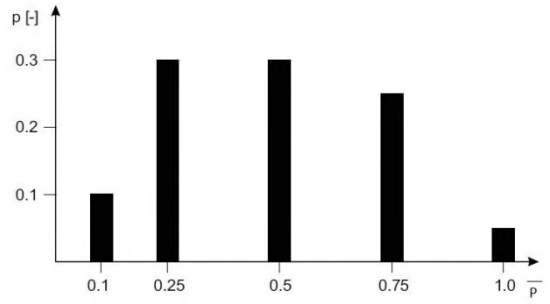

Fig. 2. Load distribution of a ship power plant [1]

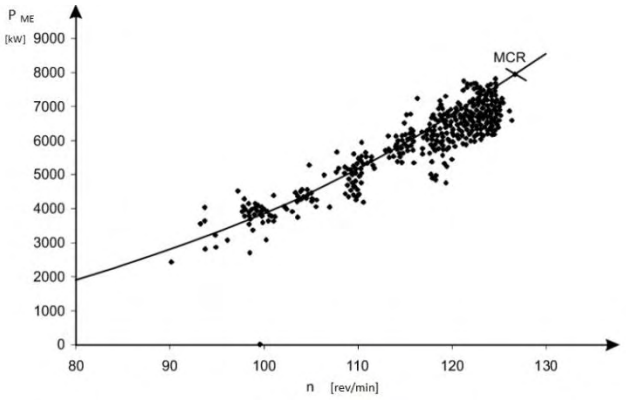

Fig. 3. Ship main engine load and speed distribution [1]

Currently, more and more hybrid propulsion systems are used, especially on specialized vessels (Fig. 1). If the electrical energy storage is capacious or the unit is often maneuvering, there is a chance for long-term operation of the engine with a full load and then idling. This way of operation indicates the need to change the tests to those shown in Fig. 4.

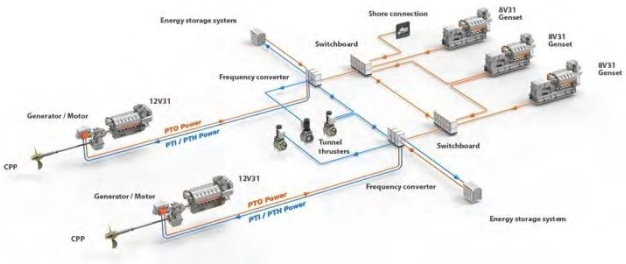

Fig. 4. Modern roro/ferry ship propulsion system [2]

The hybrid propulsion system has the advantage that it can accumulate electric energy when braking the ship, but it is only useful during maneuvers in ports.

4. Design solutions for liquid fuel supply systems for two-stroke engines

After many years of production of traditional fuel systems, in 2001 the slow-speed two-stroke engine of the RT flex family appeared and the era of high-power electronically controlled engines began [11]. For the first time, electronic control of the operation of fuel injection systems, opening the exhaust valve and starting the engine with compressed air was used (Fig. 5). The fuel system used the idea adopted earlier in the automotive industry to supply fuel to the cylinder under constant pressure from a pressure accumulator.

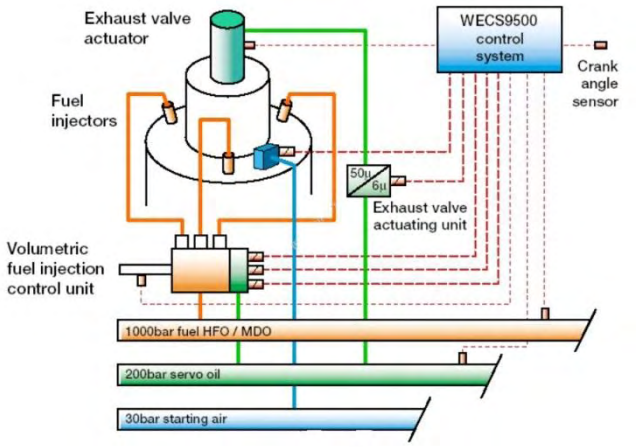

Fig. 5. Wärtsilä RT flex fuel supply system [6]

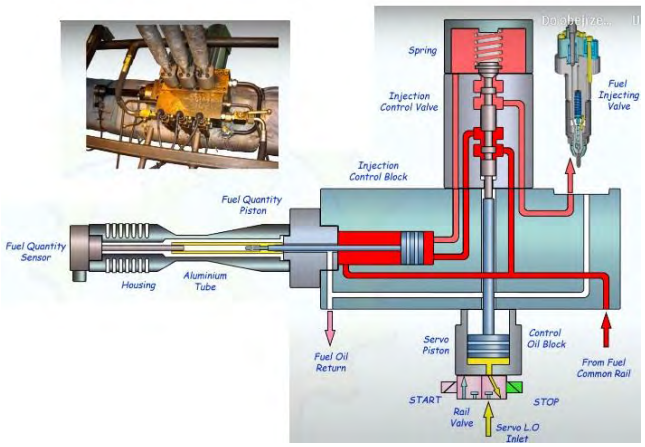

Fig. 6. Wärtsilä RT flex fuel supply [8]

However, due to the lower rotational speed and thus longer injection time, such high pressures and short injection times are not used in many phases. More important is mechanical-hydraulic rate limiting and reliability. With large cylinder diameters, 3 injectors are used.

The operation of this system is based on the fuel under pressure (100 MPa) accumulated in the tank and the use of control oil under the pressure of 20 MPa in the tank (Fig. 6).

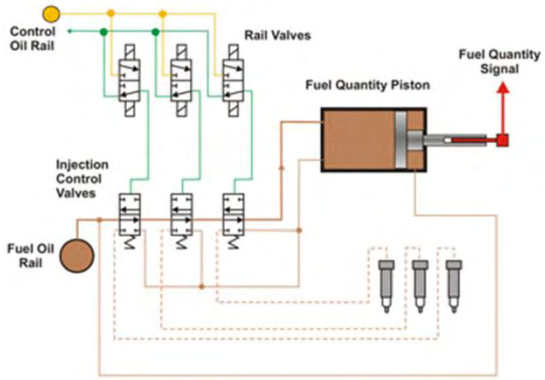

Fig. 7. Control in the RT flex fuel supply system [6]

At the beginning of the process, when the control oil does not flow into the oil cylinder, the fuel supply valve to the dose metering chamber is opened and the valve to the injectors is closed. After overriding the hydraulic distributor, the oil cylinder closes the dose metering valve and opens the filling injector. When the hydraulic distributor returns to the stop position, injection ends. Due to the 3 injectors in each cylinder, the control system for the cylinder includes 3 hydraulic distributors and one fuel tank (Fig. 7).

The described control enables full monitoring of its parameters. The screens of the monitoring program present operating parameters such as the volume of injected fuel, fuel pressure, injection times, and delay times between the signal and the actual injection start. Selected of these parameters are shown in Fig. 8.

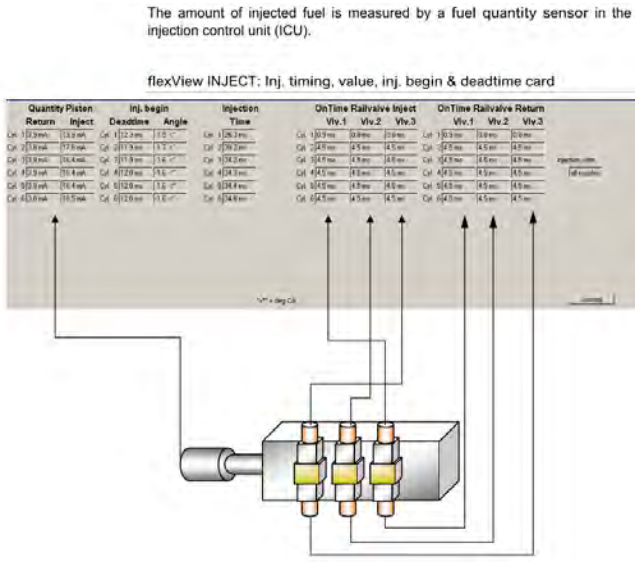

Fig. 8. Control screen of operating parameters of the RT flex power supply system [9]

In MAN engines, the design solution is also based on the use of a spool valve operated by control oil under an overpressure of 20 MPa. The difference from the previously described Wärtsilä design is the use of a hydraulic booster to create high fuel pressure. The differential piston, actuated by the control oil, expels the fuel under high pressure (Fig. 9).

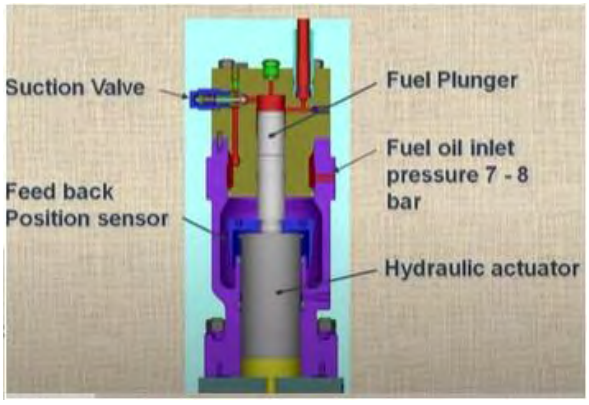

Fig. 9. Hydraulic amplifier in the fuel supply system – MAN [7]

5. Design solutions for liquid fuel supply systems for four-stroke engines

Electronic control has also been used in four-stroke engines since 2001. Due to their higher rotational speeds, the control processes must be faster. For faster fuel evaporation, a higher fuel pressure is used during injection, e.g. 160 MPa. The design of the system for MAN is somewhat similar to systems for car engines. The hydraulic diagram of the MAN heavy fuel supply system is shown in Fig. 10.

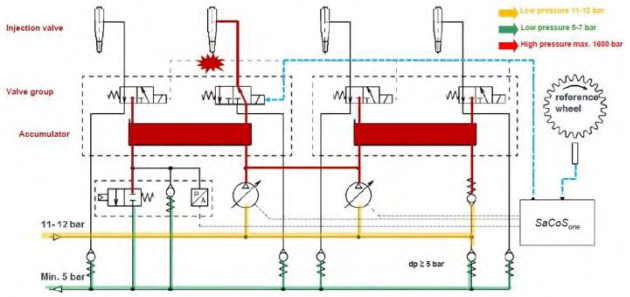

Fig. 10. Hydraulic scheme of heavy fuel supply in four-stroke MAN engines [7]

It uses three levels of fuel pressure. Power supply for high-pressure pumps is 1.2 MPa, injection pressure is 100–160 MPa and overflow pressure is 0.5 MPa. Contrary to the well-known construction of electromagnetic CR injectors in passenger car engines, the described MAN solution uses a valve with a control chamber closed with a ball (as in cars), but located at the fuel accumulator and connected to the mechanical injector by a high-pressure pipe (Fig. 11).

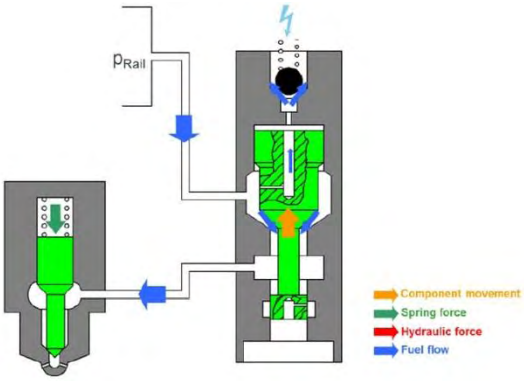

Fig. 11. Valve and injector [7]

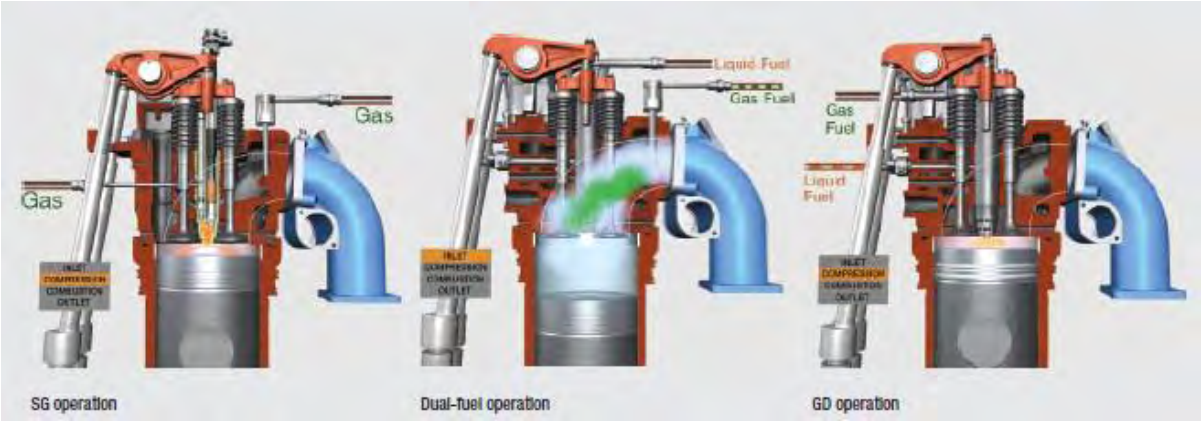

Fig. 12. Tree systems of 4 stroke engine operations: SI, dual fuel, diesel [11]

When using heavy fuel, it is necessary to flush the system with light fuel for 2 minutes before stopping the engine.

6. Gas fuel supply systems

The desire to use gaseous fuels as an alternative to liquid fuels resulted in the development of dual-fuel (diesel cycle) or spark-ignition gas engines of high power. Dual-fuel engines are used in marine and stationary propulsion systems, while gas-fired engines are used only as stationary ones. The diesel engine requires a pilot dose of diesel fuel to initiate the combustion process. The main fuel is vaporized or expanded natural gas or LPG. The cross-section of the cylinder head and combustion chamber of such an engine is presented in Fig. 12.

In four-stroke engines, direct injection into the combustion chamber is used for the pilot dose and the introduction of the main gas dose before the intake valve. As a dual fuel engine is designed for continuous operation in gas operating mode or diesel operating mode. The gas fuel (for full load operation) must have at least LHV =25 MJ/kg, methane number 70 [2]. Gas is stored in marine applications as liquid (LNG or LPG).

The Wärtsilä company introduced dual fuel engines also in the low-speed engine version.

Powerful four-stroke dual-fuel engines have been developed for many years. Recently, the technique of co-salting oil and methane for two-stroke engines has been introduced. The technical solution is significantly different Gas is introduced into the cylinder in the middle of the piston stroke through holes in the cylinder liner. Gas is the main fuel as it accounts for 99% of the energy supplied at maximum engine load. The mixture in the cylinder is lean. For effective ignition, there are 3 pre-chambers in the head and oil is injected into them. (Fig. 13).

7. Development trends of fuel supply systems

Recent literature mentions the design of other fuels in dual fuel systems. Their task is to replace some of the carbon-containing fuels with hydrogen carriers. Ammonia may be such a carrier. In the article [12] the co-combustion of ammonia and methane in a high-pressure medium-speed four-stroke natural gas engine was modeled. As it is already implemented in SI gas engines, the authors propose a pre-chamber for ignition initiation. The use of a pre-chamber proved necessary when the research on flame formation and the formation of toxic exhaust compounds was carried out. Ammonia pyrolysis promotes the formation of a flame. This flame then travels from the induction chamber to the main chamber. Then, strong charge vortices are created in the main chamber and the flame can spread despite the lean mixture zones in the main chamber. The trends in nitrogen oxide emissions were not clear because when NO decreased, N_2O increased. Ammonia turned out to be a catalyst for NO decomposition.

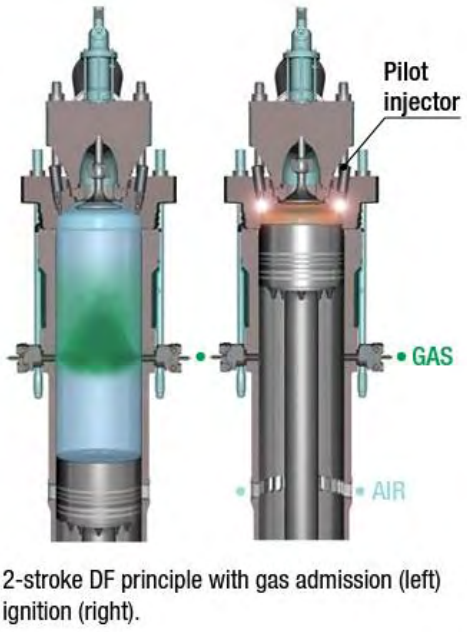

Fig. 13. Dual fuel two stroke engine [10]

In multi-cylinder engines, uneven loading of individual cylinders results in many unfavorable phenomena, such as crankshaft vibrations, pressure fluctuations in the intake and exhaust systems, and deterioration of cylinder flushing. Exhaust gas temperature sensors were introduced to prevent uneven loading of the cylinders. In the past, such sensors were used by the crew to monitor engine operation. Currently, they operate automatically in the feedback loop, controlling the size of the injected dose and the division into injection phases.

Diagnosis methods based on rotational speed measurement are also being developed [4]. In this article, the authors developed the theory of diagnosing the combustion process based on the course of the instantaneous rotational speed. The possibility of mounting a precise shaft speed transducer in a large motor improves the quality of the data obtained. They called their prototype measurement and analysis system SpeedMA.

8. Mathematical modeling of processes in high power engines

Currently, methods of mathematical modeling of processes are being developed to improve environmental and operational parameters. They are based on the black box approach of elemental neural networks [5, 14].

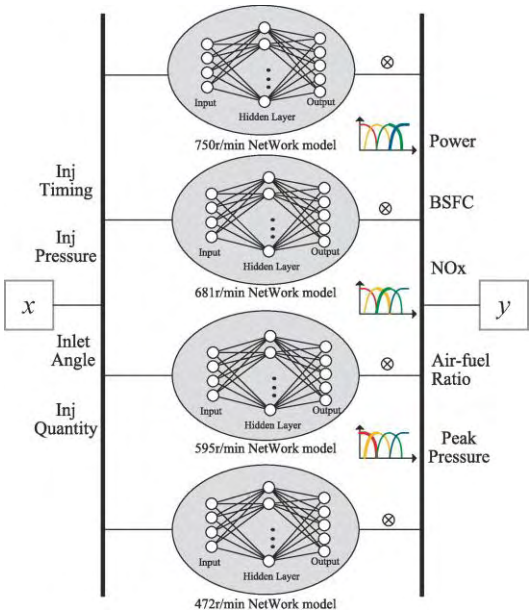

Fig. 14. The structure of the data-driven model [14]

The methods of assessing changes in the crankshaft speed were and are used in car engines in on-board diagnostic systems of the OBD type at the end of the 1990s. Simple algorithms were used to calculate the acceleration of the crankshaft in the expansion strokes of individual cylinders. Engine running erratically is a warning sign of large increases in exhaust emissions, especially hydrocarbon emissions. The authors of the publication [5] significantly developed the theory in order not only to diagnose but also to improve fuel dosing control. They used fuzzy logic to build a mathematical model describing many different processes in the engine. This complicated model is shown in Fig. 14.

Conclusion

High-power engines are fundamentally different in the construction of fuel systems from those used in the automotive industry. The main reason for the differences is different fuels and long-term operation at constant load. I notice a tendency to use gaseous fuels instead of liquid fuels. Control systems that make the operation of the fuel system dependent on the properties of fuels are being developed. Recent literature mentions the design of other fuels in dual fuel systems. Their task is to replace some of the carbon-containing fuels with hydrogen carriers. Ammonia may be such a carrier. The co-combustion of ammonia and methane in a medium-speed four-stroke natural gas marine engine is considered. As it is already implemented in SI gas engines. The pre-chamber is proposed for ignition initiation. The development of fuel systems is influenced by three main factors use of new fuels, new emission regulations, and changes in load distribution.

Efforts are being made to introduce models of engine operation using machine learning for their control under changing operating conditions.

Due to the use of fuels with inferior properties, control algorithms appropriate for the current fuel are introduced.

Nomenclature

CI	compression ignition
LNG	liquefied natural gas
OBD	on-board diagnostic
LPG	liquefied petroleum gas
SI	spark ignition

Bibliography

[1] Balcerski A, Kropiwnicki J. Remarks upon adequacy of conditions of ISO 8178 emission tests with regards to real operation conditions of marine engines. Journal of KONES. 2008:23-30.

[2] Electic shiping and hybrid ships. https://ww.wartsila.com/marine/products/ship-electrification-solutions

[3] IMO Marine Engine Regulations https://dieselnet.com/standards/inter/imo.php

[4] Kazienko D, Chybowski L. Instantaneous rotational speed algorithm for locating malfunctions in marine diesel engines. Energies. 2020;13:1396. https://doi.org/10.3390/en13061396

[5] Kowalski J. The model of combustion process in the marine 4-stroke engine for exhaust gas composition assessment. Combustion Engines. 2016;165(2):60-69. https://doi.org/10.19206/CE-2016-208

[6] Mańczak J. Silnik okrętowy RT-flex 60C/RT-flex 60C Marine Diesel Engine. Silniki Spalinowe. 2004;118(1):10-18.

[7] MAN Energy Solutions. www.man-es.com

[8] RT Flex Fuel Operation. www.youtube.com/watch?v=dOEMn7LhbaA

[9] Wartsila: Manual Operator flexView. FlexView configuration revision 3496 with lexView.exe version 3.9.7.

[10] Wartsila: Wartsila low-speed dual-fuel solution.

[11] Woodyard D. Pounder's Marine Diesel Engines and Gas Turbines. 8th Edition, 2003 eBook.

[12] Wu X, Feng Y, Gao Y, Xia C, Zhu Y, Shreka M et al. Numerical simulation of lean premixed combustion characteristics and emissions of natural gas-ammonia dual-fuel marine engine with the pre-chamber ignition system. Fuel. 2023; 343:127990. https://doi.org/10.1016/j.fuel.2023.127990

[13] Xie L, Sun S, Dong F. The non-uniformity control strategy of a marine high-speed diesel engine based on each cylinder's exhaust temperature. Processes. 2023;11(4);1068. https://doi.org/10.3390/pr11041068

Zbigniew Kneba, DSc., DEng. – Faculty of Mechanical Engineering and Ship Technology, Gdansk University of Technology.
e-mail: *zkneba@pg.edu.pl*

[14] Zhang J, Meng Y, Liu D, Liu L, Ma X, Jiang C et al. Modelling and multi-objective combustion optimization of marine engine with speed maintaining control target. Thermal Science and Engineering Progress. 2023;41:101852. https://doi.org/10.1016/j.tsep.2023.101852

Article citation info:
Kubica G. Combustion of LPG/DME gas mixtures in an SI engine with correction of the ignition advance angle. Combustion Engines. 2023;194(3):147-152. https://doi.org/10.19206/CE-168401

Grzegorz KUBICA

Combustion Engines
Polish Scientific Society of Combustion Engines

Combustion of LPG/DME gas mixtures in an SI engine with correction of the ignition advance angle

ARTICLE INFO

Received: 31 May 2023
Revised: 15 June 2023
Accepted: 15 June 2023
Available online: 4 August 2023

The paper presents the results of tests on a SI engine fueled with an LPG/DME blends of various composition. A number of experimental studies and calculations using a mathematical model were carried out to examine the suitability of this fuel. These tests allowed for the analysis of the changes taking place in the combustion process and the assessment of the main operating parameters of the engine. The engine was powered by an LPG/DME fuel mixture with different proportions of components. The share of DME ranged from 0% to 30% of the fuel mass. The obtained results reflect the operation of the engine in the full load range and selected rotational speeds. Measurement series were made for different settings of the ignition advance angle. Based on the obtained results, a corrected map of the ignition advance angle was developed. The obtained results confirm the usefulness of using the LPG/DME mixture to power the SI engine.

Key words: *LPG/DME, fuel blend, combustion, SI engine*

1. Introduction

One of the main directions of energy transformation in the global economy is the increase in the use of renewable fuels. Dimethyl ether (DME) is a real part of this strategy because it has favorable physical and chemical properties and can also be obtained using renewable energy sources [15]. Research results published in recent years show DME as a modern fuel, both in diesel engines [3, 6, 14, 16, 17] and in SI engines as an addition to LPG [4, 13, 18].

Features of modern fuel include the possibility of a significant reduction of PM and NO_x emissions in a diesel engine [12]. Tests of LPG/DME mixtures also confirm the possibility of meeting the applicable exhaust emission standards in a car with an SI engine, while maintaining similar traction properties [5, 11]. The results of the conducted research indicate the possibility of increasing the share of DME in the mixture to 30% by weight. Such fuel can also be used in liquid-phase injection power systems [1].

The superior attribute of this fuel is the fact that it can be an element of the fuel chain based on the use of so-called green hydrogen [13]. In this system, DME is a product made using H_2 and CO_2. The main attribute is obtaining a high-energy fuel, the storage and distribution of which is much less energy-intensive than in the case of hydrogen. In addition, there is also the possibility of reusing the emitted CO_2 [10]. Due to the above aspects, research on the use of DME in various branches of the economy is intensively conducted. Therefore, the use of DME as a fuel requires a thorough knowledge of the combustion process and its products in relation to the performance parameters of the engine [2, 9, 19].

The above aspects motivate to carry out research with this fuel and to analyze the combustion process. Contrary to the published test results, the scope of this study also includes measurements made at partial engine loads. This scope of the experiment is much more in line with real engine operation in road conditions.

2. Experimental studies

2.1. Measurement set-up

The popular passenger car powered by a 1.6 liter engine, naturally aspirated with a compression ratio of 9.6, port fuel injection, two valves per cylinder, flat pistons and without external EGR was used in the experiments. The experiments were performed on a MAHA MSR500 chassis dynamometer. The main features characterizing the engine installed on the tested vehicle have been listed in Table 1. Engine performance has been estimated on the basis of acquired dynamic characteristics, defining the power on wheels in the function of vehicle speed. The test stand has been equipped with various transducers and sensors allowing the identification of engine operating conditions. Basic measurements and control systems allowed continuous acquisition of engine operating conditions, through registrations of:

- in-cylinder pressure
- crank angle, with the TDC identification
- power on wheels
- manifold pressure
- inlet air temperature
- exhaust gases temperature
- fuel mass flow to the engine.

Table 1. Engine specification

Parameter	Value
Engine code	X16SZR
Cylinder number and layout	4 R
Maximum power	55 kW@5200 rpm
Maximum torque	128 N·m @2800 rpm
Displacement	1598 ccm
Bore x stroke	79.0 × 81.5 mm
Compression ratio	9.6

The in-cylinder pressure was measured by Kistler 6121 piezoelectric pressure transducers and a charge amplifier, Kistler 5011A. The signals were processed in type NI PCI-

6143 board in a computer for online pressure measurements. The pressure recording system was also connected to the Kistler 2613B crank angle encoder giving the temporal resolution of the pressure recordings of 0.5 deg CA.

The pressure measurements were recorded and stored on a computer, with recordings performed for 150 subsequent cycles in each test, and were further processed with the help of a script debugged in LabView 7.1 environment.

Fig. 1. Tested car on dynamometer chassis

Fig. 2. Stand for preparing of LPG/DME blends

2.2. Methodology of research

The main purpose of the conducted research is to determine the effect of changes in the ignition advance angle on the basic parameters of engine operation using fuels with different DME content. The change of the ignition advance angle is carried out by introducing into the algorithm of the engine controller a set value correcting the angle determined by the controller. During the tests, two additional degrees of correction were applied, increasing the ignition advance by 3 and 6 degrees CA compared to the factory controller settings. For each measurement point, three measurements were made, one at the nominal ignition timing (without correction) and two more using the given correction values. The scope of the tests carried out included measurements in steady states of engine operation at selected rotational speeds and variable engine load. The following rotational speeds were selected for the tests: 2000, 2500 and 3000 rpm. The degree of engine load is equivalent to the width opening of the throttle (WOT). The test was performed for the following engine loads: 21, 33, 48, 60, 75, 90 and 100%.

3. Simulation studies of the combustion process

Experimental tests carried out on a chassis dynamometer allowed for the measurement of the most important operational parameters and, at the same time, for a detailed analysis of the combustion process involving DME mixed with LPG in various proportions. The basic parameter determining the possibilities of using DME is the power measured on the wheels of the vehicle. The IA correction carried out in the second series of tests revealed the possibility of increasing the power of the tested engine. The results of these measurements were presented in an earlier publication [8].

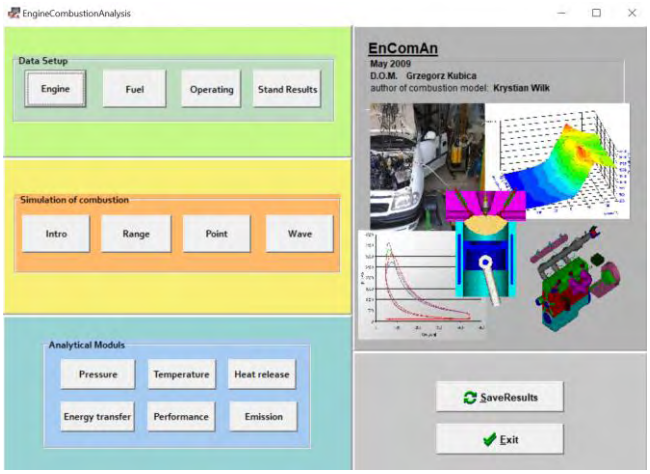

Fig. 3. The main form of the simulation program

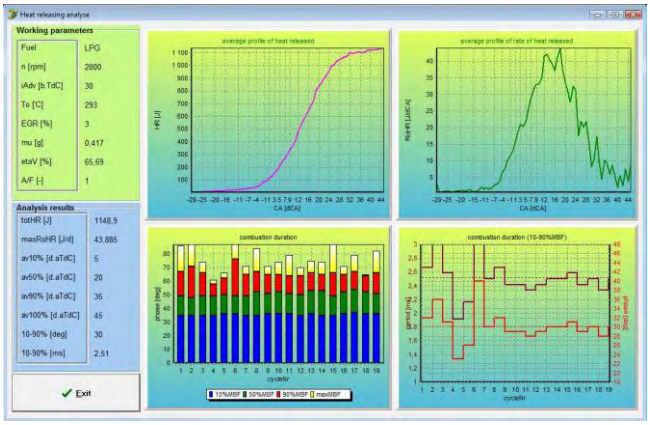

Fig. 4. One of the *EnComAn* calculation form

On the basis of the recorded experimental results, calculations of thermodynamic parameters characterizing the combustion process were performed. Simulation studies were performed using the *EnComAn* application (Fig. 3), which is a proprietary product. The program is designed for

comprehensive calculations of thermodynamic processes in the engine cylinder, using a mathematical model [7]. Simulation calculations are carried out on the basis of the course of pressure in the combustion chamber recorded in experimental tests (Fig. 4). The analysis of this signal allows to determine the so-called representative sample and perform statistical calculations of the indicated pressure. The *EnComAn* simulation program calculates a number of parameters describing the combustion process. These include:

– fresh charge and exhaust gas temperatures
– heat release in the combustion process
– current exhaust gas composition (including 10 components)
– heat transfer between the walls and gases in the combustion chamber
– engine operating parameters.

4. Discussion of the results

The addition of DME to LPG changes the composition of the fuel. The most significant change is the presence of oxygen in the DME molecule. This means that the need for oxygen-containing air to burn the load decreases. Providing oxygen in this form increases the efficiency of filling, which has a positive effect on the performance of the engine. The second important feature of DME is its ease of self-ignition, which is reflected in its high cetane number. Therefore, a detailed analysis of the course of the combustion process is important. The introduction of the correction of the ignition advance angle makes it possible to assess the possibilities of obtaining the best organization of this process, both in terms of the heat release function and the effects of its course. The corrected map of the IA angle settings is shown in the diagram (Fig. 5).

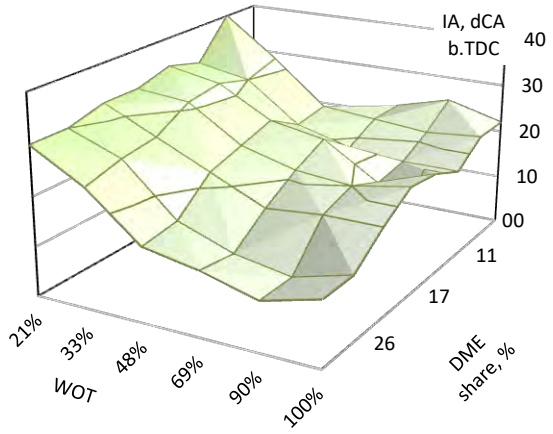

Fig. 5. Corrected map of IA angle, n = 3000 rpm [8]

The correction of the ignition advance angle ensures an increase in engine power in practically the entire engine load range. The indicated power at nominal IA settings is shown in the diagram (Fig. 6). The maximum values of the obtained power after IA correction are shown in the graph (Fig. 7), while the averaged trends of changes for all tested LPG/DME mixtures are shown in a separate graph (Fig. 8).

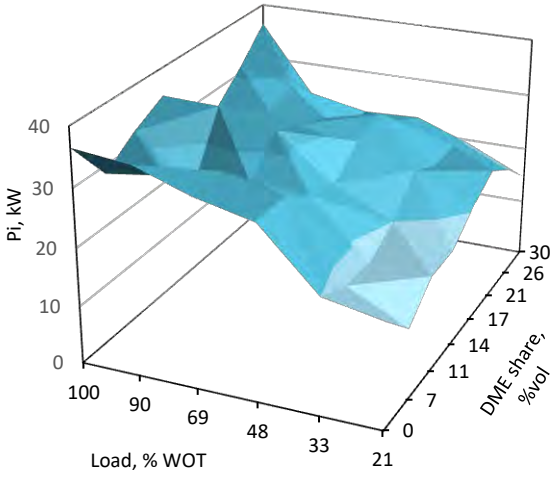

Fig. 6. Indicated power before IA correction, n = 3000 rpm

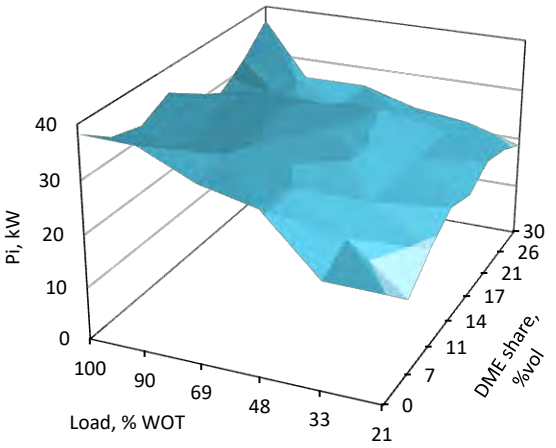

Fig. 7. Indicated power after IA correction, n = 3000 rpm

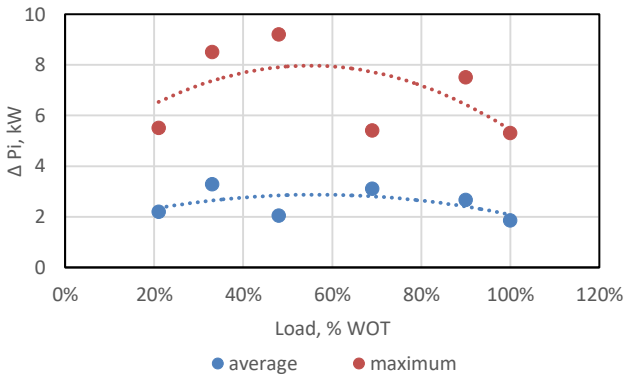

Fig. 8. Changes in indicated power, averaged for all tested fuel blends

As further results indicate, this is related to the amount of energy released in the combustion process, as HR changes in the entire range of tests show similar trends (Fig. 9 and Fig. 10). For all tested loads, there is a slight increase in this parameter (Fig. 11). These changes result rather from a greater dynamics of the charge exchange, because the IA settings do not directly affect the filling of the cylinder and the amount of fresh charge.

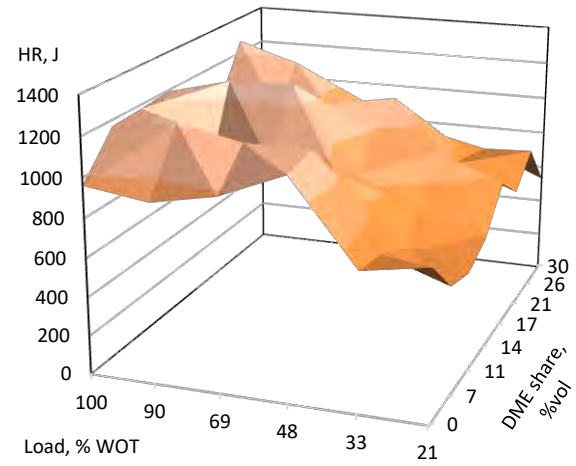

Fig. 9. Heat release amount before IA correction, n = 3000 rpm

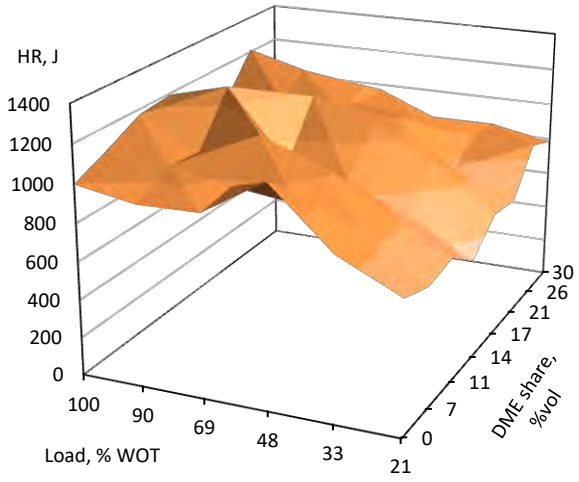

Fig. 10. Heat release amount after IA correction, n = 3000 rpm

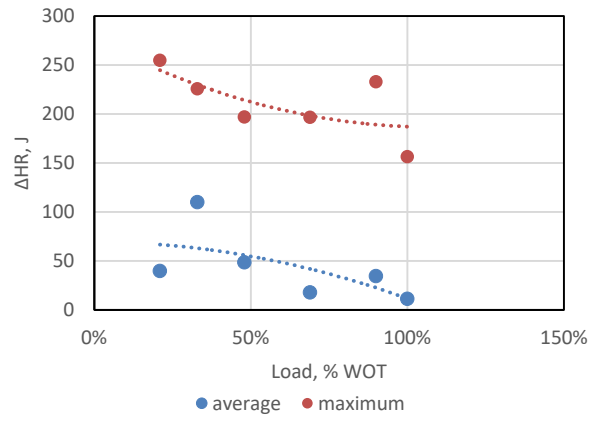

Fig. 11. Changes in HR, averaged for all tested fuel blends

The correction of the IA most strongly interferes with the nature of the combustion process, because it changes its correlation with changes in the pressure in the cylinder caused by the movement of the piston. This is also visible in the changes in the temperature of the gases in the combustion chamber (Fig. 12). The maximum temperature inside the cylinder chamber at nominal IA settings is shown in the diagram (Fig. 13). The area of greatest changes includes mixtures with a share of 7%, 11% and 14% DME. A clear increase in gas temperature occurs in the entire engine load range (Fig. 14).

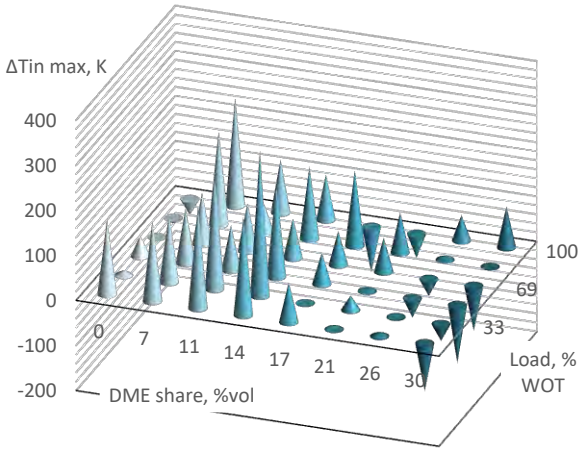

Fig. 12. Changes in the maximum temperature in the cylinder, n = 3000 rpm

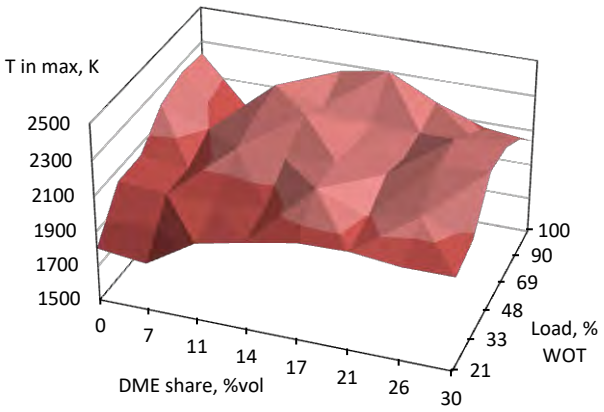

Fig. 13. The maximum gas temperature in the cylinder, IA nominal

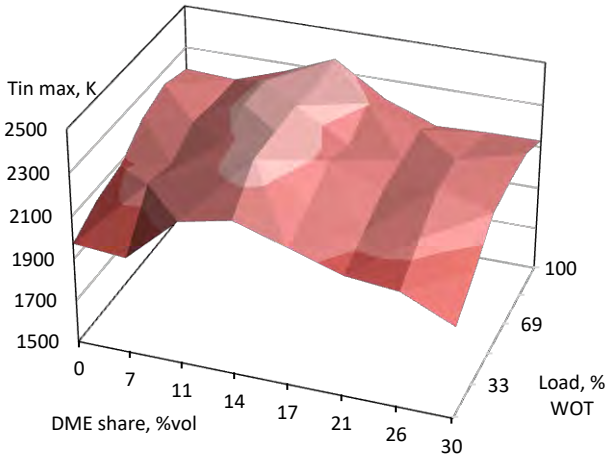

Fig. 14. The maximum gas temperature in the cylinder, IA corrected

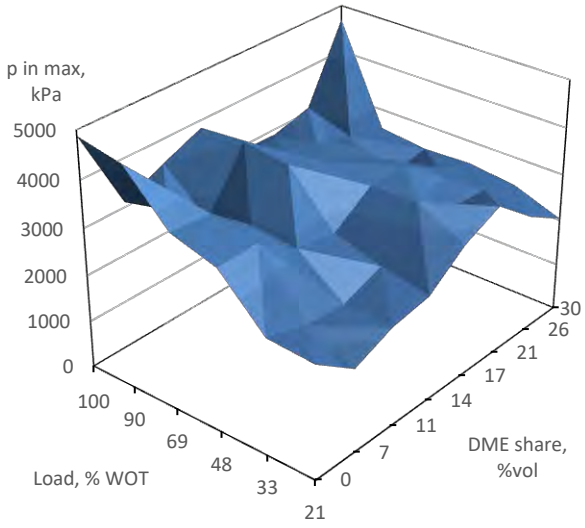

Fig. 15. The maximum in cylinder pressure, IA nominal

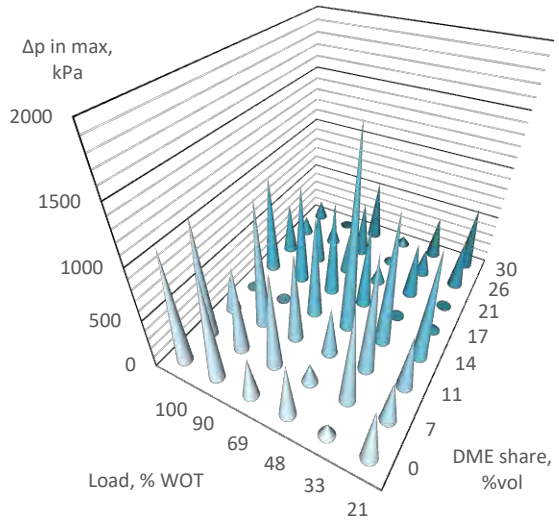

Fig. 16. Changes of the maximum in-cylinder pressure, n = 3000 rpm

The parameter that reflects the influence of all factors shaping the changes taking place in the engine cylinder is the indicated pressure. The maximum in-cylinder pressure for nominal IA settings is shown in the diagram (Fig. 15). The obtained measurement results show an increase in the pressure value practically throughout the entire range of tests (Fig. 16). Of course, the increase in pressure also results in an increase in engine performance, which is desirable. However, too high increase in pressure, especially caused by a rapid increase in dp/dφ, leads to loss of control over the combustion process and so-called burnout may occur. knocking combustion. The control parameter for such behavior is the standard deviation of the mean pressure indicated by COV_{imep}. The test results indicate that although in some operating states, there may be a greater non-repeatability of subsequent work cycles (Fig. 17), this increase is small, below 2%. The average values of changes in this parameter are negative in the entire load range, which indicates that the combustion process is generally stable and the repeatability of successive work cycles is greater.

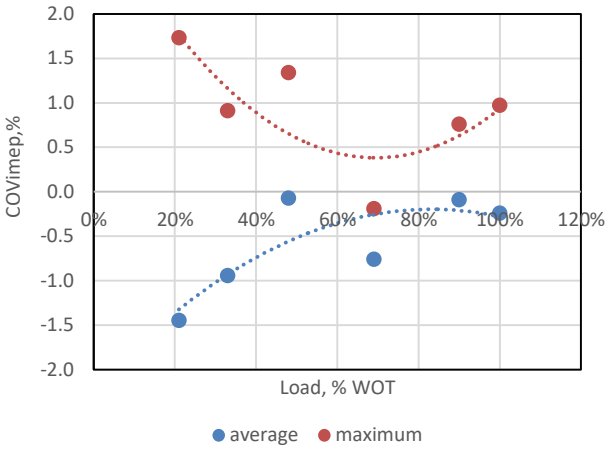

Fig. 17. Changes of value COV_{imep} after IA correction, averaged for all tested fuel blends, n = 3000 rpm

5. Conclusions

The course of the conducted tests and the analysis of the obtained results allow to conclude that:

1. The use of the DME additive in a mixture with LPG is, in terms of observation of dynamic parameters and the combustion process, a fully valuable and useful fuel that does not impair the performance of an engine fueled only with LPG.
2. Introduction of an additional correction of the IA angle, in relation to the factory settings, allows to obtain higher power values, on average by 3 kW (Fig. 6).
3. The correction of the IA does not significantly affect the total amount of HR in the engine's working cycle, but it improves the dynamics of the combustion process, which results in an increase in temperature and pressure in the cylinder. The highest increase in these parameters occurred for mixtures containing DME in the range of 7–14%. The temperature rise in this area is 80–100 K for all load levels tested.
4. The results of the measurements indicate higher values of the indicated pressure in the whole range of engine load changes, for all tested LPG/DME mixtures. However, the occurring pressure increases are not the result of disturbances in the combustion process, as evidenced by the calculated changes in COV_{imep} values.
5. Despite the fact that the results of published tests carried out in other centers show that the requirements of emission standards are met [5, 11] and the possibility of reducing CO_2 emissions [16], in the case of interference with the engine control parameters, it is necessary to carry out appropriate exhaust emission tests, to determine the total usability of this type of fuel.

Nomenclature

b.TDC	before top dead center
CA	crank angle
COV_{imep}	cyclic variation of indicating mean effective pressure
DME	dimethyl ether
EGR	exhaust gas recirculation
HR	heat released
IA	ignition advance
LPG	liquified petrolum gas
PM	particulate matter
SI	spark ignition
WOT	width opening of the throttle

Bibliography

[1] Baek S, Lee S, Shin M, Lee J, Lee K. Analysis of combustion and exhaust characteristics according to changes in the propane content of LPG. Energy. 2022;239:122297. https://doi.org/10.1016/j.energy.2021.122297

[2] Cai P, Liu Z, Li M., Zhao Y, Li P, LI S et al. Experimental study of effect of equivalence ratio and initial turbulence on the explosion characteristics of LPG/DME clean blended fuel. Energy. 2022;250:123858, https://doi.org/10.1016/j.energy.2022.123858

[3] Donggon L, Chang Sik L. Effects of DME-isobutane blended fuels on combustion and emissions reduction in a passenger car diesel engine. J Energ Eng. 2017;143(41):04017003. https://doi.org/10.1061/(asce)ey.1943-7897.0000428

[4] Fabiś P. DME as a fuel for SI engines cars. Diagnostyka. 2021;22(1):93-99. 2021. https://doi.org/10.29354/diag/133476

[5] Flekiewicz M, Kubica G. The influence of selected gaseous fuels on the combustion process in the SI engine. Transport Problems. 2017;12:135-146. https://doi.org/10.20858/tp.2017.12.3.13

[6] Kozak M, Lijewski P, Waligórski M. Exhaust emissions from a hybrid city bus fuelled by conventional and oxygenated fuel. Energies. 2022;15:1123. https://doi.org/10.3390/en15031123

[7] Kubica G. An efficiency of energy conversion in a spark ignition engine fuelled with a low-carbon gaseous fuels. Monographic publishing series Library of Operational Problems – Studies and Dissertations, Publishing House of the Institute for Sustainable Technologies-National Research Institute in Radom. 2013 (in Polish).

[8] Kubica G, Marzec P. An influence of correction of the ignition advance angle on the combustion process in SI engine fuelled by LPG with the addition of DME. Journal of KONES. 2019;26:285-292. https://doi.org/10.2478/kones-2019-0119

[9] Marszałek N. The impact of thermodynamics parameters of turbofan engine with ITB on its performance. Combustion Engines. 2020;182(3):16-22. https://doi.org/10.19206/CE-2020-303

[10] Mondal U, Yadav GD. Perspective of dimethyl ether as fuel. Part I. Catalysis, Journal of CO_2 Utilization. 2019;32: 299-320. https://doi.org/10.1016/j.jcou.2019.02.003

[11] Pathak S, Sood V, Singh Y, Gupta S, Channiwala SA. Application of DME 20 fuel in a gasoline passenger car to comply with Euro IV emission legislation. SAE Technical Paper 2017-01-0872. 2017. https://doi.org/10.4271/2017-01-0872

[12] Putrasari Y, Lim O. Dimethyl ether as the next generation fuel to control nitrogen oxides and particulate matter emissions from internal combustion engines: a review. ACS Omega. 2022;7(1):32-37. https://doi.org/10.1021/acsomega.1c03885

[13] Semmel M, Ali RE, Ouda M, Schaadt A, Sauer J, Hebling C. Power-to-DME: a cornerstone towards a sustainable energy system. Power to Fuel. 2021:123-151. https://doi.org/10.1016/B978-0-12-822813-5.00010-2

[14] Smolec R, Idzior M, Karpiuk W, Kozak M. Assessment of the potential of dimethyl ether as an alternative fuel for compression ignition engines. Combustion Engines. 2017; 169(2):181-186. https://doi.org/10.19206/CE-2017-232

[15] Stepanenko D, Kneba Z. DME as alternative fuel for compression ignition engines – a review. Combustion Engines. 2019;177(2):172-179. https://doi.org/10.19206/CE-2019-230

[16] Sun C, Liu Y, Qiao X, Ju D, Tang Q, Fang X et al. Experimental study of effects of exhaust gas recirculation on combustion, performance, and emissions of DME-biodiesel fueled engine. Energy. 2020;197:117233. https://doi.org/10.1016/j.energy.2020.117233

[17] Wang J, Yu H, Li M, Liang X, Liu H. Experimental and numerical study on effects of impingement parameters on fuel-air mixture formation in the near wall region for diesel-DME blended fuels. SAE Technical Paper 2018-01-0920. 2018. https://doi.org/10.4271/2018-01-0920

[18] Zhang Q, Chen Y, Fan T, Yuan M, Liu Z, Huang P et al. Flame dynamics and flammability limit of DME(30%)/LPG blended clean fuel in elongated closed pipeline under multi-factors. Fuel. 2019;254:115731. https://doi.org/10.1016/j.fuel.2019.115731

[19] Zubel M, Lehrheuer B, Pischinger S. Impact of increased injector nozzle hole diameters on engine performance, exhaust particle distribution and methane and formaldehyde emissions during dimethyl ether operation. Int J Engine Res. 2021;22:503. https://doi.org/10.1177/1468087419860954

Grzegorz Kubica, DSc., DEng. – Faculty of Transport and Aviation Engineering, Silesian University of Technology, Katowice, Poland.
e-mail: *grzegorz.kubica@polsl.pl*

AIR FORCE INSTITUTE OF TECHNOLOGY
INSTYTUT TECHNICZNY WOJSK LOTNICZYCH

ul. Księcia Bolesława 6, 01-494 Warszawa, Poland
tel.: +48 261 851 300; fax: +48 261 851 313
www.itwl.pl e-mail: poczta@itwl.pl

SUPPORTING OPERATIONS & MAINTENANCE OF AERONAUTICAL ENGINEERING:

- tribological diagnostics of lubrication systems in power units and hydraulic systems
- endoscopic examinations of power units
- measurements of operation parameters of power units using one's own and company systems and their analysis

DEVISING AND DEVELOPING NEW DIAGNOSTIC METHODS:

- CT examinations – V/tome/X CT system
- blade vibration measurements using the tip-timing method

NEW TECHNOLOGIES FOR UNMANNED AERIAL VEHICLES:

- technical condition monitoring system of mini jet engine
- hybrid drive of unmanned aerial vehicle

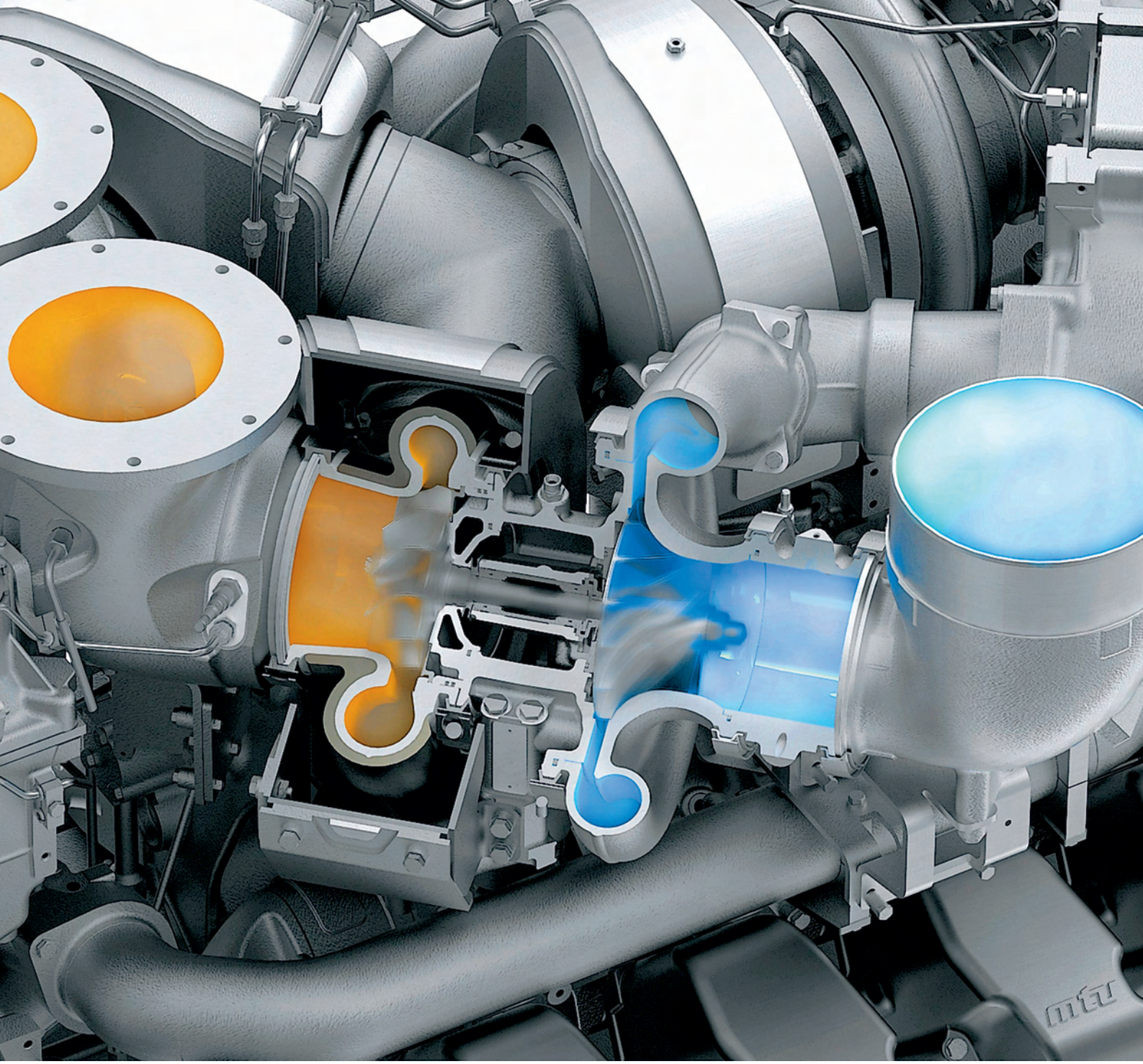

Publisher:

Polish Scientific Society of Combustion Engines

ISSN: 2300-9896
eISSN: 2658-1442

Combustion Engines

Polskie Towarzystwo Naukowe Silników Spalinowych

www.combustion-engines.eu